7-29-2019

A Novel Approach to Generating Lipid Membranes of Arbitrary Shape and Composition

Kevin Boyd
University of Connecticut - Storrs, kevin.boyd@uconn.edu

A Novel Approach to Generating Lipid Membranes of Arbitrary Shape and Composition

Kevin Boyd, PhD

University of Connecticut, 2019

Biomembranes are essential to cell structure and function. The function of these membranes is dependent not just on their composition of lipids and proteins, but also the distinct morphologies and shapes they present. In recent years, both experiments and simulations have begun to explore the relationship between membrane function and shape, but in this field, there is much to still be explored. The bulk of this work is dedicated to the development and application of techniques to build and study curved membranes in molecular dynamics simulations, using mitochondrial membranes as the primary biological system of study.

The inner mitochondrial membrane (IMM) houses the ATP generating machinery of Eukaryotic cells. IMM morphology consists of flat boundary regions coupled to highly curved cristae, with the various protein components of the membrane distributing to specific regions of these structures. Chapter 2 of this thesis explores the structural properties of mitochondria-mimetic membranes through simulated buckling, particularly studying the effects of cardiolipin, the signature lipid of the mitochondrion. Through buckled membranes we also gain insight into curvature-mediated partitioning of lipid components.

Chapter 3 of this thesis further explores the role of cardiolipin through study of monolysocardiolipin, a biosynthesis intermediate of cardiolipin which accumulates in

several diseases. Cardiolipin and monolysocardiolipin are studied in a comparative manner using both atomistic and coarse-grained molecular simulations, and potentially important differences in structural and dynamic properties between these membrane components are identified at both molecular and mesoscales.

A limitation of the work in Chapters 2 and 3 is the reductionist nature of studying pure lipid systems in flat or buckled states. Chapter 4 attempts to more closely model physiological membrane conditions by modeling cristae-like structures, a difficult task which requires new techniques for generating and maintaining membrane shapes. We further attempt to model more realistic membranes by studying the membrane structural effects of embedded ATP synthase – a key protein not only for energy production but also for maintaining mitochondrial morphology.

The curvature-related explorations of this and other studies highlight the need for a framework in which molecular simulations of curved membranes can be set up in a fast and flexible manner – a feat that has been accomplished for simulations of *flat* membranes, but not fully developed for curved systems. Chapter 5 of this thesis presents BUMPy, a python tool developed for this specific purpose. BUMPy is fast, flexible in both the range of shapes it can create as well as membrane composition, and can accurately model interleaflet area differences arising from curvature.

A Novel Approach to Generating Lipid Membranes of Arbitrary Shape and Composition

Kevin J Boyd

B.S., University of Connecticut, 2014

A Dissertation

Submitted in Partial Fulfillment of the

Requirements for the Degree of

Doctor of Philosophy

at the

University of Connecticut

2019

APPROVAL PAGE

Doctor of Philosophy Dissertation

A Novel Approach to Generating Lipid Membranes of Arbitrary Shape and Composition

Presented by

Kevin J Boyd, B.S.

Major Advisor

_____

Eric May

Associate Advisor

_____

Nathan Alder

Associate Advisor

_____

Philip Yeagle

University of Connecticut

2019

Acknowledgements

I'd first like to thank Eric, for being an incredible mentor both when I was an undergrad and during my PhD. Eric offered support whenever I needed it, and gave me the freedom to work on projects that interested me. He was supportive not just in a scientific context, but also whenever I went through hard times. I'll fondly remember all of our whiteboarding and brainstorming sessions.

Next, I'd like to thank Nathan, my coadvisor, who was also a fantastic collaborator throughout my PhD. The projects I ended up pursuing related closely to the work of the Alder lab. When I had health issues and my career was in flux, Nathan and Eric graciously welcomed me back and we embarked on a joint project that has produced fantastic results.

I'd like to thank the other members of my committee, who provided excellent insights. I believe I benefited from having advisors with particular expertise in specific areas. Philip Yeagle, Elena Dormidontova and Peter Gogarten provided important insights in areas such as membrane biophysics, technical details of mesoscopic simulations, and understanding of the relevant bioenergetics. In addition, they have all been incredibly supportive during this process.

The May Lab has been a fantastic group to work with all these years. I have the distinction of having worked with every single member of the May Lab, and we've all grown as scientists together. Shout out to past members Allyn Bryce, Deaneira Lakheram, Maneesh Koneru, Mickey Ward, Prakhar Bansal, and Shaan Kamal, and current members Aaron Feinstein, Aberdeen Taylor, Asis Jana, IC Duay, JD "JD"

Tamucci, Shivangi Nangia, and most of all Jason Pattis, who's been with (read: put up with) me since the beginning.

I've worked on a number of cool side projects, collaborating with both the Robinson Lab and Alder lab. I'd like to thank everyone from both of those labs, particularly Melissa Brundin, who's been an amazing collaborator. Thanks also to Peter Burkhard and his lab, especially Chris Karch.

I'd like to thank the rest of the 2nd floor of BPB, and the rest of the squad in the department and our friends: all of you maniacs. Special shout out to my current and former roommates Stephen, Dylan, Richard, Jason and Tyler.

One of the key aspects to finishing a PhD is not dying of cancer first. With that in mind, I'd like to thank the doctors and nurses of Yale-New Haven hospital.

I've had fantastic opportunities for personal and professional development. The software engineering skills I've developed over the last few years have directly impacted the quality of my PhD work, and have set me up for the future. The Gromacs team was incredibly helpful in this area, accepting a newbie into their project and guiding my development. I believe I've received much more in that exchange than I've given.

My parents have kept me sane during this process (or near enough). Their emotional support and advice have been indispensable. I can't imagine finishing this PhD without being able to call them at any time, and we've been through quite a lot these past 5 years. I'd like to thank my brothers as well, for the good times and needed distractions. There's also my dog Casey, who's somehow managed to last all this time. The rest of my family has been fantastic, especially after my parents and brothers moved out of

Connecticut. I'd like to particularly mention my uncle Lou, who is no longer with us; he helped me out a lot, and will be missed.

Finally, there's Emma. I don't know where I'd be without you, and there's nobody I'd rather share this moment with.

List of Figures

Table of Contents

Chapter 1: Introduction

A defining feature of all cellular life is the compartmentalization of self from non-self. In the typical cellular context, the cell divides its internal constituency from the aqueous surroundings via a membrane composed of (predominantly) lipids and proteins. This compartmentalization accomplishes several goals. It allows for the propagation of genetic material through cellular division, facilitates the accumulation of important metabolites, and serves as a layer of protection from harmful pathogens.

Eukaryotic cells take further advantage of the compartmentalization offered by biomembranes through internal division of the cellular space into organelles, allowing for much more functional complexity. Genetic material is encapsulated in the nucleus, while the majority of energy production occurs in mitochondria. The secretory apparatus of cells is composed of a series of vesicles and sac-like compartments that iteratively post-process nascent proteins bound for various other cell compartments or the extracellular space.

In addition to forming physical barriers and transport containers, membranes also play an active role in most cellular processes. Membranes house a large number of proteins both embedded and peripheral, which are essential for cellular function. Lipids of the membrane themselves can act as substrates for enzymes or signaling molecules. In sum, biological membranes are both an essential structural and functional feature of cells.

Membrane curvature plays a key role in modulating the function of membrane components, and likewise the components of a membrane play an active role in sculpting its morphology. This curvature can be seen from the mesoscale in the shape of cell membranes down to the nanoscale with tightly curved morphologies of organelles such as the mitochondrion.

The bulk of this thesis is dedicated to exploring membrane-curvature related phenomena through molecular dynamics simulations. Through a variety of methods, we study the effect of both protein and lipid components on curved membrane stability, and then use curved

membrane systems to study the effect of curvature on structure, dynamics, and spatial self-organization.

The study of membrane curvature requires an understanding of the physics underlying curvature energetics. Section 1 of this introduction will introduce the key physical concepts that govern membrane curvature and shape, and Section 2 will provide an overview of previous work in the simulation field to study various aspects of membrane curvature. While this introduction is focused on the relevant physics and simulation techniques, relevant biological background will be provided in the introductions of Chapters 2, 3, and 4.

1.1 The physics of membrane curvature

At the mesoscale, it is most common to model a lipid bilayer as a planar continuum with finite thickness. This continuum can then undergo several modes of deformation with associated energetic states.

1.1.1 Area expansion and contraction

A flat bilayer with finite size can undergo expansion and/or contraction in the lateral plane of the membrane. The energetics of these deformations is described in Equation 1[1]

$$E_{stretch} = \frac{K_A(A - A_o)^2}{2A_o} \qquad (1.1)$$

where A is the area, A_o is the pre-stretch (equilibrated) area, and K_A is the area expansion modulus. The extent of resistance of a bilayer to stretching or compression is then only dependent on K_A. Expansion moduli of lipid bilayers can be probed by pipette aspiration of giant vesicles[2] or by atomic force microscopy probing of flat bilayers.[3] Measured K_A values for a number of phosphatidylcholine (PC) lipids have been determined, with the observed values lying in a tight range about 240 mN/m.[2]

1.1.2 Edge effects in finite membranes

Many lipid bilayer shapes form closed surfaces (such as spheres). However, one can also describe a bilayer patch that contains edges. These edges incur energy penalties, the magnitude of which can be described as $E_{edge} = \gamma \int ds$, where γ is the edge tension and the integral term corresponds to the arc of the curved edge[4]. The energy of an unmatched bilayer edge is therefore directly proportional to the length of the exposed edge. The edge tension of bilayers can be explored experimentally by induction of pores in membranes[5].

The energetic contributions of edge effects have important consequences for bilayer morphology. The interplay of bending energetics and edge tension can dictate the equilibrium in the formation of shapes such as vesicles.[4] The edge tension plays a role in the activity of membrane pores and yields a "critical" pore size beyond which a membrane will rupture[6]. Finally, the edge tension will influence the shape of a membrane patch will exposed edges. Given a specific lipid area, a circular shape minimizes the exposed edge and therefore the edge tension. A similar effect can be seen with phase separation in membranes. In a lipid bilayer with two distinct phases, the line tension determines the energy at the barrier between the separated phases. The energetic gain of phase separation must overcome this energetic penalty[7].

1.1.3 Bending energetics – the defining equation

At any point along a surface, the total curvature is composed of two orthogonal principal curvatures, C_1 and C_2. Curvature is the inverse of radius of curvature, and thus has units of inverse length (figure 1.1). In 1973, Helfrich put forth an expression for membrane bending energy per unit of area[8]:

$$E_b = \frac{1}{2} k_c (C_1 + C_2 - C_o)^2 + \bar{k} K \qquad (1.2)$$

where k_c is the bending modulus, C_o is the spontaneous curvature, $\bar{k}$ is the Gaussian curvature modulus, and K is the Gaussian curvature. Gaussian curvature is the product of the two principal curvatures. K_c, C_o, and $\bar{k}$ are properties intrinsic to membranes, and are dependent on the lipid composition. The bending energy of a non-lamellar lipid in a flat bilayer is thus $E_b = \frac{1}{2} k_c C_o^2$. Why then do flat bilayers with non-cylindrical lipids not spontaneously curve? In a bilayer with monolayers of identical composition, the drive to form curved geometries in one leaflet is matched exactly by a drive to curve in the opposite direction from the other leaflet, making the net spontaneous curvature zero.

1.1.4. The bending modulus

The bending modulus effectively acts as a spring constant for curvature of bilayers, and so is important in calculating the energetics of any number of relevant morphologies in the cell. The bending modulus can be probed using several approaches, such as pipette aspiration experiments or shape fluctuations, though these approaches can lead to different observed values for the same system[9]. Most observed k_c values for typical membranes are on the order of 10^{-19} J.[9]

The bending modulus is not only important for assessing the energetics of membrane conformations, but also plays a role in the dynamics of flat bilayers, which undergo undulations orthogonal to the lateral plane. In a tensionless membrane with area A, the amplitude (u) of an undulation with wavenumber q is governed by the following equation[10]

$$< u^2(q) > = \frac{kT}{Ak_c q^4} \quad (1.3)$$

Indeed, the aforementioned shape excitation experiments take advantage of this relationship to calculate k_c.

1.1.5 Spontaneous curvature

The spontaneous curvature C_o is an indicator of the preferred geometric environment of the membrane. C_o, which has units of inverse length, can be interpreted as the inverse of the energy-minimal radius of curvature. Deviations from this ideal curvature incur a quadratic energy penalty modulated by the bending modulus (equation 2). Spontaneous curvature can be determined for either a bilayer or monolayer. In the context of a monolayer, a positive C_o indicates a preference for curvature with the head groups on the convex side of curvature, and *vice versa* for membranes with negative spontaneous curvature.

According to the amphiphile shape hypothesis, the preferred phase of a lipid is determined by the size of its hydrophilic head group relative to that of its acyl chains. This relationship can be quantified using the shape parameter[11]:

$$S = \frac{V}{a * l} \qquad (1.4)$$

in which *V* is the volume occupied by the acyl chains, *a* is the head group area, and *l* is the length of the acyl chain. Lipids preferring the lamellar phase have S values around 1, while Hexagonal I(H_I) and micellar phases are characterized by lipids having S < 1 (positive C_o), and Hexagonal II (H_{II}) lipids have S > 1 (negative C_o). The driving force for this lipid phase behavior is lateral monolayer packing (figure 1.2). Lipids with S ~ 1 are roughly cylindrical in shape, and thus optimally pack side by side in a plane to form lamellar phases[12]. In contrast, conically shaped lipids pack optimally in a curved monolayer. H_I prone lipids curve with their headgroups facing out (lining the convex surface of the curved phase); H_{II} prone lipids curve with headgroups facing in (lining the concave face of the curved phase.

Non-lamellar lipids can still form lamellar bilayers in mixed systems. For instance, phosphatidylethanolamine (PE), a highly H_{II} preferring lipid, can be made to form lamellar

phases *in vitro* in mixtures with phosphatidylcholine (PC), a lamellar lipid, with a PC concentration as low as 20%.

1.1.6 The Gaussian curvature modulus

The Gaussian curvature modulus $\bar{k}$ is less well studied than the other elastic constants. The energetic term arising from the constant is proportional to the *product* of principal curvatures at any point on a surface (termed the Gaussian curvature), rather than the sum. Thus, both the magnitude and sign of the Gaussian curvature are important for determining the Gaussian contribution to the bending energy. While the Helfrich Hamiltonian places no restriction on the sign or magnitude of $\bar{k}$, it has been known for some time that the sign of $\bar{k}$ is negative,[10] and Templer et. al[13] have derived restrictions on the monolayer $\bar{k}$ in the range of [-k_c, 0]. Therefore, one can safely say that a shape with positive Gaussian curvature has a stabilizing contribution proportional to the Gaussian curvature magnitude and $\bar{k}$, and vice versa for shapes with negative Gaussian curvature.

It is instructive to look at the Gaussian curvature energy of different membrane shapes. For example, a simple cylindrical geometry (found in membrane tubules) only has nonzero curvature along one principal axis. Therefore, the Gaussian contribution is 0. On the other hand, a spherical vesicle has the same curvature in both principal axes for every point, both on the inner and outer leaflets. Therefore, the Gaussian curvature is positive at every point (regardless of if the mean curvature is negative), and the Gaussian contribution to the bending energy is stabilizing. Such differences may be important in cylinder vs spherical shape preference.

On the other hand, Gaussian curvature considerations do not play a role in the relative energetics of closed shapes (think vesicles of different sizes). The reason for this is explained with the Gauss-Bonnet theorem, which states that in a boundary-less system, the total Gaussian curvature is a topological invariant. This decoupling in closed shapes has made it difficult for

researchers to devise experimental setups to measurer $\bar{k}$. Most estimates of $\bar{k}$ come from simulations of bicontinuous cubic lipid phases[13–16] or phase-separated vesicle-like systems[17,18]. The observed magnitudes typically fall in the proscribed range described above, and k_c and $\bar{k}$ are typically found to have similar magnitudes[1]. Simulation methods that attempt to access $\bar{k}$ are described in section 1.2.2.

While the Gaussian curvature modulus does not affect the formation of closed shapes, it plays a very important role in fusion and fission intermediates. These shapes can have both positive and negative Gaussian curvature, and the energies of these transient structures has been estimated (for $\bar{k} \sim -k_c$) to be on the order of 250 k_bT[1]. Another relevant membrane shape displaying interesting curvature characteristics is a “neck” that couples curved regions such as tubules to flat boundaries. Stable examples of these shapes can be found in mitochondrial junctions.

1.1.7 Monolayer vs bilayer considerations

When one describes the elastic constants representing the deformation energetics of a membrane, it is important to distinguish between the monolayer and bilayer quantities, which can be described separately. For instance, a homogenous monolayer of a conical lipid such as phosphatidylethanolamine has a negative spontaneous curvature, and yet one can create stable flat bilayers of systems composed of 80% PE. Whereas the *monolayer* C_o is negative, the bilayer C_o is 0 through symmetry, *if* the individual monolayers have identical compositions. A nonzero bilayer spontaneous curvature can only arise from transverse asymmetry. The incorporation of non-bilayer lipids into flat bilayers induces internal stress, which can be observed in the local magnitudes of lateral stress profiles.

1.1.8 The Lateral Pressure Profile

Membranes display marked heterogeneity normal to the bilayer plane, from the bilayer center out to the solvent. These different regions of the membrane vary strongly in hydrophobicity, solvent accessibility, and mechanical stress. This latter quantity is related to the considerations discussed above. The average pressure in a lateral “slice” of membrane can vary by several orders of magnitude compared to the average bulk pressure. For instance, a reasonable estimate for physiological pressures is 1 bar, but local pressures can exceed 1000 bar[19] in simulations.

The lateral pressure profile (LPP) can be computed as the difference between lateral and normal pressures as one traverses normal to the membrane plane. For the purposes of discussion (and as a general convention), we say that the x and y dimensions are the planar dimensions of the bilayer, and the transverse lateral pressure profile traverses the z dimension. Given a stress tensor σ, at any point z, the lateral pressure $P_L = -0.5 * (\sigma_{xx} + \sigma_{yy})$, and normal pressure $P_N = -\sigma_{zz}$ contribute to the LPP: $\pi(z) = P_L(z) - P_N(z)$. It should be noted that we use both “stress” and “pressure” in discussions of these profiles. Technically, stress and pressure are related by a factor of -1, explaining the negative terms in the calculation of P_L and P_N from the stress tensor. At any point along the LPP, a positive pressure indicates repulsive interactions and a desire to expand, while a negative pressure indicates a drive to condense.

A simple representative LPP is shown in figure 1.3. Most bilayer LPPs have a number of common features. Moving from the center of the bilayer, one encounters positive repulsive forces in the acyl chain region arising from steric clashes (point 1), which are enhanced by lipid tail insaturations[19]. At the boundary between hydrophilic and hydrophobic regions, a large negative peak (point 2) is observed, which is attributed to the interfacial tension arising from the hydrophobic effect. Finally, head group repulsion (point 3) contributes another positive peak, and the LPP should level out at 0 in the solvent regime.

LPPs are quantitatively related to a number of physical properties of the membrane and its environment. One useful relation (particular for error checking in MD simulations) is that the integral of the LPP should equal the bulk pressure, or for a given system pressure P, $P = \int_0^\infty \pi(z)$. LPPs can also be related back to several elastic constants, as the integral of the first moment of the LPP corresponds to the product of the bending modulus and spontaneous curvature:

$$k_c c_o = \int_0^\infty z * \pi(z) \quad (1.5)$$

The second moment of the LPP is related to the Gaussian curvature modulus, with

$$\bar{k} = -\int (z - \delta)^2 \pi(z) \quad (1.6)$$

which unfortunately requires an estimate of δ, the location of the neutral surface. In addition, the validity of results obtained using this relationship have been questioned[4,20].

LPPs are difficult to probe experimentally due to the limited resolution of biophysical experiments, and so most quantitative reports of LPPs come from simulations (see section 1.2.2), though qualitative pressure readings can be performed using mechanosensitive fluorescent probes[21].

1.2 Molecular Dynamics simulations of membrane curvature

1.2.1 Representative models

One of the key limitations of MD simulations is spatial and temporal resolution. An enormous amount of effort in the field has gone into developing enhanced sampling techniques for proteins to accelerate their conformation sampling (see references [22] and [23] for reviews). Most of these techniques cannot be applied to pure membrane systems, as membrane properties are

emergent from the disordered dynamics of a large number of components (though they can be applied to proteins *within* membranes). With a few exceptions, membrane curvature typically occurs on the scale of tens of nanometers, which require significant time and computational resources to simulate. Nevertheless, a number of atomistic simulations have provided important insight into dynamics of curved morphologies (see sections 1.2.4 and onwards). In addition, important mesoscale properties can be inferred from simulations of smaller flat patches of bilayers whose dynamics converge on acceptable timescales (see section 1.2.2). However, to simulate larger systems and longer timescales, researchers typically must reduce the computational burden of simulations. For membrane systems, there are two (not mutually exclusive) commonly used ways to achieve simulation speedups – elimination of explicit solvent and coarse-graining.

Depending on the system dimensions, solvent tends to make up the majority of the particles. This is particularly problematic in curved membrane systems – the membrane component of a solvated vesicle might only be 5% of the system. Therefore, models that make solvent contributions implicit accelerate sampling by multiple orders of magnitude. A popular way to represent solvent implicitly is the Generalized Born method[24], which represents water as a dielectric continuum. The interface of solvent and bilayer cannot fully be captured via continuum models, however. To bridge this gap, a mean field boundary approach has been suggested[25], in which a small shell of solvent keeps vesicles solvated, and is maintained in the membrane vicinity by artificial potentials. Another proposed alternative is to treat the inside of a vesicle with explicit solvent, while treating extravesicular solvent implicitly[26].

The second approach to accessing the timescales necessary to study curvature-related phenomena is the use of coarse-grained models. Coarse graining involves replacing atomistic details with more granular representations. A large number of approaches exist to coarse-graining, but perhaps the most popular for membrane simulations is MARTINI[27], created and

maintained by the groups of Tieleman and Marrink. In this model, groups of up to 4 heavy atoms are represented by single beads, with the goal of the coarse-graining being that each bead retains the chemical signature of the constituent atoms. It should be noted that the computational benefits of this type of coarse-graining are not just the reduction of particle counts. In addition, the coarsening out of fast degrees of freedom (mainly h-bond vibrations) allows for larger integration timesteps. A third consideration is that coarse-graining typically smoothens the energy landscape, increasing conformational sampling compared to atomistic simulations[28]. MARTINI does have several drawbacks. Long range electrostatics are ignored in the typical MARTINI setup[28], and solvated ions are difficult to represent. Work has gone into extending MARTINI with a polarizable water model[29–31], and future work by the Marrink group will attempt to address some coarse-graining related accuracy issues with a multi-resolution model in future iterations (http://cgmartini.nl/).

While the MARTINI model is the most popular CG forcefield for membrane simulations, a few other approaches should be noted. Voth and colleagues have developed CG protein and membrane forcefields that are designed to reproduce atomistic behavior by basing interaction functions on atomistic observables[32]. While this requires fine-tuning of parameters for any molecule one wants to simulate, it can avoid CG-related inaccuracies from naïve mapping of atoms into beads representing a chemical grouping. This model has been applied for membrane-protein simulations as well, exploring topics such as membrane sculpting by BAR domains[33].

Another CG forcefield that has added value to the simulation field is the Cooke model, developed by Cooke and Deserno[34]. In this model, most lipids are represented simply as 3 connected beads, with two “tail” beads and one “head” bead. The tails are generally attractive, mimicking the hydrophobic effect responsible for membrane assembly and stability. Importantly, the relative “size” of the head group compared to the tails can be modulated by changing the

radius of its repulsive potential. This allows observation of lipid-geometry related membrane phenomena such as membrane phase and shape pereferences[35]. Even further levels of coarse-graining are possible (for instance, 1-bead lipid representations[36]), but one needs to more carefully consider the tradeoffs between simulation accessibility and accuracy. Indeed, at the most extreme level of coarse-graining one might prefer exploring problems using a continuum numerical model without particle dynamics.

1.2.2 Obtaining elastic constants from simulation

The elastic constants of membrane deformation also govern aspects of the structure and dynamics of flat membranes. Simulations have utilized these relationships in a number of ways to infer elastic parameters from computationally tractable simulations of flat bilayers. This section details some of the ways flat membrane simulations can contribute import results regarding curvature-related dynamics.

The Bending modulus - The bending modulus importantly governs the extent of energetic penalty arising from curvature deformations. A large number of methodologies have been proposed to extract k_c from simulations, most of them from flat atomistic systems. It should be noted that one difficulty in assessing the validity of these approaches is that strong variability exists in *experimental* measurements of k_c[37,38], depending on the technique used, and so it is difficult to obtain a "true" k_c value to validate simulations against.

Most k_c estimates from flat bilayers in essence analyze the spatial fluctuations of the bilayer using variations of the theory described in equation 1.3[39,40]. Some of these models also tie in the role of lipid tilt and orientation in thermal fluctuations[41,42]. Refinements to these methodologies are continually being contributed[43,44] and in some cases generalized for both lamellar and curved environments[45]. One can also explore undulations in a nonequilibrium

manner. Using an artificial restraint, one can force membranes to adopt specific amplitudes. The energy required to maintain those poses can be used to calculate k_c[46,47].

Harmandaris and Deserno were the first to design a simulation methodology to extract elastic constants from *curved* membranes. By measuring the tensile force arising from simulations of cylinders of various radii, the bending modulus can be determined and compares favorably to experiments and other computational methods[48]. Sodt and Pastor extract the bending modulus of lipids from simulations of H_{II} phases at varying hydration levels[49].

Compressibility – Similarly to the bending modulus, K_A can be extracted from both equilibrium fluctuations or from deforming the bilayer. In an equilibrium simulation, K_A is related to the lateral fluctuations of the simulation box size with[39,50]:

$$K_A = \frac{a_o}{<(a-a_o)^2>} k_b T \quad (1.7)$$

Where a and a_o are the average and instantaneous bilayer areas. This approach has the advantage of only requiring a single simulation to obtain elastic parameters. A recent approach has estimated K_A from equilibrium simulations by measuring bilayer thickness fluctuations, rather than area fluctuations[51]. This method has the advantage of being able to locally calculate quantities around proteins or in individual monolayers, important for asymmetric membranes.

K_A can also be extracted from simulations with non-zero surface tension. By running simulations with several surface tensions[50] and examining the resulting average areas, a linear fit of

$$\left(\frac{\partial \gamma}{\partial A_o}\right)_T = K_A / A_o^* \quad (1.8)$$

will yield K_A, with surface tension γ and the area at zero surface tension A^*_o. It should be noted that alternatively the box size can be fixed at a number of total areas, and the resulting calculated surface tensions used for the above fit[52].

Intrinsic curvature – There are several ways to obtain C_o estimates from simulations. The first of these is through the relationship between C_o and the features of LPPs. Equation 1.5 demonstrates that the integral of the first moment of the LPP corresponds to the product of bending modulus and spontaneous curvature, and so C_o can be extracted with an estimate of k_c[53,54]. Indeed, measurements of C_o from this method are a popular way to validate new CG forcefields[27,55]. However, we have demonstrated that the obtained values are quite sensitive to quite minor changes in the profile shape (reference [56], reproduced in chapter 3), and so the results of this method should be interpreted with caution.

A second method to calculate C_o in simulations is to mimic experimental measurements of hexagonal phases, by measuring at which curvature the phase is tensionless. *In silico*, this approach was first performed by Sodt and Pastor[49], who found that the two computational methods for obtaining C_o were comparable.

Gaussian curvature modulus – $\bar{k}$ is a difficult quantity to measure both experimentally and computationally, due to the consequences of the Gauss-Bonnet theorem (see section 1.1.6). The relative lack of quantities to compare to means that the approaches we do have lack extensive validation. However, a number of approaches have been proposed to address measuring this challenging modulus. Perhaps the first computational approach comes from den Otter, who estimate $\bar{k}$ from the free energy of pore formation[57] in a flat membrane, though they caution that these are preliminary estimates and that the model used may ignore some important features of the pore.

An ingenious method to estimate $\bar{k}$ *in silico* was proposed by Hu, Briguglio and Deserno in 2012,[4] and relies on the relative energetics of line tension and Gaussian curvature. This method starts a number of simulations of partial spheres, ranging from nearly fully spherical to nearly flat, and extracts $\bar{k}$ based on the probability of the spheres closing during the simulation. The results of this method lie within the theoretical bounds of physically realistic $\bar{k}$ values[20]. Zelisko and colleagues point out some potential inaccuracies in this approach[58], and suggest a different methodology measuring fluctuations of free edges, but this approach yields positive values of $\bar{k}$, out of step with other measurements.

Simple continuum treatments of bilayers relate $\bar{k}$ to the second moment of the lateral pressure profile. Hu and colleagues have questioned the validity of this relationship[20], as the values extracted from this approach are far from the expected range. Recently, Terzi and Deserno[59] have uncovered an overlooked contribution to membrane energetics that relates lipid tilt to curvature dependent on $\bar{k}$. The implications of this work are that many estimates of k_c from fluctuation power spectra are contaminated by not incorporating this term, but also that perhaps $\bar{k}$ can now be extracted from simple flat bilayer simulations as has been the case with K_A and k_c for some time.

Lateral pressure profiles – LPPs have been a tempting target for MD simulations, as the resolution required for computing these profiles is beyond the limits of traditional biophysical experiments. LPPs have been calculated for a large number of both atomistic and CG systems[19,60,61], and have been used in a number of applications from validating force fields[27,60] to examining effects of insaturation[19] and lipid composition. Interestingly, lateral stress modulation has even been proposed as a mechanism of action for general anesthetics[62].

To obtain the stress tensor from which LPPs are computed, contributions of all forces in the system need to be accounted for. This leads to a few complications for MD systems. One of

these is the contribution of electrostatics. Long range charged forces are typically treated with the Particle-Mesh Ewald summation, which is not easily decomposed[63]. Typically, a long-range cutoff is employed in these calculations, which when sufficiently large leads to converged LPP shapes[19,63]. Moderate changes in these profiles, however, can affect observations of elastic constants from integrating moments of the LPP[56] (see chapter 3).

Another interesting problem is the treatment of holonomic constraints. In a number of atomistic simulations, fast-vibrating bonds are treated with constraints such as the LINCs algorithm[64], which cannot be directly mapped into the stress tensor as forces. Vanegas and colleagues detail artifacts arising from improper treatment of the contributions of constraints[19], which can lead to nonphysical variations in the normal component of the LPP.

1.2.3 Curvature from flat membranes

Separate from thermal undulations, one can study local induced curvature in simulations of flat membranes. Such local curvature can be found in pure membrane systems or arising from interactions with peripheral or embedded proteins. Koldsø and colleagues demonstrate correlation between nanoscale enrichment of the glycolipid GM3 and local concave membrane curvature[65]. It should be noted that the cause and effect relationship is not explored in this study; it is unclear whether GM3 migrates to transient curvatures induced by thermal fluctuations (and either stabilizes them or does not), or if transient GM3 clusters induce local curvature.

More drastic membrane curvatures have been observed arising from membrane-protein interactions. A popular topic of study is BAR domains, regions of peripheral proteins which have been shown experimentally to sculpt membrane shapes[66]. Blood and Voth[67] observed bending of membranes to match the local concavity of the BAR domain, while Yu and Schulten probe more details of the importance of the BAR domain conformations, and explore larger-scale organization of membranes through multimeric BAR organization[68].

Embedded proteins also play an important role in membrane curvature. Proteins embedded in the membrane affect properties such as curvature, thickness, and lipid composition in their immediate vicinity[69], while other proteins have more drastic and long-range effects on local membrane properties. In particular, simulations by Davies and coworkers demonstrate that ATP synthase dimers induce membrane curvature on the scale of 10s of nanometers[70], and in this and a follow-up study[71] show that formation of rows of ATP synthase dimers in mitochondria are driven by the energetics of these induced curvatures. The interaction of ATP synthase with membranes is explored more thoroughly in Chapter 5.

1.2.4 Self-assembly

Lipids are self-assembling by nature, driven by the hydrophobic effect. One can create a dispersion of lipids and (optionally, depending on the force field) solvent, and expect some superstructure to emerge. Often, the predominant structure is a bilayer[72,73], and indeed before the advent of automated bilayer builders (see section 1.2.10), this was one approach to generating bilayers for the purposes of other studies. However, given a sufficiently large system size and (typically) a coarse-grained model, one can observe self-assembly of other phases and shapes. For example, Cooke and Deserno use a geometrically tunable model[34] to examine the effect of head-group size on shape preference from dispersions[35]. A number of self-assembly simulations have been performed with the MARTINI forcefield, examining the structural results of components such as lysolipids[74,75], PEGylated lipids[76], externally applied electric fields[77], and incorporation of fusion peptides[78].

1.2.5 Membrane buckles

Buckles are a popular way to study curvature, and are useful both to extract mechanical properties from bilayers and also to provide a curved scaffold to observe membrane dynamics. Buckles can be generated by inducing anisotropic lateral pressure in one lateral dimension of a

bilayer while keeping the second lateral dimension fixed[79], and allowing the transverse dimension to adjust to the buckle. Alternatively, one can emplace an excess of lipids in the lateral plane, from which buckles can arise if the lateral dimensions are fixed and the transverse dimension has sufficient space to accommodate a buckle[80].

The first simulations of membrane buckles were performed by Stecki[81] and followed closely by den Otter[82], studying the shape and transitions of buckled bilayers. Noguchi[83] then studied surface tension properties arising from buckled bilayers. From 2013 onward, Deserno and colleagues have made use of buckled membranes in a number of studies, using buckles to study gel phases[84], and developing protocols to extract a number of mechanical properties from buckling simulations, including k_c[85], the lipid tilt modulus[86], and the location of the pivotal plane[87] (see also Chapter 5).

More recently, buckles have been used to study effects of differential membrane compositions. Wu and Liang[80] observed domain formation at the curved regions of buckles in CG simulations of cholesterol-containing bilayers, and partitioning of helical peptides. Boyd, Alder and May studied the effect of incorporation of cardiolipin on the buckling tendencies of membranes, and observed non-domain forming aggregation of cardiolipin to regions of negative curvature in buckled membranes[56,79] (see also Chapters 2 and 3). The results of this work were replicated by Elías-Wolff and colleagues[88], who further developed a framework for understanding the energetics of lipid partitioning in buckled bilayers[89].

Recently a technique similar to membrane buckling has been proposed by Masone and colleagues, who formulate a collective variable for curvature that can be explored in an enhanced sampling context[90]. This allows one to closely tune the extent of curvature in a system, and to extract free energies of bending with e.g. different lipid or protein components.

1.2.6 Vesicles and cylinders

Vesicles are ubiquitous within the cell, and thus are a popular subject of study in experimental and simulation setups. Computational restrictions have limited the size of vesicles that can be simulated to radii on the order of ~10 nm, roughly the same size as the smallest stable vesicles in experimental studies[91]. Self-assembly of vesicles has been observed in both atomistic[92] and CG[93] systems occurring on time scales on the order of 10 to 100 ns. Another studied process that can be observed on these timescales is vesicle fusion[94,95].

Whether a vesicle is formed through spontaneous self-assembly or pre-formed through some tool (see section 1.2.10 and Chapter 5), once formed one can probe into the dynamics of the constituent lipids. For example, multiple studies have shown membrane thinning with tightly curved vesicles[96,97]. Studies of deformed vesicles are also useful – Markvoort and colleagues[98] observed interesting vesicle morphologies by tuning the spontaneous curvature of their constituent lipids. One can additionally impose deformations on vesicles and observe the response of the component lipids[99]. Proteins can also be incorporated into vesicles. Parton, et al. show differential aggregation tendencies of model peptides embedded into vesicles based on curvature mismatch[100].

Another topic of interest is the transverse distribution of lipids in multicomponent systems. An equilibrium simulation is unable to probe these quantities, as transverse relaxation of lipids between monolayers occurs on scales beyond those that can be reasonably simulated. However, it is possible to induce pores in the vesicle that allow lipid head groups to traverse a hydrophobic milieu and accelerate transverse mixing[25,97,101,102]. Using these protocols, it has been demonstrated that phosphatidylethanolamine (PE) lipids prefer the negatively curved inner monolayer of vesicles compared to phosphatidylcholine (PC) lipids, as predicted by molecular geometry considerations[97] and supported with experimental evidence[103,104]. An interesting finding of the same study was that di-unsaturated lipids have a preference for the outer leaflet, as their lipid tails can fold back inwards.

Cylinders (or commonly tubules) are another commonly found structure in the cell. Fewer MD studies have been performed to observed lipid dynamics in cylinders. Vidal and colleagues used a similar pore-forming protocol to that described above to discern lipid partitioning between monolayers[101]. Other studies have used simulations of cylinders to observe bulk membrane properties. Harmandaris and Deserno[48] used cylinders to extract k_c (called tethers in their publication). Wang and Deserno then calculated the location of the monolayer pivotal plane from equilibrium number ratios of lipids in cylinders[87].

Cylinder-like structures can also be created from drawing lipids out from a flat bilayer, mimicking experimental studies of pulling tubes from vesicles. *In silico*, this is accomplished through imposition of a geometrically restrained force. Several studies have utilized this technique to observe lipid partitioning between various curved regions of these tether shapes[105–107].

1.2.7 Fission and fusion intermediates

Membrane fusion and fission events in cells happen quite transiently and on small length scales, making them difficult to access experimentally. Thus, a number of simulation studies have attempted to study these processes. The prevailing model of membrane fusion is through a hemifusion intermediate[108] stage. A number of studies have attempted to model these intermediated stages and extract free energies of the fusion transition.[109–112], and some have modeled in fusion mediating proteins such as SNARES[113]. These studies also provide an opportunity to examine the effect of specific lipids in mediating the fusion process[112,113], and measuring the aggregation tendencies of those same lipids in these systems[114,115].

1.2.8 Supported and sculpted membranes

Experimentally lipid bilayers can be laid down on corrugated substrates, inducing controlled nanoscale curvature[116–118], and these setups can be used to study e.g. lipid partitioning and

domain formation. de Jong and Heuer reproduce such a setup in CG simulations[119]. Beyond mimicking experimental conditions, a technique similar to this has potential applications for supporting membranes of arbitrary shapes. Yesylevskyy and coworkers designed curved membranes bracketed on either side by fixed “dummy particles”, which only interact with the hydrophobic core of the membrane[120]. In this setup, a stable curved membrane does not interact with the scaffolding, and repulsive interactions gently sculpt the membrane if it has a tendency to change shapes. This approach has been used to study the effect of curvature on uptake of cancer drugs[121].

The potential applications of the dummy-particle approach can be generalized to sculpting any arbitrary membrane shape. This is important for simulating unstable shapes such as necks and junctions. In chapter 4 of this work, we extend the dummy particle protocol to calculate local instability of membrane shape by measuring forces on individual dummy particles.

1.2.9 Nonbilayer phases

Inverse hexagonal (HII) phases are important experimentally to determine lipid spontaneous curvature. Sodt and Pastor extracted C_o from atomistic simulations, and interestingly provide a qualitative metric of the pivotal plane location[49]. Johner and colleagues use HII phases to demonstrate how elastic properties such as k_c can change with the curvature environment.

Cubic phases are more rarely studied (or found in nature), but can also be useful for extracting the Gaussian curvature modulus (see section 1.1.6). Marrink and Tieleman first simulated a lipid system of a diamond cubic phase[122] and observed a cubic to hexagonal transition[123]. Bicontinuous cubic phases have been simulated in the presence of fusion peptides[78], and in systems composed of ceramides[124].

A few other interesting lipid related structures should be mentioned. Detergent micelles are popular experimental tools, and thus have corresponding interest in the simulation field. The small size of detergent micelles (relative to e.g. vesicles) makes them amenable to atomistic simulations[125–127]. Similarly, bicelles offer the solubility of detergents with perhaps a more bilayer-like interior. Simulation studies of bicelles have explored their interactions with drug-delivery materials[128] and transitions between the bicelle and vesicular phases[129].

Another relevant lipid structure is the lipid droplet, which in cells are used to store long-term energy in the form of triglycerides[130]. These systems are typically composed of an outer monolayer of phospholipid, with an internal hydrophobic core of triglycerides. The structure and interfacial properties of lipid droplets have been explored in-depth by Vanni and colleagues[131,132].

1.2.10 Tools for building curved lipid systems

The construction of lipid bilayer configurations for MD simulations is an interesting problem. The unstructured nature of the liquid phase of bilayers leads to nearly endless conformational heterogeneity in the acyl chain region. Starting structures must provide a reasonable representation of such a chaotic system, while avoiding clashing contacts between atoms that would lead to high energy configurations and numerically unstable simulations. The average area per lipid needs to be faithfully represented, and all of these considerations must be maintained for systems with strongly heterogeneous membrane components both within and between monolayers.

Luckily for the average researcher, great effort has gone into providing support for setting up membrane systems. Numerous tools exist for generation of starting configurations of simple and complex bilayers. Perhaps the most popular of these is the CHARMM-GUI server[133], which provides membrane setups for the CHARMM forcefield[134], the coarse-grained MARTINI

forcefield[27] and its implicit-solvent variant[26], and the PACE mixed-resolution forcefield[135]. Further support for the MARTINI forcefield comes from the simple *insane* python tool[136]. Numerous other web servers provide various levels of support for membrane configurations, including (but not limited to) MemBuilder[137], MemGen[138], and LipidBuilder[139].

The tools listed above are (for the most part) focused on generating planar bilayers, for two reasons. First, simulations of curved membrane setups typically require significantly more computational resources – scaling a flat bilayer to larger sizes increases the atom count proportional to the area, whereas scaling a vesicle increases the system size cubically. Only recently have computational resources become powerful enough to allow researchers to access these larger spatial scales. Second, the setup of curved shapes poses several technical challenges not encountered with flat bilayers.

The first of these challenges is the morphological heterogeneity of possible membrane shapes. In cells, membranes display a wide variety of morphologies (for examples, see Chapter 5). It is a difficult problem to create a tool that can flexibly adapt to create an arbitrary number of morphologies. For this reason, a number of tools exist that can only generate the most common type of curved membrane, spherical vesicles. Tools that can accomplish this task include the CHARMM-GUI coarse-grained vesicle builder[102], MemBuilder[137], and PackMol[140], the latter of which can build other simple shapes like cylinders. Only more recently has there been a drive to be able to create shapes with (nearly) arbitrary configurations, a task which both the python-based tools LipidWrapper[141] and BUMPy[142] can accomplish. The second technical challenge in building these systems is the estimation of interleaflet area differences between leaflets of curved membranes. For example, the inner leaflet of a vesicle should have fewer lipids than the outer leaflet. As transverse relaxation of area mismatch through lipid flipflop is typically beyond the time-resolution of MD simulations, it is important to set up curved systems with correct lipid ratios. Only a few of these tools attempt to address this challenge. The CHARMM-GUI coarse-

grained builder attempts to estimate areas using an empirical model, while BUMPy uses a pivotal-plane based area estimator (see chapter 5).

Support is growing for generating starting configurations for nonbilayer lipid systems as well. The CHARMM-GUI server has supported construction of micelles since 2013[143], as does (in a more limited capacity) MemBuilder[137], and more recently this functionality is also provided by the Micelle Maker online tool[144]. Hexagonal phases can be created using the CHARMM-GUI server as well[145]. Work is ongoing in supporting other nontraditional systems such as bicelles, though to our knowledge, other interesting phases such as bicontinuous cubic systems have no present implementations.

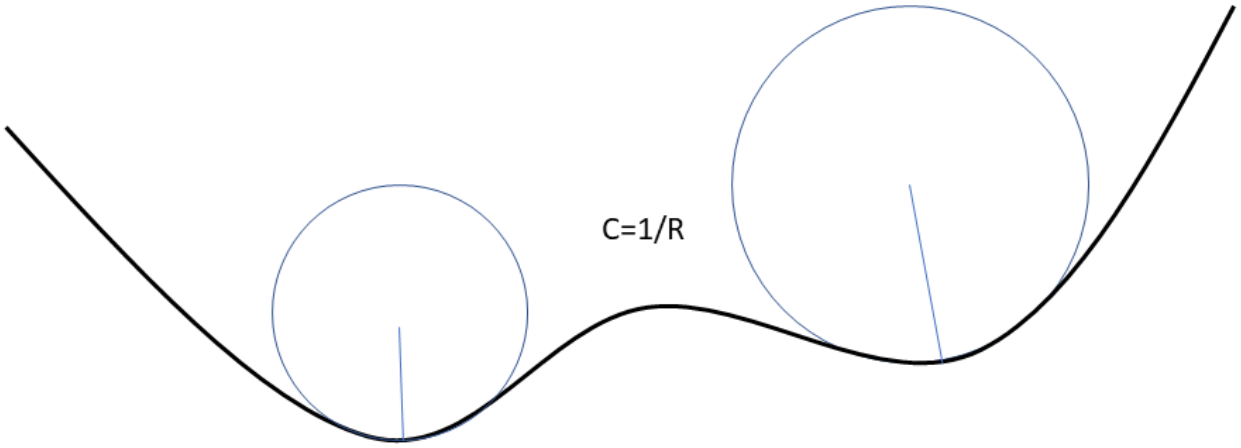

Figure 1.1 Curvature of a surface. The curvature of any point along a curve can be described by drawing a circle tangent to that point. The curvature of that point is then the inverse of the radius of that circle.

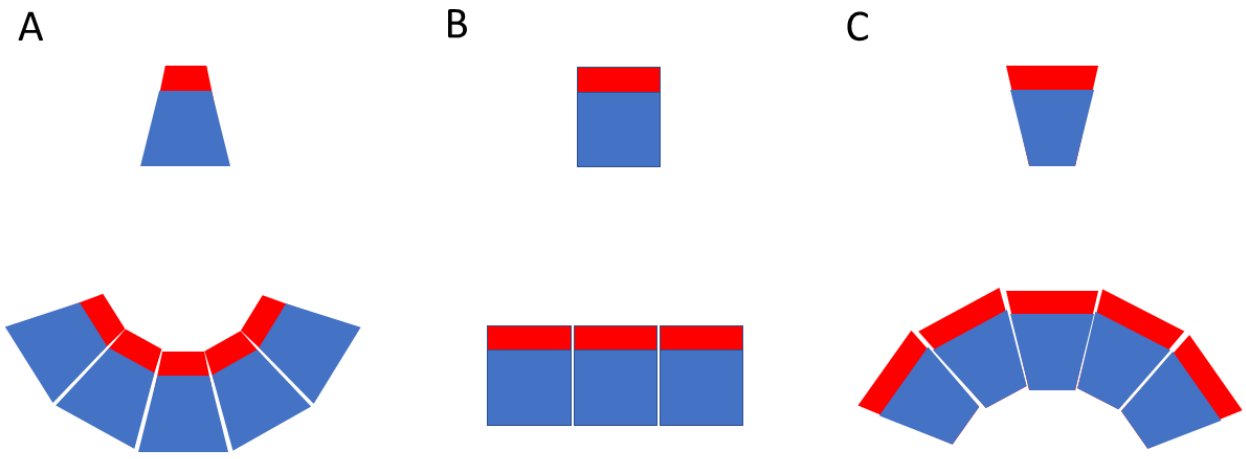

Figure 1.2. Intrinsic curvature and lipid packing. Head groups are represented in red. A) Single lipid and packing arrangement of a conical lipid with a negative C_o. B) The same for a cylindrical lipid, and C) for a lipid with a positive C_o

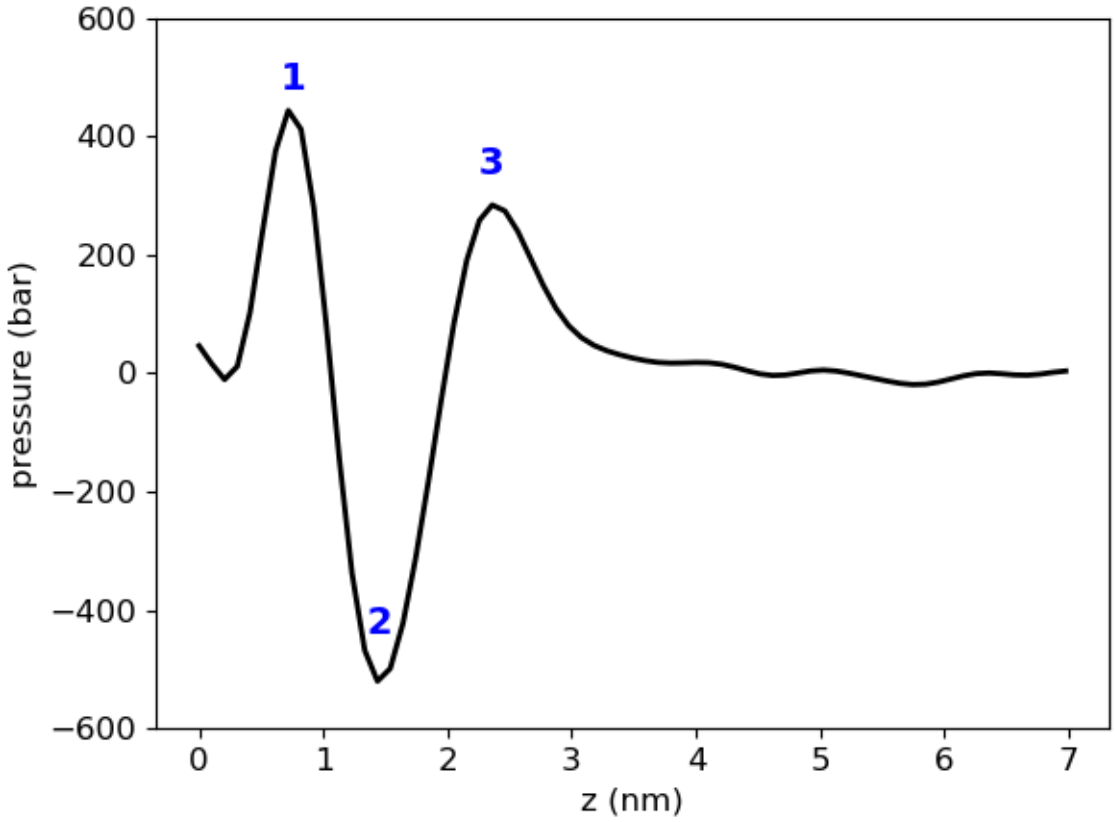

Figure 1.3. A sample lateral pressure profile. z=0 represents the center of the bilayer. Point 1 is the peak caused by tail insaturation. Point 2 is the negative interfacial tension. Point 3 is the peak caused by head group repulsion.

Chapter 2:

Buckling Under Pressure: Curvature-Based Lipid Segregation and Stability Modulation in Cardiolipin-Containing Bilayers

Reproduced with permission from:

Boyd, Alder and May. “Buckling under pressure: curvature-based lipid segregation and stability modulation in Cardiolipin-containing bilayers. *Langmuir* (2017), 33 (27), 6937-6946

The following changes have been made:

- The manuscript has been reformatted to meet University Standards
- Figures numbers have the chapter number prepended
- References have been renumbered to match the rest of the thesis

Home | Create Account | Help

Title: Buckling Under Pressure: Curvature-Based Lipid Segregation and Stability Modulation in Cardiolipin-Containing Bilayers

Author: Kevin J. Boyd, Nathan N. Alder, Eric R. May

Publication: Langmuir

Publisher: American Chemical Society

Date: Jul 1, 2017

LOGIN

If you're a copyright.com user, you can login to RightsLink using your copyright.com credentials.

Already **a RightsLink user** or want to learn more?

PERMISSION/LICENSE IS GRANTED FOR YOUR ORDER AT NO CHARGE

This type of permission/license, instead of the standard Terms & Conditions, is sent to you because no fee is being charged for your order. Please note the following:

- Permission is granted for your request in both print and electronic formats, and translations.
- If figures and/or tables were requested, they may be adapted or used in part.
- Please print this page for your records and send a copy of it to your publisher/graduate school.
- Appropriate credit for the requested material should be given as follows: "Reprinted (adapted) with permission from (COMPLETE REFERENCE CITATION). Copyright (YEAR) American Chemical Society." Insert appropriate information in place of the capitalized words.
- One-time permission is granted only for the use specified in your request. No additional uses are granted (such as derivative works or other editions). For any other uses, please submit a new request.

BACK | CLOSE WINDOW

Buckling Under Pressure: Curvature Based Lipid Segregation and Stability Modulation in Cardiolipin Containing Bilayers

Kevin J. Boyd, Nathan N. Alder, Eric R. May

Department of Molecular and Cell Biology, University of Connecticut, Storrs, CT 06269

Abstract

Mitochondrial metabolic function is affected by the morphology and protein organization of the mitochondrial inner membrane. Cardiolipin (CL) is a unique tetra-acyl lipid that is involved in the maintenance of the highly-curved shape of the mitochondrial inner membrane as well as spatial organization of the proteins necessary for respiration and oxidative phosphorylation. Cardiolipin has been suggested to self-organize into lipid domains due to its inverted conical molecular geometry, though the driving forces for this organization are not fully understood. In this work, we use coarse-grained (CG) molecular dynamics (MD) simulations to study the mechanical properties and lipid dynamics in heterogeneous bilayers both with and without CL, as a function of membrane curvature. We find that incorporation of CL increases bilayer deformability and that CL becomes highly enriched in regions of high negative curvature. We further show that another mitochondrial inverted conical lipid, phosphatidylethanolamine (PE), does not partition or increase the deformability of the membrane in a significant manner. Therefore, CL appears to possess some unique characteristics that cannot be inferred simply from molecular geometry considerations.

Introduction

The mitochondrion is a double-membraned, energy generating organelle found in eukaryotes. The mitochondrial outer membrane provides an encompassing envelope with protein pores to control material flux into and out of the organelle. The inner membrane is the site of eukaryotic cellular respiration. It contains morphologically distinct domains: the flat inner boundary membrane which maintains close proximity to the outer membrane, and the highly curved cristae membrane which houses the oxidative phosphorylation machinery, as well as other protein complexes[146,147]. The inner boundary membrane and cristae membrane are contiguous membranes that are separated by highly curved tubular structures called cristae junctions. The morphology of the inner membrane allows for localization of the proton-motive force-generating machinery in close proximity to the proton-motive force-utilizing ATP synthase, and alteration of inner membrane morphology has been shown to affect metabolic function[148,149]. Furthermore, the inner membrane can adjust its shape to account for ADP levels and oxidative stressors[150–152], effecting respiratory regulation through morphological changes. Thus, the mitochondrion must maintain inner membrane superstructure and protein organization within that superstructure, while being able to sense and respond to changing cellular conditions. Inner membrane morphology is maintained by several proteins, chief among them the MICOS complex, which maintains the cristae junction[153–155], and ATP synthase in the cristae. ATP synthase forms rows of dimers along curved regions of the cristae, imposing positive curvature on the matrix-facing leaflet[156–158]. Additional proteins affecting morphology include the apoptotic factor[159] as well as mitofilin[160].

Cardiolipin (CL) is a lipid enriched in the inner membrane inner membrane that also plays a role in morphology maintenance. CL is composed of two phosphatidyl groups joined by a central glycerol (Fig. 2.1A). Recent experiments indicate that the two ionizable phosphates are both deprotonated at physiological pH[161–164], imparting a head-group charge of -2, though other

studies have suggested circumstances in which CL would carry a -1 charge[165–168]. Under certain conditions the effective size of the CL head-group can be small relative to the volume occupied by its four acyl-chains. Lipids which have this molecular shape are referred to as having an inverted conical geometry, and these types of lipids will aggregate into inverse hexagonal (HII) phases. CL aids in assembly and stability of the respiratory complex[169] and may affect inner membrane inner membrane morphology in two ways. First, CL-containing bilayers are prone to adopt highly curved and non-bilayer structures in the presence of high ionic salt concentrations (particularly calcium) or low pH[170–177]. A pair of studies have shown that cristae-like invaginations can be induced by directing a flow of protons at giant unilamellar vesicles containing CL, and that this effect is CL dependent[178,179]. Second, CL specifically binds or interacts with many mitochondrial proteins[180,181], and the partitioning of CL to regions of the inner membrane may influence the spatial organization of the proteins. This influence has been demonstrated by depletion of native CL by mutation of cardiolipin synthase or the CL-remodeling protein tafazzin in drosophila cells, which leads to disruption of the network of ATP synthase dimer rows and aberrant inner membrane superstructures[182,183].

CL-dependent protein organization implies that CL can self-organize in an otherwise homogenously distributed bilayer. CL-enriched domains have been observed in bacterial cell membranes via specific staining with the fluorescent dye Nonyl Acridine Orange (NAO)[184–186]. These domains occur at the poles and fission sites of rod-like bacteria. The proposed mechanism of CL enrichment is lipid geometry-mediated: CL's inverted conical shape minimizes curvature frustration in negatively curved regions of bilayers.

Curvature-driven partitioning has been explored in recent years for pure lipid systems[35,117,187–189] as well as membrane embedded proteins[80,100,190], though CL has yet to be examined in this context. Molecular Dynamics (MD) simulations have been used in several of the curvature-based partitioning studies and provide a powerful means to examine the molecular

underpinnings of macromolecular behavior. Previous MD studies involving CL containing bilayers have been performed at both all-atom and coarse-grained modeling levels. One such study involved examination of how the number of acyl chains affects the phase behavior of homogenous CL systems[74]. Many other studies have examined the equilibrium structural properties of cardiolipin-containing bilayers in low curvature/flat geometries[191–195]. No large-scale organization of CL has been demonstrated in these studies, although Dahlberg and Maliniak have shown very localized head-group clustering in their work on coarse-grained CL-containing bilayers[194]. In this work we have extended our understanding of CL-containing bilayers through coarse-grained (CG) MD simulations of highly curved systems. We assess the curvature-dependent mechanical properties and enrichment dynamics of CL in these highly curved (buckled) heterogeneous bilayers and demonstrate that CL has unique properties in its ability to promote curved phases and to laterally segregate to regions of high negative curvature. These observations are enabled by a curvature mapping analysis, where we show CL has a much stronger curvature-based segregation propensity than another inverted conical lipid, phosphatidylethanolamine, PE.

Methods

Simulations were performed using the coarse-grained MARTINI 2.2 force-field with nonpolarizable water[27] and implemented using the GROMACS 5 software package[196]. A timestep of 30 fs was found to be stable and used for all simulations. According to convention, reported simulation times are scaled by a factor of 4 to approximate experimental diffusion rates[27]. Non-bonded interactions were calculated following the suggested parameters by de Jong and coworkers[28], where the Lennard-Jones interactions are shifted to zero at the cutoff distance of 1.1 nm using the potential-shift-Verlet modifier. Electrostatics were calculated with a relative dielectric constant of r=15 and the potential and forces were shifted to zero at the cutoff of 1.1 nm using the reaction field method. Temperature was maintained at 303 K using the v-

rescale algorithm with a time constant of 1 ps. Solvent and lipids were coupled separately. Partitioning behavior of select bilayers was also assessed at 280K, 320K and 350K (see Fig. 2.S1).

Anisotropic pressure coupling was maintained using the Parrinello-Rahman method[197,198] with a time constant of 12 ps. In each system, pressure coupling was turned off in the short lateral dimension (X), fixing the box size in that dimension. To generate the initial buckled membranes, pressure in the membrane normal dimension (Z) was maintained at 1 bar, while pressure in the long lateral dimension (Y) was incrementally increased starting from 1 bar. In other simulations, frames were extracted from along the buckling trajectory and simulated in the NVT ensemble, to perform simulations at constant compressional strain (γ), which is a proxy for constant curvature simulations.

All simulations were carried out on the local UCONN high performance computing cluster (hornet). Simulations were run on compute nodes containing 24 Intel Haswell CPUs. Typical simulations would utilize 96 cores per job and would run at a rate of approximately 52 μs/day. Nodes in the cluster are connected with a high-speed, low-latency FDR infiniband network.

System Setups

All bilayer systems were generated using the CHARMM-GUI Martini Maker[102]. The system dimensions were 10 nm by 30 nm in the X and Y directions (bilayer plane), respectively, and 30 nm in the Z direction (bilayer normal). To mimic mitochondrial membrane composition bilayers were composed of 40% palmitoyl-oleoyl-phosphatidylcholine (POPC), 40% palmitoyl-oleoyl-phosphatidylethanolamine (POPE), and 20% tetraoleoyl cardiolipin (CL) to represent the IM or 50% POPC and 50% POPE with no CL to represent the outer membrane (OM). The effect of net head group charge on CL was investigated by performing simulations both when the head-group was singly deprotonated (-1 charge, CL^{-1}) or doubly deprotonated (-2, CL^{-2}). In the CL^{-1}

model the head group charge was asymmetrically distributed on the phosphate beads, such that one phosphate carried a -1 charge and the other phosphate was neutral. In additional bilayer simulations, the concentration of POPC was increased to 80% and the remaining fraction was composed of either POPE (PC/PE (4:1)) or CL^{-1} (PC/CL (4:1)). A full list of the bilayer systems studied including the compositions and total lipid count can be found in Table 2.1; all percentages indicate the mol %. Sodium ions were added to neutralize system charge. All systems were energy minimized and equilibrated as suggested by CHARMM-GUI, which involved energy minimization followed by 5 rounds of restrained MD in which restraints on lipid head group beads were successively lowered and the time step was incrementally increased starting from 2 femtoseconds.

Table 2.1. Lipid Composition of Simulated Bilayers

System Name	% PC	% PE	% CL^{-1}	%CL^{-2}	# of Lipids
PC/PE (1:1)	50	50	0	0	948
PC/PE (4:1)	80	20	0	0	930
PC/CL (4:1)	80	0	20	0	750
IM^{-1}	40	40	20	0	810
IM^{-2}	40	40	0	20	810

Data Analysis

Simulations were analyzed using GROMACS Tools and custom scripts written in MATLAB 2016. The extent of bilayer compression was quantified by the compressional strain γ,

$$\gamma = \frac{L_{y,0} - L_{y,i}}{L_{y,o}}$$

in which $L_{y,0}$ is the original box length in the dimension of compression (Y) and $L_{y,i}$ is the current box length[85]. Monolayer curvatures were calculated by extracting the lipid head-group coordinates from individual leaflets in the Y (buckling) and Z (normal) directions. The monolayer Y-Z coordinates were fit by a series of cubic smoothing spline functions (see Fig. 2.S2). First and second spatial derivatives along the curve were calculated from the spline-fits and the pointwise curvature, C(y), was calculated from

$$C(y) = \frac{f''(y)}{(1 + f'(y)^2)^{\frac{3}{2}}}$$

where f' and f'' are the first and second derivative of the monolayer height function with respect to the Y-dimension, respectively; C has units of inverse distance. The sign of curvature for the top leaflet was inverted to match the convention of curvature sign for a lipid monolayer. This approach allowed us to characterize lipid concentration with respect to curvature, since we can readily assign a local curvature to each lipid, based upon the head group position. These head-groups were then binned according to curvature and relative concentrations at each curvature were calculated.

Ion binding calculations were performed using the gmx mindist tool in GROMACS, with the default cutoff value of 0.6 nm. Molecular packing was examined by considering several geometric properties of PE and CL lipids in non-buckled states. The tail splay and the tail extension were measured by calculating the distance in the lateral (xy) plane (splay) or normal (z) direction (extension) between a reference bead in the head group and the terminal bead of the lipid chains. The phosphate bead was chosen as a reference for PE, and the central glycerol bead was chosen for CL. The area/head group was also computed by taking the simulation box dimensions and dividing by half the total number of head groups. CL was considered as having two head groups in this calculation.

Results

To investigate the curvature dependent properties of cardiolipin containing bilayers, we initially laterally compressed bilayers to generate buckled morphologies (Fig. 2.1B). This was done to accomplish two goals: first to characterize the effect of CL on buckling propensity, and second to develop a system to study the dynamics of mitochondrial lipids in a curved environment. Table 2.1 describes the bilayer composition for each simulation. We focus first on bilayers mimicking mitochondrial compositions, PC/PE (1:1) is an equimolar binary system of PC and PE without CL and serves as an OM approximation, while our IM systems (inner membrane) refer to ternary systems containing 20% CL carrying either a -1 (IM^{-1}) or -2 (IM^{-2}) charge. We also examine two other binary systems (PC/PE (4:1), PC/CL (4:1)), which have a dominant composition of PC and a minor component of either CL^{-1} or PE, to evaluate differences between the inverted conical lipids PE and CL in the same background lipid environment. A CG representation of CL is shown in Fig. 2.1A, and a schematic of the buckling procedure is presented in Fig. 2.1B.

Effect of bilayer composition on buckling transition

Bilayer buckling was induced by applying pressure along the long axis (Y) in the plane of the bilayer, while fixing the box size in the short dimension (X). Pressure in the bilayer normal direction (Z) was maintained at 1 bar while lateral pressure was initiated at 1 bar and increased in increments of 1 bar every 12 μs. In each simulation, lateral compression yielded a single buckle in the simulation box along the axis of compression (Fig. 2.1B) All simulations reached a maximum compressional strain of roughly $\gamma \approx 0.6$ (Fig. 2.2) and displayed geometrically similar buckles. Once buckling occurred, application of greater lateral pressure did not result in further compressional strain. With pressure increments of 1 bar, transitions from flat to buckled states occurred rapidly at critical pressure differences (Fig. 2.2B) and did not sample stable intermediate states between flat and strongly buckled states. Notably, CL-containing bilayers

required lower pressures to induce buckling. The IM^{-1} bilayer buckled at 4 bars of applied pressure, the IM^{-2} bilayer at 5 bars, while PC/PE (1:1) bilayer a required a 6 bar Y-pressure to buckle.

Molecular geometry theory predicts that the introduction of inverted conical lipids, like CL, leads to destabilization of bilayer integrity and a preference for curved environments. The destabilization energy is attributed to a curvature frustration, which is caused by a mismatch between the spontaneous curvature of a given lipid species and the actual monolayer curvature. The difference in behavior between charged CL variants can be explained in terms of head-group electrostatics: charge repulsion at the level of the head group is increased in CL^{-2}, increasing effective head group area and imparting a more cylindrical lipid geometry, decreasing the curvature frustration. Our findings are in agreement with the experimental work of Nichols-Smith[199], et al, who suggested that CL-containing bilayers have a propensity to create folds, and the computational work of Dahlberg and Maliniak[194], who showed that introduction of CL to PC and PE bilayers decreases the bending modulus, with CL^{-1} having a greater effect than CL^{-2}.

Stability Modulation of Intermediate Curvatures

We next focused simulations near the buckling transition pressure difference to observe if the system displayed the ability to maintain intermediate curvature states or if the system undergoes an abrupt buckling deformation once a critical pressure difference has been exceeded. For each bilayer, we repeated the previous compression procedure though now using a finer pressure increment and longer simulation times to ensure intermediate states were not artifacts of insufficient sampling times. The pressure was increased in increments of 0.1 bar, along the previously discovered buckling ranges (3.1 to 3.9 bar, 4.1 to 4.9 bar, and 5.1 to 5.9 bars for IM^{-1}, IM^{-2}, and PC/PE (1:1) respectively). Each simulation at a given pressure was run for 36 μs, resulting in 324 μs of sampling for each system. IM^{-1} and IM^{-2} bilayers displayed plastic behavior

in response to 0.1 bar pressure increases (Fig. 2.3A-B), indicating these systems could be stable in intermediate curvature states in a precise pressure range. These intermediate states display greater curvature fluctuations compared to the stable flat or buckled states. For example, in the IM^{-1} bilayer system, the average standard deviation of γ (σ_γ) at pressures between 3.1 and 3.6 bars (calculated for each pressure, then averaged) was 0.064, whereas the stable unbuckled (3 bar) and fully buckled (4 bar) states displayed σ_γ values of 0.028 and 0.020, respectively.

In contrast to the malleable CL-containing bilayers, the PC/PE (1:1) bilayer did not show any tendency to sample intermediate curvatures and displayed a two-state characteristic (Fig. 2.3C). For the PC/PE (1:1) system, as the buckling transition point is approached the bilayer remains relatively flat, exhibiting $\gamma < 0.2$ between 5.1 and 5.3 bar. The simulation at 5.4 bar appears to be at (or very near) the critical buckling pressure, as the system jumps to the buckled state ($\gamma \approx 0.6$) and then returns to flat state within the same simulation. Stable buckled configurations were observed for pressures of 5.5 bar and above.

While a reduced bending modulus in CL-containing bilayers suggests they are more pliable than CL-lacking bilayers[194], one might still expect a CL-lacking bilayer to sample intermediately curved morphologies. Instead, in our systems only the IM^{-1} and IM^{-2} bilayers can tune the extent of curvature in response to pressure, whereas the PC/PE (1:1) bilayer samples only two states. One possibility is that a larger system size may allow for CL-lacking bilayers to bend more moderately in response to applied pressures, but we note that our compression dimension (30 nm) is roughly equivalent to the diameter of cristae tubules[200], so our simulations approximate the relevant biological system size magnitudes. These results indicate that CL not only enhances the ability of the mitochondrial IM to assume curvature that is consistent with cristae geometry, but also that CL allows bilayers to respond to more moderate physical stimuli, including the presence of curvature-inducing proteins. We note that while a lateral applied pressure difference may not have a consistent physiological counterpart, it has been shown that

exposure of retinal ganglion cells to elevated hydrostatic pressures leads to morphological changes in the mitochondrial which may be related to optic nerve impairment in glaucoma patients[201]. Our observed curvature tuning capabilities of CL-containing bilayers may have significant implications for understanding the importance of CL in generating and maintaining curved morphologies in the mitochondria.

Curvature based lipid partitioning

We next examined lipid dynamics and clustering in the context of curved bilayers. To enforce a constant curvature environment for bilayers of different compositions, we extracted system configurations along the buckling transition corresponding to specific γ values. We then initiated new simulations in which we fix the box size (NVT) to control the extent of buckling, example configurations at various γ-values are shown in Fig. 2.4A. In these fixed γ simulations we were able to assign a curvature to each head group position, from derivatives of the spline fit function (eq. 2) for each monolayer. This curvature mapping approach is illustrated in Fig. 2.4B and Fig. 2.S2. The distribution of head-group curvatures is dependent on the degree of buckling, but is generally characterized by a large peak at moderate positive curvature and a broad shoulder extending into the negative curvature regions (Fig. 2.5A). Asymmetry between positive and negative curvatures is a consequence of bilayer shape: every invagination with negative curvature has a corresponding patch of positive curvature in the opposite leaflet with a larger radius of curvature.

The lipid probability distributions for the IM^{-1} system at γ=0.3 are shown in Fig. 2.5A, where each distribution is normalized. This analysis allowed us to observe that CL^{-1} is enriched in the negative curvature regions and is suppressed in the positive regions (red curve), whereas PC has the opposite features of accumulating in positive curvatures and reducing in negative curvatures (green curve). Interestingly, PE does not show any curvature dependence as the PE

distribution (blue curve) matches that of the entire bilayer (black curve). To normalize for the asymmetric distribution of head-group curvatures, we performed an additional analysis by calculating the relative fractional lipid concentration at different curvatures. Fig. 2.5B presents the relative lipid fractions with respect to curvature for the IM^{-1} bilayer at $\gamma = 0.3$. Consistent with our visual inspections and the probability distributions (Fig. 2.5A), this analysis again illustrates that CL^{-1} migrates to regions of negative curvature and depletes within positive curvature regions. PC shows an opposing trend, enriching at positive curvature and decreasing at negative curvature. This analysis also shows PE is effectively insensitive to curvature variation in this system, showing only slight depletion at the highest negative curvatures. The IM^{-2} bilayer showed similar partitioning behavior to IM^{-1} (Fig. 2.6, S3-S4), although the effect was less dramatic, especially at high γ values. An interesting feature of the lipid fraction analysis is that at zero curvature, we recover the bulk lipid factions for all species. The lipid fractions versus curvatures for all systems described in Table 2.1 for γ values ranging from 0.05 to 0.45 are presented in Fig. 2.S3-S7.

We next addressed the degree to which CL self-associated (to form pure CL nanodomains) within regions of negative curvature. To analyze this, we subdivided the IM^{-1} system at $\gamma=0.3$ into 10 regions based upon monolayer curvature. In each of these regions we computed the bulk fraction of CL, and also computed a local fraction of CL around each CL molecule. The local fractions were determined by considering the six nearest neighbors around each CL. At all curvatures, the local CL fraction matches the bulk fraction, and therefore CL is well-mixed and does not form self-associating clusters, Fig. 2.5C.

Another analysis we performed was to track the lipid composition in regions of different curvatures as a function of compressional strain (γ). To reduce the dimensionality, we characterize membrane sections as negatively curved ($C < -0.05$ nm^{-1}), neutral (-0.05 $nm^{-1} \leq C \leq 0.05$ nm^{-1}) or positively curved ($C > 0.05$ nm^{-1}). This coarse partitioning results in similar

sampling statistics for the three curvature regions, due to the non-linearity in the curvature-probability curve (Fig. 2.5A). Accumulation of CL at negative curvatures was apparent at membrane strains as low as γ=0.05 (Fig. 2.7C) which has a mean unsigned curvature of 0.07 nm^{-1}. Increasing γ enhanced lipid segregation at both positive and negative curvatures for both PC (Fig. 2.7A) and CL^{-1} (Fig. 2.7C) lipids. PE concentration was consistently unaffected by γ for IM^{-1} (Fig. 2.7B) and IM^{-2} (Fig. 2.S8). The flat segments of every bilayer had fractional compositions equivalent to the bulk bilayer concentrations, a trend that was also independent of γ. The lipid fractions as a function of compressional strain for all other systems described in Table 2.1 are presented in Fig. 2.S8-S11.

The differential partitioning behavior of CL and PE cannot be explained simply by molecular geometry or a propensity for formation of inverted hexagonal phases (HII). PE is a highly inverted conical lipid with a more negative spontaneous curvature than CL[202] and CG simulations have predicted similar bending moduli for pure PE and CL^{-2} bilayers[194]. An explanation for the lack of PE accumulation in negatively curved regions could be that PE is outcompeted for negative curvature positions by CL. To investigate if PE does have a propensity for negatively curved regions, we examined curvature partitioning in binary systems at γ=0.30. We simulated binary lipid bilayers containing compositions of 80/20 PC/CL^{-1} and 80/20 PC/PE, to compare PE and CL^{-1} partitioning behavior in a background of PC lipids. As in the ternary bilayer systems, CL was found to be highly enriched within high negative curvature regions (Fig. 2.8). In the absence of CL, PE showed a slight propensity for negative curvature, but even at the most negative curvatures the enrichment was modest, increasing to a lipid fraction of 0.3 in a system with an overall 0.2 PE fraction. Stated another way, in the highest negative curvature regions PE shows a 50% increase in concentration, while the CL^{-1} concentration increases by 150% over the bulk fraction. Our results regarding PE clustering is relatively consistent with a

previous studying examining DPPC/DOPE in a hemi-fusion system by CG-MD. In that work 80% enrichment of DOPE was observed in the most negatively curved regions[115].

Charge Effects

An interesting and perhaps unexpected finding is that CL^{-1} and CL^{-2} show similar partitioning behavior (see Fig. 2.S3-S4), despite an expected difference in charge repulsion between head groups and resultant change in molecular geometry. A possible explanation for the lack of significant difference between CL^{-1} and CL^{-2} is that sodium ions have stronger binding to the IM^{-2} bilayer than the IM^{-1} bilayer, and provide more screening of the head group charges. We have examined the ion binding for γ=0.30 and observe the number of bound ions to IM^{-2} is more than double that of IM^{-1}, and the surface charge density of the two systems are comparable. IM^{-1} has 100 +/- 5.2 bound counterions and a surface charge density of -0.11 e/nm^2, while IM^{-2} has 225 +/- 7.4 bound counterions and a surface charge density of -0.17 e/nm^2). In the absence of counterions the surface charge density for the two systems would be approximately -0.27 e/nm^2 for IM^{-1} and -0.54 e/nm^2 for IM^{-2}.

Discussion

The motivations for conducting this study are numerous. The determination of mechanical properties of bilayers from molecular simulations have been a field of intense investigation for many years[4,45,203,204], including approaches which induce buckling to determine these properties[83,85,86]. Understanding these properties in multicomponent systems, and particularly how concentration gradients may couple to curvature variations remains an area of open inquiry. In our approach, we are able to correlate curvature and concentration fields, which may provide an important advance for developing more refined theories on concentration effects on membrane properties.

Beyond the interesting and complex questions which arise in purely physical lipid bilayer systems, curved membrane environments can be used to model a number of biologically and physiologically relevant conditions as well. In this work, we have analyzed the effect of CL on bilayer buckling tendencies separately from partitioning behavior of CL in curved bilayers. However, the *in-organello* implications of these effects may be synergistic. A feedback-loop maybe at play, where CL partitioning can stabilize negative curvatures, which in turn may recruit more CL, which further stabilizes or increases the degree of curvature. Additionally the role of curvature mediating proteins, such as ATP synthase dimers, likely contributes to this effect as well[70,157]. ATP synthase dimers organization in mitochondrial is affected by depletion of CL[183], which may indicate its role to can nucleate regions of high curvature, which promotes accumulation of CL, which facilitates further induction of curvature and more recruitment of ATP synthase dimers. The accumulation of these curvature inducing proteins may relate to our simulations as a physical analog to the pressure differential used to generate curved bilayers in-silico.

Of particular interest is understanding mitochondrial morphology and how aberrant cristae morphology and protein organization may be the result of lipidic modifications[183]. Other circumstances found in healthy mitochondria can also be examined in curved bilayers. For example, the transverse distribution of inner membrane CL has been shown to be asymmetric, with significantly more CL in the matrix-facing leaflet than the IMS-facing leaflet[205]. The impact of this asymmetry in both buckling propensity and partitioning ability is well suited for the current approach and will be an avenue of future study. Another unique characteristic of the inner membrane is its extremely high protein density, and while some work has been done on the effect of dense protein concentrations on lipid diffusion in flat bilayers[206], we can extend these studies into curvature environments which more closely mimic the inner membrane.

Further work will be required to understand what are the driving forces, beyond molecular geometry/curvature matching, to induce lipid partitioning. As illustrated in our comparisons between PE and CL lipids it is clear that equilibrium molecular packing geometry alone cannot predict the portioning properties. However, it is possible that when the bilayers are under an applied stress (non-zero surface tension), the lipid components could have a differential response to the applied stress. We have examined three molecular properties of PE and CL^{-1}, in the background of 80% PC lipids. We calculated the lipid tail splay, tail extension and mean head group area, as a function of increasing applied lateral pressure (Fig. 2.S12). We only considered simulations in which the bilayer has not buckled. We find that CL^{-1} shows a greater response to applied pressure in that it both increases the tail splay and has a more dramatic reduction in head group area compared to the PE system. Taken together this could imply that CL^{-1} is adopting a more inverted conical (negative curvature preferring) geometry. This could relate to a more negative spontaneous curvature, which in the Helfrich theory[8] of membrane bending contributes quadratically toward the total bending energy, whereas the bending modulus only has a linear relationship with the bending energy.

In general, the extent of lipid partitioning arises from opposing forces of the energetic benefit of curvature matching and the demixing entropic cost. A theoretical model suggests these contributions are of the same order of magnitude[207]. Huang and colleagues proposed that the energetic bonus of curvature matching for a single lipid at physiological curvatures is on the order of 1% of k_BT, indicating that curvature preference alone is insufficient for significant partitioning at the cellular scale[208]. Instead, clustering of self-interactive lipids is a prerequisite for significant curvature sensing, and that the aggregate cluster is then targeted to curved regions, as partitioning larger membrane components comes at a reduced entropic cost. For CL, short-range attractive forces (mediated by positive counterions) would be counterbalanced by long-range repulsive electrostatics, dictating cluster size. This view is supported by the

observation that CL-localization to bacterial cell poles has a minimum concentration threshold[186].

Our simulations however show CL accumulation at negative curvature even without nanodomain formation (Fig. 2.5C). The physical basis for this partitioning in the absence of thermodynamic benefits from clustering, as well as the differential behavior of PE and CL are not yet understood and will require further analysis. However, we can speculate on a few factors that may be driving this partition effect. As suggested by Huang, partitioning a larger species comes at less entropic cost, and therefore the intrinsic larger size of CL relative to PE could play a role in the differential portioning characteristics. If we imagine there are a given number of sites available in the highly curved regions and CL would occupy two of these sites while PE would only occupy one. The configurational entropy can be idealized as a product of the curved region multiplicity and the flat region multiplicity. By requiring fewer, larger CL lipids in the curved region to achieve a given lipid fraction (above the bulk lipid fraction), allows for a greater number of CL to be available to the flat region. Having a greater number of the minor component lipid in the larger flat region would have a multiplicative (entropic) benefit.

A final consideration is that we are generating curved phases which have zero Gaussian curvature (the product of the principal curvatures). Cristae morphology is highly varied, but our model approximates common cristae shapes having zero Gaussian curvature, such as tubular cristae and lamellar cristae with curved ridges. Membrane shapes exhibiting significant Gaussian curvature are possible in regions of the inner membrane, such as where tubular cristae junctions merge the cristae to the flat inner boundary membrane. A possible driving force for our observed partitioning behavior is that CL has a preference for zero Gaussian curvature, possibly due to an asymmetric molecular geometry whereas PE may have a stronger preference non-zero Gaussian curvature phases, such as the inner leaflet of highly curved vesicles. Such a

preference could then impact membrane constituent organization between morphologically distinct domains with similar magnitudes of principal curvatures.

Conclusions

In this work we have examined the curvature-based partitioning of lipids, including cardiolipin, in mixed bilayer systems. From these studies, we have been able to draw several conclusions:

(i)The presence of CL reduces the pressure difference required to generate buckled bilayers.

(ii) CL containing bilayers can sample a range of curvature states near the buckling transition pressure difference. This stands in contrast to PC/PE systems, which behave in a two-state fashion, adopting only flat or highly buckled states. This result is suggestive that the presence of CL creates bilayers that are more “tunable”, possibly in response to curvature inducing proteins, and can sample a greater range of morphologies.

(iii) CL accumulates in regions of negative curvature, while PE (which is also an inverted conical lipid), displays a much weaker propensity to aggregate in regions of negative curvature.

Understanding why CL has these unique properties may provide key insights into understanding mitochondrial organization and why disease states characterized by altered concentrations of CL and its variants led to aberrant mitochondrial morphologies.

Supporting Information

The supporting material contains additional figures (2.S1-S11), describing the temperature dependence of CL partitioning, the spline fitting to lipid head groups, the lipid fractions as a

function of curvature and the lipid fractions in different curvature regions as a function of compressional strain.

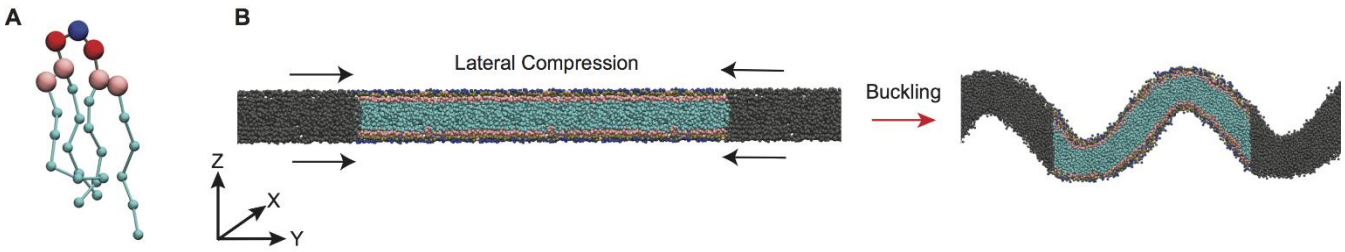

Figure 2.1. Coarse-grained representation of mitochondrial-mimicking membranes. A) MARTINI representation of CL; blue=central glycerol, red=phosphate, pink=glycerol, cyan=acyl chains. Beads are not drawn to scale B) Side view of the transition from flat to buckled bilayer. Colored beads are the lipids in the main simulation cell, while the grey beads represent lipids in the neighboring periodic images.

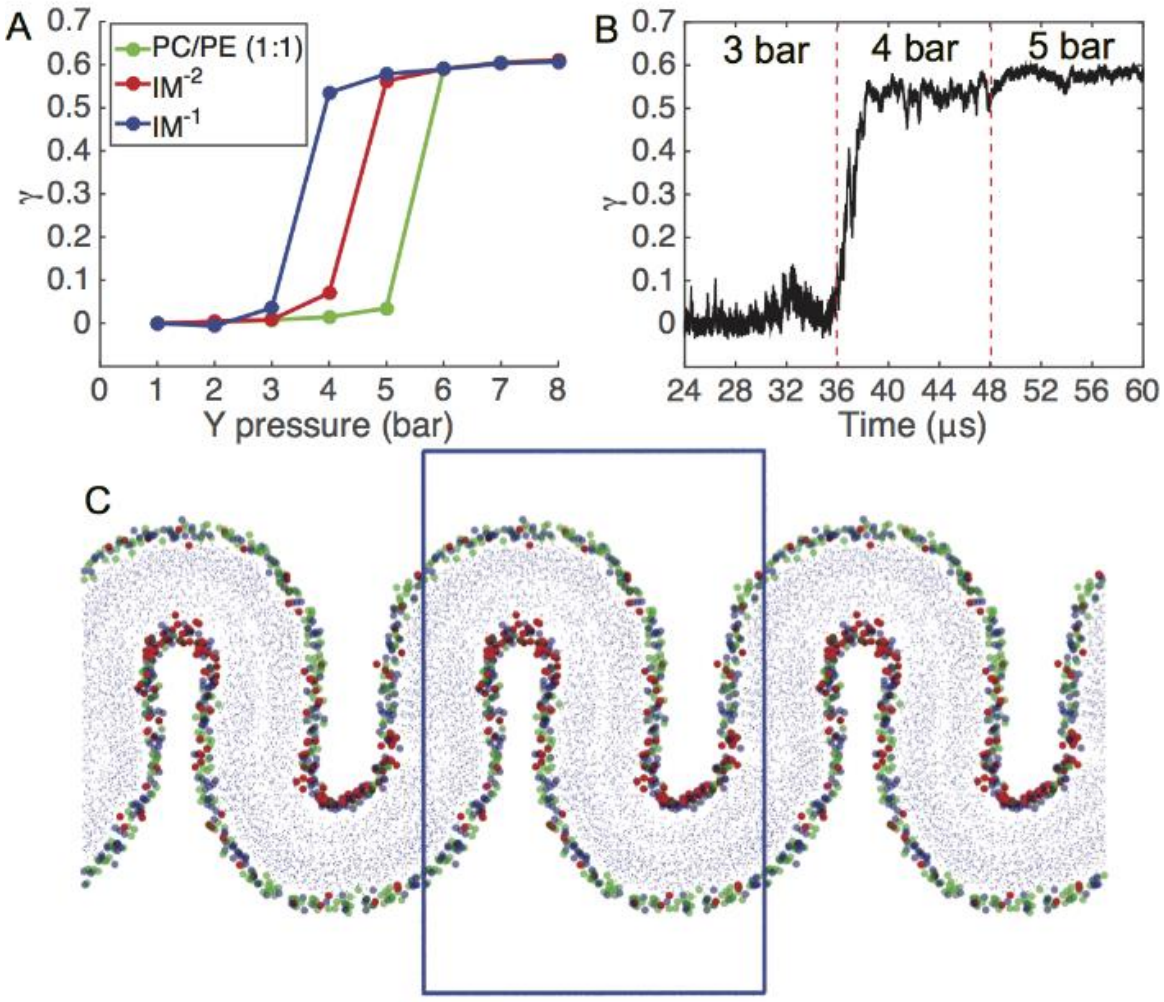

Figure 2.2. Pressure induced buckling of mitochondrial membrane mimetic bilayers. A) The compressional strain (□) is plotted against the *Y*-dimension pressure. Each data point represents an averaging of the final 6 □s of a 12 □s simulation. (B) Time course of a buckling event for IM^{-1} system, which undergoes a buckling transition at the threshold lateral pressure of P_y = 4 bar. (C) Snapshot of fully buckled state for IM^{-1}. Head group beads are colored according to: blue=PE phosphate, red=CL^{-1} central glycerol, green=PC phosphate, blue box represents the main simulation cell.

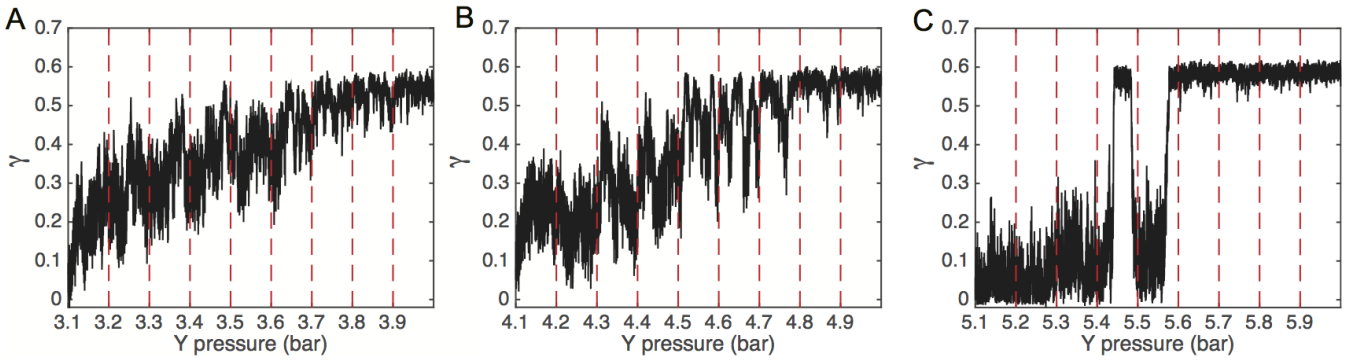

Figure 2.3. Compressional strain *(□)* vs. lateral pressure near the buckling transition point. The IM^{-1} (A), IM^{-2} (B), and PC/PE (1:1) (C) systems were evaluated by running 36 □s simulations at each pressure in 0.1 bar increments. The dashed red lines indicate points at which the pressure was incremented.

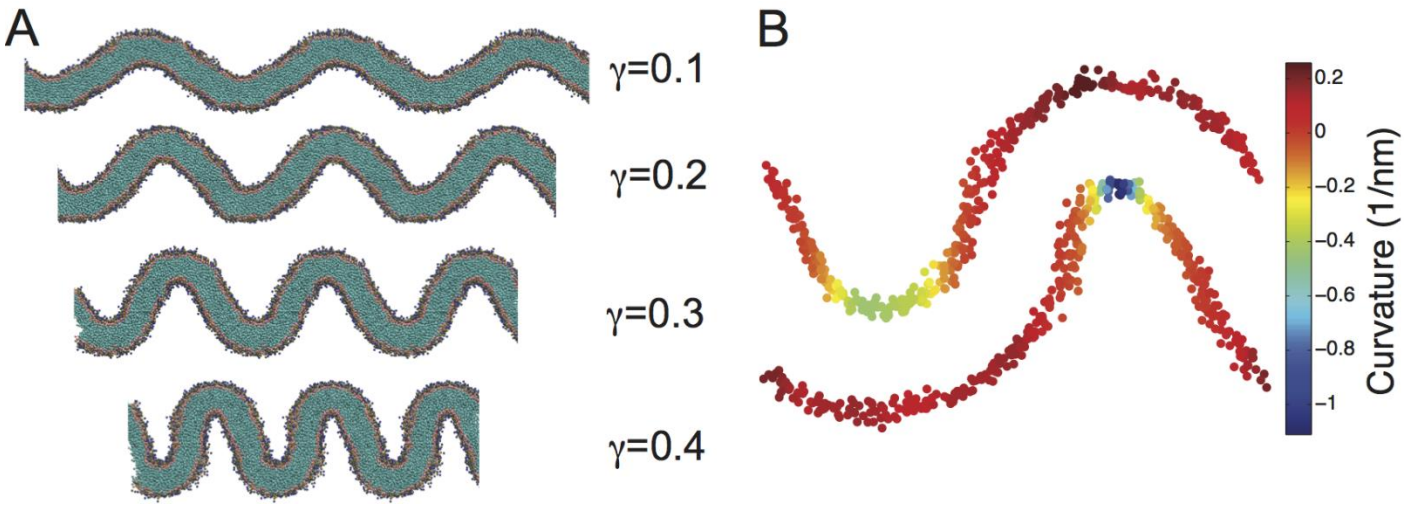

Figure 2.4. Buckling and curvature mapping. A) Depiction of bilayers as a function of induced strain (γ). B) Snapshot of the mapping of bilayer curvature onto the lipid head group positions for a γ=0.3 system.

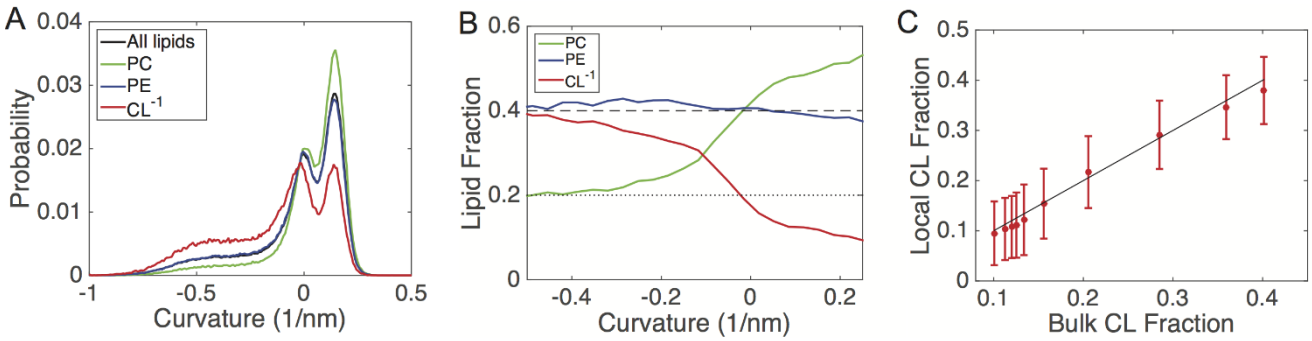

Figure 2.5. Curvature characterization in buckled bilayers, all data are shown for the IM^{-1} system at □=0.3. A) Probability distributions of curvatures. Each distribution is normalized by the amount of each lipid type, such that the sum of probabilities for all curves equals one. B) Lipid fractions as a function of curvature for the same system shown in panel A, the dashed line represents the bulk fraction of PC and PE (40%), and the dotted line represents the bulk fraction of CL^{-1} (20%). C) Clustering analysis for CL^{-1}. The system was subdivided based upon curvature, and the bulk fraction of CL^{-1} is compared with the percentage of CL nearest neighbors around each CL molecule. The solid line represents the well-mixed case (no clustering), where the local concentration matches the bulk concentration.

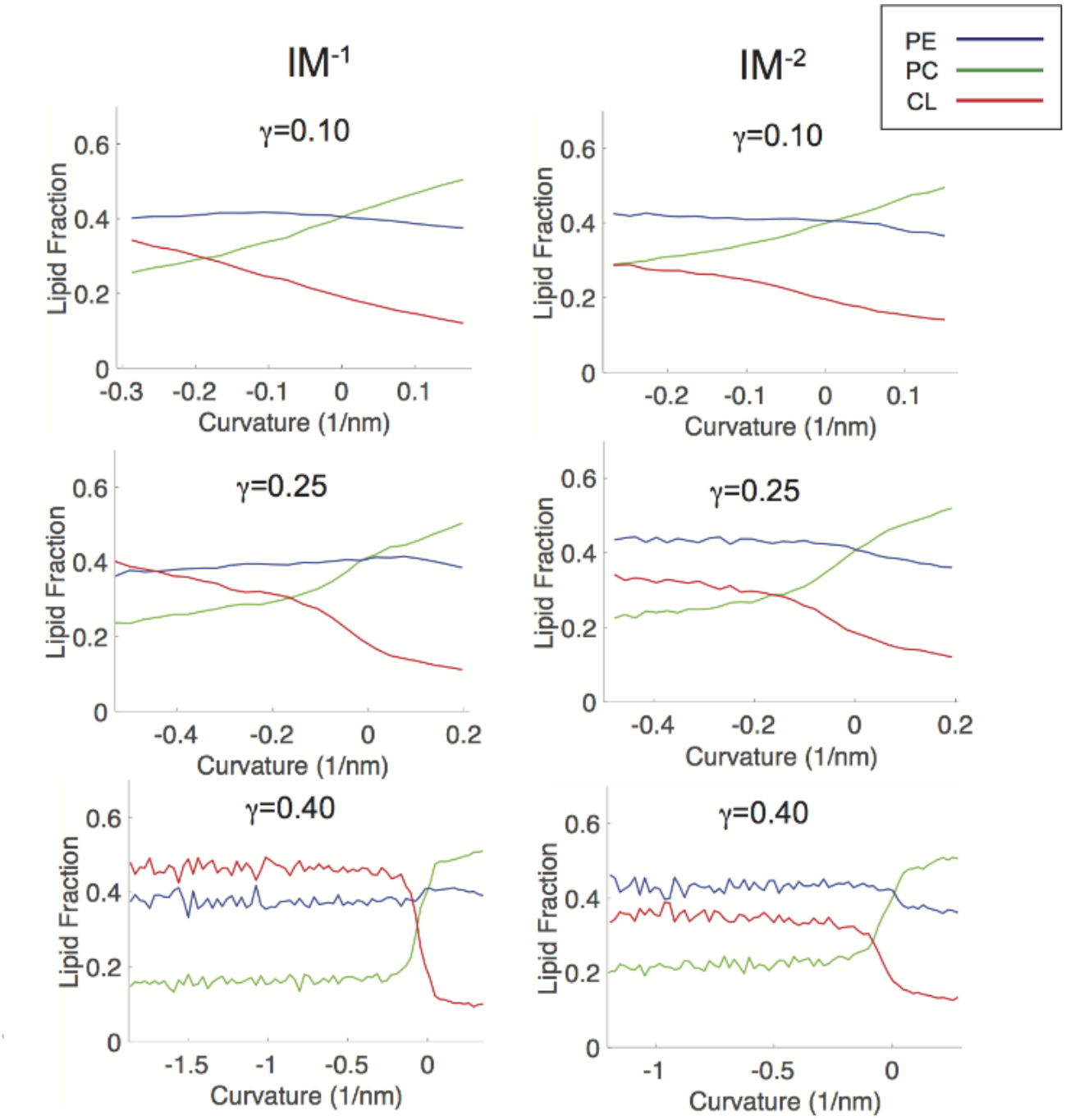

Figure 2.6. Curvature based lipid partitioning comparison between ternary systems containing CL carrying either a -1 or -2 charge. The IM^{-1} systems are shown in the left column and IM^{-2} systems are shown on the right column. The partitioning curves are shown at three different compressional strain states (γ=0.1, 0.25 ,0.4).

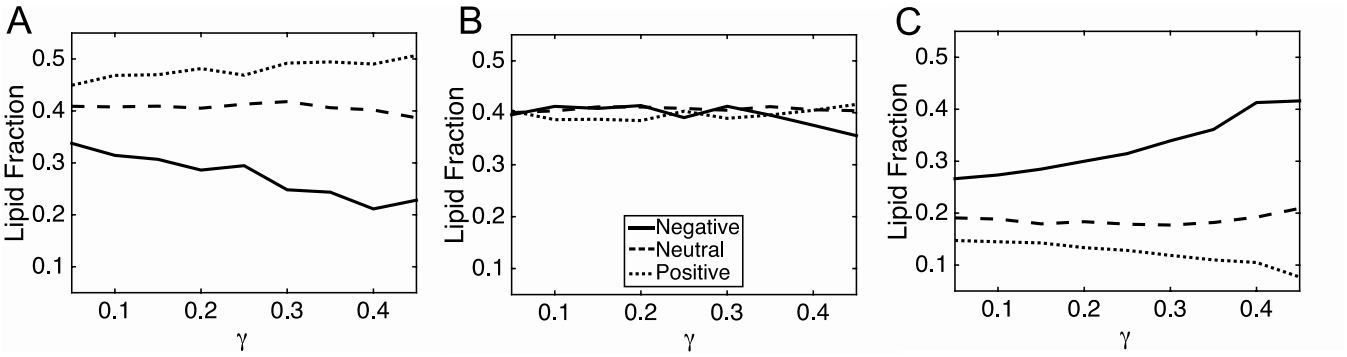

Figure 2.7. Lipid fractions as a function of compressional strain (curvature) for the IM^{-1} system. The lipid fraction of PC (A), PE (B) and CL^{-1} (C) are shown. The legend in B applies to all panels. The curvature regions were defined as follows: negative: $C < -0.05$; neutral: $0.05 \leq C \leq 0.05$; positive: $C > 0.05$, where curvature units are nm^{-1}.

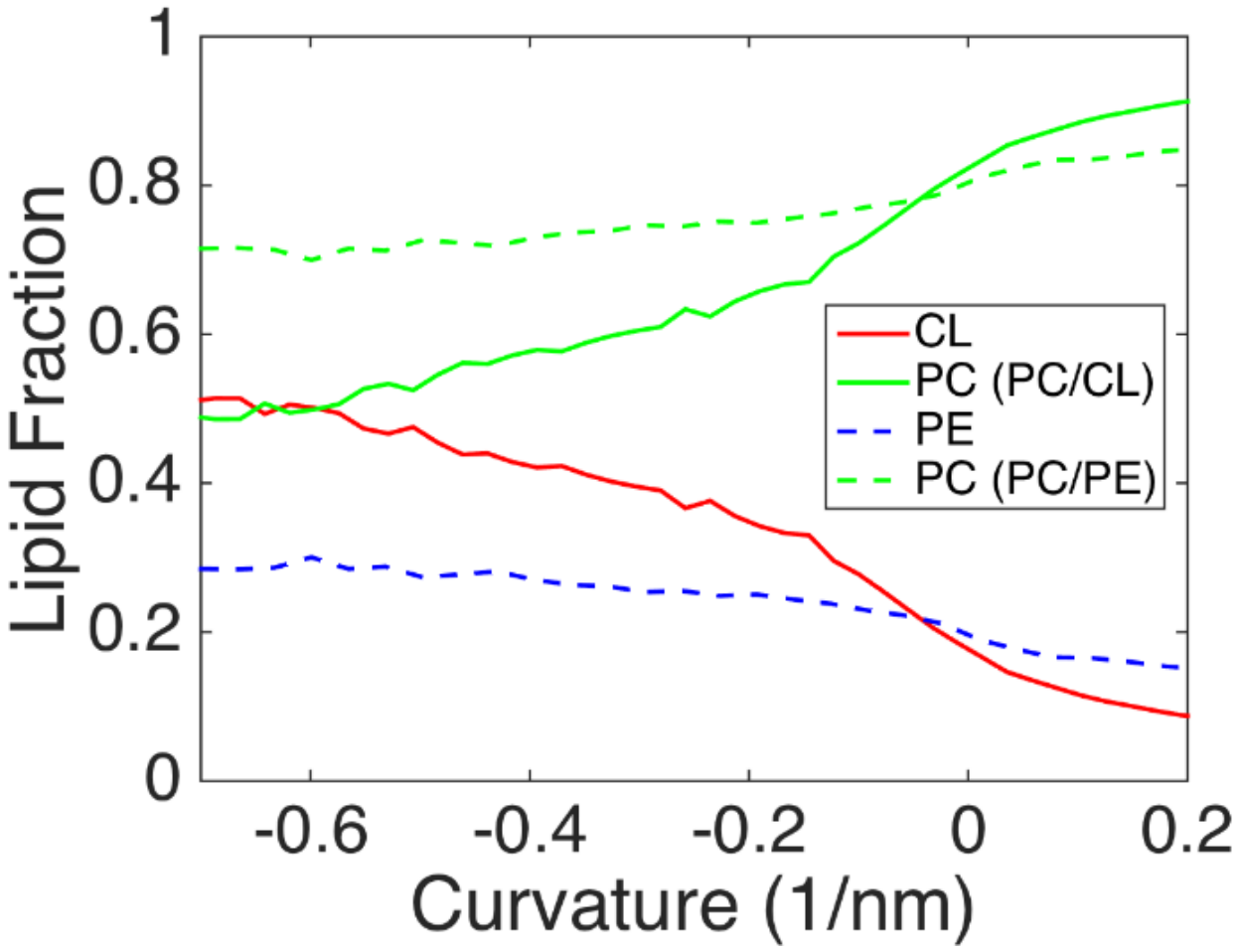

Figure 2.8. Curvature-mediated partitioning of inverted conical lipids in binary bilayer systems. The curvature-based lipid factions are presented for PC/CL^{-1} (4:1) (solid) and PC/PE (4:1) (dashed) system

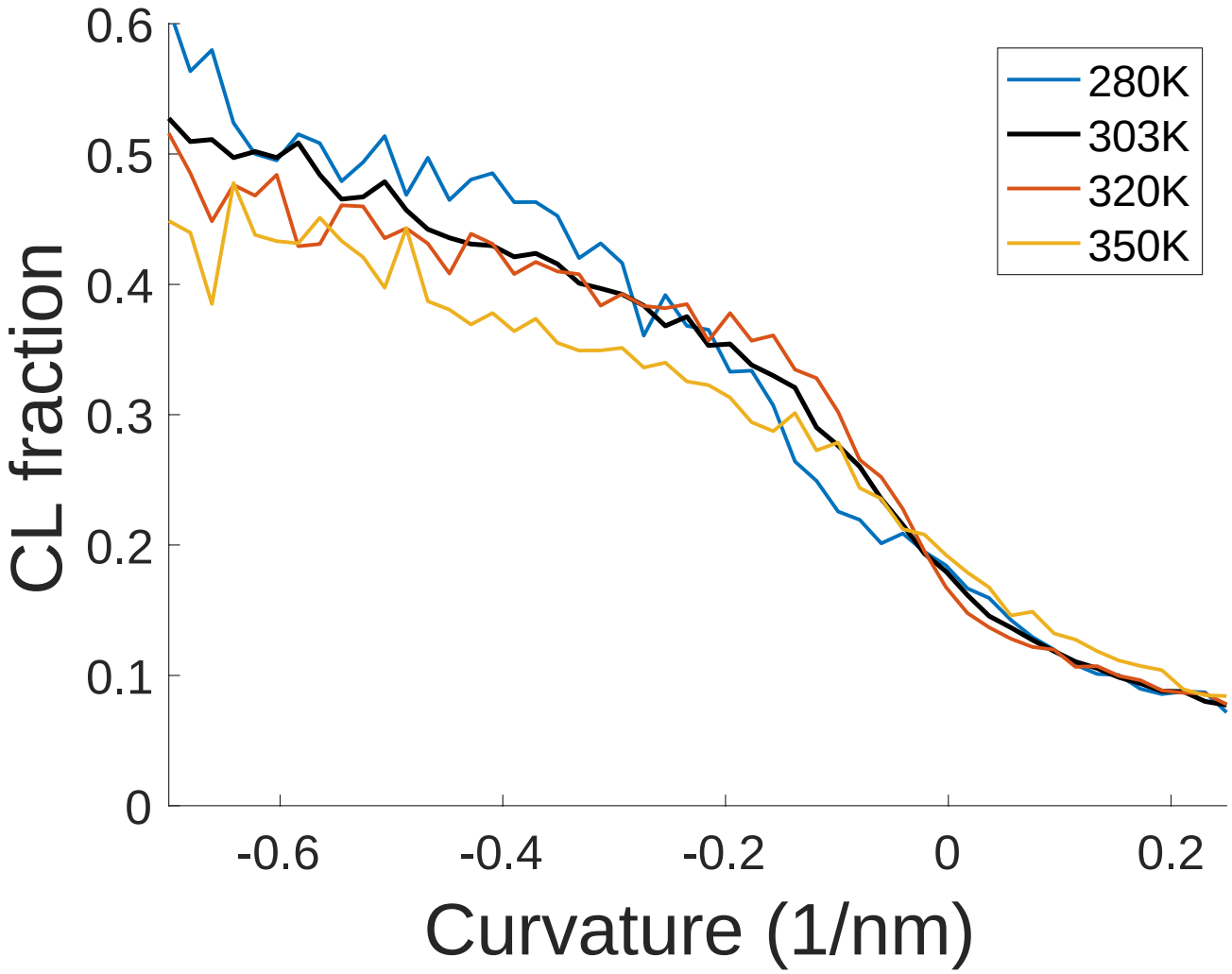

Figure 2.S1. CL partitioning in PC/CL (4:1) system at ***γ***=0.3 as a function of temperature. There is very little temperature dependence to the partitioning in this temperature range.

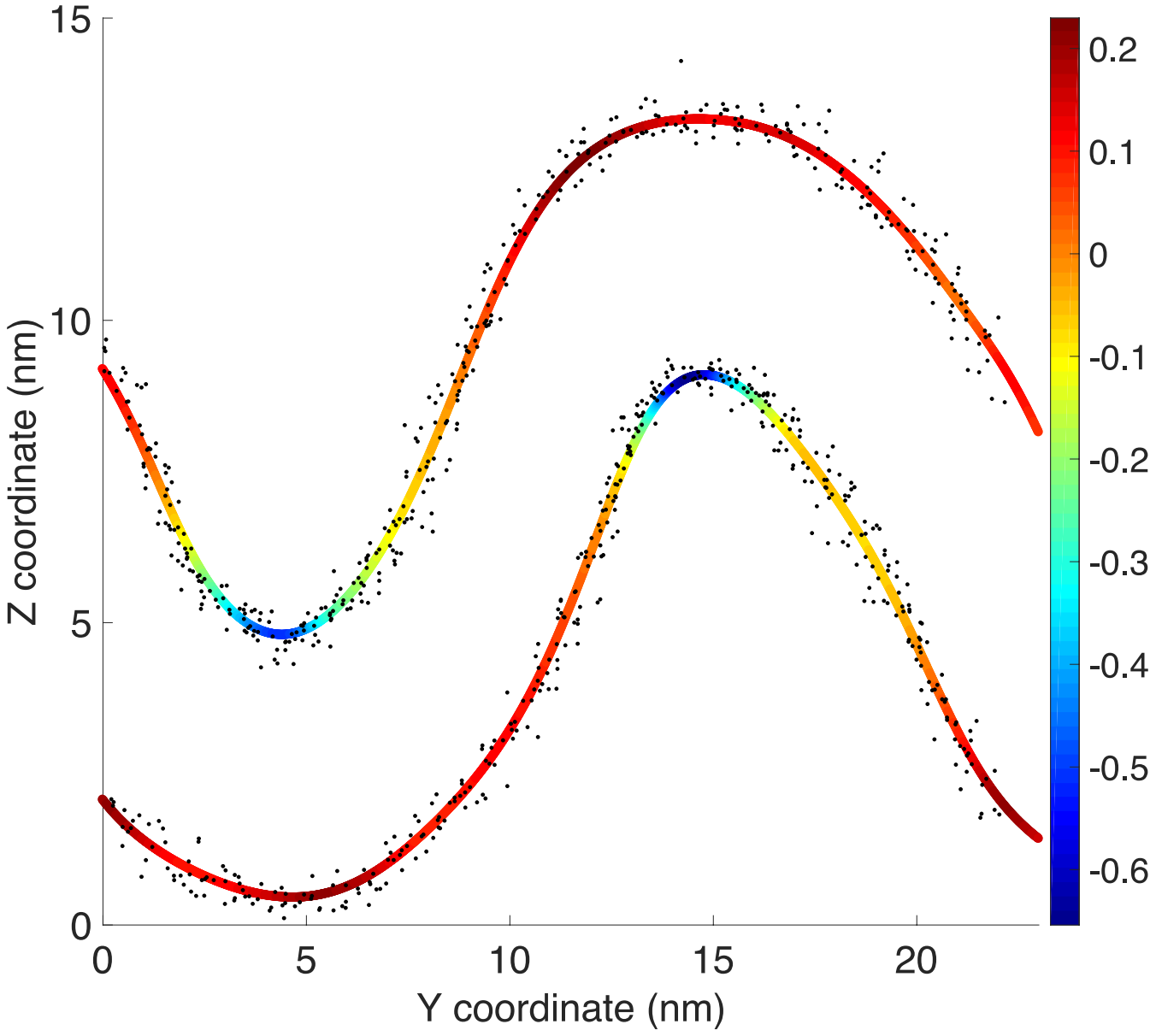

Figure 2.S2. The spline fit (multicolored line) is overlaid with the phosphate head groups (black dots) used to generate the curve fit. The color-coding of the fit is the curvature (units of nm^{-1}), calculated from eq. 2 in main text. The phosphate positions are taken from a random snapshot of the IM^{-1} system at □=0.3 compression.

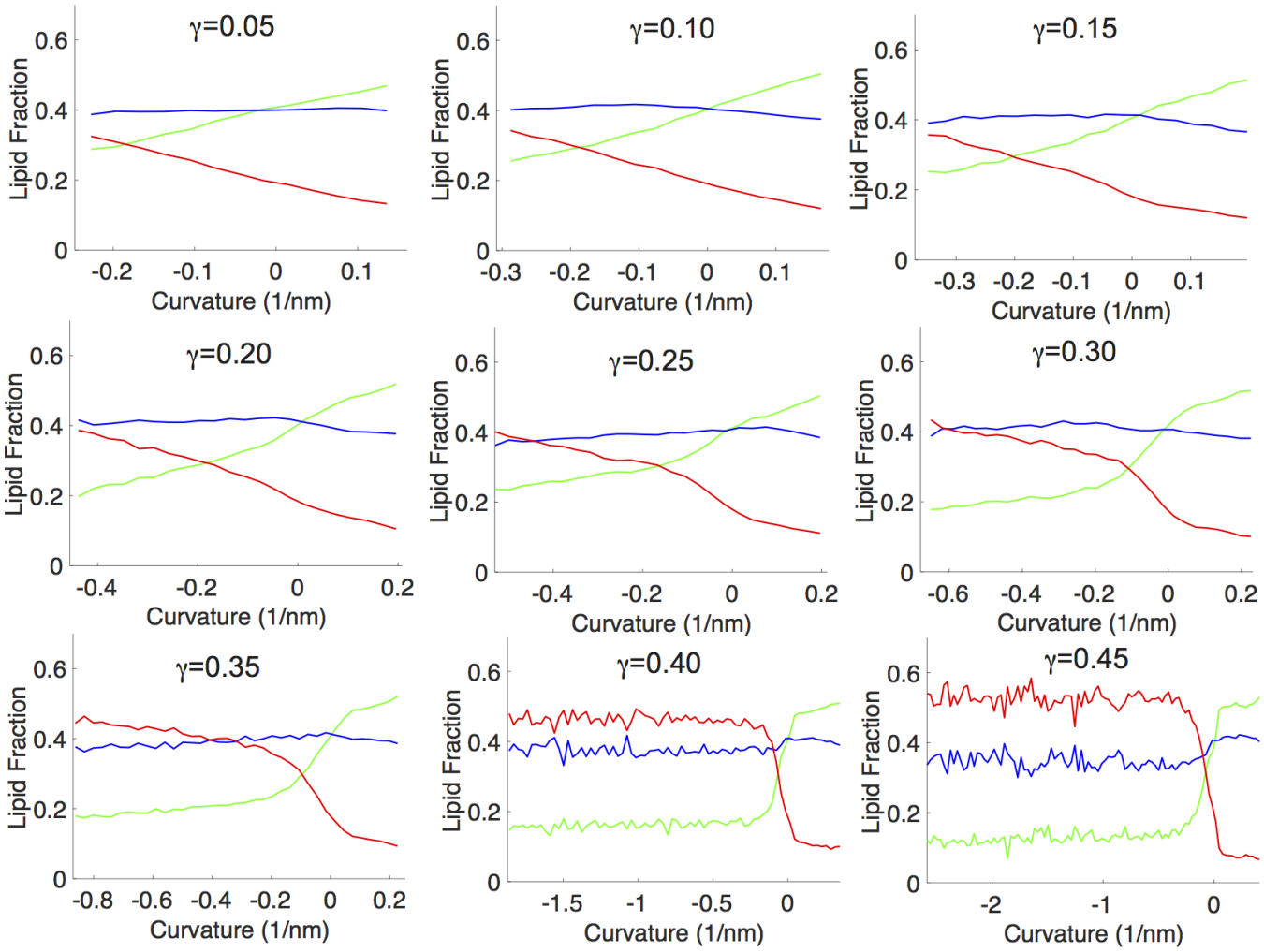

Figure 2.S3. Lipid fractions a function of curvature for the IM^{-1} system, for □=0.05-0.45. Line colors are the following: PC=green, PE=Blue, CL=Red. The *X*-axis range was fixed at curvatures encompassing 98% of head group curvature data points, discarding points at extreme positive and negative curvature due to poor sampling.

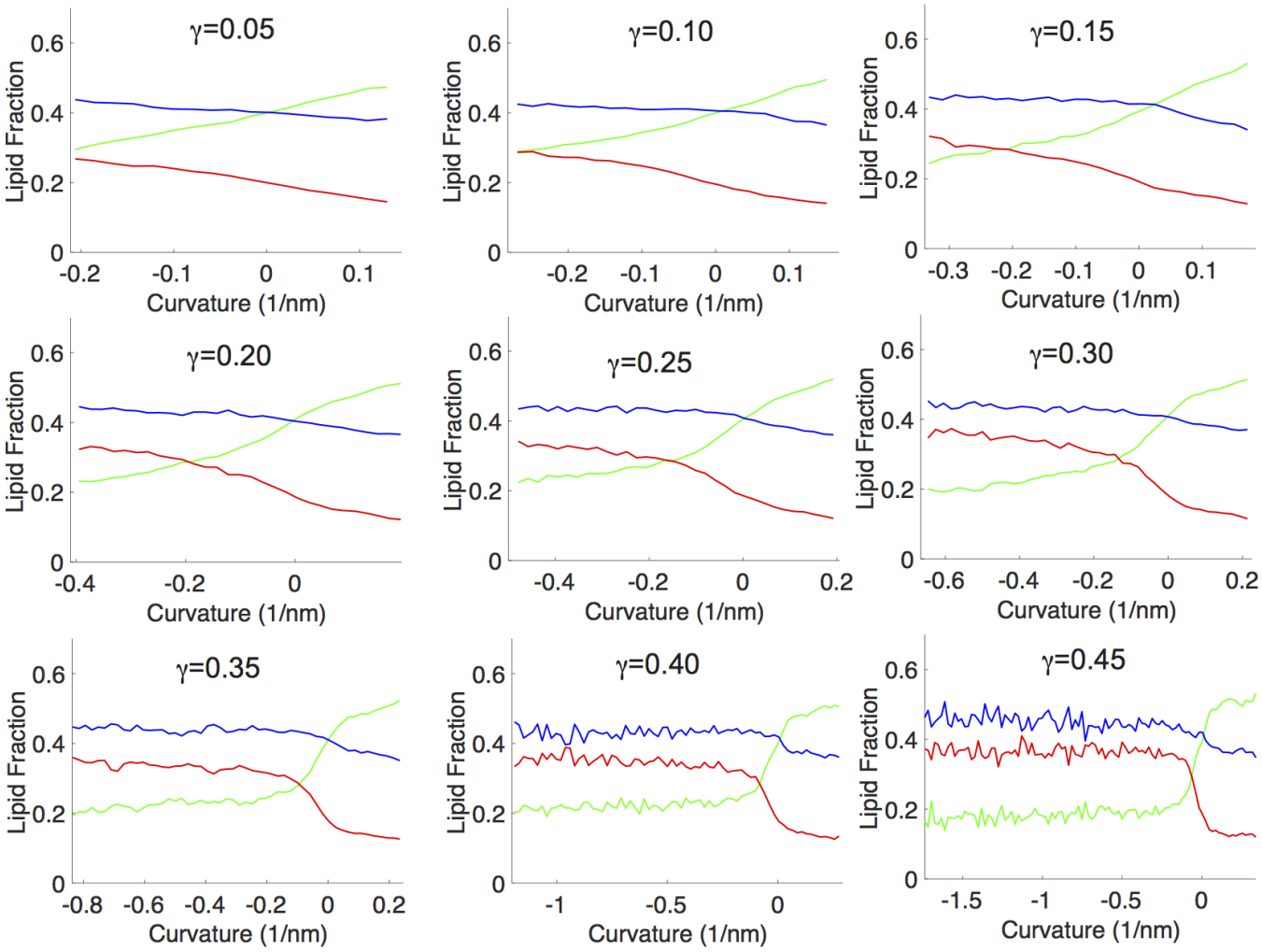

Figure 2.S4. Lipid fractions a function of curvature for the IM^{-2} system, for □=0.05-0.45. Line colors are the following: PC=green, PE=Blue, CL=Red. The *X*-axis range was fixed at curvatures encompassing 98% of head group curvature data points, discarding points at extreme positive and negative curvature due to poor sampling.

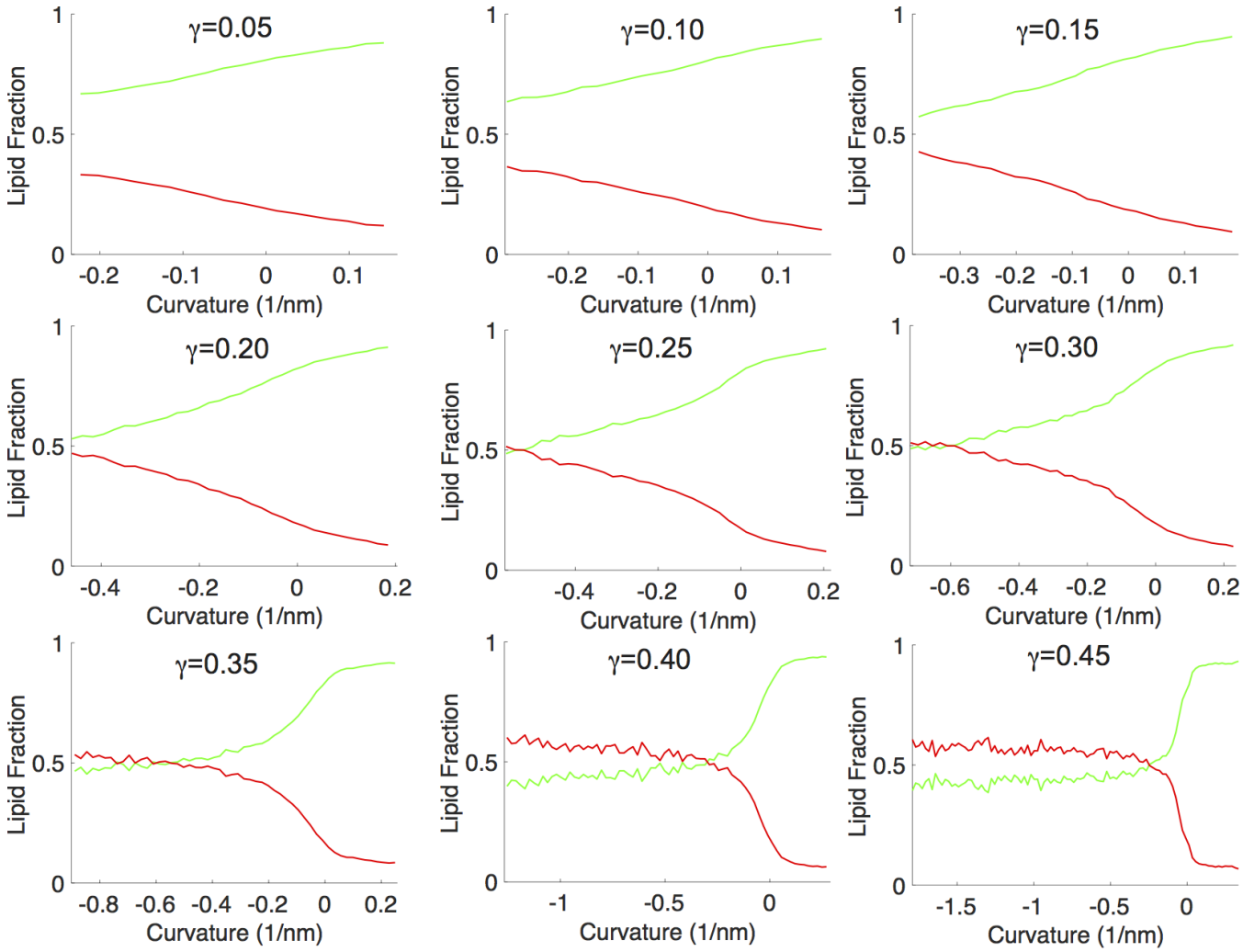

Figure 2.S5. Lipid fractions a function of curvature for the PC/CL (4:1) system, for □=0.05-0.45. Line colors are the following: PC=green, CL=Red. The *X*-axis s range was fixed at curvatures encompassing 98% of head group curvature data points, discarding points at extreme positive and negative curvature due to poor sampling.

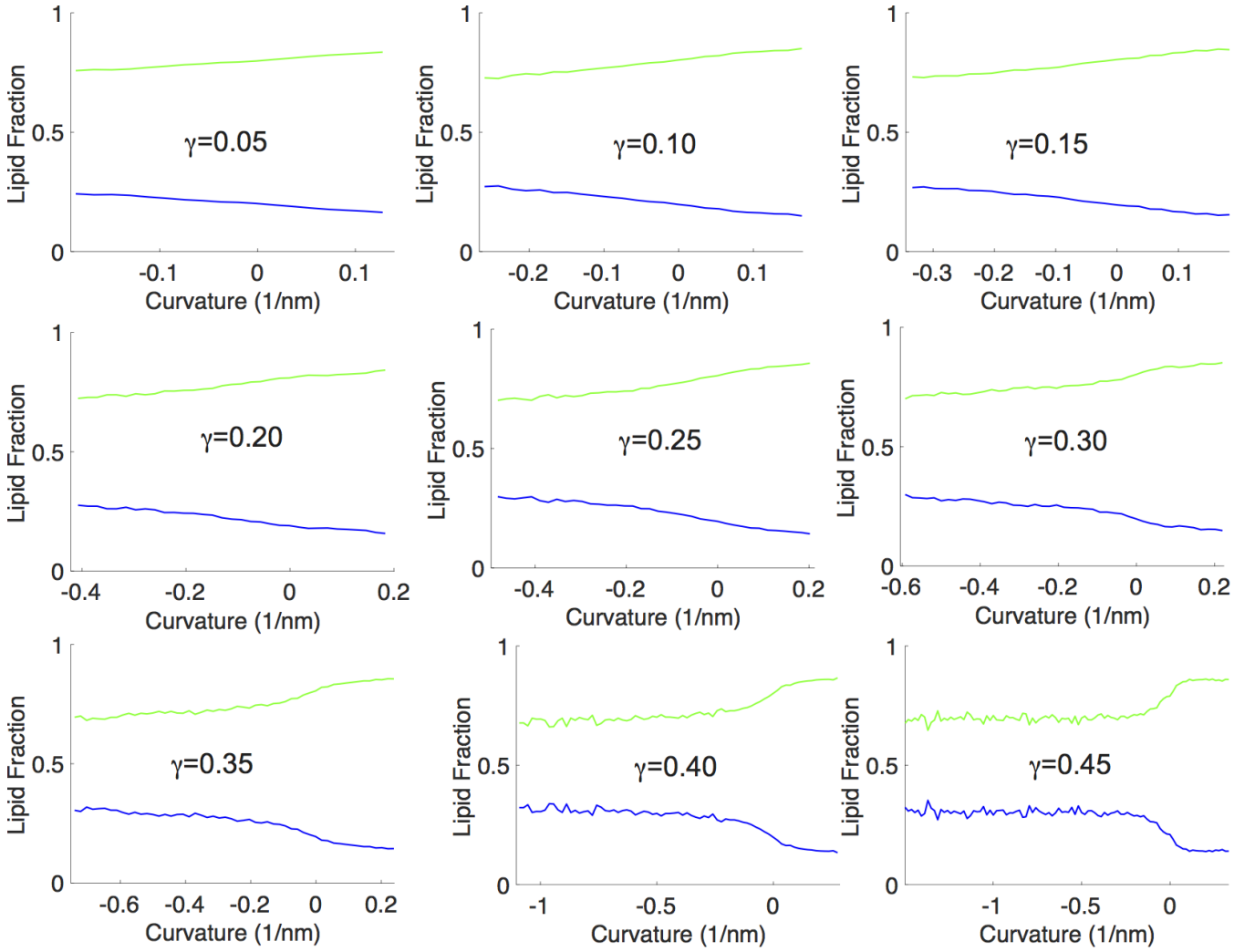

Figure 2.S6. Lipid fractions a function of curvature for the PC/PE (4:1) system, for □=0.05-0.45. Line colors are the following: PC=green, PE=Blue. The *X*-axis range was fixed at curvatures encompassing 98% of head group curvature data points, discarding points at extreme positive and negative curvature due to poor sampling.

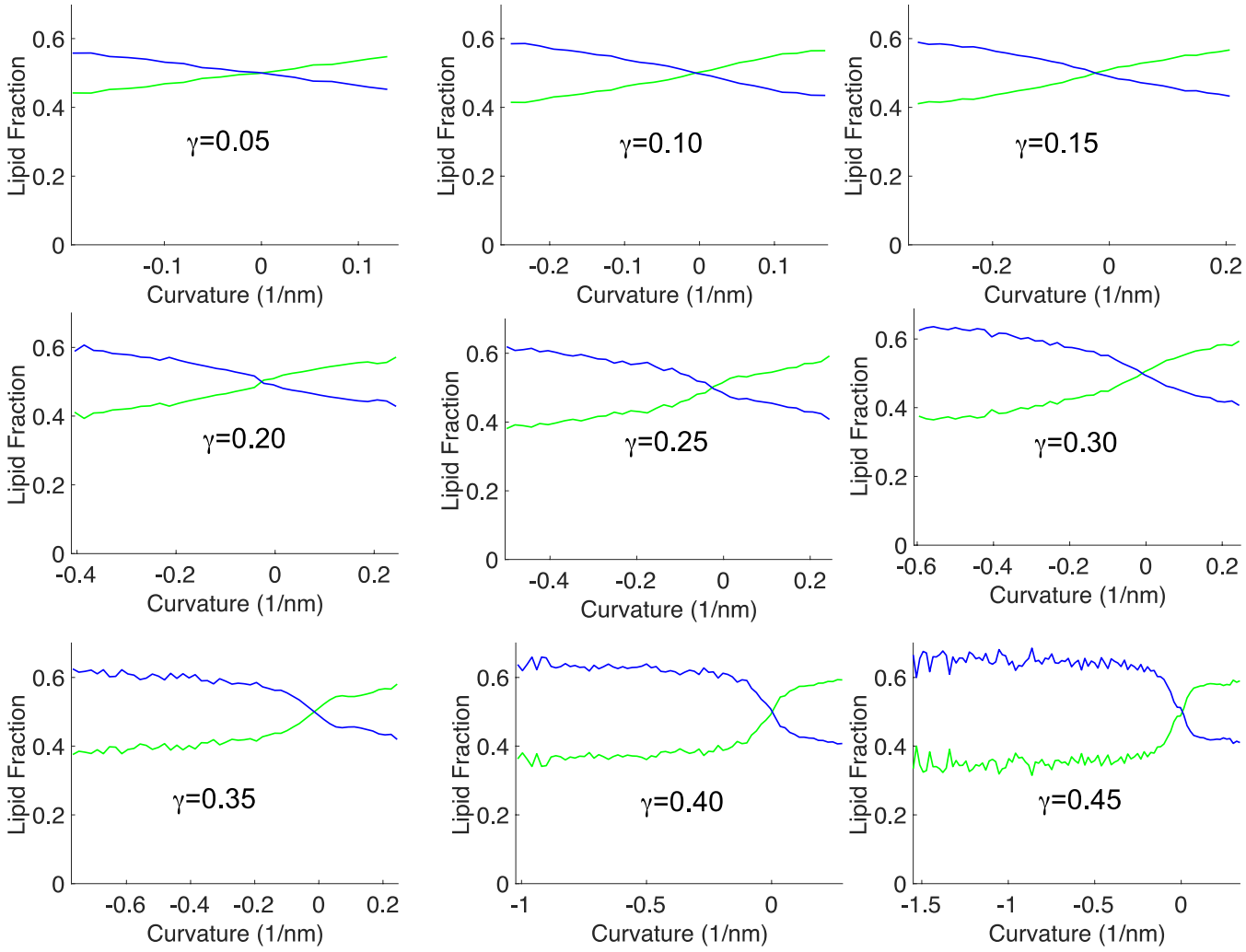

Figure 2.S7. Lipid fractions a function of curvature for the PC/PE (1:1) system, for □=0.05-0.45. Line colors are the following: PC=green, PE=Blue. The *X*-axis range was fixed at curvatures encompassing 98% of head group curvature data points, discarding points at extreme positive and negative curvature due to poor sampling.

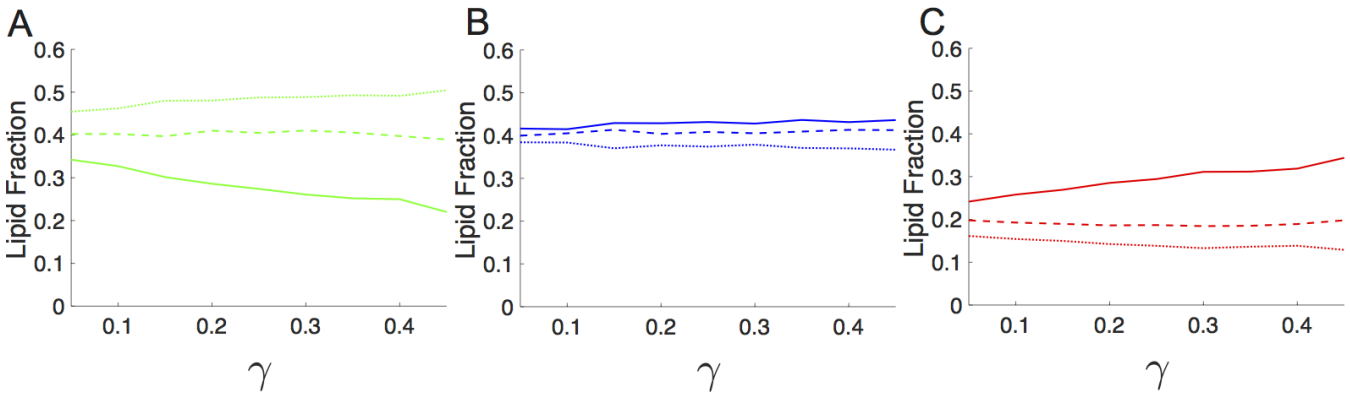

Figure 2.S8. Lipid fractions as a function of compressional strain for the IM^{-2} system. The lipid fraction of PC (A), PE (B) and CL^{-2} (C) are shown. The solid lines represent the negative curvature region, the dashed lines represent the neutral curvature regions, and the dotted lines represent the positively curved regions. The curvature regions were defined as follows: negative: $C < -0.05$; neutral: $-0.05 \leq C \leq 0.05$; positive: $C > 0.05$, where curvature units are nm^{-1}.

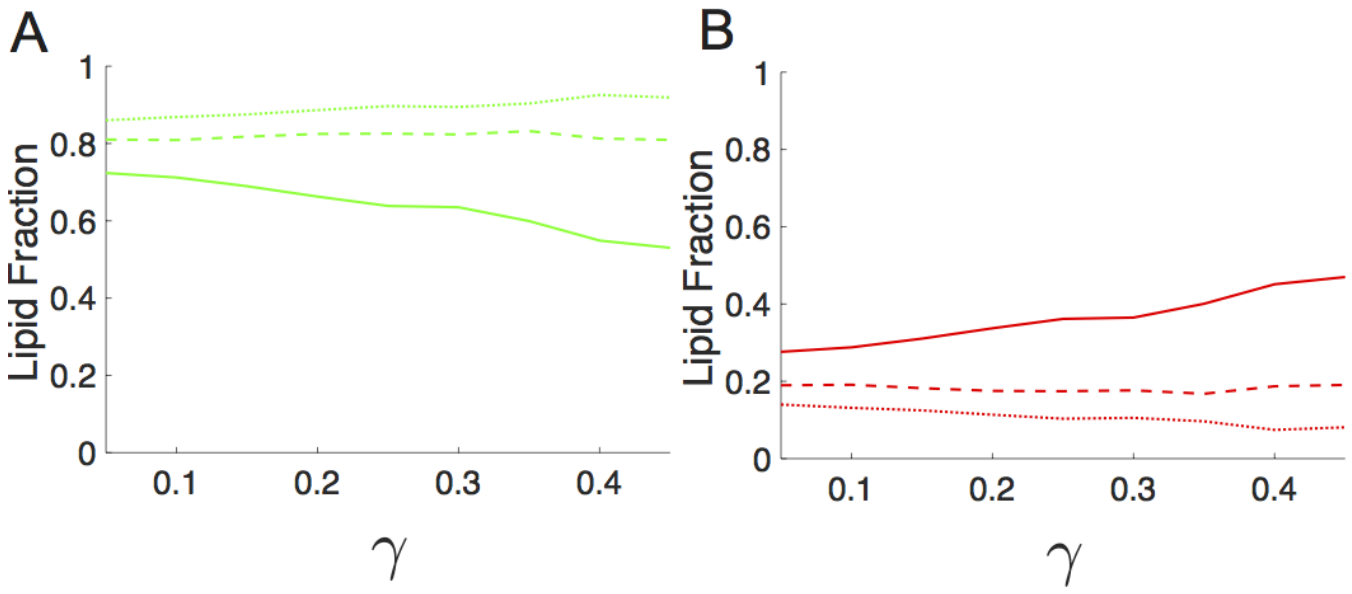

Figure 2.S9. Lipid fractions as a function of compressional strain for the PC/CL (4:1) system. The lipid fraction of PC (A), and CL^{-1} (B) are shown. The solid lines represent the negative curvature regions, the dashed lines represent the neutral curvature regions, and the dotted lines represent the positively curved regions. The curvature regions were defined as follows: negative: $C < -0.05$; neutral: $-0.05 \leq C \leq 0.05$; positive: $C > 0.05$, where curvature units are nm^{-1}.

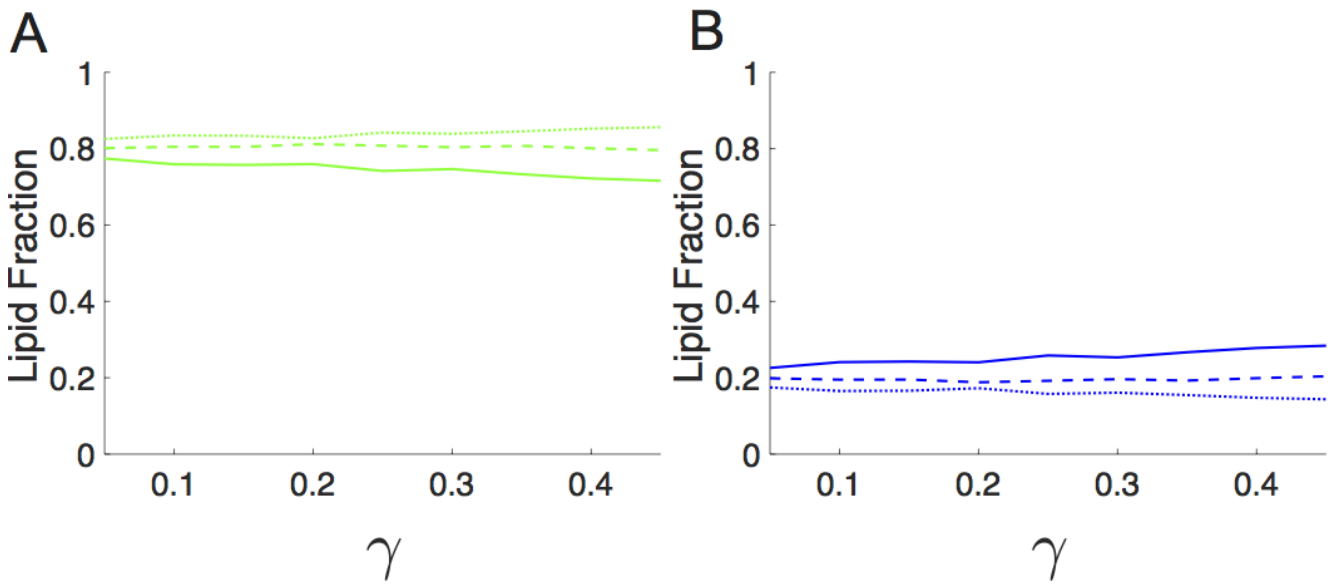

Figure 2.S10. Lipid fractions as a function of compressional strain for the PC/PE (4:1) system. The lipid fraction of PC (A), and PE (B) are shown. The solid lines represent the negative curvature regions, the dashed lines represent the neutral curvature regions, and the dotted lines represent the positively curved regions. The curvature regions were defined as follows: negative: $C < -0.05$; neutral: $-0.05 \leq C \leq 0.05$; positive: $C > 0.05$, where curvature units are nm^{-1}.

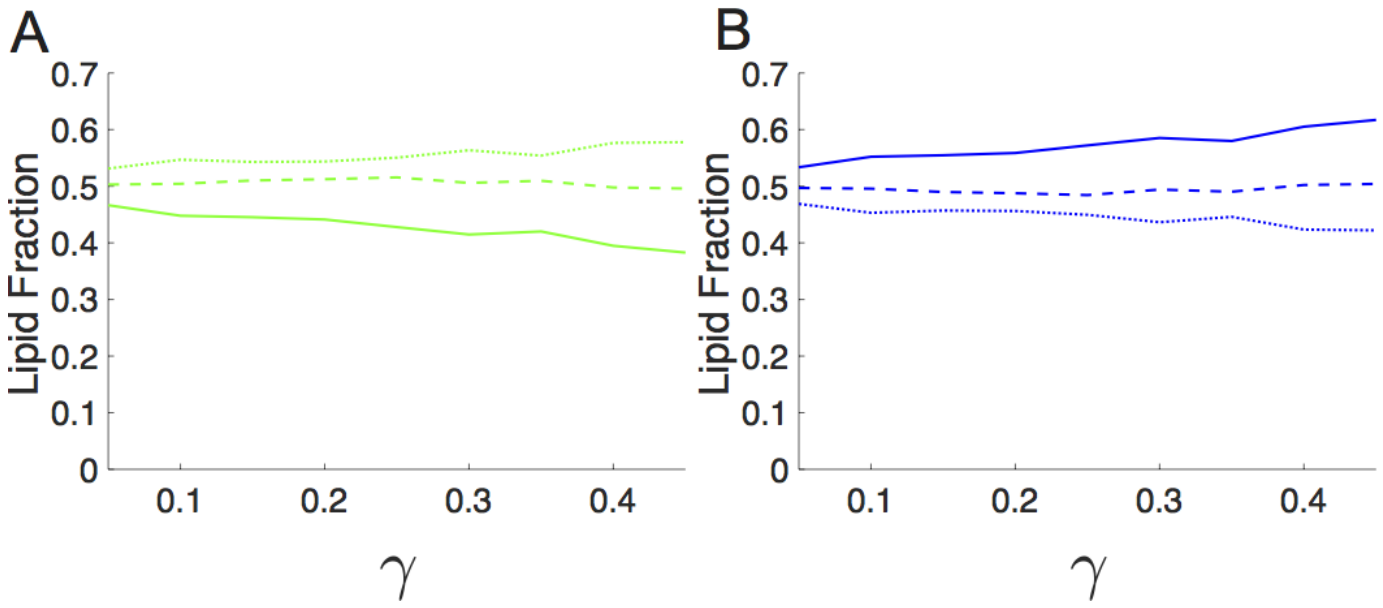

Figure 2.S11. Lipid fractions as a function of compressional strain for the PC/PE (1:1) system. The lipid fraction of PC (A), and PE (B) are shown. The solid lines represent the negative curvature regions, the dashed lines represent the neutral curvature regions, and the dotted lines represent the positively curved regions. The curvature regions were defined as follows: negative: $C < -0.05$; neutral: $-0.05 \leq C \leq 0.05$; positive: $C > 0.05$, where curvature units are nm^{-1}.

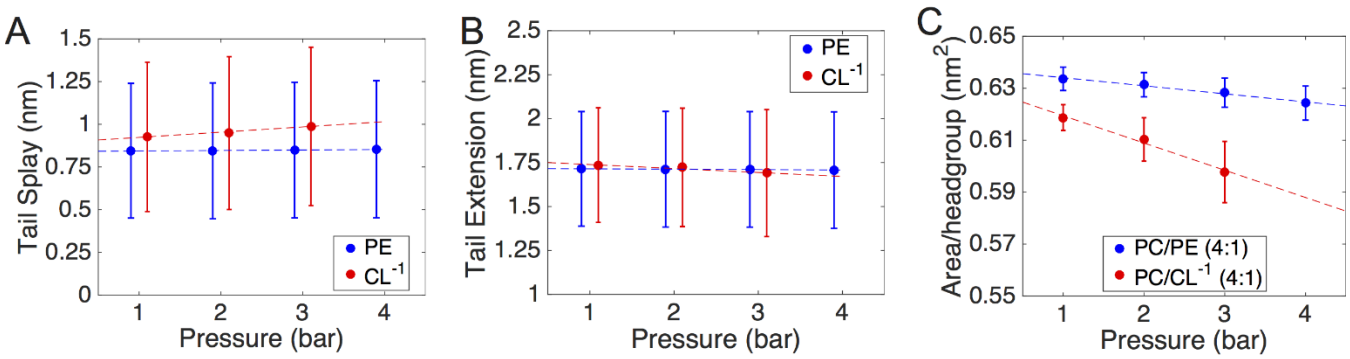

Figure 2.S12. Molecular geometry of PE and CL in PC/PE (4:1) and PC/CL-1 (4:1) systems, respectively. A) The lateral splay of the lipids tails. B) The normal direction extension of the lipid tails. C) The area per lipid head group, each CL is considered as having two head groups. The pressure is the applied Y-dimension pressure.

Chapter 3:

Molecular Dynamics Analysis of Cardiolipin and Monolysocardiolipin on Bilayer Properties

Reproduced with permission from:

Boyd, Alder and May. “Molecular Dynamics Analysis of Cardiolipin and Monolysocardiolipin on Bilayer Properties. *Biophysical Journal* (2018), 114 (9), 2116-2127

The following changes have been made:

- The manuscript has been reformatted to meet University Standards
- Figures numbers have the chapter number prepended
- References have been renumbered to match the rest of the thesis

Characterization of molecular and bilayer scale properties of cardiolipin and monolysocardiolipin from multi-scale molecular dynamics simulations

K.J. Boyd, N.N. Alder, E.R. May

Abstract

The mitochondrial lipid cardiolipin (CL) contributes to the spatial protein organization and morphological character of the inner mitochondrial membrane. Monolysocardiolipin (MLCL), an intermediate species in the CL remodeling pathway, is enriched in the multisystem disease Barth syndrome. Despite the medical relevance of MLCL, a detailed molecular description that elucidates the structural and dynamic differences between CL and MLCL has not been conducted. To this end, we performed comparative atomistic molecular dynamics studies on bilayers consisting of pure CL or MLCL to elucidate similarities and differences in their molecular and bulk bilayer properties. We describe differential headgroup dynamics and hydrogen bonding patterns between the CL variants, and show increased cohesiveness of MLCL's solvent interfacial region, which may have implications for protein interactions. Finally, using the coarse-grained Martini model, we show that substitution of MLCL for CL in bilayers mimicking mitochondrial composition induces drastic differences in bilayer mechanical properties and curvature-dependent partitioning behavior. Together, the results of this work reveal differences between CL and MLCL at the molecular and mesoscopic levels that may underpin the pathomechanisms of defects in cardiolipin remodeling.

Introduction

Cardiolipin (CL) is an unusual phospholipid with a headgroup consisting of two phosphatidic acid moieties bridged by a central glycerol and four acyl chain tails. In eukaryotes, CL localizes predominantly to the inner mitochondrial membrane (IMM), to a concentration of up to 20 mol%[209]. CL plays a role in many organellar functions and has been shown to bind to a variety of mitochondrial proteins[180]. Two important roles of CL involve maintaining the highly curved morphology of mitochondrial cristae[182,183], and aiding the assembly of respiratory supercomplexes[169].

Under certain physiological conditions, CL can assume a negative spontaneous curvature that results from an inverted conical geometry due to a small headgroup size relative to the large volume occupancy of its four acyl chains. In prokaryotic cell membranes, this leads to enrichment of CL at the highly curved polar regions and fission sites of rod-like bacteria[184–186]. The ionization state of the two phosphate moieties of CL has been a debated topic. Recent studies suggest that CL is doubly deprotonated at physiological pH and carries a charge of -2[161–164], though other literature indicates circumstances in which CL can carry a -1 charge[165–168]. The tuning of CL's charge state will affect the headgroup charge repulsion and modulate molecular geometry. Indeed, the phase behavior and intrinsic curvature of CL depend on both pH and ionic concentration[170,171,173–175,178,179].

Following the *de novo* biosynthesis of nascent CL within the IMM, the lipid undergoes a remodeling process to yield the mature CL fatty acid composition, consisting of four unsaturated hydrocarbon chains[210]. CL is first deacylated by a CL-specific phospholipase[211,212] that cleaves an acyl chain from a headgroup glycerol, rendering the

tri-acyl species monolysocardiolipin (MLCL) with a hydroxyl group at the site of cleavage (**Fig 3.1**). Multiple enzymes have been identified that catalyze the re-acylation of MLCL. Most MLCL remodeling is driven by tafazzin, an MLCL transacylase encoded by the nuclear X-linked *TAZ* gene. *TAZ* deficiency causes accumulation of MLCL and abnormal fatty acid profiles of tetra-acyl CL, which results in aberrant IMM morphology and disruption of the assembly and spatial organization of IMM protein complexes[182,183]. In humans, mutations in the *TAZ* gene lead to Barth syndrome, a multisystem disorder that clinically presents with cardiomyopathy, skeletal muscle weakness, growth retardation and possibly death in young males[213].

CL-containing bilayers have been well-characterized through a variety of biophysical studies, yielding information about ionization states, polymorphic phase behaviors, and lipid-protein interactions. In contrast, there is a relative dearth of experimental studies on the structural and dynamic properties of MLCL despite its clinical relevance. It has been shown that MLCL can modulate the activity of the apoptotic factor tBid[214] in a different manner than CL, and that MLCL-containing bilayers have a stronger preference for lamellar phases than those containing CL[215]. Computational studies have also focused on the more prominent CL species. A number of computational molecular modeling and molecular dynamics (MD) studies have explored the structural and dynamic properties of tetra-acyl CLs[79,191–195], whereas to our knowledge only a single MD study has interrogated the physical characteristics of MLCL using a coarse-grained (CG) model to investigate the polymorphic phase-behavior in homogeneous lipid systems[74].

The molecular scale differences between tetra-acyl and tri-acyl CL species may impact bulk bilayer properties, which may give rise to different morphological

characteristics of bilayers with differing CL-MLCL ratios. However, the molecular scale properties are yet to be thoroughly investigated. To study the local effects arising from molecular differences between CL and MLCL, we performed atomistic MD simulations on bilayers composed purely of tetraoleoylcardiolipin (TOCL) or trioleoylmonolysocardiolipin (hereby used synonymously with MLCL). We describe the headgroup orientation and acyl chain ordering resulting from tail number asymmetry. The orientation and hydrogen (H)-bonding partners of the lyso hydroxyl group are quantified. We characterize differences in headgroup cohesion between the species and suggest a mechanism that could explain the effects of MLCL on protein-lipid interactions. To study larger scale bilayer mechanical properties, we performed CG-MD on heterogeneous bilayers mimicking the composition of the IMM, implementing a previously described buckling protocol[79] to examine trends in critical buckling pressure and curvature-based lipid segregation.

Methods

All-atom simulations

Atomistic MD simulations were performed using the GROMACS 5 package[216] and the CHARMM36 force field[217]. Initially, a solvated bilayer consisting of 50 TOCL (-2*e* charge) molecules per leaflet was generated using the CHARMM-GUI input generator[218]. The bilayer was solvated with 8482 water molecules, and 200 sodium ions were added to neutralize the total system charge. The TOCL system was used as the basis to generate the initial MLCL system. This was accomplished by replacing one *sn*-2 chain in each TOCL molecule by a hydroxyl group, as depicted in **Fig 3.1**. The topology file was

modified to accommodate the chain deletion, and the parameters chosen for the new hydroxyl group matched that of the central glycerol hydroxyl. A GROMACS compatible topology file (.itp) for MLCL is included in the appendix **File S1**.

Energy minimization and equilibration steps were performed according to the CHARMM-GUI guidelines, with steepest descent minimization for 5000 steps followed by NVT equilibration for 50 ps with a timestep of 1 fs followed by NPT equilibration with position restraints on the headgroup phosphorus atoms for 325 ps at a timestep of 2 fs, with semi-isotropic pressure coupling accomplished using the Berendsen barostat. Both TOCL and MLCL bilayers were equilibrated using the same protocol.

Unrestrained MD simulations were run for 500 ns for both bilayers using a timestep of 2 fs. Temperature was maintained at 303 K using a Nose-Hoover thermostat[219,220] with a coupling time constant of 1 ps. A semi-isotropic pressure coupling scheme was implemented using the Parrinello-Rahman barostat[197] with a coupling constant of 5 ps. Bilayer compressibility was set to 4.5×10^{-5} bar^{-1}, and the reference pressures both in the bilayer plane (X-Y) and normal (Z) to the bilayer were set to 1 bar, to generate a zero surface tension ensemble. Van der Waals interactions were cut off at 1.2 nm, with the interactions modified using the force-switch method between 1.0 nm and 1.2 nm. Long-range electrostatics were calculated using the Particle Mesh Ewald (PME) method, with a real-space cutoff of 1.2 nm. The first 200 ns of unrestrained MD was considered further equilibration, leaving 300 ns for production MD to be analyzed. Bilayers were visually inspected using VMD 1.9[221]. Analyses of simulations were performed using a combination of GROMACS tools and in-house MATLAB scripts. Acyl chain order parameters were calculated with the following equation:

$$S_{CH} = \frac{3}{2}\langle \cos^2 \theta \rangle - \frac{1}{2} \qquad (3.1)$$

, in which θ for a given acyl carbon is defined as the angle between the bilayer normal and the vector originating at the acyl carbon and terminating at the acyl hydrogen.

Interdigitation of monolayer acyl chains was calculated by integrating the dimensionless overlap parameter ρ_{ov},[222]

$$\rho_{ov}(z) = 4 * \frac{\rho_t(z) * \rho_b(z)}{\left(\rho_t(z) + \rho_b(z)\right)^2} \qquad (3.2)$$

$$\lambda_{ov} = \int_0^{L_z} \rho_{ov}(z)\, dz \qquad (3.3)$$

where ρ_t and ρ_b are the acyl densities along the z coordinate of the top and bottom leaflets respectively. Integrating the overlap parameter (Eq. 3.3) over the box z dimension (L_z) yields an interdigitation length, ρ_{ov}, which characterizes the extent of interleaflet interdigitation.

Lateral pressure profiles (LPPs) were calculated using GROMACS-LS[19], a modified version of GROMACS 4.5.5. The calculation of the LPPs are based on 100 ns of simulation data, with a save rate for position and velocities every 5 ps. While the simulations were run using PME, GROMACS-LS does not permit PME and electrostatics must be calculated with a straight cutoff. The recommended cutoff for GROMACS-LS is 2.2nm[19], but we found that a cutoff of 3.2 nm was necessary to observe convergence. Further discussion of GROMACS-LS parameter choices and convergence is presented in the Supporting Material and **Fig 3.S1-S3**.

The output parameters of Gromacs-LS are the components of the stress tensor, σ, as a function of the z dimension (bilayer normal). The lateral and normal components of the pressure profile are $P_L = -0.5 * (\sigma_{xx} + \sigma_{yy})$ and $P_N = -\sigma_{zz}$, respectively, and the LPP is given by the difference in these components, $\pi(z) = P_L(z) - P_N(z)$. The first moment of π(z) links the LPP to the bending modulus (k_c) and spontaneous curvature (c_0):

$$k_c c_0 = \int_0^\infty z * \pi(z) dz \qquad (3.4)$$

where the bilayer is centered at z=0.

All reported error estimates are standard errors, calculated using block averaging. For each observable, appropriate block lengths were determined by scanning a range of block sizes and observing the effect of block size on estimated error.

Bilayer defect analysis

The hydrophobic core accessibility was analyzed in the atomistic simulations by a method similar to Vamparys, et al[223]. The simulation box was divided into square grids with a grid spacing of 0.5 Å. The occupancy of each grid voxel was determined by first projecting the volume occupancy of the bilayer atoms, calculated with the volmap tool in VMD, onto the grid. Each X,Y grid position was then scanned from the top down, until an occupied voxel was reached. The X,Y grid position was then assigned as either headgroup (if the first occupied grid encountered was a headgroup atom) or tail(if an acyl carbon). The headgroups included linking glycerols and all carbons bonded to oxygen, including the

ester carbon that begins the acyl chains (see **Fig 3.1**). This allowed us to construct a 2D map indicating if the first grid box contacted would be occupied by the headgroup or tail. From this we could determine the fraction of the bilayer surface allowing access to acyl chains. To then discriminate small gaps in the headgroup coverage from larger "defects," each grid point assigned as tail on the 2-D surface was treated as the center-point of a spherical probe with a specific radius. If the grid point and all neighboring grid points within this radius were classified as tails, those grid points were then assigned as defects. In this way, only hydrophobic patches with sizes and shapes that could accommodate the spherical probe were classified as true defects.

Coarse-grained simulations

Coarse grained simulations were conducted in GROMACS 5 using the Martini force field[27]. A heterogeneous bilayer consisting of palmitoyloleolyphosphatidylcholine (POPC), palmitoyloleoylphosphatidylethanolamine (POPE), and tetraoleoylcardiolipin (TOCL) was generated using the CHARMM-GUI Martini bilayer generator[102]. To generate a model for MLCL, a single *sn*-2 connected chain was removed from the TOCL model. The glycerol bead type that was connected to the deleted tail was changed from Na to P1, matching the form that represents other lysolipids in the Martini lipid repository. The Martini representation of the TOCL head group consists of a central glycerol bead connected on both sides by a phosphate bead followed by two glycerol beads, each with one acyl chain attached (the "*sn-2*" equivalent chain attached to the glycerol bead proximal to the phosphate, and the "*sn-1*" equivalent chain attached to the terminal glycerol bead). To generate MLCL, the *sn-2* chain on one side was removed, and the attached glycerol bead

type converted to a P1 polarity level, which matches other lysolipids found in the Martini lipid repository.

The original Martini parametrization of CL (taken from [30]) contains several harmonic angle potentials at the headgroup level, with 3-atom angle combinations of phosphate-central glycerol-phosphate (PGP – 105^0), central glycerol-phosphate-proximal glycerol (GPG – 110^0), and phosphate-proximal glycerol-distal glycerol (PGG – 120^0). We assumed the only angle potential that could be affected by removal of an acyl chain to be the PGG angle. Therefore, we ran equilibrium simulations of our CG systems both with and without the PGG potential, and assessed the effect of the angle potential on inter-phosphate distances and headgroup tilt. We found no significant differences arising from removal of the potential (**Fig 3.S4**), and thus decided to keep the PGG potential for our CG model of MLCL. A GROMACS compatible topology file (.itp) describing the Martini MLCL model is included in appendix **File S2**.

CG simulations were run with a timestep of 30 fs. Lennard Jones interactions were shifted to 0 at a cutoff of 1.1 nm using the potential-shift-Verlet implementation. Electrostatics were shifted to 0 at the same cutoff using the reaction field method. Temperature coupling was accomplished using the v-rescale thermostat, with a reference temperature of 303 K and a time constant of 1 ps. The Parrinello-Rahman barostat was used to maintain constant pressure with a time constant of 12 ps. Reported simulations times are multiplied by 4 as per Martini convention[27].

Coarse-grained buckling protocol

To examine mechanical stability and curvature-based partitioning of MLCL-containing CG bilayers, we applied a previously described methodology[79]. Briefly, a bilayer consisting of 40% POPC, 40% POPE, and 20% MLCL is generated with dimensions of 30 nm by 10 nm in the XY (bilayer) plane. The specific lipid concentrations were chosen to allow for direct comparison to our previous study involving TOCL. Systems were fully solvated (> 15000 water beads in every simulation) and 324 sodium ions were added to the TOCL and MLCL-containing systems to neutralize the total charge. Lateral pressure in the long dimension is incrementally increased by 1 bar every 9 μs while the short lateral dimension is kept constant, and the normal direction pressure maintained at 1 bar. At a certain applied lateral pressure, the bilayer adopts a highly curved buckled state, to relieve the strain from the applied pressure. This 1 bar increment is then simulated again at 0.1 bar increments for 36 μs each to allow finer-tuned inspection of the buckling process. The extent of bilayer buckling was quantified by calculating the lateral compressional strain:

$$\gamma = \frac{(L_o - L)}{L_o} \qquad (3.5)$$

In which L is the length of the simulation box in the dimension of applied pressure, and L_o is the original box length at 1 bar. Snapshots from the buckling process are then extracted, and simulated in the NVT ensemble, allowing the box size to be fixed and control the curvature. The system is simulated at fixed curvatures for 9 μs. To determine the extent of curvature-based partitioning, the concentration of lipid constituents within each monolayer are then calculated as a function of the local curvature environment. The calculation of curvature is described in our previous work[79]. Briefly, the headgroup

coordinates of each monolayer are separately fit to a cubic smoothing spline function, and the curvature (*C*) at any point along the curve direction (y) is given by

$$C(y) = \frac{f''(y)}{(1+f'(y)^2)^{\frac{3}{2}}} \qquad (3.6)$$

where *f'* and *f''* are the first and second derivative of the monolayer height function with respect to the *Y*-dimension, respectively; *C* has units of inverse distance.

Results and discussion

Headgroup geometry

We begin with an investigation of the structural and dynamic molecular properties of MLCL in comparison to CL in homogeneous bilayers. The inter-phosphate distance has been used previously as a measure of the compactness of the CL central glycerol and has been used to parametrize the Martini CG CL model[74,194]. **Fig 3.2A** shows the inter-phosphorus atom distance distribution. The profiles are very similar, with MLCL displaying a slight shift toward shorter inter-phosphate distances.

To determine if the acyl chain asymmetry of MLCL causes changes to the headgroup orientation, we calculated the angle between the phosphorous-phosphorous vector (**P**) and the bilayer normal, pointing into the membrane (**Fig 3.2B**). We defined the directionality of the **P** vector as initiating from the P_N phosphorus (native side) and terminating at the P_L phosphorus (lyso side); thus, an angle less than 90^o indicates the lyso side tilts down into the membrane; conversely an obtuse angle indicates the lyso side tilts out of the membrane toward the solvent. The tilt angle definition and an example of a lipid with an obtuse tilt angle is presented in **Fig 3.2C**. As TOCL lacks a lyso side, the

“lyso” phosphorous was assigned to be on the side from which an acyl chain was cleaved when converting to MLCL. As expected, the TOCL angle distribution was found to be symmetric around 90° (mean = 90.1° ± 0.1°, |skew| = 0.01). In contrast, the MLCL distribution was shifted toward obtuse angles (mean = 98.1° ± 0.2°, |skew| = 0.12), indicating the lyso side phosphate orients away from the hydrophobic core of the bilayer.

Lyso OH characterization

We next examined the behavior of the lyso hydroxyl group of MLCL and its interactions with proximal molecular components. Replacing a fatty acid group with a hydroxyl group has several potential implications. First, the small hydroxyl group of MLCL has less steric bulk than the acyl chain of TOCL, which may allow for greater local conformational flexibility. Second, the polar hydroxyl group may tend to orient itself more towards the polar headgroup region rather than the hydrophobic core. Third, addition of an additional hydrogen bond donor has potential implications for altering the inter-molecular H-bonding network, which may result in changes to the structure and dynamics of the lipid, as the only H-bond donor in TOCL is the central glycerol hydroxyl. To determine the orientational preference of the hydroxyl group, we calculated the angle between the glycerol C-O bond vector (pointing from C to O) and the inward pointing bilayer normal for both the *sn*-1 and *sn*-2 glycerol carbons on the lyso and native sides of TOCL and MLCL. A typical TOCL *sn*-1 C-O bond points sharply into the bilayer at an average angle of around 30° **(Fig 3.3A),** while a typical TOCL *sn*-2 C-O bond extends into the bilayer at an average angle of 60° **(Fig 3.3B)**. The native side of MLCL displays a nearly identical distribution to that of TOCL for both *sn*-1 and *sn*-2 bonds. On the lyso side, the *sn*-1 angle is slightly shifted to higher angles, pointing less directly down into the membrane. As expected, the lyso

hydroxyl (**Fig 3.3B, yellow line)** does not maintain a similar angle distribution to its counterpart ester bond on the native side. Instead, the distribution is very broad, reflecting an increase in rotational freedom of the significantly smaller hydroxyl group, and is centered around 100°, pointing toward the water-headgroup interface of the associated monolayer.

We determined the hydrogen bonding partners of the lyso hydroxyl group using the gmx hbond program. The results are displayed in **Table 3.1**, and are separated into self (intra-molecular) and non-self (inter-molecular) interactions. 25% ± 4.1% of the lyso hydroxyl groups formed intra-molecular hydrogen bonds, primarily with the oxygens of the adjacent phosphate group, with smaller contributions from the linking ester groups. 28.1% ± 3.6% of lyso hydroxyl groups were found to create inter-molecular hydrogen bonds with other MLCL molecules. A majority (17.5% ± 3.6%) of these H-bonds were formed with phosphate oxygens. The asymmetry between bonding to non-self $PO4_N$ and $PO4_L$ (7.1% ± 1.7% to 10.4% ± 3.2%) may be caused by headgroup tilting (**Fig 3.2B**), which positions the $P04_L$ groups closer to the water interface. Hydrogen bonds to water compose 31.4% ± 0.2% of lyso hydroxyl H-bonds. In sum, MLCL lyso OH groups participated (as donors) in intra- and intermolecular H-bonds 84.5% ± 5.5% of the time.

Table 3.1. Hydrogen bond partners of lyso OH†

H-bond acceptor	Self	non-self	Total
lyso OH	N/A	3.3% ± 0.2%	3.3% ± 0.2%
Central OH	0.9% ± 0.2%	0.4% ± 0.2%	1.3% ± 0.3%
$PO4_N$	0.9% ± 0.9%	7.1% ± 1.7%	8.0% ± 1.9%
$PO4_L$	20% ± 4%	10.4% ± 3.2%	30.4% ± 5.1%
ester O	3.2% ± 0.1%	6.9% ± 0.2%	10.1% ± 0.2%
Water	N/A	31.4% ± 0.2%	31.4% ± 0.2%
Total	25.0% ± 4.1%	59.5% ± 3.6%	84.5% ± 5.5%

† Standard errors were estimated using block averaging

Only 13.4% ± 0.3 of the lyso hydroxyl hydrogen bonds were satisfied by H-bond acceptors at the lyso glycerol level (ester oxygens and other lyso OH groups), whereas the rest of the hydrogen bond acceptors are geometrically above the glycerol. The hydroxyl group must then point out of the membrane to access those hydrogen bond donors, which provides a plausible explanation for both the tilted headgroup (**Fig 3.2B**) and shifted angle distribution (**Fig 3.3B**). An example of a tilted headgroup with intramolecular H-bond between the lyso hydroxyl hydrogen and lyso phosphate oxygen is presented in **Fig 3.2C.**

Acyl chains

In addition to characterizing the MLCL headgroup structure, we performed analyses of the acyl chains. We focused not only on similarities and differences between TOCL and MLCL, but also on the asymmetry between the native and lyso sides of MLCL. To gain insight into the structure and flexibility of the *sn*-1 and *sn*-2 acyl chains, we calculated acyl chain order parameters (S_{CH}, see Eq. 3.1), which measures the orientational mobility of C-H bonds at different positions along the acyl chain. We found that the S_{CH} values of MLCL chains on the native side of the membrane reveal a depth-dependent pattern similar to those of TOCL, but with an overall decrease in order throughout the chain (**Fig 3.4**)**.**

When comparing the native MLCL *sn*-1 to TOLC *sn*-1 (**Fig 3.4A**) or comparing the *sn*-2 chains between MLCL and TOCL (**Fig 3.4B**), S_{CH} follows a similar pattern of decreasing order from the headgroup-proximal end toward the bilayer center. While the

magnitudes of the order parameters are uniformly reduced comparing TOCL to native-side MLCL, the lyso side *sn*-1 chain of MLCL differs significantly from the other trends. The lyso side *sn*-1 chain of MLCL displays increased ordering in headgroup-proximal chain positions compared to the native-side chain of MLCL, more closely matching the level of order in TOCL. We attribute this difference to the headgroup tilt shown in **Fig 3.2B**. As the lyso side of the headgroup tilts out of the headgroup plane, it pulls the acyl chains more into the hydrophilic interfacial region. This may cause the interface-proximal acyl chain components on the lyso side to adopt a more rigid conformation to keep the chain oriented towards the hydrophobic core of the bilayer.

Taken together, the H-bonding, chain order parameters and MLCL head group geometry are likely related. When the lyso OH forms H-bonds between the central glycerol or phosphates, as it does 38.4% of the time, these interactions may cause the lyso side of MLCL to be pulled toward the solvent phase. The enthalpic gain from these additional H-bonds may compensate for increased chain ordering in the lyso side chain compared to the native-side chains in MLCL (**Fig 3.4A)**. These analyses suggest a possible mechanism by which the presence of MLCL could disrupt lipid-lipid and lipid-protein interactions. Namely, the presence of the lyso OH group could disrupt H-bonding patterns observed between TOCL and PC or PE lipids. Furthermore, the CL phosphates are known to mediate specific ionic contacts with IMM-proteins, which may be diminished/disrupted in the presence of high MLCL concentrations because the phosphate oxygens become partially occupied with H-bonds to the lyso OH groups.

Molecular packing geometry

To understand the molecular shape characteristics of MLCL and TOCL we considered both measurements based upon the bulk membrane properties and molecular scale analyses. We calculated the area per headgroup for both bilayers to determine to what extent this geometric parameter modulated molecular shape (Table 3.2). The area per lipid of TOCL was found to be 129.0 ± 0.3 $Å^2$, in good agreement with the experimental value of 129.8 $Å^2$ determined by Pan, et al using small angle x-ray and neutron scattering[52]. The area per lipid of MLCL was 109.0 ± 0.2 $Å^2$, a reduction of 15.5%. While the area per lipid arises from the properties of both the headgroup and tails, we have calculated the average area per acyl chain, which shows MLCL chains occupy a greater area than TOCL (36.3 $Å^2$ ± 0.1 vs 32.2 $Å^2$ ± 0.1). However, the increase in area/tail in MLCL (13%) is not sufficient to compensate for the reduction in number of tails (25%), for the molecular shape of MLCL to be equivalent to TOCL. The increased area/tail in MLCL is caused by MLCL chains splaying to a greater extent than those of TOCL. The chain splay was analyzed directly by calculating the splay angle, measured between the vector connecting the central glycerol carbon with the terminal acyl chain carbon and the bilayer normal vector. From the splay angles, the splay distance was determined (as the projection of the splay vector onto the X-Y plane, **Fig 3.S5**). The average splay distance was increased in MLCL (9.6 Å ± 0.1 Å) compared to TOCL (9.1 Å ± 0.1 Å) by 5.5%. Since the tails in MLCL are sampling wider angle distribution, this results in a reduced hydrophobic thickness compared to TOCL (28.3 ± 0.1 Å to 30.9 ± 0.1 Å), measured as the distance between the average position of the ester carbons at the start of the acyl chains in each leaflet.

Table 3.2. Geometric properties of MLCL and TOCL†

	Area per lipid (Å^2)	Area per acyl chain (Å^2)	Hydrophobic thickness (Å)	Interdigitation (Å)	c_0 (1/Å)
TOCL	129.0 ± 0.3	32.2 ± 0.1	30.9 ± 0.1	5.49 ± 0.03	-0.0012 ± 0.003
MLCL	109.0 ± 0.2	36.3 ± 0.1	28.3 ± 0.1	6.54 ± 0.04	0.020 ±0.004

†Area per lipid is calculated by dividing the average bilayer area by the number of lipids per leaflet. Area per acyl chain is the area per lipid divided by 4 for TOCL and 3 for MLCL. Hydrophobic thickness is average distance between the first carbon in the acyl chains between leaflets. Standard errors were estimated using block averaging.

The increase in area per chain in MLCL is consistent with a decreased density of monolayer chain atoms. This decreased density may generate “hydrophobic gaps” at the interface of the monolayers, allowing for increased interdigitation between the lipid monolayers for MLCL. We calculated the extent of interdigitation for both bilayers (see Methods), and found that the $\Box_{ov}$ increased by 18% from TOCL to MLCL (5.49 ± 0.03 Å and 6.54 ± 0.04 Å, respectively), indicating increased acyl interdigitation in the MLCL bilayer. The increased interdigitation presumably factors into the decreased hydrophobic thickness in MLCL as well.

The large reduction in total tail cross-sectional area may drastically change the shape of MLCL relative to TOCL, if the cross-sectional headgroup area is unchanged. This assumption is supported by the similar inter-phosphate distances shown in **Fig 3.2A,** however the headgroup tilting (**Fig 3.2B**) would contradict a constant headgroup area

assumption. We can estimate the effect of lipid tilt on headgroup area by treating the headgroup as a disk and calculating the projected area of the tilted disk onto a flat plane, where $A_{proj} = A_{flat} \times \cos(\theta - 90^0)$, where □□is the tilt angle. Based upon the probability distributions of θ(**Fig 3.2B**), TOCL has an $A_{proj} = 0.837 \times A_{flat}$ and MLCL has an $A_{proj} = 0.733 \times A_{flat}$. Under the assumption that TOCL and MLCL have the same A_{flat}, which is supported by the similar inter-phosphate distance distributions (**Fig 3.2A**), the projected area of the MLCL is decreased by 12.5% compared to the projected headgroup area of TOCL. While the tilting of MLCL does have a substantial effect on reducing the lipid headgroup area, the loss of an acyl chain has a more significant effect on altering the molecular geometry of MLCL (15.5% reduction in tail area vs. 12.5% reduction in headgroup area). Therefore, the reduction in tail area in MLCL is not fully compensated for by headgroup tilting, which we predict will result in a shifting of the MLCL molecular geometry towards a more cylindrical shape than TOCL.

Lateral Pressure Profiles

To assess the stress within the bilayers and estimate the sign of the spontaneous curvature, we calculated the lateral pressure profiles (LPPs) for the MLCL and TOCL bilayers using Gromacs-LS[19]. **Fig 3.5** presents the LPPs of the TOCL and MLCL bilayers, symmetrized about the bilayer center (z=0). Moving from the bulk solvent toward the bilayer center, both LPPs display a moderate positive pressure peak (I) attributed to the repulsion in the headgroups, with the MLCL peak occurring at slightly lower z-position (closer to bilayer center) due to the difference in bilayer thickness. A large negative peak (II) is seen in both bilayers, indicative of the lipid-water interfacial tension, followed by another positive peak (III) closer to the center of the bilayer, which is typical of unsaturated

lipids and has been demonstrated to align with the location of the acyl chain double bound[19]. The negative interfacial tension peak (II) and positive double-bond peak (III) of MLCL are both smaller in magnitude than that of TOCL, indicating that the monolayers experience less lateral stress in those regions. In addition, the TOCL LPP has a positive peak at the bilayer center (IV) that MLCL lacks. This difference in lateral pressure can be rationalized in terms of the respective lipid geometries: the inverted conical shape of TOCL would lead to larger stresses at the tip of its acyl chains, while the cylindrical MLCL lacks such strain. The increased interdigitation in MLCL is consistent with the slightly negative pressure at the bilayer center as it promotes association of the two monolayer acyl chains.

The first moment of the lateral pressure profile is equal to the product of the monolayer bending modulus (k_c) and spontaneous curvature (c_0) according to Eq. 3.4. From our LPPs we calculated $k_c c_0$ to be $-1.2 \times 10^{-21} \pm 3 \times 10^{-21}$ J/nm for TOCL and $20.4 \times 10^{-21} \pm 4 \times 10^{-21}$ J/nm for MLCL. The bending modulus will always be positive and therefore the sign of c_o is negative for TOCL and positive for MLCL. c_o cannot be determined without a confident estimate of the k_c, and we caution that the obtained values of the first moment of the LPPs were highly dependent on the electrostatic cutoff used for analysis (see **Fig 3.S3**). However, the bending modulus of TOCL has been measured experimentally[52] to be approximately 10^{-19} J, and if assume this value of k_c for both TOCL and MLCL we can estimate the value c_0. With this assumption of k_c, we obtain c_0s of -1.20×10^{-3} A^{-1} and 2.0×10^{-2} A^{-1} for TOCL and MLCL, respectively. Our observed c_o of TOCL is consistent within error with experimental measurements of TOCL in the absence of divalent cations[202]. It is clear that removal of an acyl chain shifts the spontaneous

curvature from a moderate negative value to a highly positive value. We note that the transition from small negative intrinsic curvature to high positive intrinsic curvature has also been observed when comparing spontaneous curvatures of phosphatidic acid and lysophosphatidic acid[224].

Lipid diffusion

We next investigated the spatial dynamics of MLCL to determine if the reduction in acyl chain numbers of MLCL increases lateral mobility. To this end, we calculated the two dimensional mean squared displacement (MSD) of both species at a range of lag times (**Fig 3.S6**) and extracted the diffusion coefficients from the slope of the curve using the equation $MSD = 2dD\tau$, where d is the dimensionality (2 in our case), D is the diffusion coefficient, and τ is the time lag. The lateral diffusion coefficient of TOCL was found to be $4.0 \pm 0.01 \times 10^{-8}$ cm^2/s, and the diffusion coefficient of MLCL was $3.8 \pm 0.1 \times 10^{-8}$ cm^2/s.

The assumption that lateral diffusion would increase with fewer acyl chains appears to be incorrect. This incorrectness of this assumption may be due to several factors. First, the increased hydrogen bonding capacity of the MLCL headgroup may bridge adjacent lipids, creating temporary networks with decreased motions. Second, we observe tighter packing of MLCL headgroups seen through reduced area per headgroup and greater interdigitation (**Table 3.2**). The increased interdigitation and tighter headgroup packing may lead to more drag on the system. It should be noted that artifacts due to periodic box size can impact observed diffusion rates, an effect that requires very large system sizes to fully dissipate[225,226]. However, this effect likely impacts observed diffusion rates to the same extent for both systems, and therefore the observed decreased mobility of MLCL should be valid for larger system sizes as well.

Acyl chain accessibility

Area per lipid calculations indicate that the headgroups of MLCL pack tighter than those of TOCL. We reasoned that this tighter packing may lead to increased cohesion of the headgroup region and decreased accessibility of solvent to acyl chains. Such an effect may have an important effect on membrane-protein interactions. For example, Vanni et. al[227] showed through a combination of experimental techniques and MD simulations that the binding of the amphipathic packing lipid sensor (APLS) protein is dependent on the formation of "defects" in the headgroups of bilayers which expose the hydrophobic interior. To examine this possibility, we constructed 2D surface maps of our bilayers and assigned the surface as either headgroup or acyl chain, based upon the first atom that was encountered as a probe descended from above the bilayer (**Fig 3.6A**). A simple measurement of headgroup integrity is the fraction of the surface map that shows exposed acyl chain, F_{exp} (**Fig 3.6B**). We find that TOCL consistently displayed a larger F_{exp} (0.365 ± 0.003) than MLCL (0.306 ± 0.003).

While a useful first indicator, total exposure of chains does not take into account the geometry of gaps in the headgroup. A gap may only be relevant for protein binding if it is large enough for the protein to sense. Indeed, Vanni and colleagues show that binding of APLS is dependent upon the insertion of aromatic side chains, and that a gap of sufficient size must be present for insertion (they estimate a defect area of at least 0.2 nm^2 for the insertion of phenylalanine). To examine our surface maps for the presence of biologically relevant (larger) defects, at each acyl exposed grid point we examined the surrounding grid points in a given probe radius. If all surrounding grid points also had acyl chain exposure, the entire probed region was assigned as a defect (**Fig 3.6A** – red). The

corresponding membrane fractions are presented in **Fig 3.6C** for a range of probe radii. As with total acyl exposure, the MLCL bilayer surface exposed fewer defects than the TOCL bilayer for all measured probe radii. For larger probe radii, the difference between the two bilayers grows larger. **Fig 3.6D** presents the percent decrease in defect exposure from the TOCL to MLCL bilayers. As the probe radius increases, the difference between them grows. We estimate that a relevant probe size for protein side-chain insertion is a radius of 2.5 Å (area of 0.196 nm^2), at which the MLCL bilayer displays 47.9% fewer defects than TOCL. Thus, moderate differences in headgroup coverage can result in drastic differences in the presentation of defects on scales relevant to protein binding.

CL binds several peripheral proteins in addition to over 60 integral proteins[180]. MLCL clearly provides a higher barrier than TOCL for such proteins attempting to interact with the hydrophobic interior of the bilayer. However, not all peripheral proteins interact with membranes via defect sensing. To our knowledge, the only comparative study of protein binding examining both CL and MLCL was with the apoptotic factor tBid, in which the affinity of the protein was *greater* for MLCL than for CL[214]. This suggests that tBid-bilayer interactions may be headgroup dependent rather than hydrophobic, in which case the modified headgroup dynamics or orientation may play a role in differential CL binding.

Mechanical properties

The membrane properties studied to this point have been molecular in scale, but the molecular differences between TOCL and MLCL may also manifest at larger length scales. In a recent study[79], we subjected bilayers containing CL to applied external pressures to induce buckling in a coarse-grained (Martini[27]) model. The buckling procedure provided insight into the mechanical properties of these bilayers and provided

a platform for studying curvature-based demixing tendencies of the component lipids. To assess the effect of MLCL on these properties, we repeated our previous procedure, replacing TOCL with MLCL in a bilayer containing 40% POPC, 40% POPE, and 20% CL, which serves as simplified model for the IMM. For reference, we also present data from a bilayer lacking CL, consisting of 50% POPC and 50% POPE. **Fig 3.7A** shows the effect of applied pressure on box compression, quantified by the compressional strain γ, described in Eq. 3.5. The changes in γ in the 4-6 bar range indicate buckling events, where buckled bilayers have γ > 0.5. The TOCL containing bilayer buckled at a lower pressure than the MLCL bilayer, indicating it is more susceptible to shape deformations from applied pressures.

The 1-bar pressure increments in **Fig 3.7A** lead to complete buckling events; none of the simulations persist in an intermediately buckled state. To determine if stable intermediates are present along the buckling pathway, we performed simulations in 0.1 bar pressure increments along the previously determined buckling pathway (**Fig 3.7B**). We previously observed that TOCL-containing bilayers sampled intermediately buckled states, whereas we now find the MLCL-containing bilayer behaves in a two-state fashion only sampling the completely flat and completely buckled states. For both buckling procedures, the MLCL-bilayer closely mimicked the properties of the POPC/POPE bilayer.

Bilayer deformability is crucial to maintaining the highly curved cristae membrane. A more rigid bilayer accrues a larger energetic penalty when forced into curved morphologies. The more brittle nature of the MLCL-containing bilayer may partially explain the abnormal morphologies commonly seen in tafazzin-deficient mitochondria.

Further, the mitochondrion regulates its morphology and can rapidly effect changes in cristae structure to modulate metabolic rates[148,228]. Our data indicate that MLCL-containing bilayers are insensitive to small applied pressure changes. While lateral pressure is used here as a computational tool and pressure changes of this magnitude are unlikely to be experienced *in vivo*, these observations may reveal important differences between MLCL and TOCL in modulating bilayer curvature in response to cellular stimuli. Supporting this idea, a ^{31}P NMR study on CL phase behavior showed that while tetra-acyl CL undergoes a lamellar (L_{β}) to inverted hexagonal phase (H_{II}) transition under high salt conditions, MLCL is restricted to the lamellar phase under similar conditions[215]. The effect of monovalent salt likely causes a reduction in the headgroup area through direct binding and electrostatic screening. The shape of MLCL should be more cylindrical than TOCL and therefore a greater reduction in the headgroup area would be required to induce a L_{β} to H_{II} conversion. Furthermore, the orientation of the MLCL headgroup, with the phosphates adopting positions out of the bilayer-water interface plane, may result in less sensitivity to ionic screening.

Curvature-based partitioning

Our analysis of bilayer buckling is a valuable tool to study curvature-dependent lipid sorting, as buckled membranes contain regions of both positive and negative curvature. Previously we have shown that TOCL partitions strongly to regions of negative curvature[79]. We extracted frames from the buckling trajectories of the systems containing 40% POPC, 40% POPE and 20% TOCL/MLCL and simulated them without pressure coupling, fixing the box size and therefore the extent of curvature. The simulations were run for 9 μs, and the concentrations of lipids at positive and negative curvature (*C*) were

determined. **Fig 3.8** displays a visual representation of the TOCL/MLCL partitioning in a buckled bilayer, as well as quantification of the concentrations of TOCL and MLCL in different curvature regimes. The bilayer snapshots in **Fig 3.8A**, illustrate the strong portioning of TOCL to negative curvature regions, which MLCL does not exhibit the same degree of partitioning. Curvature-based lipid partitioning is determined in negative curvature regions (C < -0.05 nm^{-1}, **Fig 3.8B-top**), in flat regions (0.05 nm^{-1} > C > -0.05 nm^{-1}, **Fig 3.8B-middle**) and positive curvature regions (C > 0.05 nm^{-1}, **Fig 3.8B-bottom**). MLCL partitioning to regions of negative curvature is greatly reduced at all buckling magnitudes (**Fig 3.8B-top**), and depletion of MLCL is reduced at regions of positive curvature (**Fig 3.8B-bottom**) when compared to TOCL. We observe that the fraction of TOCL or MCLC in the flat regions (**Fig 3.8B-middle**) match the bulk concentration of 20 % for both systems.

Molecular geometry is the main determinant of lipid spontaneous curvature; therefore, reduction of curvature-based partitioning in our CG system suggests that MLCL is more cylindrical than TOCL, in agreement with calculations from the atomistic simulations. Furthermore, we don't believe these are model-dependent observations as the molecular geometry is well preserved in the CG model. The lipid headgroup tilt distributions are highly similar between the atomistic and CG models for both TOCL and MLCL (**Fig 3.S4**). Membrane bending energetics depend on both the pliability (bending modulus) and spontaneous curvature of the lipid bilayer constituents, so both aspects examined in these CG simulations may play a role in differential mitochondrial morphology.

The effects of MLCL on cristae curvature may also go beyond simple bending energetics. A variety of proteins shape the IMM, including ATP synthase, which self-organizes into rows of dimers along the cristae tips where regions of high curvature are apparent[157]. This organization is disrupted in *tafazzin*-deficient mitochondria[183]. CL may be essential in maintaining these dimer rows, in which case the impact of MLCL extends to disrupting curvature-generating proteins. Alternatively, the organization of ATP synthase may depend on preexisting curved morphologies which are maintained by CL.

Summary

In summary, we performed MD simulations on multiple scales to elucidate molecular- and bulk-scale similarities and differences between TOCL and MLCL. Through atomistic simulations, we characterized differences in headgroup tilt, acyl chain dynamics, and solvent accessibility to the hydrophobic bilayer core, and determined the orientation and H-bonding partners of the lyso hydroxyl group of MLCL. The potential implications of these molecular-scale effects may include disruption of specific lipid-lipid patterning and direct lipid-protein interactions. Molecular geometry analysis was performed on the atomistic simulations, which suggested that the molecular shape of MLCL is more cylindrical than the inverted-conical shape of TOCL. However, the change in the molecular geometry of MLCL may be slighter than what would be predicted based solely on the loss of an acyl chain. The headgroup tilting of MLCL results in a smaller headgroup area and partially compensates for the tail area reduction from the acyl chain reduction. Nonetheless, the effect of replacing TOCL with MLCL is profound, as we observed in CG simulations. The CG simulations showed that MLCL-containing bilayers are more resistant to shape changes upon applied lateral pressure, and that in buckled bilayers

MLCL showed reduced partitioning to regions of negative curvature. The differences in the molecular and bilayer-scale properties of MLCL compared to TOCL, may be important factors in presentation of aberrant mitochondrial morphologies associated with disease states such as Barth syndrome.

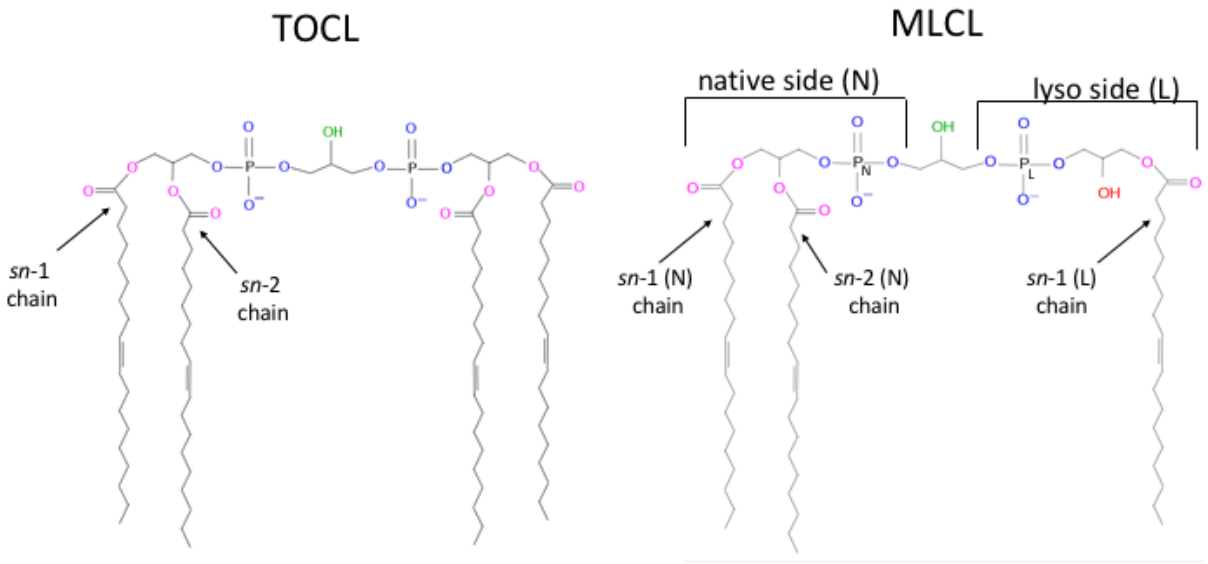

Figure 3.1. Structures of TOCL and MLCL. Hydrogen bond acceptors are colored (pink: ester oxygens, blue: phosphate oxygens, green: central hydroxyl, red: lyso hydroxyl of MLCL). MLCL is partitioned into the native (N) side with full acyl chain complement, and the lyso side (L) at which the *sn*-2 acyl chain is lysed.

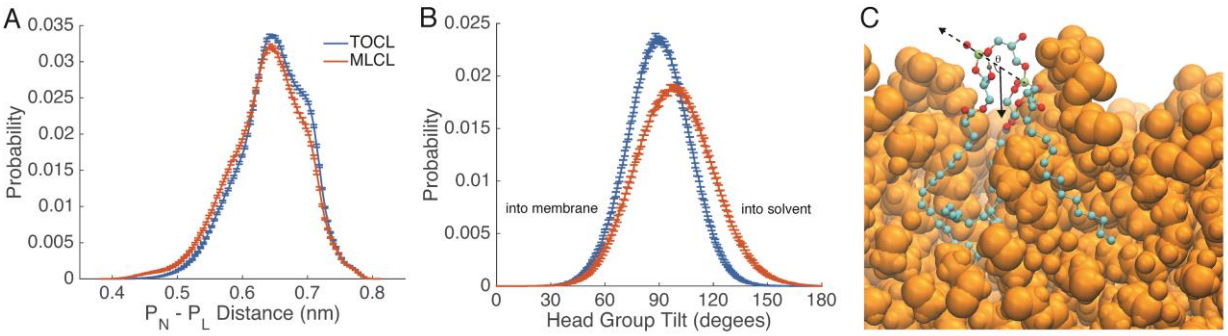

Figure 3.2. Geometry and orientation of headgroups. (A) Intra-molecular distance between phosphorus atoms. (B) Headgroup tilt measured as the angle between the bilayer normal and the vector pointing from the P_N phosphorus to the P_L phosphorus. Legend in (A) also applies to (B), and error bars represent block averaging based standard errors. An example of an obtusely tilted (107.2°) headgroup is shown in (C). The dotted line is the P_N-P_L vector and the solid line is the downward Z-vector. All hydrogens are removed except for the lyso hydroxyl hydrogen, which is depicted in gray. Coloring of other atoms are as follows: phosphorous=lime, carbon=cyan, oxygen=red. The orange spheres represent other lipids in the bilayer.

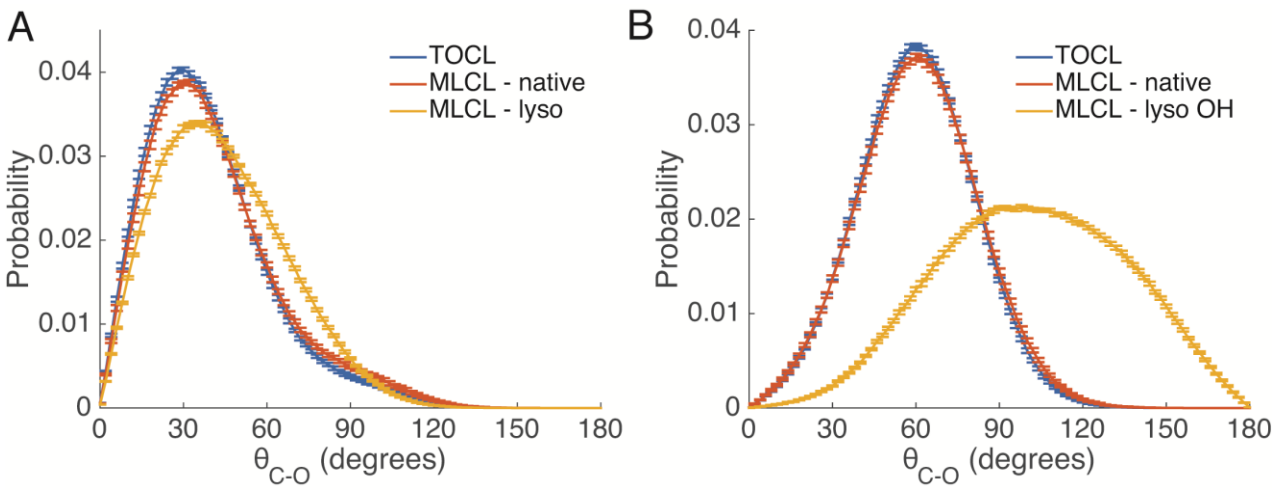

Figure 3.3. Orientation of glycerol *sn*-1 and *sn*-2 C-O bond vectors. Angles between glycerol C-O bond vectors and bilayer normal for *sn*-1 chains (A) and for *sn*-2 chains and MLCL lyso OH (B). Error bars represent block averaging based standard errors.

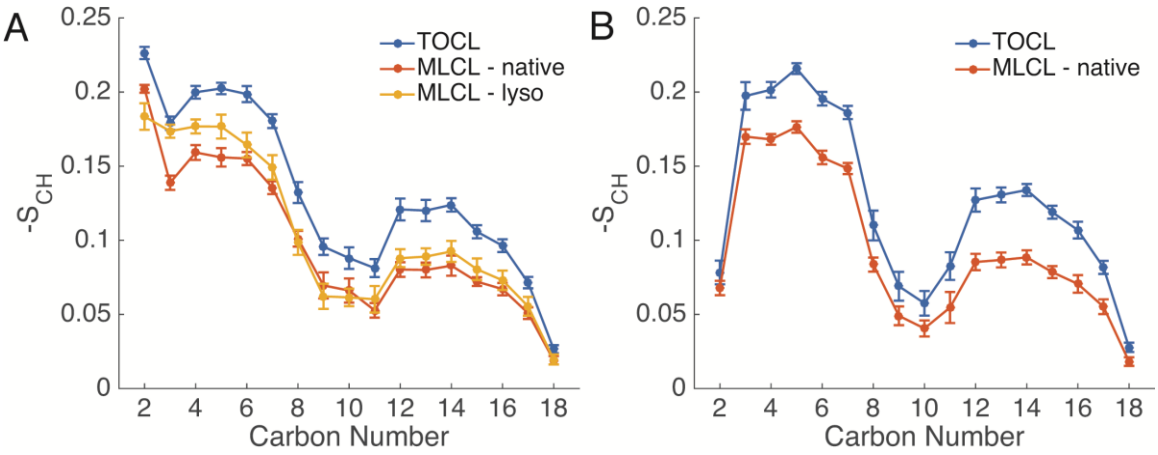

Figure 3.4. Acyl chain order parameters. -S_{CH} order parameters along the *sn*-1 (A) and *sn*-2 (B) acyl chains for TOCL and MLCL, calculated using Eq. 1. Error bars represent block averaging based standard errors.

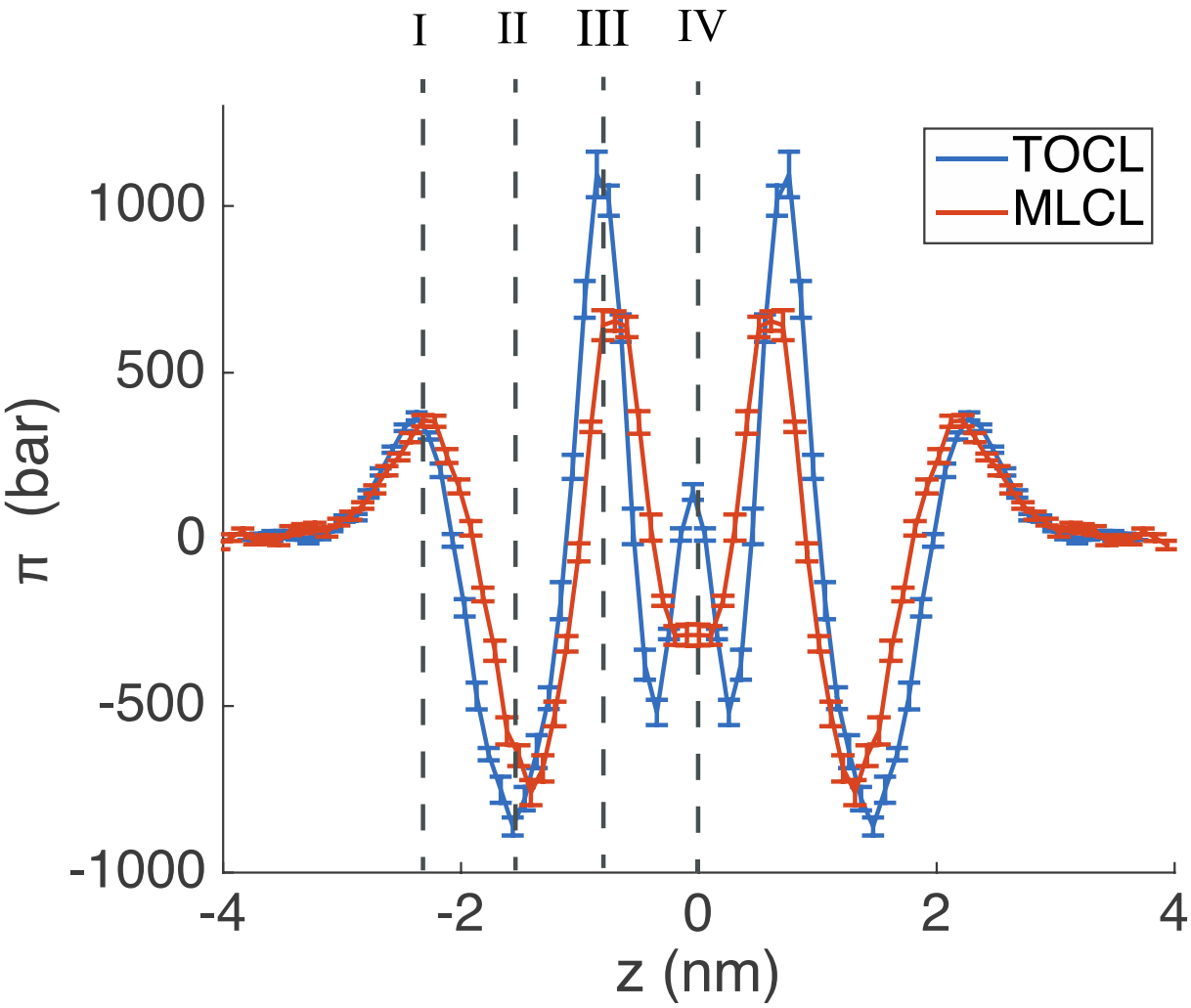

Figure 3.5. Lateral Pressure Profiles for TOCL and MLCL bilayers. The LPPs are calculated with GROMACS-LS, the bilayer center is at z=0.

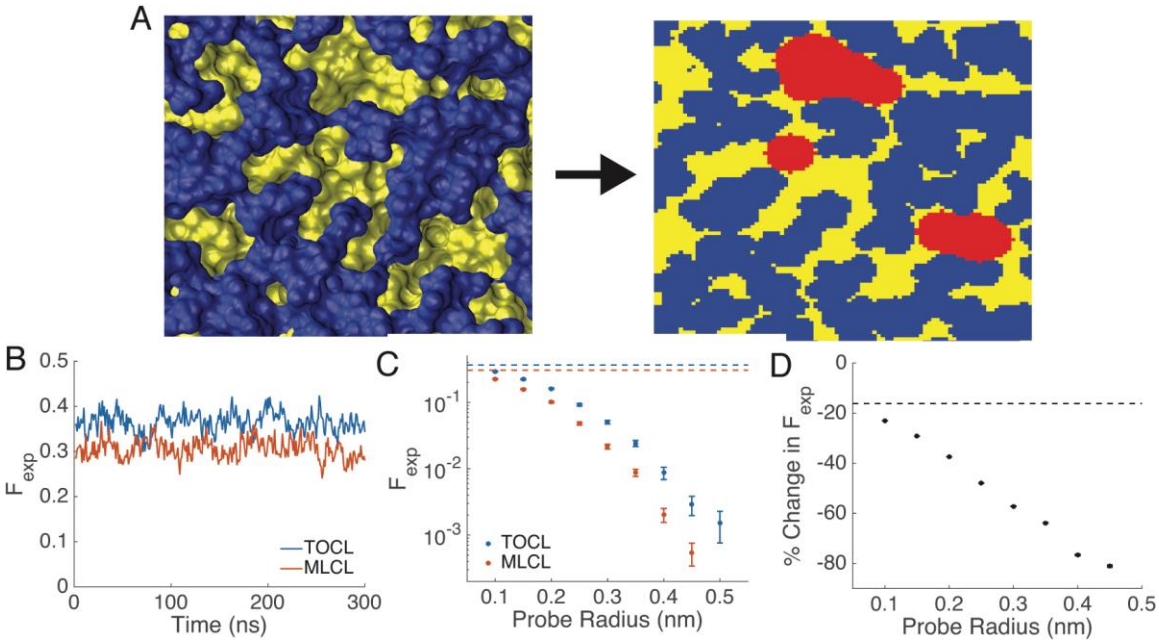

Figure 3.6. Bilayer defect analysis. (A) Top-down surface representation of a frame in the TOCL bilayer simulation. Blue corresponds to headgroups, yellow to acyl chains. The right panel shows the 2D surface grid, using the same color scheme. Red areas indicate defects found using a probe with radius 2.5 Å. (B) Time-course of the total fraction of the 2D grid points assigned as acyl chain accessible. (C) Fraction of bilayer calculated to be a “defect” as a function of defect probe radius for TOCL and MLCL. The dotted reference lines are the averages of panel B, error bars represent block averaging based standard errors. (D) Percent change in fraction of membrane defined as a defect, from TOCL to MLCL, as a function of probe radius. The dotted line is the % change in total acyl accessibility from panel B.

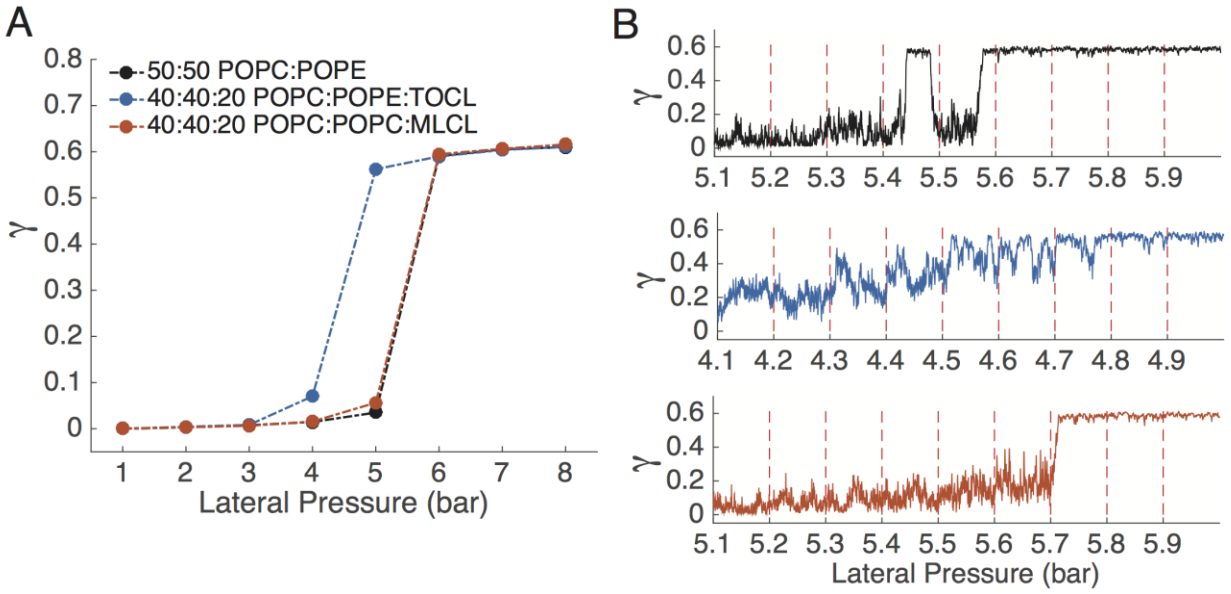

Figure 3.7. Buckling of coarse-grained bilayers. (A) Response of bilayers to induced lateral pressure. γ=0 corresponds to a flat bilayer, γ~0.6 to a maximally compressed bilayer. (B) Time-course of smaller incremental (0.1 bar) pressure increases. Each pressure increment was run for 36 μs. The colors of the trends in panel B, are consistent with the colors in panel A, and therefore indicate the bilayer composition. Data for POPC:POPE and POPC:POPE:TOCL was previously reported in [35], and is reproduced here for comparison to MLCL containing bilayers.

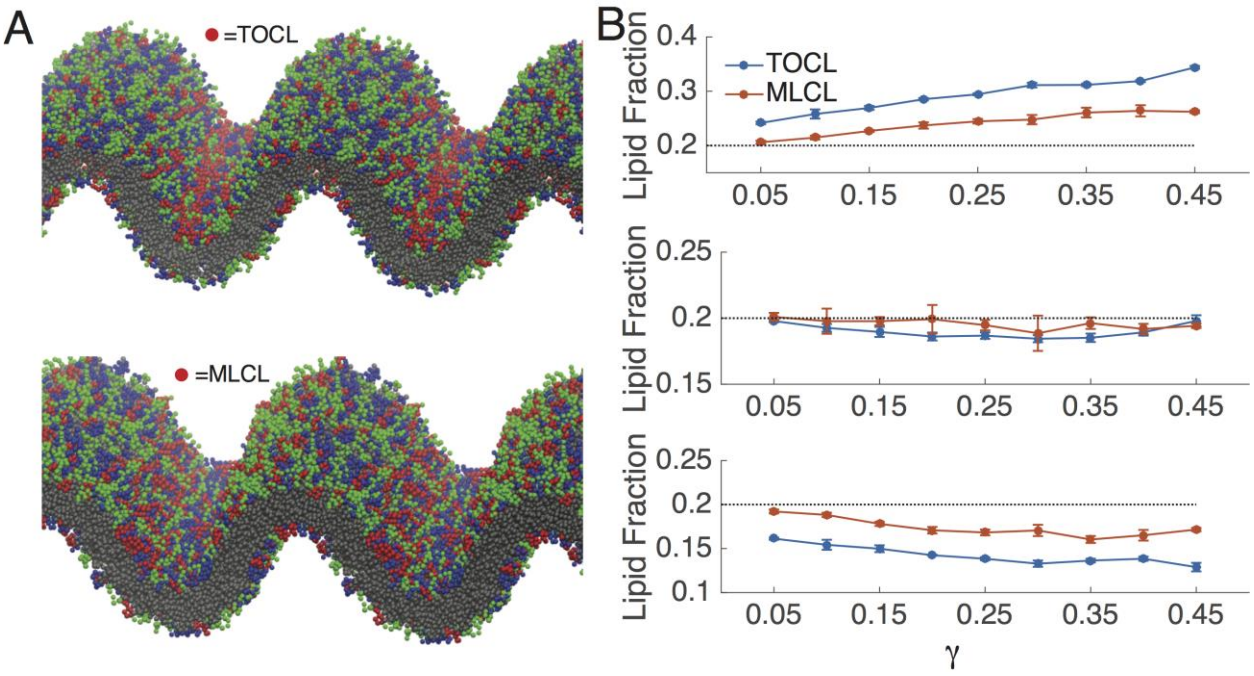

Figure 3.8. Curvature-driven segregation of TOCL and MLCL. A) Snapshots from the final frame of the fixed box γ=0.30 simulation illustrate partitioning propensities. TOCL and MLCL headgroups are colored red, POPC headgroups are colored green, POPE headgroups are colored blue, all tail beads are colored grey. The compositions of the bilayers contain 40% POPC, 40% POPE, and 20% TOCL (top) or 20% MLCL (bottom). (B) Concentrations of TOCL and MLCL in bilayers fixed at compression levels ranging from γ=0.05 to γ=0.45. Concentrations in regions of high negative curvature (C < -0.05 nm^{-1}) are shown on top, concentrations in regions with low curvature (C > -0.05 nm^{-1}, C < 0.05 nm^{-1}) are shown in middle and concentrations in regions of high positive curvature (C > 0.05 nm^{-1}), are shown on bottom. The dotted line is a reference to the bulk concentration (20%) of TOCL/MLCL in these bilayers. Error bars represent block averaging based standard errors.

Characterization of molecular and bilayer scale properties of cardiolipin and monolysocardiolipin from multi-scale molecular dynamics simulations

K.J. Boyd, N.N. Alder, E.R. May

Supplementary Methods

Electrostatics in GROMACS-LS

The current implementation of GROMACS-LS[19] does not support PME electrostatics to calculate the electrostatic forces component of the virial. The electrostatic force in GROMACS-LS must be calculated using a cutoff treatment for electrostatics, with the cutoff length extended beyond the typical short-range cutoff used for the direct space electrostatic calculation when using PME. It has been demonstrated that a cutoff of r_{ES} = 2.2 nm is sufficient for convergence of the LPP for a neutral lipid membrane, and is the recommended parameter choice of r_{ES} in GROMACS-LS.[19] However, the cardiolipin bilayer systems are highly charged and we were concerned that the electrostatic component of the virial may not be adequately calculated with r_{ES} =2.2 nm and may require a longer cutoff. We scanned a range of r_{ES} values for the TOCL membrane, we found that the profiles appear converged at a cutoff of 2.4 nm, **Fig 3.S1.**

However, while the shape of the TOCL LPP is converged at r_{ES} = 2.4 nm, several key observables of the system continue to change as r_{ES} is increased. The average lateral and normal system pressures continue to change beyond the 2.4 nm cutoff. If the electrostatic treatment in the analysis (with a straight cutoff) is closely approximating the

forces calculated during the production run (treated with PME), then the calculated total lateral pressure (P_L =[P_{xx} + P_{yy}] / 2) and normal pressure (P_N = P_{zz}) from the analysis should match the pressures from the simulation run, which are being coupled to a pressure bath at 1 bar. **Fig 3.S2** presents the calculated bulk lateral and normal pressures over a range of cutoffs. At short cutoffs, P_L is overestimated, which was also observed by Vanegas et al. in a POPE bilayer.[19] At a cutoffs of 2.6 nm and above, P_L approaches the correct bulk pressure (1 bar) but fluctuates in the range of +10 bar to -10 bar. P_N is slightly underestimated at low cutoffs and converges to the correct simulation pressure, within error estimate, at a cutoff of 3.0 nm.

The treatment of cutoffs in GROMACS-LS should be even more stringently considered when estimating elastic parameters from the LPP. We calculated the first moment of the LPP which is equal to the product of the bending modulus (k_c) times the spontaneous curvature (c_0) for TOCL over a range of electrostatic cutoffs (**Fig 3.S3**), and found that the observed value of $k_c c_0$ decreased roughly linearly from a cutoff of 1.6 nm to 2.6 nm. The calculated values of $k_c c_0$ in the cutoff range of 2.8 nm to 3.2 nm were more similar to each other, indicating that the value was approaching convergence with respect to the cutoff length, but was still slowly decreasing. We note that the sign of $k_c c_0$ was only negative at the highest cutoff (3.2 nm). The sign of c_0 is inferred from the sign of $k_c c_o$; therefore, it is essential to check the convergence of the first moment of the LPP when attempting to estimate the sign of spontaneous curvature.

The dependence of system observables on electrostatic cutoff length in our system cannot necessarily be generalized to all lipid systems, as our TOCL and MLCL bilayers have a highly negative surface charge and required a high concentration of sodium ions

to balance the total system charge. A zwitterionic lipid bilayer with typical counterion concentrations may show converged properties at a lower cutoff, which would be advantageous as the computational requirements for calculating electrostatics with a straight cutoff scales cubically with distance. However, we suggest that for any analysis beyond simply observing the shape of the LPP, it is necessary to test the effect of electrostatic cutoffs on the parameter of interest.

Supplementary Figures

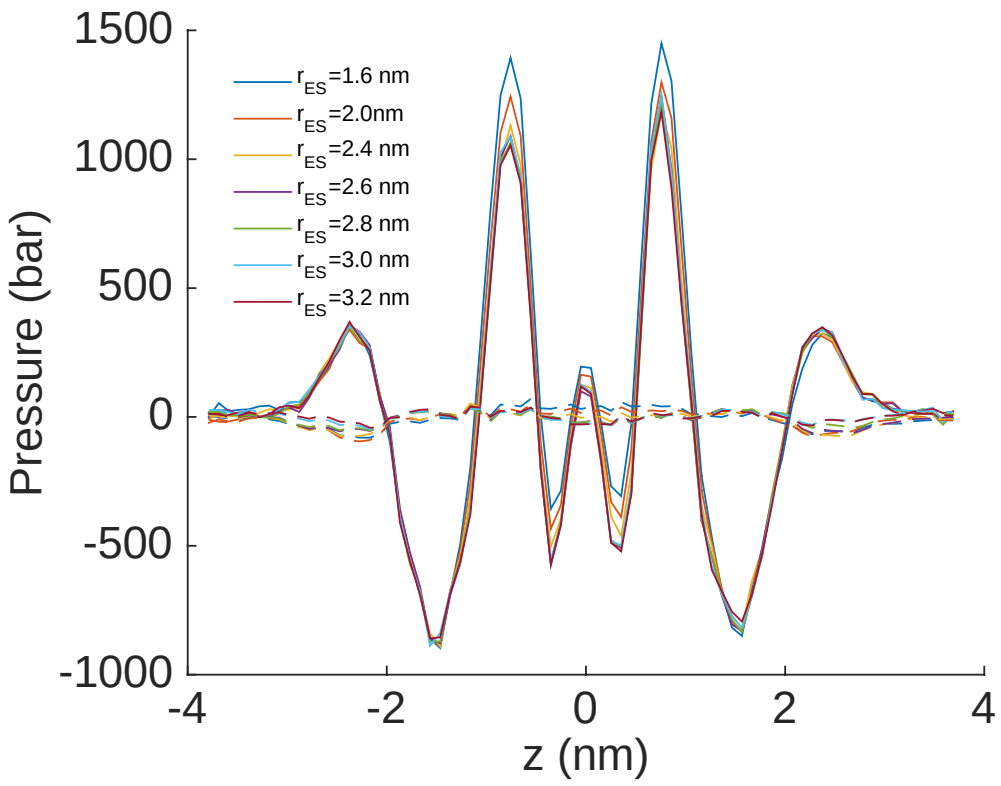

Figure 3.S1. Pressure profile for a TOCL bilayer calculated for a range of electrostatic cutoff distances. Both the lateral (solid) and normal (dashed) components of the pressure profile are shown.

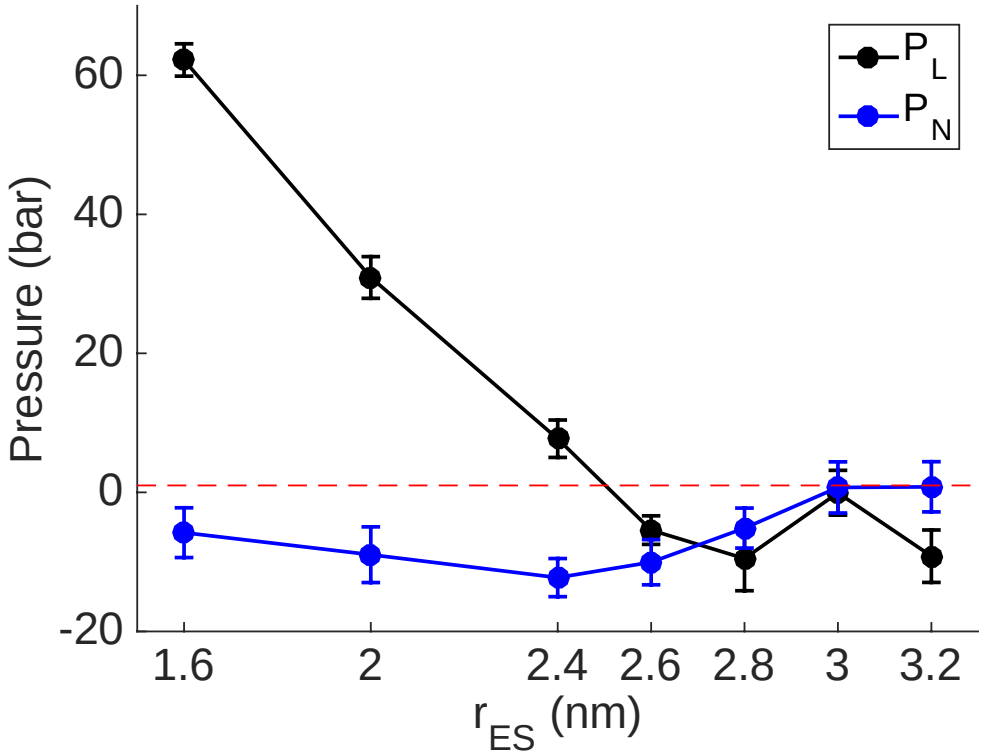

Figure 3.S2. System pressures from GROMACS-LS. The lateral and normal components of the total system pressure for the TOCL bilayer were calculated over a range of electrostatic cutoffs by integrating $P_L(z)$ and $P_N(z)$ over the z dimension of the simulation box and dividing by the z dimension of the box. Dashed red line is drawn at 1 bar.

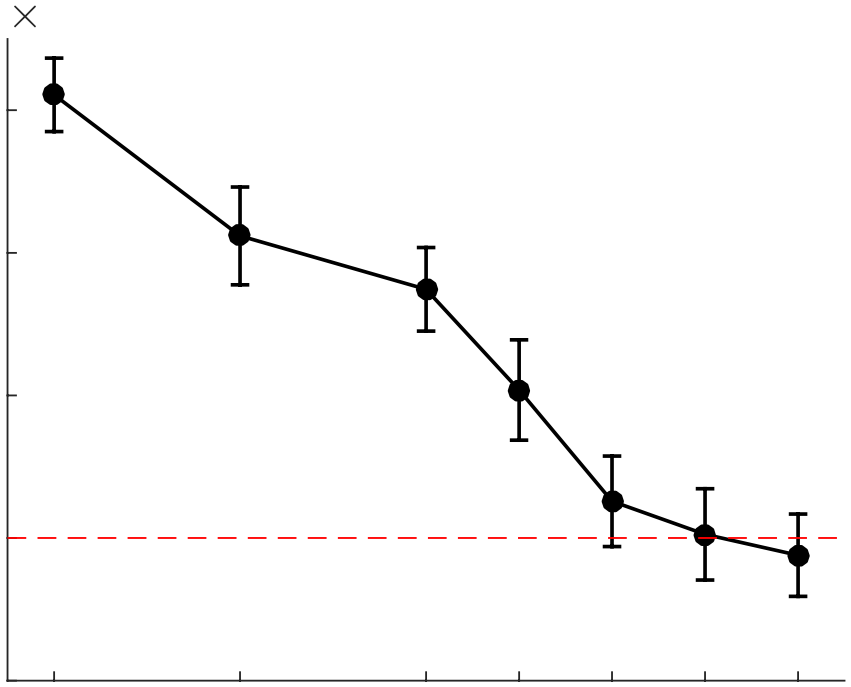

Figure 3.S3. Effect of electrostatic cutoffs on $k_c c_o$. The first moment of the LPP of the TOCL bilayer ($k_c c_o$) was calculated over a range of electrostatic cutoffs. Error bars are standard errors of the mean. Dashed red line is drawn at $k_c c_0 = 0$

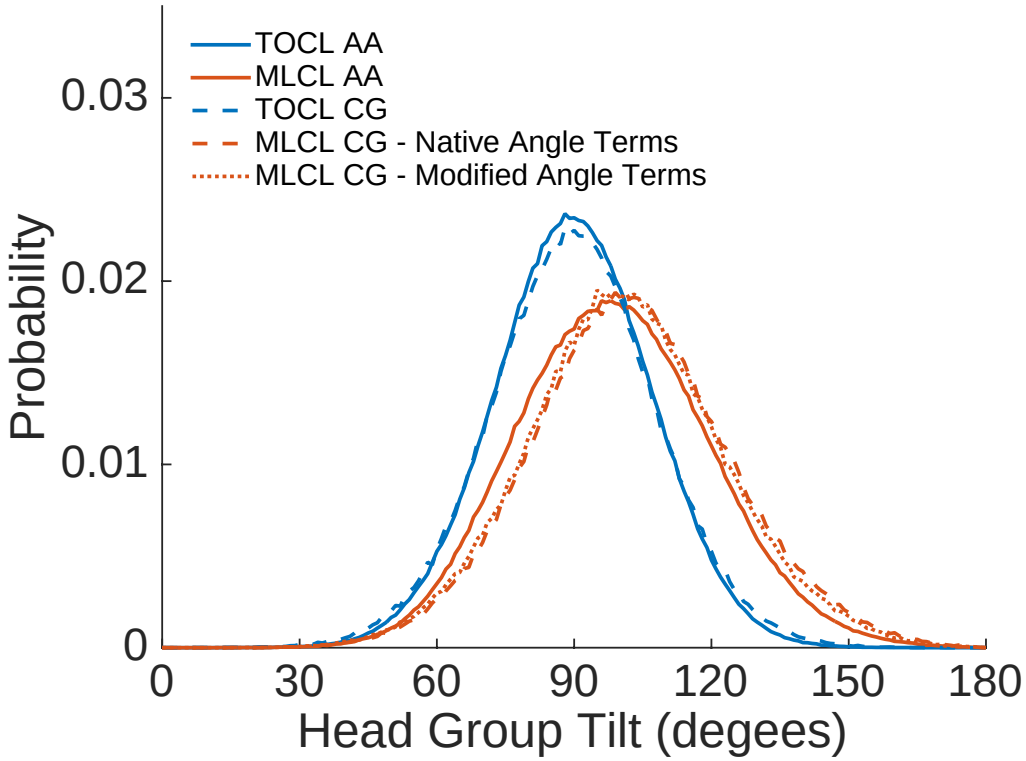

Figure 3.S4. Comparison of headgroup tilting between atomistic and CG models. TOCL and MLCL tilting is compared between homogeneous bilayers using the CHARMM36 force field (AA) and Martini force field (CG). For the Martini MLCL the lyso side PGG angle term was removed (modified), but it showed no effect compared to when the PGG term was retained (native).

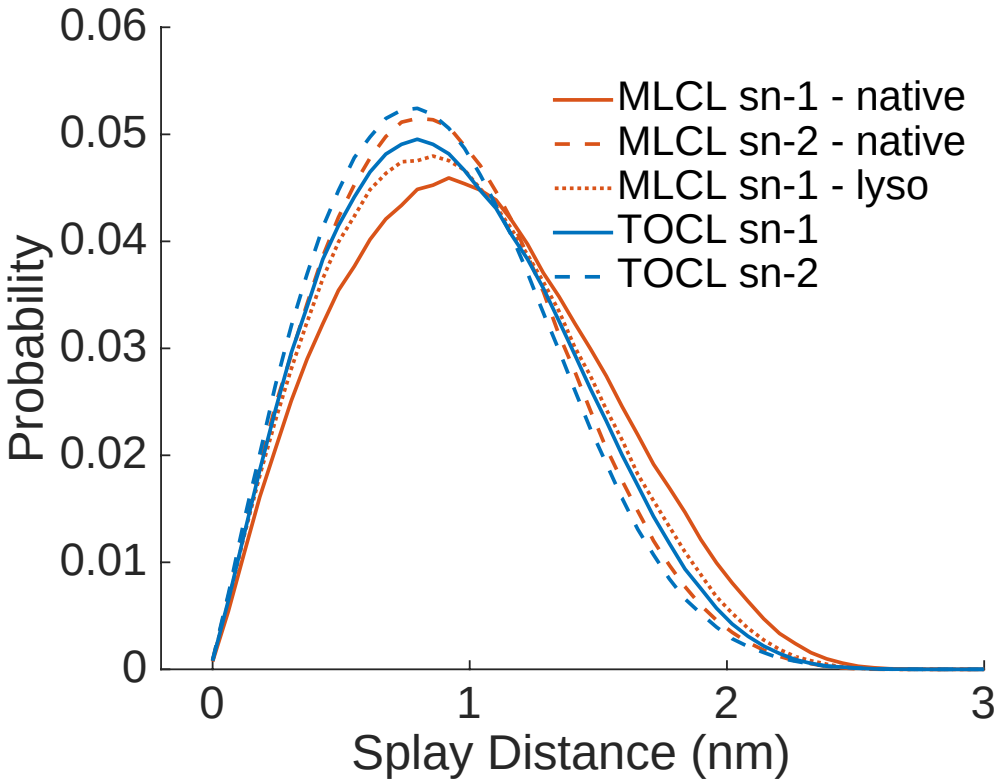

Figure 3.S5. Acyl chain splay distances. The splay distances were calculated by projecting the vector connecting the central glycerol carbon to the terminal acyl chain carbon onto the *x*-*y* plane.

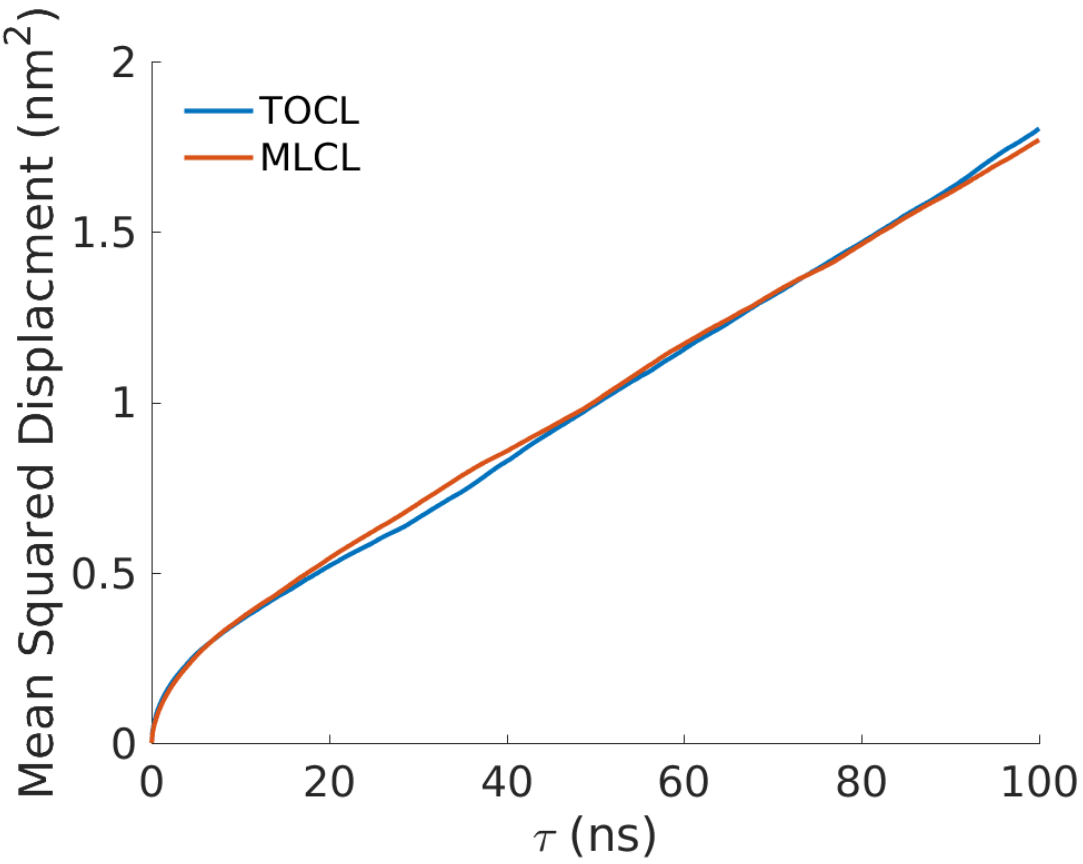

Figure 3.S6. Lateral diffusion of atomistic TOCL and MLCL bilayers. Lateral mean squared displacements at a range of time lags (τ values) were calculated using gmx msd. Diffusion coefficients were extracted from a linear fit of the data ranging from τ=20 ns to τ=100 ns.

Chapter 4:

Towards realistic modeling of mitochondrial superstructures

Abstract

The inner mitochondrial membrane is complex in morphology and composition, and the interplay of lipid and protein components with membrane curvature is essential for mitochondrial function. Two of these key components which regulate mitochondrial morphology are the lipid cardiolipin and the protein ATP synthase. To investigate the two-way relationship between membrane shape and composition, we used coarse grained molecular dynamics simulations of mitochondrial mimicking shapes. We demonstrate the effects of cardiolipin on mitochondrial shape stability, and observe the effects of “necks” and Gaussian curvature on cardiolipin partitioning. Using reductionist systems, we probe the energetics of ATP synthase dimer rotation and self-organization in simple cylindrical bilayers.

Introduction

The mitochondrial inner membrane is composed of a flat boundary membrane and highly curved invaginations called cristae, typically linked by tight structures termed cristae junctions[154]. Cristae can present a number of morphologies depending on cell type and metabolic health[148,228], with shapes such as flattened sacs or tight tubular cylinders, with regions of tight curvature being the defining feature[229]. Aberrant mitochondrial morphology is linked to a number of metabolic disorders[213].

A large number of factors contribute to sculpting mitochondrial morphology. Cristae junctions are supported at least in part by the MICOS complex[230]. Inner membrane proteins such as tBid and mitofilin have also been shown to play a role[159,160]. Lipid composition is key to mitochondrial shape, particularly the tetra-acyl lipid cardiolipin (CL).

CL promotes negative curvature in the presence of divalent cations or low pH[171,173,202], and indeed localized pH gradients in CL-containing vesicles have been shown to induce cristae-like invaginations on their own[178]. Disruption of the CL biosynthesis pathway leads to aberrant cristae morphology and leads to metabolic disorder[213].

Perhaps the most well-known sculptor of inner membrane morphology is the ATP synthase complex. In cells, ATP synthase forms a dimer with an inter-monomer angle between 80 and 120 degrees, which requires high local membrane curvature to match[157]. In simulations of flat bilayers, this geometry has been shown to locally deform the membrane on length scales of ~10-20 nm[231]. Cryo-EM tomography studies have shown large-scale organization of these dimers into long rows along the tightly curved regions of the cristae[156,157,231]. Simulations have shown that in flat membranes such self-association is driven through a desire to minimize membrane perturbuation[71]. It is thought that the tight curvature imposed by these dimers “staple” the inner membrane down, maintaining mitochondrial morphology. Indeed, these long dimer rows are not seen in mitochondria exhibiting aberrant morphologies[157], and interestingly this organization is dependent on cardiolipin[183].

Therefore, while we have clear evidence of a link between ATP synthase, cardiolipin, and inner membrane curvature, the causality is unclear. Does the lack of ATP synthase dimer rows in mitochondria with aberrant morphology indicate that those rows were the major driving force for tight curvature, or is the lack of curvature causative of the dissociation of dimer rows? Likewise, is the CL-ATP synthase organization relationship

direct, or does a lack of CL lead to a lack of tight curvature, leading to dimer row dissociation.

In this study, we attempt to bridge some of the gaps in the field of mitochondrial simulations. Multiple studies of ATP synthase have been performed in flat bilayers[71,231,232], but none have incorporated curvature as a starting point. Simulations have been performed on cardiolipin in a curved environment[56,79], but these have been done in simple buckled systems which do not closely match the tripartite mitochondrial organization of boundary, junction, and crista. To address these issues, we perform coarse-grained molecular dynamics simulations of ATP synthase in cylindrical curved systems, and study how curvature affects the dynamics and association properties of ATP synthase dimers, as well as the organizational effect of cardiolipin in these systems. To further explore cardiolipin in a mitochondrial-mimetic setup, we set up simulations of cardiolipin-containing bilayers in unique coupled morphologies, and maintain these shapes using a dummy-particle based approach developed by Yesylevskyy and others[120] that we further validate herein. Together our results take steps towards more realistic modeling of mitochondrial membranes.

Methods

System setup

All simulations used the Martini 2.2 forcefield[27] with nonpolarizable water. Flat simulation configurations of CG bilayers were constructed using a modified version of the *insane* python tool[136]. Bilayer systems were composed of combinations of palmitoyl-oleoyl phosphatidylcholine, dioleoylphosphatidylethanolamine, and our newly developed

tetraoleoylcardiolipin model (TOCL, see results for details). Using the starting configurations as input, curved membranes were created using the *BUMPy* python tool[142]. Two curved shapes were simulated – simple cylinders, and mitochondrial mimicking systems. Mitochondrial systems were approximated with a double-bilayer setup. The two bilayers are connected by an apposed cylinder, with toroidal junctions making smooth continuous connections between the components (figure 4.1). The lipid compositions and geometric arguments provided to BUMPy for the various simulations are detailed in table 4.1. In all systems carrying a net negative charge (containing TOCL or ATP synthase), neutralizing sodium ions were added.

Morphology	Composition	Dummy particles	ATP synthase	Z_o	BUMPy Arguments	Notes
Flat	100% TOCL (5 bead)	No	No	N/A	N/A	CL validation
Flat	100% TOCL (4 bead)	No	No	N/A	N/A	CL validation
Cylinder	100% TOCL (4 bead)	No	No	1.0 nm	$R_{cylinder}$: 10 nm $L_{cylinder}$: 30 nm	CL pivotal plane calculation
Flat	100% POPC	1 layer	No	N/A	N/A	Dummy particle validation, variety of pulling forces and pressure coupling schemes
Mitochondrial	100% POPC	Yes	No	0.96 nm	$R_{cylinder}$: 10 nm $L_{cylinder}$: 30 nm $R_{junction}$: 10 nm L_{flat}: 56 nm	
Mitochondrial	80% POPC, 20% DOPE	Yes	No	0.934 nm		
Mitochondrial	80% POPC, 20% TOCL	Yes	No	0.949 nm		
Cylinder	100% POPC	No	1	0.96 nm	$R_{cylinder}$: 5 nm $L_{cylinder}$: 80 nm	Rotational energetics. 5 nm system lengthened to avoid periodic boundary issues
Cylinder	100% POPC	No	1	0.96 nm	$R_{cylinder}$: 10 nm $L_{cylinder}$: 45 nm	
cylinder	100% POPC	No	1	0.96 nm	$R_{cylinder}$: 15 nm $L_{cylinder}$: 45 nm	
cylinder	100% POPC	No	2	0.96 nm	$R_{\_cylinder}$: 10 nm $L_{\_cylinder}$: 100 nm	distance umbrella sampling

Table 4.1: Composite details about each simulation

The ATP synthase dimer structure for *Saccharomyces cerevisiae* was taken from PDB entry 6B8H (reference [233]). Chains e, g, u and s were not well-resolved in this

structure, and so were removed. Missing sidechains were modelled in using Modeller[234]. The structure was then converted to Martini using the *martinize.py* script (http://cgmartini.nl), with an elastic network with default force constants restraining the conformation of the protein. ATP synthase dimers were embedded in cylindrical bilayers using custom python scripts to yield proper orientation and embedding depth. To avoid clashes, any lipids containing beads within 0.1 nm of any protein bead were removed. This combined with the soft-core potentials described in the next section allowed equilibration of systems without crashes.

Simulations of ATP synthase occurred in two types of setups. First, cylindrical systems containing single copies of ATP synthase dimers were created with varying radii, and umbrella sampling was performed on the dimer angular coordinate with respect to the direction of the cylinder. Second, two copies of ATP synthase dimers were placed on the same cylinder, and umbrella sampling was performed to observe long-range interactions between the dimers.

Simulation methods

Simulations were run using Gromacs 2018 (CL validation, dummy particle validation, and mitochondrial shape simulations) and Gromacs 2019 (ATP synthase simulations). Systems were first minimized using the steepest descent method with Van der Waals interactions scaled down with a soft-core potential, followed by a steepest descent run with normal potentials. For MD simulations, the timestep was gradually increased from 2 fs to 20 fs in a series of 10,000 step simulations with restraints on the lipid head groups.

Production simulations were run using the MD integrator with a propagation time of 20 fs. Temperature was maintained at 310K with the v-rescale algorithm, with a time constant of 1 ps. Some systems were run in the NVT ensemble, with pressure coupling turned off, while other simulations used pressure coupling (see table 4.1). Pressure was maintained at 1 bar with the Parrinello-Rahman barostat[197] with a time constant of 12 ps and compressibility of $3 * 10^{-4}$ bar^{-1}. In flat bilayer simulations, pressure coupling was semiisotropic. Short-range Van der Waals interactions were treated using the potential shift modifier method with a cutoff of 1.1 nm. Coulombic interactions were treated with the reaction field method with the same cutoff.

A number of simulations were constructed with bracketing dummy particles. Dummy particle grids were constructed using BUMPy[142], with inter-leaflet dummy layer separation of 6.5 nm and lateral grid spacing of 0.5 nm. Dummy particles only have repulsive interactions with the hydrophobic tail beads (C1 in the Martini model), modeled with a Lennard-Jones potential with a $C_{(12)}$ potential of 0.0258 kJ mol^{-1} nm^{-12} and the $C_{(6)}$ term set to 0. Dummy particles are frozen in place in some simulations, and in others are kept in place with a restraint force of 1000 kJ mol^{-1} nm^{-1}. A subset of flat bilayer simulations were performed with a single adjacent dummy particle grid (rather than 2 bracketing grids). The bilayer was then forced to interact with the grid with Z-dimensional constant force pulling, with force constants ranging from 0 to 500 kJ mol^{-1} nm^{-1}.

To determine the pivotal plane location of pure CL bilayers, cylindrical bilayers were set up according to previously described protocols[87,142], in which pores are induced to allow equilibration between leaflets, which are maintained using a flat-bottom potential. The pivotal plane can be calculated from the resulting radius of curvature and number

ratios of components, with $z_o = R(p-1)/(p+1)$, where R is the radius and *p* is the ratio of inner to outer lipid counts. Pivotal planes for POPC and DOPE were obtained from our previous publication[142].

Single ATP synthase dimers were inserted into cylindrical membranes starting at an angle of 0^o (the angle at which the monomer-monomer center of mass vector aligns with the long axis of the cylinder). To generate umbrella windows, steered MD was performed using the angle-axis option in Gromacs, with a pull rate of 0.0001 degrees / picosecond and a force constant of 500 kJ mol^{-1} radian^{-1}. Windows were created from snapshots in 3-degree increments (31 windows from 0 to 90 degrees). Umbrella windows were then run with a force constant of 12,000 kJ mol^{-1} radian$^{-`}$. For a description of simulation lengths and convergence, see the data analysis methods section.

Pairs of ATP synthase dimers were inserted in a cylindrical bilayer with center of masses 12 nm apart. To generate umbrella windows, the distance between dimer center of masses was increased using a pull potential of 1000 kJ mol^{-1} nm^{-1} and a pull rate of 0.0001 nm/ps. It was necessary to maintain the angle of individual dimers at 90^o with respect to the long axis of the cylinder (see description in results). To accomplish this, an angle-axis potential was applied with a force constant of 50,000 kJ mol^{-1} nm^{-1}, applied between the membrane-bound rings and the solvent exposed “lobes” of the ATP synthase monomers. Umbrella windows were extracted in intervals of 0.5 nm from 10.0 nm to 28.0 nm, and simulated with a force constant of 200 kJ mol^{-1} nm^{-1}.

Analysis methods

Most analyses were performed with a combination of custom python scripts and MDTraj routines[235], including calculation of interphosphate distances. Areas per lipid were calculated using the Gromacs gmx energy tool. Lateral pressure profiles were calculated using Gromacs-LS, a modified version of Gromacs 4.5.5, and a reference atomistic profile was taken from Boyd, Alder and May[56].

For analysis of lipid dynamics upon interaction with dummy particles, lipid splay was calculated as the angle between the bilayer normal and the vector connecting the phosphate bead to a terminal tail bead. Diffusion coefficients were calculated using a linear fit of mean squared displacement plots, with $MSD = 2dD\tau$, where d is the system dimensionality (2 for a flat bilayer), D is the diffusion coefficient, and τ is the specific time lag for a given MSD.

For some flat and mitochondrial systems, the force upon dummy particles was calculated. In frozen systems, the force can simply be read from Gromacs .trr files. As the dummy particles only interact with the hydrophobic core of the membrane, this can be simply interpreted as the force exerted to maintain curved membrane shapes. For simulations with restrained unfrozen dummy particles, the force can be calculated from the average position of the dummy particle relative to its reference position, given a specific spring constant.

For umbrella sampling, initial “burn-in” periods were estimated using the statistical inefficiency metric from Chodera[236], and the initial data flagged as being correlated was not used in the calculation of free energy profiles. Simulations were run until every window contained at least 200 ns of usable data. Autocorrelation plots then ensured that the

decorrelation time of the observables were low with respect to total simulation time. The free energy profiles along the reaction coordinates were calculated using the dTRAM method of PyEMMA[237]. To estimate errors, the simulation data were then divided into 4 equal chunks, and a separate free energy profile was calculated for each subset of the data. Error bars were then calculated from the standard error of the mean from each window.

Results and Discussion

Parametrization of CL model – The current Martini representation for oleoyl chains of lipids is a 4 bead model (CDCC, where D induces a kink in the chain)[136]. However, the CL model used in CG simulations to date[56,74,79,194,232] still model the oleoyl chains with a 5 bead model (CCDCC). To best model the mitochondrial membrane, we modified the tail parameters of TOCL to have all 4 chains composed of CDCC (figure 4.2 A).

We then simulated pure TOCL bilayers with both the old and new bead parameters, and compared several observables to atomistic simulations with the same composition. The atomistic trajectory analyzed was taken from[56]. The first parameter looked at was bilayer thickness, taken as the interphosphate distance (the central phosphorus atom was chosen for the atomistic measurement), shown in figure 4.2 C. The 5-bead model was thicker than the atomistic model (4.602 +/- 0.004 nm and 3.98 +/- 0.01 nm, respectively), whereas the new 4-bead model closely matches the thickness of the atomistic model (3.92 +/- 0.01 nm). We also calculated the average area per lipid of each system, shown in figure 4.2 B. The 4-bead and 5-bead models showed no significant differences(1.238 +/- .002 nm^2 and 1.236 +/- 0.002 nm^2, respectively), both

underestimating APL compared to the atomistic value of 1.290 +/- 0.006 nm^2, which closely matches an experimentally reported area per lipid of 1.298 nm^2.

For a more detailed comparison, we calculated the lateral pressure profiles (LPP) of both CG systems, and compared them to the data from reference [56] (figure 4.3). The magnitudes of the positive and negative peaks do not greatly change between the CG models. However, the negative interfacial tension peak is shifted to better overlap with the same peak in the atomistic model. Likewise, the small head-group repulsive peak localizes closer to the atomistic peak, as does the internal peak signifying strain from the insaturation. Together, our results indicate that the 4-bead model better represents CL in a number of observables, while not significantly changing the area per lipid.

Effect of Dummy Particles on bilayers

The use of dummy particles as scaffolds to enforce membrane shape is tantalizing as it offers an avenue to exploring otherwise unstable morphologies[120,142]. However, the interaction of bilayers with these dummy particles has the potential for inducing non-physical artifacts in bilayer structure and dynamics, particularly for the highly unstable shapes with the highest amount of interaction with the dummy particles. We therefore attempted to quantify the effects of the bilayer-dummy particle interaction with varying stabilities. This is not a straightforward task. One potential approach would be to simulate an unstable shape – e.g. a sphere with uneven lipid packing that would cause expansion or contraction. Under these conditions, the bilayer would then push up against the against the dummy particle layer, and the extent could be tuned by the degree of lipid density mismatch between the leaflets. However, in this approach, if changes in lipid dynamics

are observed, it may be impossible to distinguish dummy-particle based artifacts from normal curvature responses from lipid packing asymmetries.

Instead, we approach the problem using a flat bilayer and a single layer of dummy particles (figure 4.4 A). We enforce the interaction between the two with constant force pulling of the center of mass of the bilayer in the direction of the dummy layer, allowing us to scan a large range of interaction intensities. Given a bilayer area and a center of mass pulling with a certain force, the interaction between the bilayer and dummy grid can be expressed as a force per unit area, or pressure. We studied bilayer properties of systems with pressures ranging from 0 to 10 kJ mol^{-1} nm^{-3}. We performed this analysis for systems with both frozen and position restrained dummy particles.

We chose two metrics to judge the effects of the interaction, lipid splay angles and diffusion coefficients. Figure 4.4 B shows the effects of the interaction on splay angles at all measured pressures for a system with frozen dummy particles, with the “top” leaflet directly interacting with the dummy grid. No change in splay angle can be observed for pressures of up to ~0.3 kJ mol^{-1} nm^{-3}. For the top leaflet, increased pressure led to a decrease in the splay angle, indicating an ordering effect. The bottom leaflet remained unaffected at all measured pressures. Figure 4.4C shows the effect of the interaction on diffusion coefficients, which is negligible for all cases within our measured error. The same analyses were performed on a system with position-restrained dummy particles rather than frozen dummy particles, with largely the same result (data not shown).

Bracketing dummy particles then seem to be a safe and efficient method to sculpting unique membrane morphologies, as long as the interaction between them is below a certain threshold. It should be noted that even at larger applied pressures, the

difference in dynamics (at least measured by splay angles) is quite small. The next section will explore measuring the extent of interaction between membrane and dummy layers beyond this control experiment.

Measuring the magnitudes of bilayer-dummy particle forces

We next asked if we could measure the applied force propagated through the bilayer to the dummy particle system. This is important for two reasons. First, if one can measure the extent of pressure exerted by a curved membrane, it can easily be ascertained whether the level of interaction is within the threshold for affected dynamics. Second, this ability would allow for examination of the “stress points” in heterogeneous morphologies, showing where instability presents itself with spatial resolution. Our flat bilayer setup is particularly well suited for examining this possibility, as we can exactly control the amount of pressure applied.

We measured the applied pressure of bilayers to dummy particles in both frozen and position-restrained setups using different methods. For frozen systems, we simply measured the force on each bead over time, which can be obtained from a Gromacs .trr files. Figure 4.5 A shows the applied vs measured forces for this system. As expected, the x and y components of the average force are close to 0, as no net pressure was applied in those dimensions. The measured forces in the z dimension closely match the applied force, indicating that we can correctly measure these forces.

For the position-restrained system, the average force can be inferred from the average position of the dummy bead relative to its reference, as the applied force will induce a corresponding stretching of the position restrained “spring.” Figure 4.5 B shows

the results for this system. Though the results are slightly noisier, with increased error margins, the trend is the same as with the frozen systems.

Measuring forces on mitochondrial membranes

With our new cardiolipin model and ability to both enforce and probe the mechanical properties of membrane structure, we next wanted to study cardiolipin containing bilayers in a biologically relevant morphology. To achieve this, we constructed dual bilayer systems connected to a cylindrical “crista”, with toroidal junctions bridging the systems (figure 4.1). We first constructed systems with cylindrical and toroidal radii of 10 nm, and a cylindrical length of 10 nm, bracketed by dummy particles as detailed in the methods. To examine the effects of membrane composition on the stability of these structures we constructed three bilayer compositions; one made of 100% POPC, one with 80% POPC and 20 % DOPE, and one with 80% POPC and 20% TOCL.

To simplify the analysis, we reduced the dimensionality of our system to lateral (x/y) radius from the system center, and z dimension from the system center. Thus, moving out from the center of the cylinder, the radius stays constant until the junction is reached, while the z coordinate increases (moving in both directions from the cylinder center). In the junction region, both the radius and z dimension increase. Finally, in the flat regime only the radius increases. In this reductionist setup we can bin up both the lipids and the dummy particles and assess trends as functions of this coordinate system, and can distinguish between the two leaflets.

In the 100% POPC system, we observed stress in two main locations. First, a mild pressure was observed on the inner leaflet of the cylindrical region, in the vicinity of z=10

nm (figure 4.6 A). Second, on the opposite leaflet in the junction region. These measured pressures were also present (and enhanced in magnitude) in the 20% DOPE simulation (figure 4.6 B). In contrast, the stress profile of the 20% TOCL simulation (figure 4.6 C) showed much less measured pressure throughout the structure.

One clear implication of this result is that incorporation of physiologically relevant quantities of TOCL reduces stress in these types of morphologies, and does so in a markedly different manner than DOPE, another purportedly conical lipid. It is unclear from this setup whether this difference is a total-curvature mediated effect, or if the role of Gaussian curvature plays a role in the differential behavior. It is interesting that the little stress that does occur in the TOCL-containing system occurs on opposite leaflets – the outer leaflet of the cylindrical region, and the topmost leaflet in the flat regime.

Cardiolipin partitioning in mitochondrial membranes

We next decided to examine the distribution of lipid species in the cardiolipin-containing membrane. In a similar manner to force measurements, we discretized the system using the reduced radial-z coordinate system, and discriminated between leaflets. The results of this are shown in figure 4.7. We observed enhancement of TOCL concentration on the inner leaflet of the cylindrical region, and vice versa for the outer leaflet of the same region. This is expected given the negative curvature of the inner leaflet and the positive curvature of the outer leaflet. Interestingly, the trend for each leaflet was completely inverted in the junction region.

The driving force for this behavior in the junction regions is unclear. One possibility is that the energetics of the cylindrical region dominate the partitioning behavior, and the

corresponding distributions of the junction region are a result of the enhancements and depletions of the cylinder. Alternatively, the Gaussian curvature of the junction could play a role in partitioning. A thorough analysis of the mean and Gaussian curvature of each leaflet of the junction region may provide some insights in future work.

ATP synthase rotational dynamics in curved membranes

Minimization of curvature strain has been shown to be a driving force for ATP synthase dimer self-organization[71,231], yet these simulations have only examined ATP synthase dimers in *flat* bilayers; the impact on native membrane curvature has yet to be explored *in silico.* We wished to see if ATP synthase dimers were able to self-organize in the presence of curvature. As a first attempt, we simulated single ATP synthase dimers in cylindrical bilayers with varying radii. Using an angular reaction coordinate, we probed the free energy landscape of ATP synthase rotation in a curved membrane. Our theory was that ATP synthase would have a strong preference to orient itself to match the existing curvature of the cylinder, and that the inter-monomer center of mass vector would be most favorable at an angle of 90^{o} with respect to the long axis of the cylinder, and that this effect would be dependent on the cylindrical radius.

Figure 4.8 shows the free energy profiles of ATP synthase dimers in cylinders with radii of 5, 10, and 15 nm. Several interesting aspects of the profiles are observed. In the regime of 0 to 45^{o}, the trend was as expected. Aligning along the long axis of the cylinder comes with an associated energetic penalty. This makes sense in light of the work of Davies and coworkers[231], who noted the induced curvature of ATP synthase dimers in flat bilayer. After all, the cylindrical geometry is *flat* along this dimension, and a similar effect

is likely at play. The shapes of the profiles for all 3 systems are similar in this regime, perhaps indicating that the differences in curvature are too small to manifest in energetic differences.

An unexpected feature of the PMFs was that in the 5 nm system, the energy minimum occurred at around 40 degrees, rather than the fully cylinder-aligned 90 degrees. Similarly, the 10 nm system showed a free energy minimum at around 55 degrees. While we are unsure as to the nature of this phenomenon, we speculate that it could be due to the curvatures of the cylinders being more extreme than the preferred curvature of the synthase dimer. If this is the case, straddling the cylinders at an oblique angle may relieve the membrane from being forced into too *flat* of a configuration. This idea has some support in that the free energy at 90^{o} is highest in the 5 nm system. Additionally, the 15 nm system shows a consistently decreasing energy towards 90 degrees. If our theory is correct, the cylinder with a radius of 15 nm either matches the desired curvature of the ATP synthase dimer, or is slightly flatter.

It is tempting to speculate that the offset nature of the energy rotation could lead to variations in the morphologies that ATP synthase dimers produce. For example, in several species cristae contain tubular structures bound by helical rows of dimers[238,239]. These rows could be self-organized based on the non-aligned preference of ATP synthase dimers. In this scenario, the range of dimer association angles observed across species[157] could be tightly coupled to emergent superstructure.

Long-range effects of ATP synthase in curved systems

Pairs of ATP synthase dimers have been shown to attract each other through a long-range interactive force in flat membranes[71]. This is mediated through curvature minimization, as rows of dimers together minimize the impact on the flat membrane. However, *in organelle*, ATP synthase dimers localize to regions of tight curvature. We theorized that in these already-curved conditions, the basis for the long-range interactive force would be neutralized, and pairs of ATP synthase dimers might not sense each other through the membrane. To this end, we constructed a system of two ATP synthase dimers in a 10 nm radius cylindrical system, and performed umbrella sampling along the distance reaction coordinate analogous to the work of Anselmi and coworkers[71].

The distance PMF can be seen in figure 4.9, and can be simply interpreted. From distances of > 14 nm, the free energy profile is completely flat within error, indicating that no interaction between the dimers could be detected. This result provides evidence to support our theory that curvature-based through-membrane attraction is nullified in already-curved systems. We note that at distances < 14 nm, significant perturbation of the ATP synthase dimer structure occurred due to attractive interactions between adjacent lobes of the monomers. This interaction is likely artefactual (the Martini forcefield has been demonstrated to overestimate attractive protein-protein interactions – see reference [240]), and so we were unable to examine the energy profile at these close distances, which in another publication has been shown to be repulsive[71]. In that publication, the energy minimum is located at 13 nm, but this difference may be due to differences in the models used.

This finding suggests that while inter-membrane interactions may be key for organization of ATP synthase dimers in flat membranes, this attraction may only play a

role in the nucleation of membrane curvature, whereupon rows of ATP synthase dimers induce crista-like curvature in the membrane. Upon membrane curvature induction and the formation of proper cristae, it may be that other forces keep these rows in place, such as the rotational sensitivity demonstrated in the previous section.

Future directions

This work serves as an initial foray into physiologically relevant simulations of mitochondrial phenomena. The techniques herein should be expanded upon in future work, and the preliminary results of this chapter offer several avenues for future studies. In the mitochondrial studies, a next step would be to investigate curvature-based phenomena over a range of geometries, rather than the one geometry used here. It has been shown that in extremely tight curvature regions, cardiolipin aggregates more strongly than phosphatidylethanolamine; it would be interesting to observe this trend in more tightly curved mitochondrial setups, and also to examine the forces required to maintain these structures, which one would expect to increase with more unstable morphologies.

The work involving ATP synthase can also be extended. Our theory of curvature mismatch leading to angled dimers in cylinders could be verified by simulations of more intermediate curvatures – in this case, one would expect ATP synthase to align normal to the axis once the mean curvature matches its preferred curvature. For the translational studies, a similar expansion of curvature radius would be interesting. One might expect

that as curvatures get flatter, the curvature-based interdimer attraction might reappear at intermediate magnitudes compared to the PMF of Anselmi, et al[71].

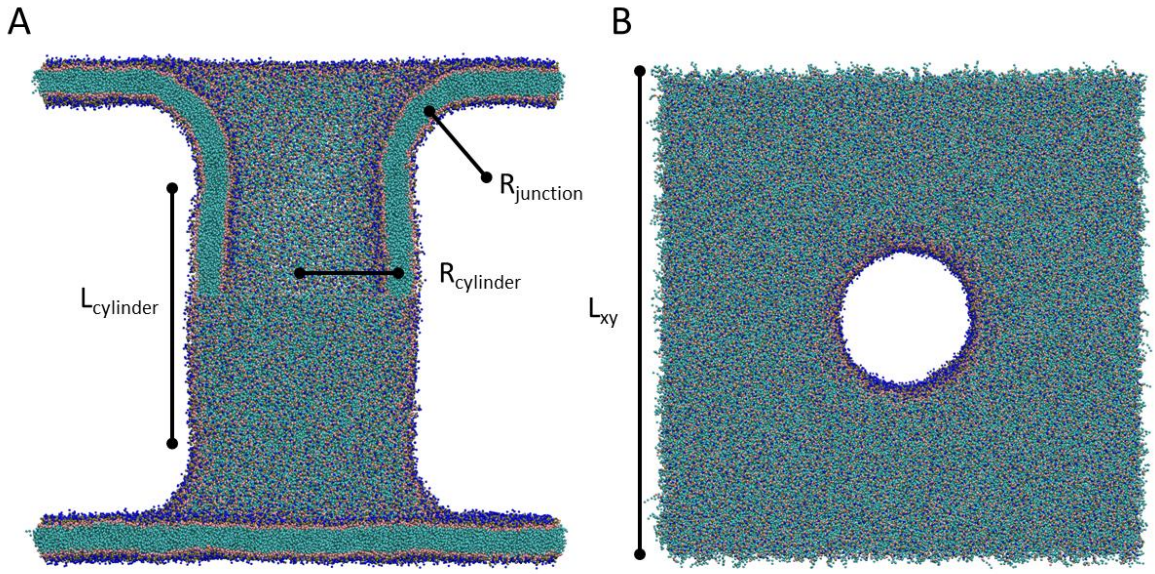

Figure 4.1 Structure of mitochondria-mimicking bilayers, annotated with the parameters describing geometry. A) Side-on view, with the top half cut away to show the bilayer cross-section. B) to-down view of the same system.

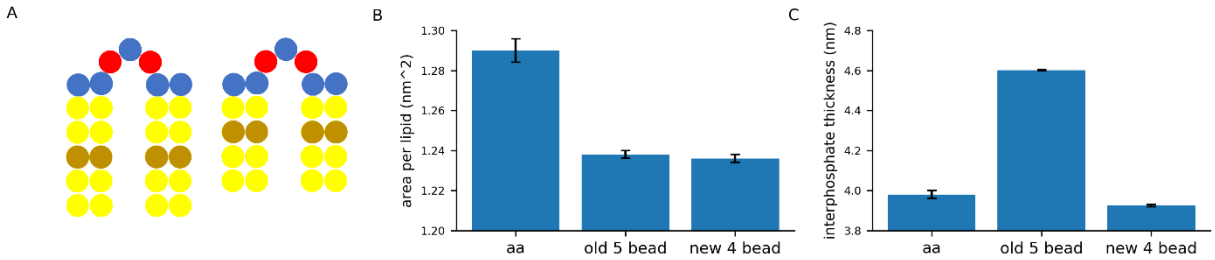

Figure 4.2. Validation of cardiolipin model. A) Schematic of the topology of the 5-bead (left) and new 4-bead (right) models. Blue beads are glycerols, red beads represent phosphate groups, yellow beads represent saturated tail beads, and the tan beads are tail chains modeling insaturation. B) Area per lipid comparison of pure CL bilayers with atomistic and two coarse-grained models. C) Bilayer thickness of the same systems, measured by interphosphate distance.

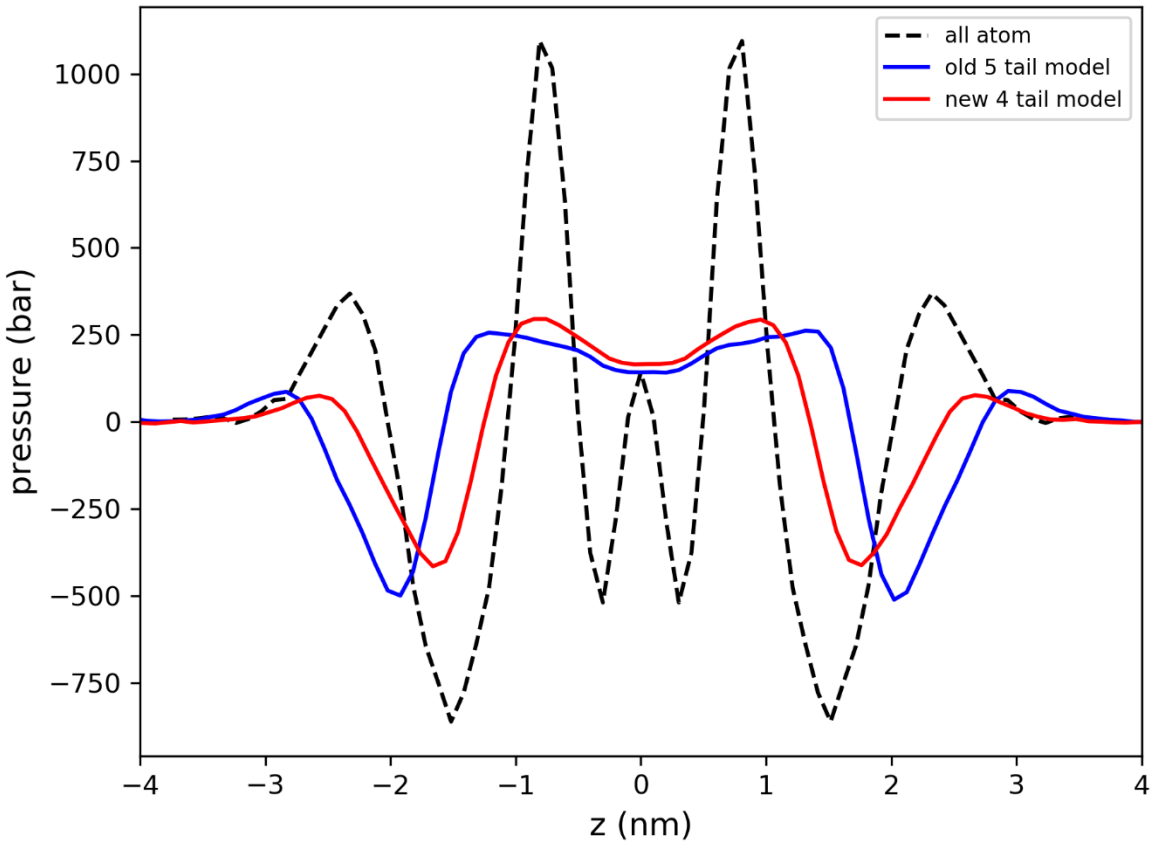

Figure 4.3. Lateral pressure profiles of pure cardiolipin bilayers with a number of models. LPPs were calculated using Gromacs-LS and the bilayer center was set to z=0.

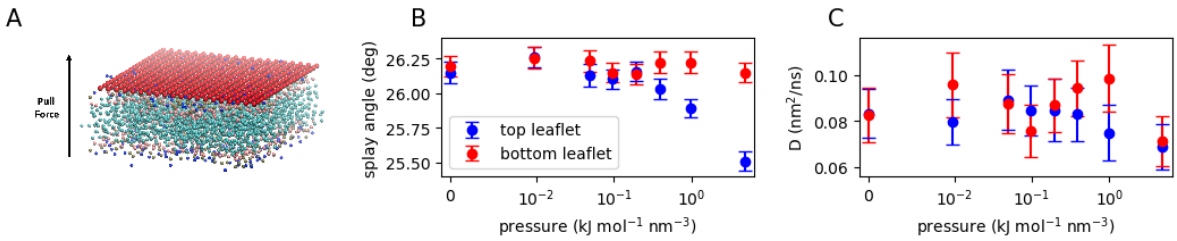

Figure 4.4. Effect of dummy particles on bilayer properties. A) Schematic of the setup, in which a bilayer is pushed into a grid of dummy particles using constant force pulling. B) Lipid tail splay angles with increasing bilayer-dummy layer interaction. The top leaflet directly interacts with the bilayer. C) Diffusion coefficients of the same system.

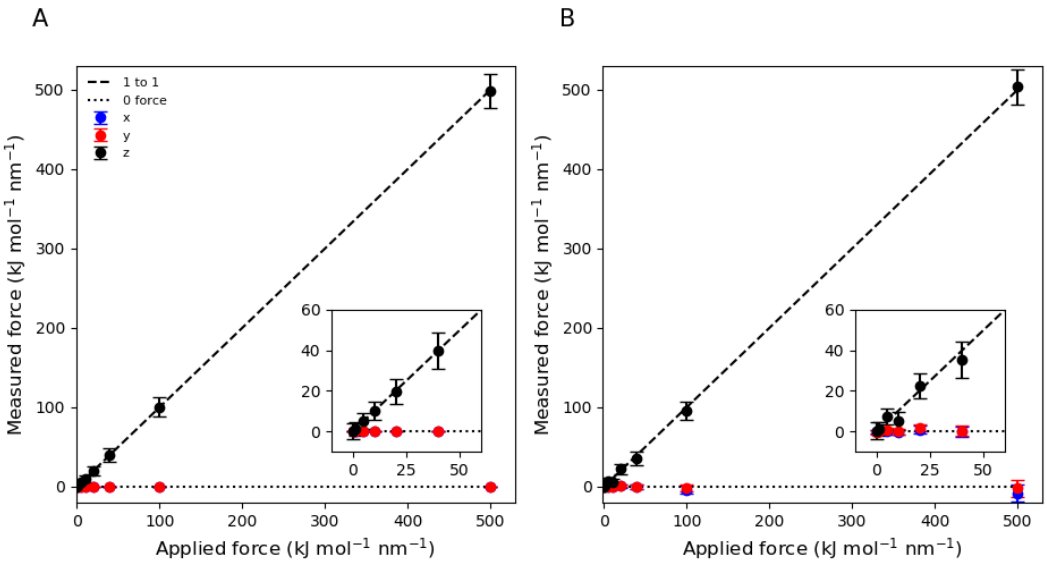

Figure 4.5 Measured forces between bilayers and dummy particles. A) the x, y, and z components of the measured force on the dummy grid compared to the applied constant force pulling, for a system with frozen dummy particles. B) The same measurement for a system with position-restrained dummy particles. Insets are zoomed in.

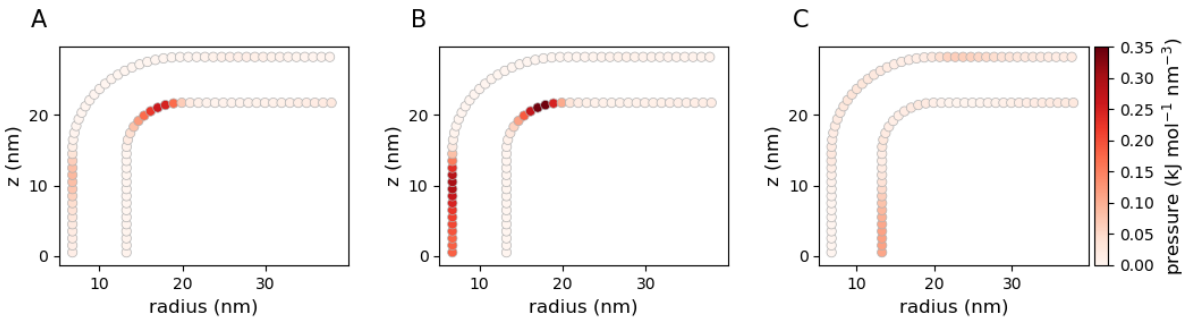

Figure 4.6. Force distributions in mitochondrial-mimicking systems for both leaflets, with compositions of 100% POPC (panel A), 80% POPC, 20% DOPE (panel B), and 80% POPC, 20% TOCL (panel C).

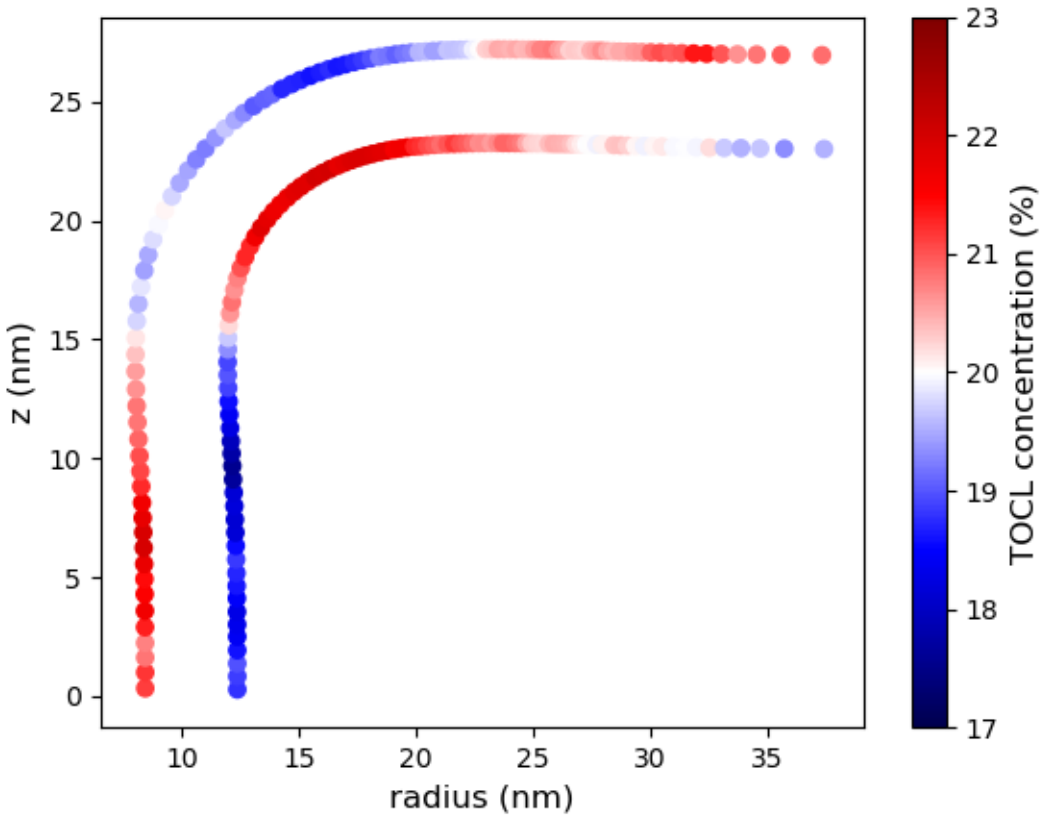

Figure 4.7 Distribution of cardiolipin in mitochondrial-mimicking systems, with dimensions $L_{cylinder}$ = 30 nm, $R_{cylinder}$ = 10 nm, and $R_{junction}$=10 nm. The bulk concentration of this system was 80% POPC, 20% TOCL.

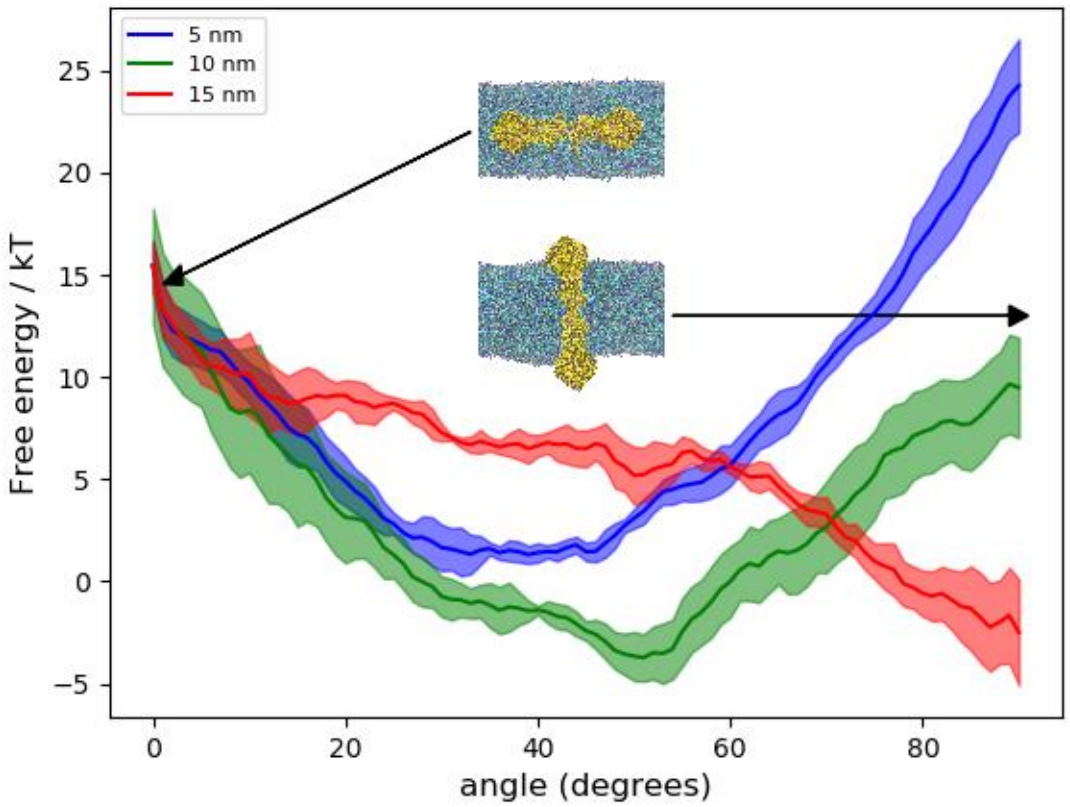

Figure 4.8 Free energy of ATP synthase dimer rotation in cylindrical membranes, on cylinders with radii of 5, 10, and 15 nm. The free energy minimum was set to 0 in each PMF. Error bars are 95% confidence intervals, obtained using details that can be found in the methods section.

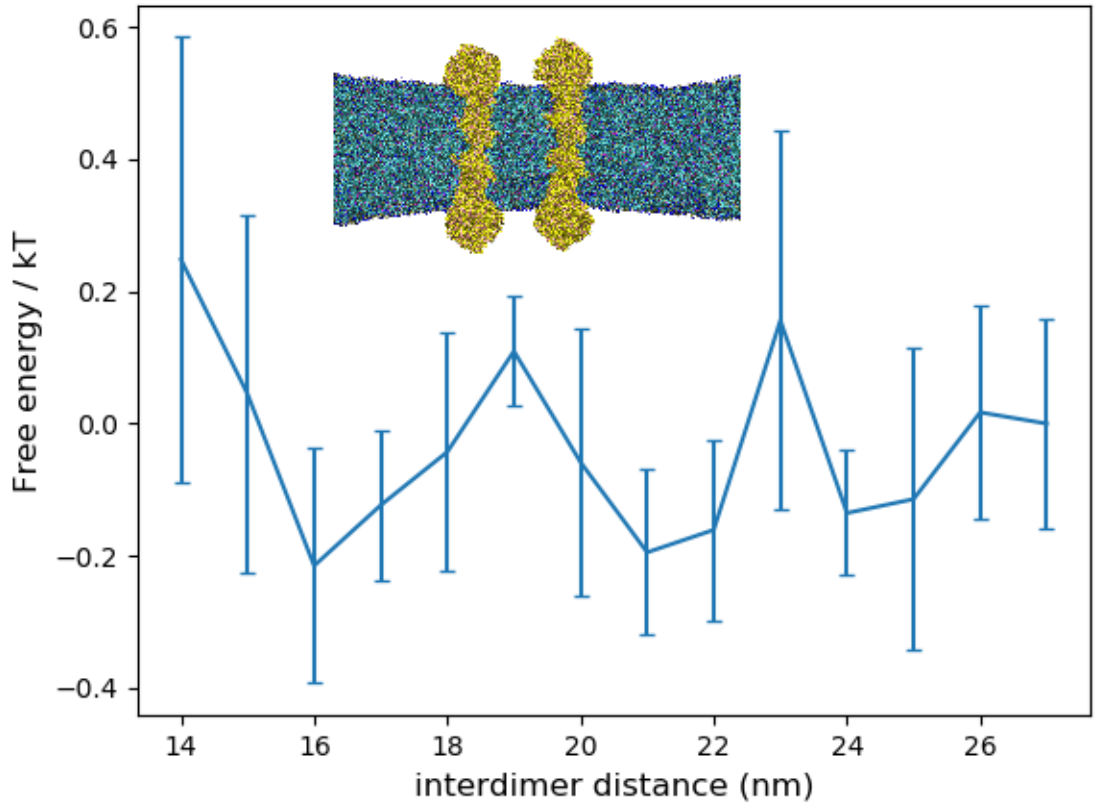

Figure 4.9. Free energy profile of ATP synthase dimer pair interactions on a cylindrical membrane with radius = 10 nm, estimated from umbrella sampling. Error bars are 95% confidence intervals from standard errors. The details of error analysis can be found in the methods section.

Chapter 5:

BUMPy: A Model-Independent Tool for Constructing Lipid Bilayers of Varying Curvature and Composition

Reproduced with permission from:

Boyd, and May. “BUMPy: A Model-Independent Tool for Constructing Lipid Bilayers of Varying Curvature and Composition. *JCTC* (2018), 14 (12), 6642-6652

The following changes have been made:

- The manuscript has been reformatted to meet University Standards
- Figures numbers have the chapter number prepended
- References have been renumbered to match the rest of the thesis

Title: BUMPy: A Model-Independent Tool for Constructing Lipid Bilayers of Varying Curvature and Composition

Author: Kevin J. Boyd, Eric R. May

Publication: Journal of Chemical Theory and Computation

Publisher: American Chemical Society

Date: Dec 1, 2018

PERMISSION/LICENSE IS GRANTED FOR YOUR ORDER AT NO CHARGE

This type of permission/license, instead of the standard Terms & Conditions, is sent to you because no fee is being charged for your order. Please note the following:

- Permission is granted for your request in both print and electronic formats, and translations.
- If figures and/or tables were requested, they may be adapted or used in part.
- Please print this page for your records and send a copy of it to your publisher/graduate school.
- Appropriate credit for the requested material should be given as follows: "Reprinted (adapted) with permission from (COMPLETE REFERENCE CITATION). Copyright (YEAR) American Chemical Society." Insert appropriate information in place of the capitalized words.
- One-time permission is granted only for the use specified in your request. No additional uses are granted (such as derivative works or other editions). For any other uses, please submit a new request.

BUMPy: A model-independent tool for constructing lipid bilayers of varying curvature and composition

*Kevin J. Boyd and Eric R. May**

Department of Molecular and Cell Biology, University of Connecticut, Storrs, CT 06269, United States

Abstract

Molecular dynamics is a powerful tool to investigate atomistic and mesoscopic phenomenon in lipid bilayer systems. These studies have progressed with the advent of increased computational power and efforts are now increasing being directed toward investigating the role of curvature and bilayer morphology, as these are critical features of biological processes. Computational studies of lipid bilayers benefit from tools that can create starting configurations for molecular dynamics simulations, but the majority of such tools are restricted to generating flat bilayers. Generating curved bilayer configurations comes with practical complications and potential ramifications on physical properties in the simulated system if the bilayer is initiated in a high-strain state. We present a new tool for creating curved lipid bilayers that combines flexibility of shape, force field, model resolution and bilayer composition. A key aspect of our approach is the use of the monolayer pivotal plane location to accurately estimate interleaflet area differences in a curved bilayer. Our tool is named BUMPy (Building Unique Membranes in Python) is written in python, is fast and has a simple command line interface.

Introduction

Molecular dynamics (MD) is an increasingly powerful computational tool for the study of structure and dynamics of biological macromolecular systems. MD studies of lipid membranes typically consist of periodically constrained lipid bilayers in a rectangular box simulated at constant pressure, which prevents the formation of high curvature or complex topological states, though some curvature-related properties such as the bilayer bending modulus[48,59,85,204,241] and the spontaneous curvature[27,53,98] can be estimated from equilibrium properties of a flat bilayer. However, biological membranes exist in complex configurations (e.g. the endoplasmic reticulum, mitochondrial inner membranes) and these configurations are often critical states in biological processes such as endocytosis, cell division, and chemotaxis. Hence, in recent years interest has grown in simulating curved lipid systems, which have included vesicles[87,96,97,99], cylinders[48,87,101], fusion intermediates[105,106,111,114,115], and membrane buckles[56,79,83,85,89].

While a number of useful tools exist for investigators to generate *flat* lipid bilayers at both atomistic and coarse-grained resolution to initiate MD simulations[102,133,136–139,218,242], the tools for generating *curved* lipid systems are more sparse. Simulations of vesicles can be set up using the CHARMM-GUI[102] coarse-grained vesicle builder, Packmol[140], or LipidWrapper[141]. Packmol has the additional capacity for setting up ellipsoid shapes as well as cylinders, while in principal LipidWrapper can generate any curved topology, though the process for creating some complex shapes in LipidWrapper requires modeling in 3rd party software. Of the above tools, the CHARMM-GUI Vesicle builder is limited to a subset of lipids in the Martini Force Field[27], while LipidWrapper and

Packmol are flexible both in force field and lipid composition. Other tools not discussed in detail here support forming nonbilayer structures such as micelles,[137,143,144] and inverted hexagonal phases[145].

An important consideration when assessing tools for generating curved lipid systems is the treatment of interleaflet ratios, as the outer leaflet in any curved bilayer will have a larger area (and therefore more lipids) than the inner leaflet. The extent of area mismatch between leaflets depends on the topology in question and the degree of curvature, and is not trivial to estimate. In a closed shape such as a vesicle, inaccuracies in interleaflet ratio estimation can lead to changes in shape and/or artifacts arising from nonequilibrium lipid packing. Of the tools listed above, only CHARMM-GUI directly addresses this concern, using an empirical model to estimate lipid counts and interleaflet ratios for vesicles. Even in this case, the CHARMM-GUI protocol recommends a lengthy equilibration process using artificial pores to account for errors in the initial estimates. Packmol and LipidWrapper do not directly control interleaflet ratios when building bilayers, and the resulting lipid ratios and densities are a result of the tools' packing procedures.

The key to calculating correct interleaflet ratios is determining the respective surface areas of the inner and outer monolayers of the curved bilayer, at which point they can be populated according to the areas per lipid calculated in flat bilayers. However, the definition of a molecular surface cannot be unambiguously defined and the choice of atoms used to define the surface will ultimately affect the surface area calculated for a curved system. The approach we have taken is to calculate the surface area of the curved shape at the monolayer pivotal plane – a surface within the monolayer that has the same

area in a flat or curved system[1]. Therefore, we believe our approach removes a degree or arbitrariness to the surface area calculation and allows us to construct curved bilayer systems with optimal interleaflet number ratios.

We are motivated by our observation that current tools for creating curved starting structures for MD simulations are limited in the range of shapes that can be created, and do not properly address the problem of accurately predicting interleaflet area differences. Herein, we present a new approach for generating *in silico* curved lipid membranes for starting configurations for MD simulations called BUMPy (Building Unique Membranes in Python). BUMPy is a versatile tool that can create any number of shapes and is independent of both lipid type and forcefield. The current BUMPy repository includes commonly simulated shapes that lack implementations in other software packages, such as buckles, tethers, and elongated vesicles. Furthermore, we demonstrate that our approach accurately addresses the interleaflet ratio problem by determination of the monolayer pivotal plane.

Methods

Geometric transformations

In BUMPy, generation of different curved shapes is accomplished by geometric transformations to the coordinates of flat bilayer systems. To generate a cylindrical shape, a flat patch of bilayer is selected with lateral dimensions corresponding to the length and circumference of the desired cylinder (**Figure 5.1A** and **B**). The Cartesian coordinates along the axis with dimensions of the cylindrical circumference are projected as angles along a circle with the desired radius, with $\theta = x/R$. The new coordinates in that

dimension are then calculated according to a sine and cosine description of a circle, with $x' = R * \sin(\theta)$ and $z' = R * \cos(\theta)$. Spherical shapes are generated using a similar procedure to that for cylinders. Rather than describing positions with Cartesian coordinates, the bilayer positions are transformed to polar coordinates, and the angles for transformation are calculated as a function of the radial coordinate, while retaining angular coordinates (**Figure 5.1C**).

It may be of interest to create geometries with radial symmetry (cylinders, spheres) and couple them to flat bilayer patches. The interface between the two systems is modeled by a toroidal junction (**Figure 5.1D**), the shape of which is determined both by the radius of the radially symmetric system being coupled, as well as a radius defining the sharpness of the junction.

Area Matching

Transformation of flat coordinates to curved shapes will create area strain if both monolayers have an equal number density of lipids. Consider the transformation of a flat patch of bilayer to a cylinder with a radius *R*, length *L* and thickness *T*. The inner leaflet will have a surface area of $A_{inner} = 2\pi L(R - T/2)$, while the outer leaflet will have an area of $A_{outer} = 2\pi L(R + T/2)$, but both leaflets have the same number of lipids as before the transformation, and therefore the resultant cylinder will have different areas/lipid in the inner and outer leaflet. Such a mismatch can only be equilibrated by interleaflet flip-flop, a process which takes place on time scales of minutes to hours[243], far beyond those accessible in typical equilibrium MD simulations.

To account for area mismatch, the leaflets of the flat bilayer are transformed separately. The size of the patch corresponding to the outer leaflet is chosen to satisfy the size of a cylinder with a given radius of $R_{outer} = (R + T/2)$, and likewise $R_{inner} = (R - T/2)$ for the inner leaflet. The coordinates of both leaflets are then scaled to fit into a box matching the original cylindrical dimensions (**Figure 5.2**). Thus, the flat bilayer patch has an uneven density of lipids, that when transformed exactly matches the correct areas for the inner and outer leaflets and maintains equilibrium area/lipid values (assuming the initial flat bilayer is well equilibrated). A similar procedure is performed for spheres and toroidal junctions: the initial outer and inner monolayer slices are chosen to be circles with different radii based on the thickness.

Spheres and junctions require an additional rescaling step before transformations, as flat surfaces cannot be directly mapped onto morphologies with multiple non-zero principal curvatures without accruing local area strain. In other words, the total number of lipids can be accurately estimated, but a simple linear scaling of the flat region into a circle with correct dimensions would lead to local density imbalances upon transformation. To account for this, in spherical and toroidal junctions the flat coordinates are scaled nonlinearly to generate an even density on the spherical surface. Details on the scaling method are provided in the Supporting Information (SI).

To match areas in the manner described above, the choice of thickness must be carefully chosen. The pivotal plane (z_o) of a monolayer is the surface that does not deform when the monolayer undergoes a curvature deformation[1,244]. Critically, this allows us to compare the areas of flat monolayers to curved monolayers by measuring the surface area of the curved bilayers at their monolayer pivotal planes. Therefore, given a bilayer

shape with a desired radius R, the area of the outer monolayer can be estimated by calculating the surface area of a shape with radius $R + z_o$, and likewise $R - z_o$ for the inner monolayer. Throughout this work we will denote the pivotal plane of a monolayer as a distance z_o from the center of a bilayer. It should be noted that z_o is more correctly the pivotal plane of a *flat* monolayer, and that the actual pivotal plane (z) varies slightly with curvature. The curvature correction to the pivotal plane distance is small for moderately curved systems[87] and is only relevant for very high curvatures as it falls off quadratically with curvature, so we will neglect the correction in our approach.

Software Implementation Details

BUMPy is implemented in Python as a command-line tool. It can be freely downloaded at www.github.com/MayLab-UConn/BUMPy, along with usage details and examples. NumPy is the only required dependency of BUMPy. BUMPy has been tested with Python 3.6.0 and NumPy 1.11.3. BUMPy is capable of building systems with upwards of 10 million particles on a typical desktop computer, and can create systems with over 500 million particles on a high-RAM machines. Performance details are provided in Supporting Information (**Figure 5.S1)**, as well as sample command line usages.

Simulation Methods

Force Fields and System Setups

The majority of simulations in this work were performed using the coarse-grained Martini forcefield with standard (nonpolarizable) water[27]. Additional simulations were performed using the atomistic CHARMM-36 additive forcefield[217]. Flat bilayer systems were created using the *insane* bilayer builder[136] for the Martini systems, while the CHARMM-GUI Membrane Builder[242] was used to create atomistic bilayers compatible with the CHARMM-36 forcefield. Cylinders, spheres, and other shapes were then generated from flat systems using BUMPy and solvated using the gmx solvate tool in GROMACS.

Coarse-grained Simulation Parameters

All simulations were performed using GROMACS 2016[216]. Energy minimization and initial equilibration followed the protocol suggested by the CHARMM-GUI Martini maker. Initial energy minimization was performed using the steep integrator with soft-core potentials for short-ranged interactions, allowing tolerance for overlapping particles. An additional round of energy minimization with the steep integrator was then performed with soft-core potentials turned off. The minimization steps were followed by several short simulations (10,000 steps) using the MD integrator, iteratively increasing the timestep from an initial step of 2 fs to a final timestep of 20 fs, while applying position restraints to the lipid phosphate beads. Simulation times here are reported without scaling.

All subsequent simulations used the MD integrator with a timestep of 20 fs. Electrostatic interactions were shifted to 0 at a distance of 1.1 nm using the reaction-field method with reaction field dielectric (ε_{rf}) set to infinity, and van der Waals interactions were directly cut off at the same distance using the Potential-shift-Verlet modifier, as

suggested by de Jong and colleagues[28]. Temperature was maintained at either 300 K or 33 K using the v-rescale algorithm with a time constant of 1 ps, with the solvent and bilayers coupled separately.

Pressure coupling was accomplished using the Parrinello-Rahman barostat[197] with a time constant of 12 ps and a compressibility of $3 * 10^{-4}$ bar^{-1}. Spherical systems were simulated using isotropic pressure coupling with a reference pressure of 1 bar. Cylindrical systems were simulated using semi-isotropic pressure coupling, with the long axis of the cylinder aligning with the *z*-dimension, using a reference pressure of 1 bar in both the *z* and *x/y* dimensions. Simulations of flat bilayers were performed with semi-isotropic pressure coupling with both the lateral and normal direction pressures coupled to a 1 bar pressure bath.

Atomistic Simulation Parameters

An all-atom vesicle composed of 1,2-dipalmitoyl-sn-glycero-3-phosphocholine lipids (DPPC) was constructed with a radius of 5 nm and simulated with the CHARMM-36 forcefield. The equilibration procedure was similar to that of the coarse-grained systems, involving a short energy minimization using soft-core potentials, followed by a longer minimization without soft-core potentials, and then successive rounds of equilibration with restraints on the phosphorus atom. A time step of 2 fs was used, with the Verlet cutoff scheme. Lennard-Jones interactions were cut off at 1.2 nm and modified with the force-switch option of GROMACS between 1.0 and 1.2 nm. Coulombic interactions were directly calculated within 1.2 nm and long-range electrostatics were treated with the

Particle Mesh Ewald method. Temperature was maintained at 330 K using the Nose-Hoover thermostat, and isotropic pressure coupling was maintained using the Parrinello-Rahman barostat, with a time constant of 5 ps, a compressibility of $4.5 * 10^{-5}$ bar^{-1}, and a reference pressure of 1 bar.

Pore Formation Protocol

Pores were induced in cylinders and vesicles using the protocol of Qi and colleages[102], using flat-bottom potentials in GROMACS to allow for lipid flip-flop and equilibration between the bilayer leaflets. The Martini 2.0 lipid forcefield provided by CHARMM-GUI contains the relevant parameters and only requires an input in the GROMACS .mdp simulation parameter file to activate the potentials. Vesicles were equilibrated with 6 pores, two along each major axis, while cylinders were equilibrated with 4 pores (along two axes), all with a force constant of 1000 kJ mol^{-1} nm^{-2}. A pore radius of 1 nm was found to be the smallest for which interleaflet flipflop was observed. Most simulations were simulated with a 1 nm radius pore for a brief (2 ns) equilibration period, followed by a 200 ns simulation with a pore radius of 2.0 nm for accelerated flipflop, then a 400 ns simulation with a 1.0 nm pore for data collection.

Dummy Particles

While BUMPy can generate bilayers of various shapes and curvatures, these systems may be unstable if the bilayer properties (e.g. spontaneous curvature, bending modulus) are discordant with the imposed geometry. Nonetheless, it can be useful to study lipid

properties under these conditions and we demonstrate how a lipid bilayer can be made to maintain an otherwise unstable shape. A semicylinder-plane system (see **Figure 5.6** and **Table 5.1**) was bracketed on either side of the bilayer with a grid of dummy particles, which is a modified version of the protocol implemented by Yesylevskyy and coworkers[120]. The dummy particle grid was created with lateral spacing of 0.5 nm and an interleaflet thickness of 4.6 nm, and particles were anchored in place with position restraints using a force constant of 1000 kJ mol^{-1} nm^{-2}. The dummy particles only interacted with the hydrophobic tail beads of the bilayer, while all other interactions were turned off. The potential between dummy particles and tail beads was modeled with a purely repulsive interaction by using a Lennard Jones potential with the $C^{(12)}$ parameter set to 0.0258 kJ mol^{-1} nm^{12} (corresponding to ϵ = 2.0 kJ mol^{-1}, and σ = 0.62 nm), and the attractive $C^{(6)}$ parameter set to 0.

Data Analysis

The pivotal plane of a lipid monolayer can be calculated from vesicles and cylinders that are in transverse (interleaflet) equilibrium. Wang and Deserno[87] derived a relationship between z_o, radius (R), and the interleaflet lipid number ratio for cylinders

$$z_{o-cylinder} = \frac{\rho - 1}{\rho + 1} * R \qquad (Eq. 5.1)$$

where ρ is the outer to inner leaflet lipid number ratio. A similar relationship exists for spheres

$$z_{o-sphere} = \frac{\sqrt{\rho} - 1}{\sqrt{\rho} + 1} * R \qquad (Eq. 5.2)$$

Therefore, to calculate z_o, we need only to simulate a vesicle or cylinder to equilibrium by inducing pores, then measure the resulting radius and interleaflet ratio.

Calculating interleaflet ratios and radii

Simulation trajectories were processed in Python using MDTraj[235]. To assign lipids to leaflets on a dynamic basis, cartesian coordinates were converted to cylindrical coordinates (in the case of cylinders) or spherical coordinates (in the case of vesicles). The radii of the phosphate beads (R_P) were then compared to the radial position of the terminal tail bead (R_t) in the same molecule, and lipids were either assigned as inner ($R_P > R_t$) or outer leaflets ($R_P < R_t$) on a frame-by-frame basis. In each frame, the radius of each leaflet was individually calculated as the average of the phosphate radii, and then the leaflet radii were averaged to obtain the bilayer radius.

Lateral Pressure Profiles

Lateral Pressure Profiles (LPPs) for flat bilayers were calculated using GROMACS-LS[19], a modified version of GROMACS 4.5.5. For analysis of LPPs, coordinates and velocities were saved every 5 ps for 100 ns, for a total of 20,000 frames per simulation. LPPs along the *z* axis of the bilayers were calculated with 0.01 nm resolution.

Diffusion coefficients

Lipid diffusion coefficients were calculated for vesicle systems by calculating the mean squared displacements of lipids over a range of lag-times and calculating a linear fit to the equation $MSD = 2dD\tau$, where MSD is the mean squared displacement at a time lag τ, *d* is the dimensionality and *D* is the diffusion coefficient. In this case, the vesicle was treated as a 2-dimensional surface (*d=2*). Mean squared displacements of individual lipids were calculated by calculating the arc length along the sphere between initial positions and positions after a lag time of τ. The measured displacements are therefore dependent on the radius of the vesicle. The use of the bilayer radius is inappropriate in this case, as the area of the outer monolayer is greater than that of the inner monolayer. We therefore calculated the displacements and diffusion coefficients of the inner and outer monolayers separately, and used the location of the pivotal plane of each monolayer as the radius for calculating arc lengths and displacements.

Results

Stability of BUMPy-generated systems

The geometric transformation procedure applied when creating shapes with BUMPy has several sources of potential problems that could create high energy states that cause

numerical instabilities. First, since all coordinates are transformed, the mapping from a flat to a curved environment causes a change to the internal coordinates of each molecules. The extent of this change depends on the magnitude of curvature, and under high curvature conditions this effect could become energetically unfavorable. Second, BUMPy is able to combine multiple “building-block” shapes into complex geometries. At the interface between building block segments steric clashes between lipids can arise, which would be unfavorable. Third, since BUMPy performs transformations on monolayers and then reassembles the bilayer, this practice can lead to clashes at the inter-leaflet interface. Particularly in the second and third cases, overlap of particle van der Waals radii can lead to systems with potential energies with magnitudes beyond machine precision, in which case energy minimization can fail. This difficulty can be mitigated with the use of soft-core potentials[245,246], which scale down the magnitude of non-bonded interactions, reducing energies so that minimization proceeds. Indeed, this is the suggested protocol (for example) when minimizing a Martini system obtained from the CHARMM-GUI. We have found that a short (50 step) soft-core minimization in GROMACS with default parameters, followed by a typical equilibration scheme is sufficient for numerical stability with every shape in the repository, and for every lipid type we have tested.

Estimating z_o from spheres and cylinders

The pivotal plane of a monolayer can be calculated as a function of the radius and interleaflet lipid ratio for spherical and cylindrical bilayer systems using **eq. 5.1** and **eq. 5.2**[87]. To allow for transverse equilibration of lipid packing densities on accessible

timescales, we implemented a modified version of a relaxation protocol that has been used in several previous studies[25,97,101,102], in which pores are induced in the bilayer using cylindrical flat-bottom potentials. Lipids can then migrate between leaflets with their headgroups facing the hydrophilic channel.

Initially, we constructed a cylindrical bilayer with a 10 nm radius to test the feasibility of measuring z_o based on interleaflet ratios and radii. To our knowledge, the only *in silico* report of z_o location comes from the work of Wang and Deserno[87], in which they calculated the z_o of a Martini DMPC bilayer to be 0.85 +/- 0.011 nm, via a buckling protocol. For comparison purposes, we adopted the same lipid composition and temperature (300 K) in our system, though we note some simulation parameter differences, notably in the timestep and pressure coupling schemes. Our initial system setup was generated using an initial guess of z_o^i = 1.0 nm. Throughout this work we will denote initial estimates of pivotal plane locations used by BUMPy to create shapes as z_o^i, while actual observed values of the pivotal plane locations once equilibrated are denoted by z_o. With a 2.0 nm pore radius, the observed z_o converged to ~0.85 nm within 50 ns (**Figure 5.S2**). After 200 ns, the pore radius was reduced to 1.0 nm, and z_o remained constant at 0.85 nm within fluctuations.

To test the robustness of our z_o estimates with respect to geometry and curvature, we constructed vesicles and cylinders with radii ranging from 5 nm to 20 nm in 5 nm increments and calculated z_o values after allowing interleaflet equilibration through pore formation. **Figure 5.3A** shows the observed radii and interleaflet ratios with reference lines fit to a z_o of 0.85 nm, and **Figure 5.3B** shows the resulting calculated z_o for each trial, with the reference of 0.85 nm drawn and shaded to the uncertainty reported by Wang

and Deserno[87]. Observed z_o values for cylinders closely matched the reported value, falling within error for all radii. In the cylindrical systems, a slight drift towards higher radii was observed. The semi-isotropic pressure coupling scheme allows for volume and aspect ratio changes, resulting in the cylinders contracting in the longitudinal dimension and expanding in the circumferential dimension. However, the observed interleaflet ratios still lie along the contour defined by a z_o = 0.85 nm (**Figure 5.3A**, red), indicating that the relationship between R, ρ and z_o is well accounted for by **eq. 5.1**.

Likewise, **eq. 5.2** appears to model the same relationship for vesicles (**Figure 5.3A, blue**). However, when determining the z_o for spherical systems, we observed a small but statistically significant and consistent difference, with z_o values for spherical systems consistently 0.03-0.05 nm higher than for cylinders of the same initial radii as the spheres (**Figure 5.3B**, blue). We are unsure as to the origin of this discrepancy, but speculate that the flat-bottom pore potential may play a role. Induction of pores in a vesicle introduces a lipid-excluded area to the vesicle surface. This must lead to either area strain in the vesicle or expansion to add more surface area. Inflating the vesicle may affect the apparent z_o on its own, but also may affect the interleaflet ratio, as the extent of curvature has changed. In contrast, the cylindrical systems can relax area strain through the pressure coupling mechanism (by expansion along the longitudinal direction at constant radius). The impact of z_o differences of this magnitude is explored below.

Convergence of pivotal plane from initial estimates

The previous systems were generated using BUMPy with an z_o^i=1.0 nm. We then generated DMPC cylinders with 10 nm radii using z_o^i = 0 nm (equal lipid numbers between leaflets) and z_o^i = 2.0 nm to assess the numerical stability of systems with an inaccurate estimate for z_o, as well as to confirm convergence to the actual z_o when subjected to pore-based equilibration. In both systems, the cylinders minimized and equilibrated without issue, and the final observed z_o values were in agreement with earlier measurements, converging within 40 ns (**Figure 5.3C**).

Effect of z_o^i on bilayer properties

The results shown in **Figure 5.3** demonstrate that a pivotal-plane based description of interleaflet area differences is consistent across a range of curvatures, and that given the ability to equilibrate, systems with different starting z_o^is will converge to the same value. However, the presence of a small but statistically significant difference between observed z_os in spheres and cylinders indicates some systematic error in the measurement of z_o. It is therefore important to determine to what extent an erroneous z_o estimate affects system properties, especially if one were to bypass the pore-based equilibration (which would be required when simulating bilayers with interleaflet compositional differences). To assess the potential impact of z_o-based interleaflet mismatches, we created spherical systems with initial radii of 10 nm, and used a range of z_o^is as inputs to BUMPy. A larger z_o^i has the effect of increasing the ratio of outer leaflet to inner leaflet lipids. The effect of z_o^i on lipid counts and areas is quantified for a 10 nm radius sphere composed of DMPC in **Figure 5.S3**. The vesicles were then simulated *without* allowing pore-based relaxation,

and several system observables were then compared between the systems. **Figure 5.4A** shows calculated radii for vesicles created with z_o^i ranging between 0 (equal interleaflet numbers) and 1.8 nm. As z_o^i is increased, the radius monotonically decreases, though between a z_o^i of 0 and 1.8 nm, the spread is only 0.2 nm total, and differences in radii between systems constructed using z_o^i values of 0.6 nm and 0.8 nm or between 0.8 nm and 1.0 nm are 0.021 nm and 0.031 nm respectively. Changing the z_o^i estimate therefore has a measurable but quite small effect on the observed radius. In each case, the observed radius is larger than the target radius of 10.0 nm by 0.05 to 0. nm, the origin of which is speculated on below.

To examine whether the differences in interleaflet ratios impact lipid structure and dynamics, we calculated the splay angles between the monolayer outward normal vector and the vector between the phosphate and a terminal tail bead (**Figure 5.4B**). With increasing z_o^i, the splay angles of the inner leaflets increase while the splays in the outer leaflets decrease. As the differences in radii between the systems are minor (**Figure 5.4A**), the findings can be interpreted simply as a result of area strain. Systems with higher z_o^is have more lipids in the outer leaflet, effectively decreasing the area per lipid in that leaflet (**Figure 5.S3A and C**), while the opposite effect is observed in the inner leaflet. The increased splay of the inner leaflet is a result of each lipid having a larger area and less lateral area strain, and vice versa for the outer leaflet.

An intriguing feature of the leaflet splay analysis is the z_o^i at which the splay angles of the inner and outer leaflets match each other does not coincide exactly with the correct z_o of 0.85 nm, as might be expected. Matching splay occurs around z_o^i= 0.6 nm, while

around z_o^i = 0.85 nm the splay angles of the inner leaflet lipids are larger than those of the outer leaflet. Such interleaflet lipid tail behaviors in equilibrated vesicles have been demonstrated before[97], and indicate that the two leaflets have differences in lateral packing. In principal, this could be problematic, as the pivotal plane area-matching theory assumes equal areas per lipid between the two leaflets. However, the magnitude of the difference in splay at the correct z_o is small (less than 5°), and such effects are expected to decrease with increasing radius. Nevertheless, the small differences observed here may indeed be responsible for the radius shifts observed in **Figure 5.4A**.

To measure the effect of z_o^i on lipid dynamics, we calculated the 2-dimensional lateral diffusion coefficients of the inner and outer leaflets (**Figure 5.4C**). The diffusion coefficients (*D*) for the outer leaflet were found to decrease with increasing z_o^i, and the opposite trend was observed for the inner leaflet. Again, the trends can be explained in terms of area mismatch; as lipids are added to the outer leaflet, increased packing of lipids slows the diffusion rates, and vice versa for the inner leaflet. Unlike with splay angles, it is not expected that the outer and inner leaflet trends should overlap at the correct z_o. Diffusion rates in spherical systems are strongly attenuated by boundary effects, with the inner leaflet (with a smaller surface area) experiencing a larger reduction in diffusion compared to an infinite planar system[247].

In sum, the effects of using an incorrect z_o^i are small but measurable, and are consistent with effects attributable to area per lipid mismatch. The range of z_o^i values explored was between 0 and 2 nm, whereas the calculated z_o values for 3, 4, and 5 tail-bead lipid models all fall within +/- 0.15 nm of a central value of roughly 1 nm, a range in which errors associated with z_o are exceedingly small (**Figure 5.4**). Therefore, an estimate

of 1 nm will (at least for Martini systems) be sufficiently accurate for most simulation purposes, circumventing the need to directly calculate z_o. For those simulations requiring extreme precision of the area per lipid, or for investigations that directly involve pivotal plane theory, the following section may provide additional insight.

Predicting z_o from flat bilayer properties

Calculating z_o via interleaflet equilibration of curved membranes requires relatively large systems and some computational expense, so ideally one would like to be able to estimate z_o with reasonable accuracy from examining flat bilayer properties that are more easily assessed. To test this possibility, we calculated z_o locations for a number of phosphatidylethanolamine (PE) and phosphatidylcholine (PC) lipids in the Martini forcefield using our cylinder-based equilibration protocol and performed simulations of flat bilayers with lipids of the same composition (see list of simulated systems in **Table 5.S1**). We calculated the average phosphate bead depths relative to the center of the bilayer, and compared them to our calculated z_o depths (**Figure 5.5**). We found a linear relationship between phosphate and z_o locations when comparing lipids with the same head group but varying acyl chain compositions. **Figure 5.5B** shows the z_o locations as fractional depths with respect to the phosphate location. We found that the z_o locations of PC lipids were consistently located at around ~50% of the phosphate depths, while the z_o of PE lipids were found closer to ~43% of the phosphate depth. The use of phosphates as an indicator of membrane thickness is common but arbitrary, so we performed the same analysis using the first acyl tail bead proximal to the glycerol groups (**Figure 5.S4A**), and found a similar trend.

Experimental work[248] and atomistic simulation[49] of H_{II} phases suggest that the pivotal plane of lipids lies close to the level of the glycerol moiety, roughly 2/3 of the distance from the bilayer center to the phosphate coordinate. In contrast, we find that z_o values lie closer to the center of the monolayer (defined relative to phosphate depth), in agreement with Wang and Deserno's calculation of z_o for DMPC. They suggested that such mismatch may be due to the coarse-grained nature of the Martini forcefield. The consistency of our results across a number of lipid types supports this suggestion.

Wang and Deserno noted that the z_o location of DMPC closely aligned with a specific peak in the lateral pressure profile (LPP), and suggested LPP features as potential predictors of z_o location[87]. To test this possibility, we calculated LPPs for all of our flat lipid systems (**Figure 5.S5**). Each lipid's z_o location was found in the general region of the first positive peak of the LPPs before the negative peak that represents interfacial tension. However, the shapes of the LPP peaks for many of the lipids are not as well-defined as that of DMPC, making a quantitative description of the positive peak unreliable. To quantify z_o location in the context of LPPs, we compared calculated z_o locations to two characteristics resolvable in all of the LPPs: i) the crossover point from positive pressure to negative pressure, and ii) the interfacial negative pressure peak (**Figure 5.S4B-C**). As with the phosphate positions, we found that the z_o positions were located at certain fractions of the LPP features, but that the PC and PE trends were consistently different. Therefore, while z_o positions can be found in similar regions of the LPP, a consistent quantitative extraction of z_o location from LPPs suffers from the same head-group dependence as estimating z_o from simpler metrics such as phosphate positions.

Application to all-atom systems

To determine the suitability of BUMPy for application to atomistic systems, we constructed a vesicle composed of DPPC with a 5 nm radius and performed a simulation using the CHARMM36 force field. The vesicle was stable over the course of a 50 ns simulation (**Figure 5.S6**), with an average radius of 5.32 +/- 0.26 nm. We note that determination of the pivotal plane using pore-based equilibration is likely computationally unfeasible for all-atom systems, and that the pivotal plane of an atomistic lipid likely does not match up with its CG counterpart. However, the pivotal plane of lipids can be calculated experimentally from inverted hexagonal phases[248], so using experimental estimates of z_o may be a plausible starting point.

Shape repository

The current list of shapes available in BUMPy are listed in **Table 5.1** and selected images are shown in **Figure 5.6**. Once a template is created, users can apply it to build the specified geometry with any combination of size parameters and any lipid composition simply by specifying the parameters at the command line interface. The strategy of creating complex shapes from simple building blocks allows us to rapidly create these templates and add them to the repository.

The capabilities of BUMPy have some overlap with existing software. For example, the ability to generate vesicles is also available in the CHARMM-GUI (but only for Martini lipids), and cylinders can be generated with PackMol. BUMPy is able to generate shapes

that have been used in previous simulations but were generated either using in-house scripts or by application of forces to the simulation. These include capped cylinders[99], buckles[79,83,85,89] and tethers[105,106] (similar to the double_bilayer_cylinder shape in the BUMPY repository). Additional shapes in the repository may not have a direct biological counterpart, but may be of interest in reductionist studies of curvature effects on membrane properties.

Table 1. Current list of shapes available in BUMPy repository, with associated geometric parameters and shape-specific notes.

Shape	Parameters	Notes
Semisphere	R_sphere	basic building block
Cylinder	R_cylinder L_cylinder	-basic building block -quarter-cylinder used as a junction between orthogonal structures
partial_torus	R_torus R_tube	-basic building block -quarter-torus used as toroidal junction
Flat_bilayer	X_dimension Y_dimension	-basic building block
Sphere	R_sphere	
Torus	R_torus R_tube	R_torus > R_tube
Capped_cylinder	R_cylinder L_cylinder	-cap radius is necessarily equal to the cylinder radius
Double_bilayer_cylinder	R_cylinder L_cylinder R_junction L_flat	L_flat >= 2 * (R_cylinder + R_junction)
Semicylinder_plane	R_cylinder L_cylinder R_junction L_flat	L_flat > 2 * (R_cylinder + R_junction)
Semisphere_plane	R_sphere R_junction L_flat	L_flat > 2 * (R_cylinder + R_junction)
Buckle	R_buckle L_buckle	L_buckle is the length in the flat dimension

Enforcing geometry using dummy particles

The equilibrium shape that a bilayer adopts is governed by the minimization of bending energy, which has been accurately described by the Helfrich Hamiltonian that has parameters of spontaneous curvature, bending rigidity and Gaussian curvature modulus[8].

Therefore if a bilayer is constructed into a shape which does not represent a minimum energy configuration, the initial configuration will be unstable . In an unrestrained system with high total or gaussian curvature, or those with lipid compositions whose intrinsic curvature preferences do not match the curvature environment, the shape will deviate from the initial configuration towards lower energy states. Indeed, a number of the shapes in our current repository either collapse upon release of position restraints, or have significant deviations in their equilibrium geometry, despite high accuracy in the estimate of the pivotal plane position.

Observation of the relative stability of various membrane geometries is an interesting topic of study in and of itself, but there may be scenarios in which it is desirable to enforce a geometry on a bilayer. Recently, Yesylevskyy and colleagues developed an approach to maintain curved lipid morphologies, in which membranes are bracketed on both sides of the bilayer by a grid of dummy particles, which only interact with the hydrophobic core of the bilayer[120]. With judicious selection of the distance of the dummy particle grid with respect to the bilayer center, and selection of the distance at which the repulsive interaction occurs, one can set up a system in which the dummy particles only interact with the bilayer when it deviates from its ideal geometry.

We have added an option to BUMPy that allows the user to add a grid of dummy particles to each side of the bilayer with a desired grid spacing and distance from the bilayer center. We have tested this implementation in a coupled semicylinder-bilayer system, and confirmed that the dummy particle setup results in maintenance of the previously unstable geometry (**Supplemental Video 1**). We note that while Yesylevskyy and colleagues[120] observed no significant artifacts in bilayer properties when the dummy

particle setup are applied to *flat* bilayers, there is as of yet no such study of the impact of dummy interactions in curved systems. We intend to test for any artifacts arising from the dummy particle protocol in future work.

Discussion

BUMPy is fast, versatile, and easy to use. To generate curved lipid systems with accurate lipid areas, the user must only provide an area-equilibrated flat bilayer and a value for the pivotal plane location. We note that this bilayer need not be minimized or equilibrated in the typical simulation sense, as the only quantity of the bilayer that must be accurately represented is the lateral area per lipid. Thus, if that quantity is known an unequilibrated bilayer with the correct area per lipid can be generated using *insane.py*[136] or some other tool and then used as an input for BUMPy.

Obtaining a reasonable estimate for z_o is therefore the largest obstacle to accurately creating curved systems. Importantly, we have demonstrated that the z_o values of a number of Martini lipids are clustered around 1 nm, and within that range, errors associated with misestimating z_o are quite small. Thus, for most cases (using Martini), no additional simulations are required to estimate z_o, and BUMPy users can proceed with an estimate of ~1nm. On the other hand, simulations for which extreme accuracy of area is required may need a more rigorous estimate z_o, in which case the pore-based equilibration protocol may be employed.

To calculate z_o when using models that do not display fast transverse relaxation, one must observe equilibrium interleaflet ratios using pore-based protocols (Wang and

Deserno put forward an additional method using buckled bilayers[87]). However, once z_o is known it can be applied to build systems with any shape or size. We have determined z_o for a small number of lipid types in the Martini forcefield (**Table 5.S2**), and will add to the repository over time. In addition, as the pivotal plane of more lipids become available, a systematic analysis of the effect of chain length, saturation and head group size may reveal trends that one can use to predict z_o from chemical principles.

One system type for which pore-based z_o measurements cannot be directly made are membranes with intra-leaflet heterogeneity (i.e. systems with multicomponent monolayers). The calculation of z_o using the method of Wang and Deserno assumes that the intrinsic area per lipid is constant between the leaflets. In a heterogeneous system with pores, lipids will partition to minimize the curvature frustration energy, disrupting the desired component concentrations in each leaflet. In these cases, one can estimate the z_o as a concentration-weighted average of the individual components. Alternatively, one could estimate z_o from H_{II} phase simulations and different hydration levels[45,49].

If one has a reasonable estimate of z_o for a given system, the pore-based equilibration procedure can be skipped, which has advantages beyond simply minimizing computational expense. One potential benefit occurs when simulating heterogeneous and/or asymmetric bilayers. Lipids in heterogeneous vesicles have been demonstrated to partition differentially between the inner and outer leaflets to minimize curvature frustration, leading to asymmetric concentrations between the leaflets[97]. While this state represents the energy minimum of the system with respect to curvature energetics, it is sometimes the case that researchers wish to simulate systems with fixed lipid ratios, for instance when the simulation attempts to reproduce an asymmetric biological membrane

composition[249]. Allowing interleaflet flipflop in a heterogeneous system inevitably leads to changes to the desired leaflet compositions.

Similarly, some of the shapes that are of interest for simulations separate the solvent in the system into multiple compartments, such as a vesicle. It may be desirable to simulate the separate water compartments with different conditions, varying factors such as ionic strength, pH, or osmotic pressure. In such situations, adding a hydrophilic channel connecting the compartments complicates maintaining those differences.

One potentially limiting factor of BUMPy is the assumption that the equilibrium area of a lipid in a flat bilayer is equivalent to that in a curved system. The consistency of z_o measurements across a variety of curvatures (**Figure 5.3**) supports this assumption, but it may not hold at the most extreme curvatures. In addition, some lipids display unique characteristics in the presence of curvature. For example, polyunsaturated lipids in the outer membrane of vesicles have been shown to fold their acyl chains back up into the membrane, potentially affecting the area per lipid in that leaflet[97]. Such effects of individual lipid types are not accounted for in the area-matching implementation of BUMPy, and should be considered carefully when setting up simulations.

While the coordinate transformation-based implementation of BUMPy leads to complete flexibility of force field and lipid type, BUMPy currently only allows creation of bilayer-organized structures where individual molecules are assigned on a leaflet basis. In the future, BUMPy could be extended to applications involving monolayer-based phases such as micellar or inverted-hexagonal phases, as the concept of the monolayer pivotal plane still applies in these systems for estimating initial lipid densities. In principal, a monolayer based approach would allow for creation of non-lipid materials which the

simulation field has explored, such as carbon nanotubes[250]. A final consideration is that BUMPy does not currently support embedded proteins. A tool already exists with facility for embedding (single or multiple) proteins into both flat and curved membranes[251], which we suggest should be used for such purposes after generating curved lipid-only systems using BUMPy.

Conclusions

We have presented BUMPy, a tool for the creation of starting configurations for MD simulations of curved bilayers. In addition to being fast and easy to use, BUMPy allows for complete flexibility of membrane composition and is forcefield independent. The use of small, simple geometric building blocks to model more complex topologies allows for generation of a wide range of biophysically relevant morphologies, many of which (to our knowledge) lack any other published implementations, and is an easily extensible approach to adapt to future needs. Through z_o-based area estimation we provide a quantitative approach to populating individual leaflets with the correct number of lipids, and in this work have elucidated the extent to which lipid packing inaccuracies affect some membrane properties.

Supporting information

The supporting information contains example usages, description of nonlinear coordinate rescaling procedure, performance metrics for BUMPy, time-course analysis of z_o convergence, theoretical calculations of lipid areas as a function of z_o, analysis of z_o

locations with respect to different bilayer observables, LPPs for a number of lipids in the Martini forcefield, a video demonstrating the effect of dummy particles on membrane shape, a table detailing all simulations involved in this work, and a table listing the current repository of known z_o locations for a number of lipids in the Martini forcefield.

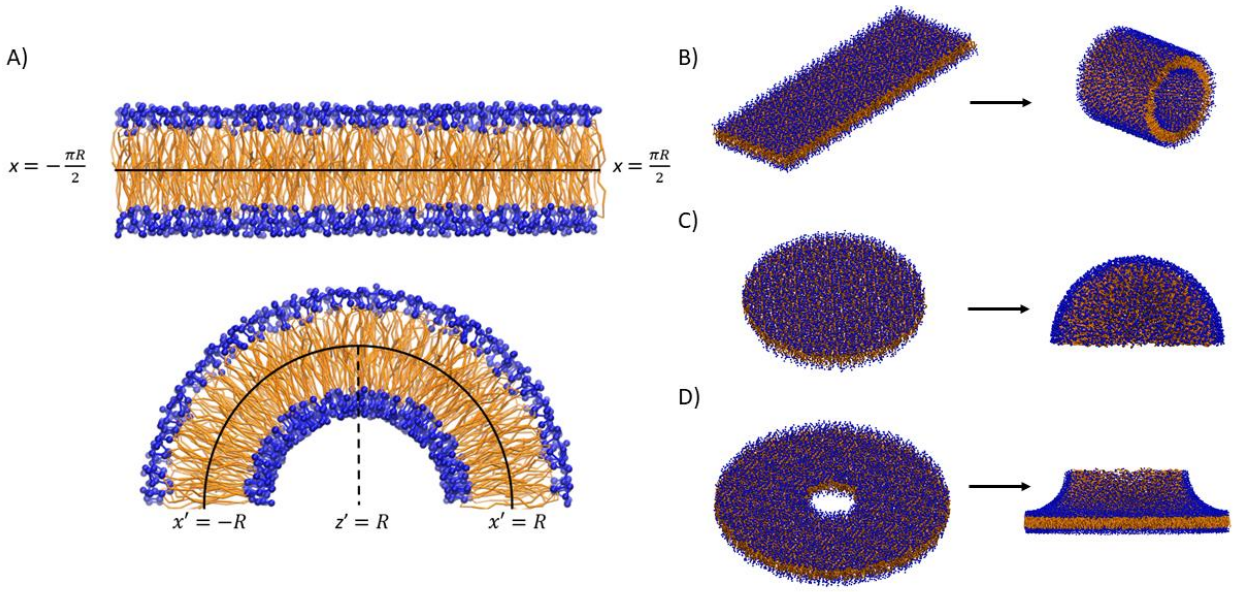

Figure 5.1. **The basic building blocks of BUMPy**. A) Transformation of a flat patch of bilayer into a cylindrical geometry. The *x* dimension of the flat bilayer corresponds to the circumference of the curved shape. B) Side view of the transformation from a rectangular patch of bilayer to a cylinder. C) Transformation of a circular patch of bilayer to a hemisphere. D) Transformation of a hollow disc into a toroidal junction.

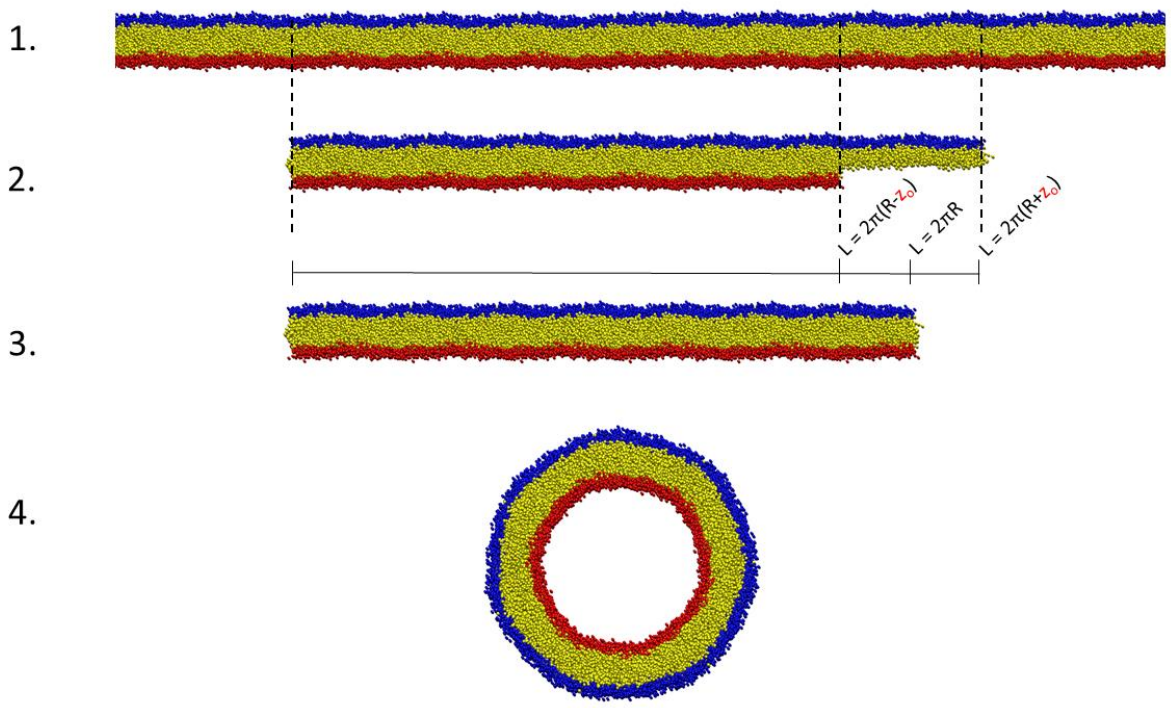

Figure 5.2. Area matching in BUMPy. 1) An initial bilayer patch is larger than the required dimensions. 2) Slices of the original bilayer are taken separately by the top and bottom leaflets to match their specific area requirements, dependent on the requested geometry and z_0 location. 3) The top and bottom leaflets are scaled laterally to occupy the size corresponding to the requested geometry. At this point, the density of lipids in the top leaflet is higher than in the original bilayer, and the density in the bottom leaflet is lower than in the original bilayer. 4) The geometric transformation takes place.

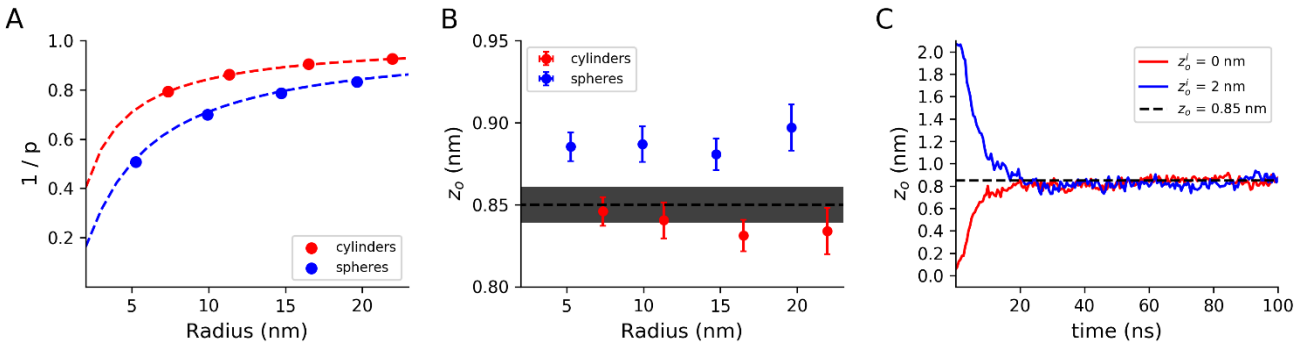

Figure 5.3. **Validation of pivotal plane-based area calculations.** All bilayers were composed of 100% DMPC. Error bars represent 95% confidence intervals estimated from standard errors A) Relationship between interleaflet ratios and radii for spheres and vesicles. The red and blue dashed lines are theoretical contours to z_o=0.85 nm for cylinders and spheres, respectively. *x* and *y* error bars are smaller than markers. B) Calculated z_o locations after equilibration for vesicles and cylinders. The dotted line is set at z_o = 0.85 nm, with grey shading to indicate 95% confidence interval reported by Wang and Deserno. C) Time-course

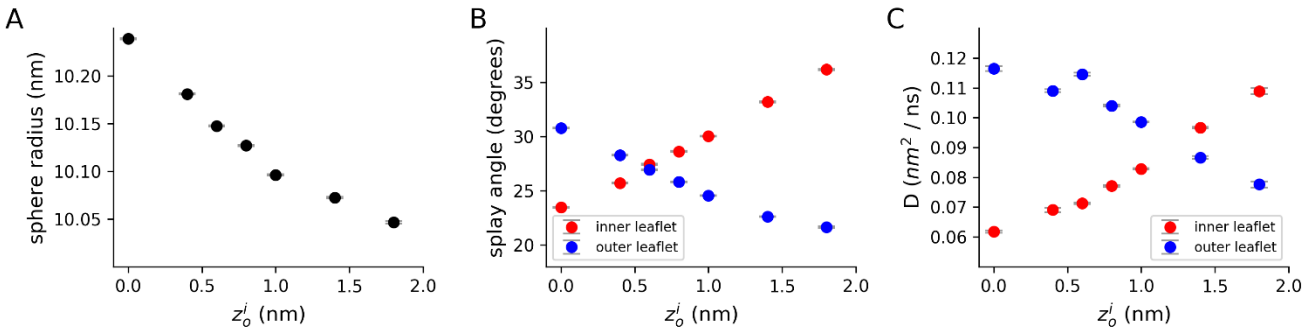

Figure 5.4. **Effect of z_o^i on vesicles properties**. Spherical vesicles were created using a range of z_o^i estimates, and simulated for 150 ns without allowing pore-based interleaflet equilibration. A) Equilibrated radius of vesicles. B) Splay angle between the phosphate beads and terminal tail beads. Splay is calculated as the angle between the outward normal vector and the vector pointing from the phosphate to the tail bead for the inner leaflet. For the outer leaflet, the inward normal vector is used. C) 2-dimensional diffusion coefficients for lipids in the inner and outer leaflets, calculated from the linear fit of a mean-squared displacement plot at various time lags.

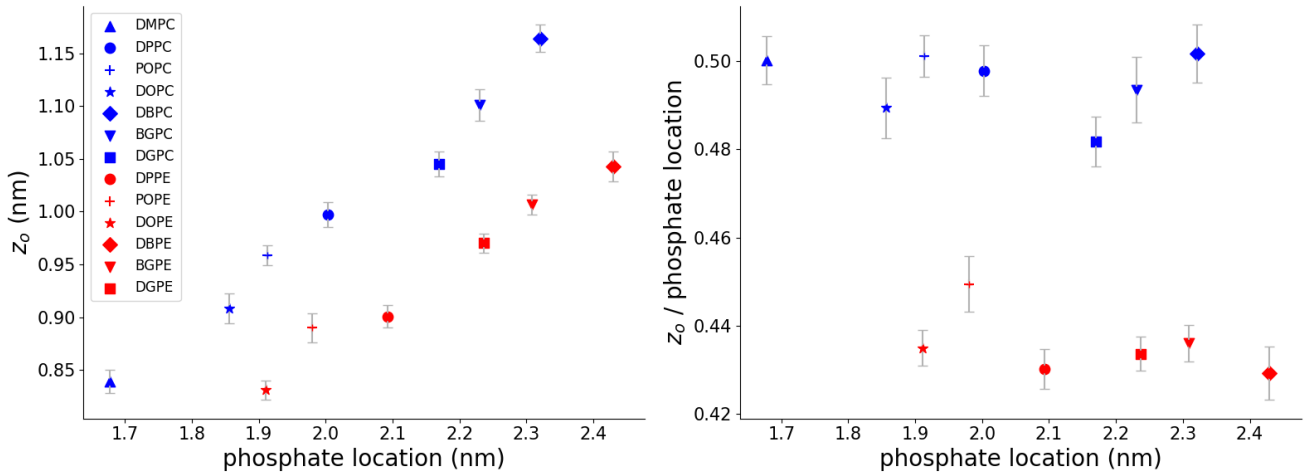

Figure 5.5. z_o for different lipids in the Martini force field. A) Relationship between phosphate positions and z_o positions. B) Same data as panel A, with the z_o locations plotted as fractions of the phosphate positions. In both figures error bars are 95% confidence intervals estimated from standard errors. Errors in the x dimension were smaller than the marker sizes.

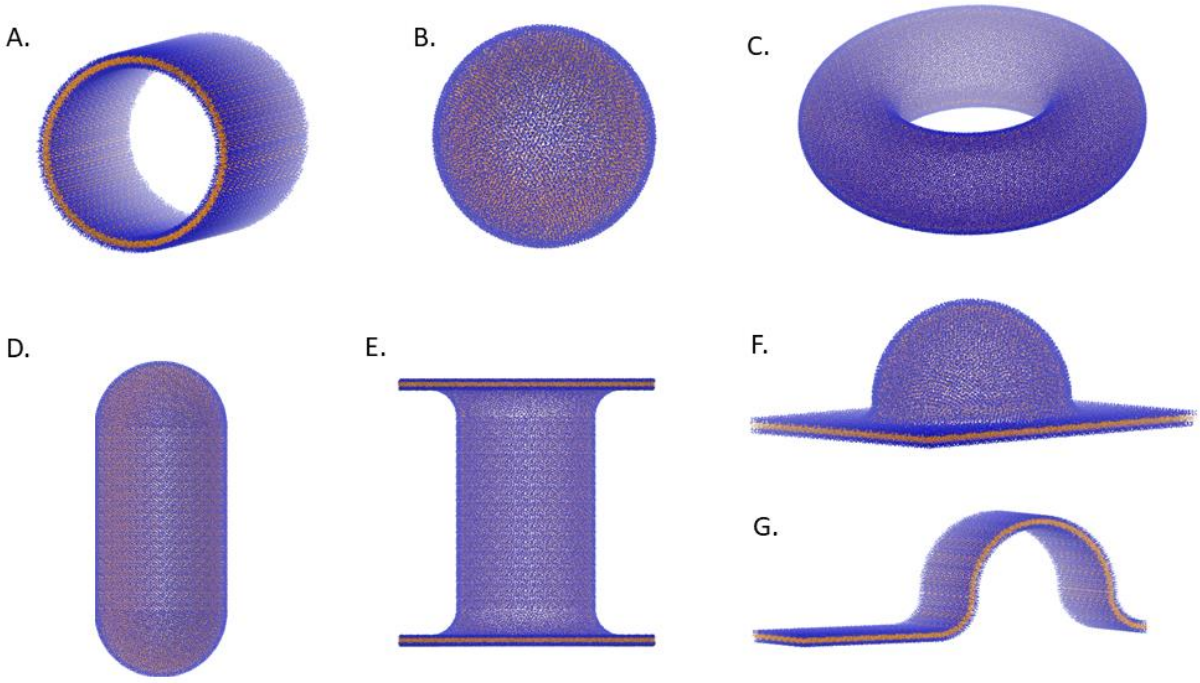

Figure 5.6. Examples of shapes in the BUMPy repository. A) Cylinder. B) Sphere. C) Torus. D) Capped cylinder. E) Double-bilayer-cylinder. F) Semisphere-plane. G) Semicylinder-plane.

BUMPy: A model-independent tool for constructing lipid bilayers of varying curvature and composition

*Kevin J. Boyd and Eric R. May**

Department of Molecular and Cell Biology, University of Connecticut, Storrs, CT 06269, United States

Supporting Information

Supporting Information contains example command line usage of BUMPy, description of the nonlinear coordinate rescaling procedure, six figures, one video and two tables.

Sample BUMPy usage

Create a cylinder with length of 20 nm, radius of 10 nm, using a z_o value of 1 nm:

```
bumpy.py -f flat_input.pdb -o cylindrical_output.pdb -z 10 -s cylinder -g r_cylinder:100 l_cylinder:200
```

Create the same system, writing out a basic GROMACS-compatible topology and index file

```
bumpy.py -f flat_input.pdb -o cylindrical_output.pdb -n index.ndx -p topol.top -z 10 -s cylinder -g r_cylinder:100 l_cylinder:200
```

Create the same system, adding a surrounding grid of dummy particles, with the spacing between the dummy particle leaflets set to 6 nm, and the intra-leaflet dummy particle spacing set to 0.5 nm

```
bumpy.py -f flat_input.pdb -o cylindrical_output.pdb -n index.ndx -p topol.top -z 10 -s cylinder -g r_cylinder:100 l_cylinder:200 --gen_dummy_particles --dummy_grid_thickness 60 --dummy_grid_spacing 5
```

A more comprehensive set of examples can be found in the BUMPy repository

Nonlinear coordinate rescaling procedure

A problem arises when transforming a flat surface into a curved surface which has two non-zero principal curvatures. This can be realized when considering transforming a circular disc into a hemisphere. Area conservation will require $A_{disc} = A_{hemi}$ (i.e. $\pi r_{disc}^2 = 2\pi r_{hemi}^2$), while the distance from the hemisphere pole to rim (at $\varphi = \frac{\pi}{2}$) should seemingly match the disc radius, implying $r_{disc} = \frac{\pi}{2} r_{hemi}$, which is incompatible with the area

conservation relationship. This can be understood because the area of a spherical cap, subtended by an angle φ, will always be smaller than the area of a disc of radius r_f, when $r_f = \varphi * r_{hemi}$. Therefore a rescaling procedure is required to maintain a constant area density in the curved surface. We elect to perform a rescaling of the flat coordinates and then transform the rescaled coordinates into the curved surface.

If it is desired to generate a hemisphere of radius r_{hemi} containing N particles then each particle occupies an area of A_{hemi}/N. The hemisphere is represented in spherical coordinates $\{r_{hemi}, \theta, \varphi\}$ where r_{hemi} is a constant, $0 <= \theta <= 2\pi$, and $0 <= \varphi <= \frac{\pi}{2}$, with $\varphi = 0$ being the pole of the hemisphere. To perform the rescaling, the φ coordinate can be subdivided into N φ_i values, each corresponding to an equal-area segment (concentric rings around the hemisphere pole). Note that the spacing of φ_i values will be nonlinear, with sparser spacing near the pole and denser spacing near the hemisphere rim ($\varphi=\frac{\pi}{2}$).

The corresponding flat bilayer upon which the geometric transformation will be performed is a circular disc of radius r_{disc} containing N particles, represented in polar coordinates $\{r_f, \theta_f\}$, where $0 <= r_f <= r_{disc}$, and $0 <= \theta_f <= 2\pi$. The radial coordinate will be rescaled (described below) mapping $r_f \rightarrow r_f'$, and the scaled coordinates can be transformed according to

eq. S1

$$r_f' = r_{hemi} * \varphi$$

The nonlinear rescaling proceeds as follows, given a target radius r_{hemi}, and a circular bilayer segment of N particles with initial radii r_f and angular coordinates θ.

1. Calculate N φ_i values in the range $(0, \frac{\pi}{2})$ such that each $d\varphi = \varphi_i - \varphi_{i-1}$ generates a ring of surface area equal to A_{hemi} / N.
2. Map each φ_i to a corresponding r_f' value in the flat segment (eq. S1), ordered from small to large
3. Sort N particles by r_f, ordered from small to large
4. From the ordered lists, replace each radial coordinate, rf, by the corresponding r_f' value
5. Proceed with geometric transformation preserving the angular coordinate, mapping $\{r_f', \theta_f\} \rightarrow \{r_{hemi}, \varphi, \theta_f\}$

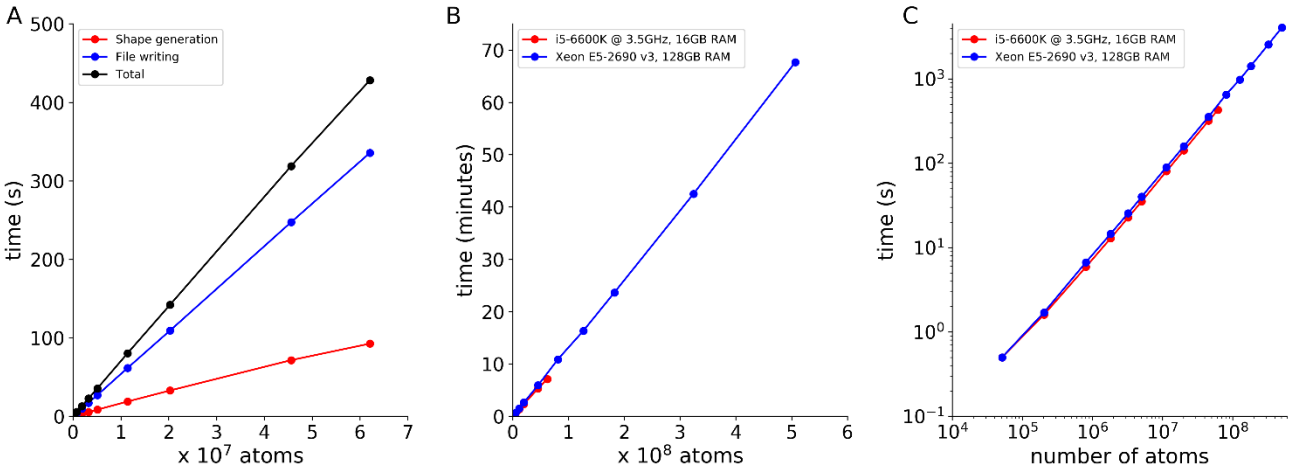

Figure 5.S1. **Performance of BUMPy**. Performance metrics were calculated by using BUMPy to create spheres with increasing radii. A) Performance of BUMPy on a desktop computer with an i5-6600K 3.5 GHz processor and 16 GB RAM. B) Total time taken to build larger systems on a Xeon E5-2690v3 compute node with 128 GB RAM. C) Same data as panel B, plotted on a log-log scale.

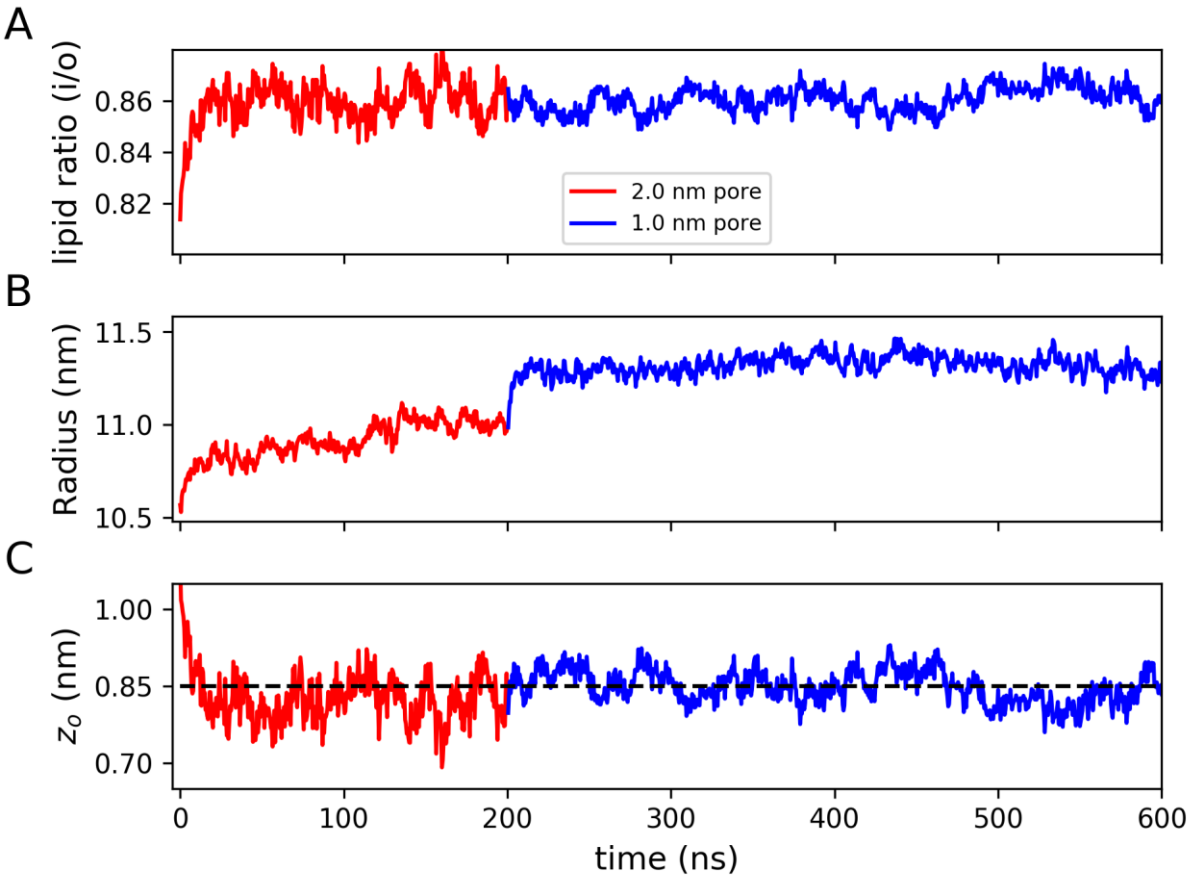

Figure 5.S2. Pore-based equilibration of cylindrical bilayer. Time course of the interleaflet ratio (A), radius (B) and z_o (C), measured in a cylinder built using BUMPy with a 10.0 nm radius with an initial z^i_o=1.0 nm. The dotted line in the bottom panel shows a reference line for z_o=0.85 nm.

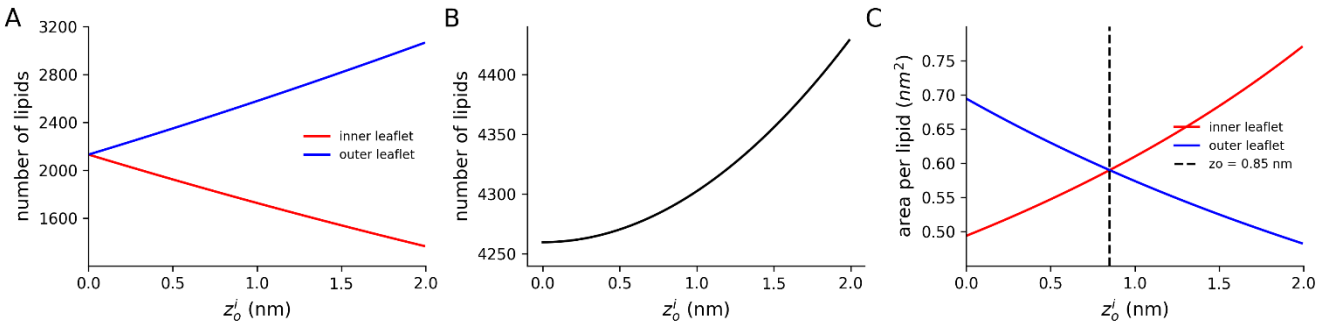

Figure 5.S3. Theoretical leaflet areas for system constructed using different z_o^is. All calculations assume a sphere with *R*=10 nm, built from a flat bilayer with an equilibrium area per lipid of 0.59 nm^2. A) Number of lipids per leaflet over a range of z_o^i estimates. B) Total number of lipids for systems with different z_o^is. C) Resulting area per lipid in each leaflet of the spherical vesicle, assuming no change in radius.

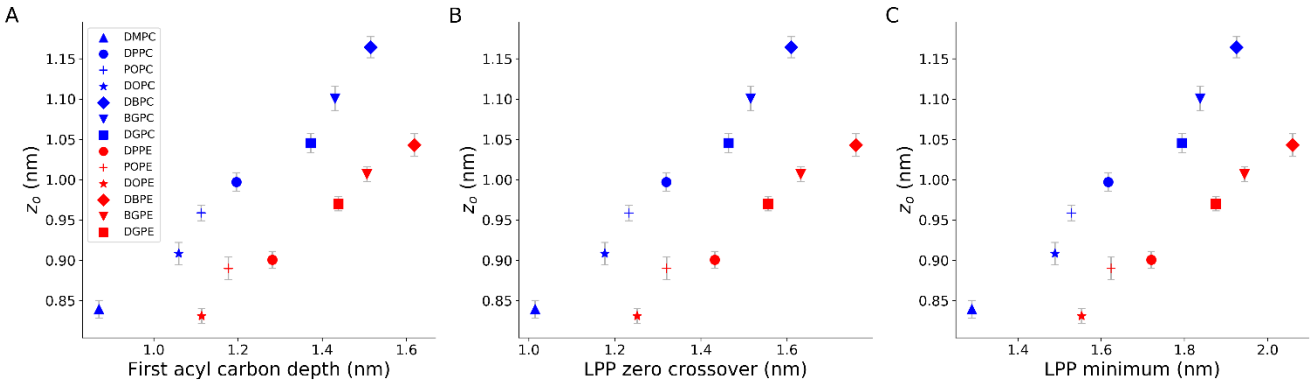

Figure 5.S4. Position of z_o with respect to bilayer features. A) z_o positions plotted against the position of the acyl bead closest to the glycerol groups. B) z_o positions plotted against the position in the LPP which transitions from positive pressure to negative pressure. C) z_o positions plotted against the location of the LPP negative interfacial tension peaks.

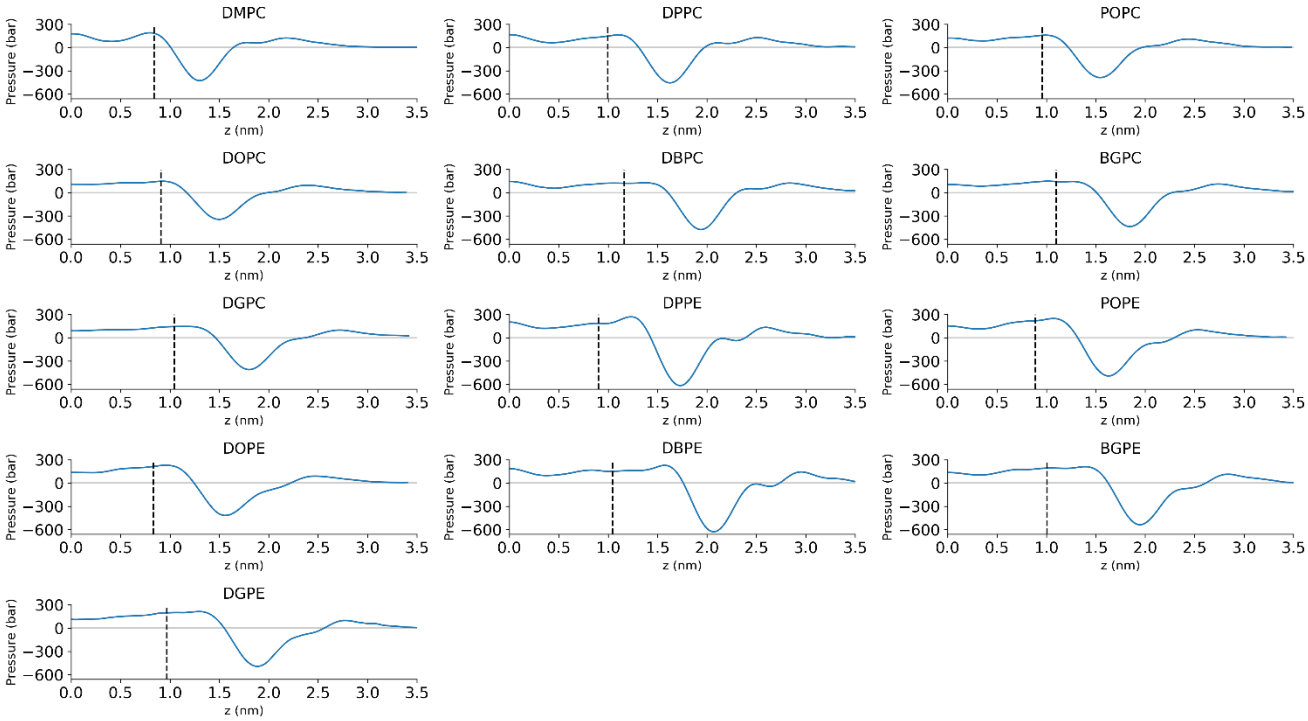

Figure 5.S5. Lateral Pressure Profiles (LPPs) of lipid bilayers at 330 K. LPPs are drawn from the center of the bilayer (z=0) to the solvent. Grey lines indicate 0 pressure. Black dashed lines indicate the z_o locations.

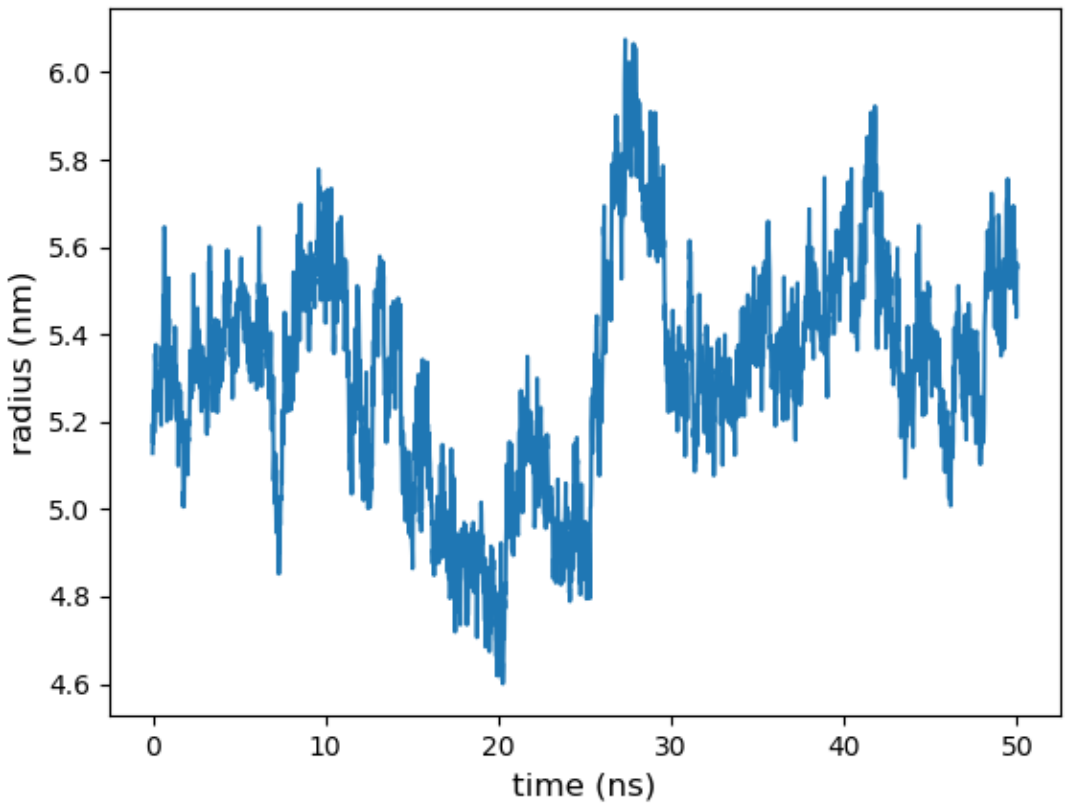

Figure 5.S6: Stability of an atomistic DPPC vesicle. The radius is plotted over the course of a 50 ns simulation. The vesicle was constructed from a pure DPPC bilayer with a target radius of 5 nm, and simulated at 330 K.

Table 5.S1. List of Martini simulations

Lipid composition	Shape	Geometric Parameters	T (K)	Dummy particles
DMPC*	Cylinder	R_cylinder: 5 nm, L_cylinder: 20 nm	300	No
	Cylinder	R_cylinder: 10 nm, L_cylinder: 20 nm		
	Cylinder	R_cylinder: 15 nm, L_cylinder: 20 nm		
	Cylinder	R_cylinder: 20 nm, L_cylinder: 20 nm		
	Sphere	R_sphere: 5 nm		
	Sphere	R_sphere: 10 nm		
	Sphere	R_sphere: 15 nm		
	Sphere	R_sphere: 20 nm		
	Semicylinder-plane	R_cylinder: 10nm, L_cylinder:10 nm, R_junction: 5nm, L_flat:		
	Semicylinder-plane	R_cylinder: 10nm, L_cylinder:10 nm, R_junction: 5nm, L_flat: 20 nm		Yes
DMPC*	Cylinder	R_cylinder: 10 nm, L_cylinder: 20 nm	330	No
DPPC				
POPC				
DOPC				
DBPC				
BGPC**				
DGPC				
DPPE				
POPE				
DOPE				
DBPE				
BGPE**				
DGPE				
DMPC*	Flat	100 lipids per leaflet	330	No
DPPC				
POPC				
DOPC				
DBPC				
BGPC**				
DGPC				
DPPE				
POPE				
DOPE				
DBPE				
BGPE**				
DGPE				

*DMPC and DLPC are equivalent in the Martini lipid repository

**The BG prefix is not in the standard Martini lipid repository. The tails of BGPC and BGPE are 5 beads long, with one tail fully saturated, the other tail with an unsaturated bead at position 3.

Table 5.S2. Current list of calculated z_os, T=330K

Lipid	z_o (nm)	±95% confidence interval
DMPC*	0.84	0.011
DPPC	1.00	0.012
POPC	0.96	0.010
DOPC	0.91	0.014
DBPC	1.16	0.013
BGPC**	1.10	0.015
DGPC	1.05	0.012
DPPE	0.90	0.011
POPE	0.89	0.014
DOPE	0.83	0.009
DBPE	1.04	0.014
BGPE**	1.01	0.010
DGPE	0.97	0.009

*DMPC and DLPC are equivalent in the Martini lipid repository

**The BG prefix is not in the standard Martini lipid repository. The tails of BGPC and BGPE are 5 beads long, with one tail fully saturated, and the other tail with an unsaturated bead at position 3.

Chapter 6: Conclusions and Future Directions

Conclusions

The work presented provides key molecular observations in studies of membrane curvature that are relevant to our understandings of both biophysical phenomena and biological mechanisms. With a novel application of a buckling protocol, we were able to show the effect of cardiolipin incorporation on the mechanics and curvature propensities of model bilayers. Within this setup, we observed partitioning of cardiolipin to regions of negative curvature, in a manner different than phosphatidylethanolamine, another conical lipid. The uniqueness of cardiolipin in inducing these effects and in its strong curvature preferences may have direct impact on the function and structure of mitochondrial membranes.

The key role of cardiolipin was then further emphasized in studies of monolysocardiolipin, the phenotypic signature of the metabolic disease Barth syndrome. Through comparative atomistic simulations we discovered significant differences in head group dynamics between cardiolipin and monolysocardiolipin, and characterized the new hydrogen bonding patterns arising from the lysolipid hydroxyl. In addition to the molecular differences, we uncovered important bilayer-scale reductions in acyl chain exposure that could potentially disrupt binding of peripheral proteins. Through coarse-grained buckling simulations, we demonstrated that the unique curvature modulation tendencies of cardiolipin are not present in monolysocardiolipin, and that monolysocardiolipin displays greatly reduced partitioning to regions of negative curvature. These findings may directly correlate to the morphological aberrations present in mitochondria from cells with the Barth syndrome mutation.

The relationship between mitochondrial membrane composition, structure, and function was further explored with a variety of molecular dynamics techniques. Membrane structures more closely mimicking the mitochondrial cristae topology were created and held in place using a novel application of a dummy particle-based protocol. In a method analogous to our buckling protocol, we observed cardiolipin partitioning to negatively curved regions of the membrane, with interesting aggregation trends in regions with both positive and negative Gaussian curvature. Extending the application of our dummy particle protocol, we were able to observe points of stress within these complicated curved structures, and showed that incorporation of cardiolipin greatly decreased the instability of mitochondria-mimicking morphologies, compared to PC and PE containing bilayers with the same shape.

We progressed further towards accurate modeling of mitochondrial membranes by incorporating ATP synthase, and extending the work of Anselmi[71] and coworkers exploring the energy landscapes of ATP synthase conformation and self-interaction. We demonstrated that the proposed long-range interactive force between ATP synthase dimers is nullified in a curved environment, supporting the original authors claims that the observed interaction were curvature mismatch-mediated. Using umbrella sampling upon a rotational coordinate, we showed that ATP synthase dimers can sense their local curvature environment, and orient to best minimize curvature frustration in interesting ways.

The work presented in Chapters 2-4 as well as other work within the field highlights the importance of simulating membranes in their natively curved states. To improve the scientific infrastructure in this field, we developed BUMPy, a tool to rapidly and flexibly

generate curved membranes of (nearly) arbitrary shape and composition. We detailed the technical challenges in building such a tool and the construction and amalgamation of simple building blocks to create more complicated morphologies. Using simulations of vesicles and cylinders with varying radii, we showed that equilibrium interleaflet area differences can be accurately estimated using a pivotal-plane based approach.

In sum, in this thesis we present a number of novel techniques and analyses to study curvature-based phenomena using molecular dynamics simulations. Our results provide insight to interesting biophysical problems while simultaneously exploring the relevant biology of mitochondrial shape and function.

Future Directions

The work performed could be added to and improved upon in a number of important ways. One useful avenue of improvement would be further validation of the models used. For the bulk of these studies, a decision was made to use the Martini force field[27]. The reason for this decision was that the mesoscopic nature of our simulations limits the time scales accessible for simulation, given the current computational resources available. The Martini forcefield is quite popular for large-scale lipid systems[252], and indeed the tuning of the Martini interaction matrix was informed by calculations of curvature-related constants of several key lipids[27]. Still, the coarse-grained nature of the model may broaden out important molecular features for the systems studied. While a full reproduction of many of these studies in atomic detail remains infeasible, reproducing a smaller subset of these simulations with an atomic resolution force field would improve the robustness of our work.

Another intriguing area of extension for our mitochondrial membrane studies would be further incorporation of *in situ* biological details. Our original simulations of buckled membranes were by necessity quite reductionist in the level of details, and while the work of Chapter 4 improves on this from a membrane geometry perspective, we can still point to some important details that were left out. One physiological occurrence that has yet to be studied by us is the asymmetric nature of lipid composition across the leaflets of a bilayer. The inner mitochondrial membrane is highly asymmetric in cardiolipin concentration; for instance[205,209]. This transverse asymmetry could have interesting effects on the curvature-based mechanics of mitochondrial bilayers.

Another important biological context that we have largely ignored in our coarse-grained studies is the effect of solvent composition. pH gradients exist between the matrix and intermembrane space in the vicinity of ATP synthase. While these differences do not manifest in significant *solution* charge differences on the volume scale of MD simulations, the effects on titratable groups can be enormous. Indeed, localized pH gradients have been shown to induce cristae-like invaginations in cardiolipin containing vesicles[178]. One way to model pH differences in our systems would be to vary the charge on the cardiolipin head groups between -1 and -2, with different concentrations of each species between the leaflets.

Similarly, we largely did not explore the effect of ion concentrations in solution. In particular, divalent cations have been shown to induce H_{II} behavior in cardiolipin containing bilayers[172]. We have been limited in this respect by the resolution of the Martini model – large ions represent both the ion and its first solvent shell, and so we cannot

accurately reproduce molecular binding of ions to head groups. An atomistic model would be more able to explore solution salt effects.

An important topic of our studies is the seemingly unique response of cardiolipin to curved bilayers. A number of interesting topics could be explored in this regard. First is the mechanism of cardiolipin partitioning. It has been proposed that lipid sorting is dampened on an individual molecular basis by the entropic cost of self-organization, and that lipid-lipid and lipid-protein interactions are essential for curvature sensing[189]. Our buckling studies seem to contradict this idea, as we demonstrate enrichment of cardiolipin in negatively curved monolayers without self-interactions. To further validate our findings, we could conduct simulations with varying concentrations of cardiolipin. If self-interaction is essential for partitioning, we should see reduction of partitioning for individual cardiolipin molecules with reduced overall concentrations.

A potentially related area of exploration is the study of the molecular characteristics of cardiolipin itself. The unique double-phosphate headgroup of cardiolipin confers a unique wedge-like shape (as opposed to a more isotropic cone). We speculate that in response to curvature cardiolipin could orient itself such that the wedge geometrically fits into the membrane morphology. To explore this, a series of cylindrical simulations could be run; if cardiolipin can sense curvature in this manner, one would expect some rotational anisotropy with respect to the long axis of the cylinder induced by curvature, and perhaps tunable with the extent of curvature. Of course, such an effect could not be observed in a spherical membrane geometry with equal curvature in all directions, cylinders do have physiological relevance in the modeling of tubular cristae.

The mitochondrial mimicking setups could be further explored as well. The work presented here shows simulations with varied lipid composition but not varied morphology. It would be instructive to simulate these systems while systematically varying quantities such as the cylindrical tube radius and junction radius, and observing the effects on both measured pressures and lipid partitioning. Given the behavior of cardiolipin in the most extremely curved regions of our buckled bilayers, one might expect interesting features to emerge with extreme curvature in our mitochondrial mimicking systems. In addition, we could also study the effects of physiological conditions such as membrane asymmetry, pH and ion concentrations that were also mentioned in regard to the buckling simulations.

Our work on ATP synthase also has several interesting extension points. An interesting observation from biophysical studies is the variety of dimer interface angles that ATP synthase dimers present between species[157]. We speculate that the dimer angle might control the preferred membrane curvature environment of ATP synthase, and the extent of curvature perturbation when ATP synthase is in a mismatched environment. Combined with our observations on the rotational free energy profiles of ATP synthase dimers on cylindrical geometries, we could explore the relationship between ATP synthase dimer angle and imposed mitochondrial morphologies in greater detail.

One more avenue which we have not yet explored is the relationship of ATP synthase with cardiolipin. It would be fascinating to reproduce each of the studies presented in this work with cardiolipin containing bilayers. Indeed, cardiolipin is interesting not just for its general influence on bulk membrane properties, but also for its direct interactions with ATP synthase. It has been demonstrated that cardiolipin has binding

modes with the F_0 rings of ATP synthase[232], and it would be quite interesting to observe if these specific bindings are accompanied by particular concentration patterns in the membrane vicinity of ATP synthase as a membrane “fingerprint” that has been demonstrated to occur with other protein and lipid combinations[69]. One can imagine that these local concentration buildups would be affected by the membrane curvature, particularly with the perturbations induced by ATP synthase in flat or near-flat bilayers.

Finally, there are further improvements to be made to BUMPy. The pivotal plane based protocol could be extended to create nonbilayer shapes such as cubic or hexagonal phases, and extensions could be made to allow embedding of proteins and other macromolecules as can be done in a number of tools such as *insane.py*[136] or the CHARMM-GUI[242].

Appendix A1

Molecular details of the interaction between the soluble domain of tim23 and cardiolipin-containing bilayers

Molecular details of the interaction between the soluble domain of tim23 and cardiolipin-containing bilayers

Abstract

Tim23 is the central component of the TIM23 mitochondrial protein import machinery. The soluble domain of tim23 interacts with multiple binding partners in the intermembrane space, and has been demonstrated to bind favorably to cardiolipin-containing bilayers. To probe the molecular mechanism of cardiolipin specificity, we performed atomistic molecular dynamics simulations of binding of the N-terminal residues of tim23 to membranes with and without cardiolipin. We reproduce the preferential binding behavior of tim23 to cardiolipin, and characterize the molecular details of the bound configuration, pointing out several potential mechanisms of tim23-cardiolipin selectivity. In conjunction with fluorescence-based experiments, we identify a glycine residue that is key to the protein-membrane interaction.

Introduction

The inner mitochondrial membrane is extremely protein dense. The majority of mitochondrial proteins are synthesized in the cellular cytosol, and then imported into the mitochondrion[253]. The Translocase of the Outer Membrane (TOM) complex is responsible for the bulk of transport across the inner membrane[254], and the Translocase of the Inner Membrane (TIM23) complex then transports proteins that are bound for either the inner membrane or the mitochondrial matrix, targeted to these regions through a cleavable presequence[255].

Tim23 is the central protein of the TIM23 transport complex. It consists of an N-terminal soluble domain exposed to the IMS, and a 4-pass integral C-terminal region that forms the main protein transport channel[256,257]. The soluble domain of tim23 (tim23N) in *Saccharomyces cerevisiae* consists of 96 residues and is largely unstructured. It is a promiscuous binder, having demonstrated affinity for the TOM complex[258], other tim proteins[259,260], and protein presequences[261]. Deletion mutants of tim23 are unable to grow at high temperatures[258].

Tim23N also interacts with membranes. An NMR-based study by Bajaj and colleagues show membrane binding sites between residues 1 to 7 and 26 to 46[181]. This interaction is greatly enhanced with membranes in the presence of cardiolipin. The authors propose that an N-terminal “hydrophobic hook” is key to this interaction, consisting of residues 3-5, a hydrophobic trio of Trp-Leu-Phe. This theory was supported with mutation studies – changing all 3 amino acids to serine completely abolished membrane binding.

The goal of this study was to further probe the mechanism of tim23-membrane binding through all-atom molecular dynamics simulations. We begin by demonstrating that MD simulations qualitatively reproduce the trend of increased binding of tim23 to cardiolipin-containing bilayers. With the increased resolution of MD, we confirm the insertion of the hydrophobic hook into membrane interiors. Further, we identify another unlikely residue that is crucial for strong binding, a linking glycine at position 6. Finally, using simulations of pure membrane systems we identify membrane properties that may lead to cardiolipin-based binding enhancement.

Methods

System setup

An extended conformation of the first 20 N-terminal residues of tim23 were generated using the Ad Bax NIH extended conformation tool (https://spin.niddk.nih.gov/bax/nmrserver/pdbutil/ext.html). For a subset of simulations, glycine 6 was mutated to proline using Pymol[262]. All simulations were run using the CHARMM-36 additive forcefield[217,263]. The C-terminal 20th residue was acetylated using the CHARMM-GUI[218] to avoid an artificial c-terminal charge.

The CHARMM-GUI Membrane Builder[242] was then used to generate solvated systems. Tim23N was placed in random orientations with a minimum distance of at least 2 nm from the bilayer through any periodic image. The x and y dimensions were initially set to 8 nm, and the z dimension was on average ~13 nm. Three lipid compositions were created, the first consisting of 100% palmitoyloleyolphosphatidylcholine (POPC). The second and third lipid bilayers were composed of 80% POPC and 20% tetraoleoylcardiolipin (TOCL), with a -1, and -2 head group charge, respectively. Systems were neutralized with sodium chloride and brought to a total ion concentration of 150 mM.

Two additional simulations of bilayers without protein were performed to calculate bilayer properties. One of these simulations was composed of 100% POPC, the other 80% POPC, 20% TOCL (-2). A list of all simulations with protein and lipid compositions can be found in Table A1.1.

Table A1.1. List of simulations*

Protein	Lipid composition	Replicates	Abbreviation
Native	100% POPC	6	POPC
Native	80% POPC, 20% TOCL(-1)	6	TOCL1
Native	80% POPC, 20% TOCL(-2)	6	TOCL2
G6P	80% POPC, 20% TOCL(-2)	6	
None	100% POPC	1	
None	80% POPC, 20% TOCL(-2)	1	

*Native protein is the N-terminal 20 residues of tim23, with an amidated c-terminus. G6P is the glycine to proline mutant at location 6. None indicates protein-less control simulations

Simulation methods:

Systems were simulated using Gromacs 5.0.1 (native tim23 simulations) and Gromacs 2018 (glycine mutant simulations). Systems were minimized with the steepest-descent minimization scheme for 2000 steps. Equilibration of each system was accomplished following CHARMM-GUI suggestions, with a brief NVT simulation followed by successive NPT simulations with position restraints on lipid head groups and the protein.

Production simulations were run using the md integrator with a timestep of 2 femtoseconds. Systems were simulated in the NPT ensemble, with temperature maintained at 303K using the Nose-Hoover[220] coupling scheme with a time constant of 1 ps, and pressure maintained at 1 bar using the Parrinello-Rahman[197] coupling scheme with a time constant of 5 ps and compressibility 4.5 E-5 bar^{-1}. Pressure coupling was

semiisotropic, with the lateral dimensions of the bilayer (x/y) coupled separately form the z dimension. Short range Van der Waals interactions were switched to zero between 1.0 and 1.2 nm using the force-switch method. Short range electrostatics were similarly treated, and long-range electrostatics were calculated using the particle mesh Ewald method.

Analysis methods:

Minimum distances between tim23 and the bilayer were calculated using the gmx mindist tool. Other protein z-coordinate analyses were performed using a combination of in-house python analysis scripts and MDTraj [235] routines. Images were created using VMD[221].

A number of quantities were calculated by discretizing z-coordinate or distance time courses to “bound” or “unbound” states based on a hard cutoff. To avoid false apparent binding and unbinding artifacts due to transient contacts, transitions between states were only counted if a change in state was observed for all frames in a 10 ns window.

Lateral pressure profiles were calculated using Gromacs-LS,[19] a modified version of Gromacs 4.4.5. Positions and velocities were saved every 10 ps. In Gromacs-LS, the PME algorithm cannot be used, and so electrostatics have to be calculated beyond the typical short-range cutoff. A recent publication[56] has demonstrated that for accurate calculation of bilayer properties such as the spontaneous curvature, this cutoff needs to be as large as 3+ nm, but for qualitative assessment a shorter cutoff is sufficient. We chose a cutoff of 2.4 nm as a balance between rigor and computational feasibility.

Defects in lipid-only membranes were assessed using the PackMem tool[264] and custom postprocessing. PackMem works by gridding up the box coordinates with fine granularity (typically, 1A). Moving from the solution to the bilayer in the z dimension, a “defect” is encountered if the first atom encountered is a nonpolar/acyl group, rather than a head group atom. PackMem further discriminates between normal defects and “deep” defects based on the z-coordinate of the defect compared to the glycerol level of the bilayer.

The default PackMem analysis is to calculate the probability that a defect is of a certain size – that is, probabilities are based on the population of defects. Instead, we calculate probabilities as the average fraction of membrane area taken by defects of a given size. This approach allows us to assess absolute differences in defect coverage in the bilayer rather than relative distributions. We further process this data as a cumulative sum of defects up to a given size; that is, the probability at any point on the bilayer surface of finding a defect of *at least* a given size.

Results

Initially, simulations of tim23N with 3 different lipid compositions were performed to reproduce experimental binding trends. We abbreviate these systems as PC (100% POPC), CL^{-2} (80% POPC, 20% TOCL, -2 head group charge), and CL^{-1} (80% POPC, 20% TOCL, -1 head group charge). As an initial indicator of membrane binding, we calculated the minimum distance between the membrane and protein for each system (**Figure A1.1 A, B, C)**. The flat line around a distance of ~.16 nm observed in a number of these simulations is indicative of constant contact with the membrane. Visual inspection

indicated that most to all interactions were occurring between the bilayer and the far N-terminus.

Lipid composition had a strong impact on the binding behavior. In both the CL^{-1} and CL^{-2} simulations, once the protein bound to the membrane it did not typically dissociate, whereas in the PC system some trials underwent multiple binding and unbinding events. Each trial of both the CL-1 and CL-2 systems (12 trials total) ended with tim23N bound to the membrane, while after 500ns for the PC system tim23N was found bound to the membrane in 3 of the 6 simulations.

Figure A1.1D displays a representative snapshot of the bound state at the end of a CL^{-2} simulation. The sidechains of the putative hydrophobic hook (W3, L4, F5) were inserted into the hydrophobic core of the bilayer, with the backbones of residues 1-5 horizontal at the bilayer interface. At G6, the peptide kinks upward out of the bilayer.

Visual inspection revealed that not all binding events assumed this posture. Particularly, in transient binding events of the PC system, the deepest point of insertion occurred at the N terminus with M1 and S2, with no hydrophobic sidechain insertion. From this we hypothesized that sidechain insertion is a prerequisite for stable membrane binding. To quantify the extent of binding, we discretized the binding time courses into three states: an unbound (U) state, when the minimum distance between the membrane and protein was greater than 0.2 nm; a loosely bound state (L), where the protein was in contact with the membrane, but has not inserted its hydrophobic hook; and a tightly bound (T) state, in which at least one of the hydrophobic residues is inserted, with insertion defined as the center of mass of the sidechain positioned below the average

lipid phosphate z coordinate. A smoothing procedure was applied to avoid spurious binding/unbinding artifacts based on close but non-binding encounters (see methods).

Discretization of the distance series closely tracked the actual binding behavior (**Figure A1.2**) in all cases, and allowed for assessment of the impact of side chain insertion. **Figure A1.3** summarizes the binding time courses for each simulation. Tight binding was observed in 10 of the 12 simulations with bilayer containing cardiolipin, and in 3 of the 6 PC simulations. Regardless of lipid composition, in each system where tight binding occurred, the protein did not dissociate from the membrane. Likewise, in the PC simulations where binding and then unbinding events occurred, these binding events were stuck in the U state.

In our simulations, tim23 had similar membrane encounter rates regardless of membrane composition, measured by mean first encounter time (**figure A1.4)**. This makes it unlikely that enhanced tim23 binding to CL-containing bilayers is due to enhanced long-range attraction though the limited scale of our systems prevents rigorous analysis of the behavior of tim23 in the vicinity of the bilayer.

A second possibility is that localized effects facilitate tim23 binding. In this case, tim23 binding would likely be dependent on local CL concentration. To explore this possibility, we calculated the local concentration of CL around the hydrophobic hook of tim23 within specific radii, and within 10 ns of loose and tight binding events (**figure A1.5**, top and bottom respectively) for the TOCL2 systems. We did not see enhanced CL concentrations around the protein, and in fact observed reduced CL concentration in the most immediate vicinity of the protein, perhaps due to the larger head group size of CL compared to POPC. Therefore, the differences observed in tim23 binding to these

membranes is likely due to a general structural effect, rather than specific molecular interactions.

The enhanced affinity of tim23 for CL-containing bilayers appears to be due to an easier transition from the L state to the T state, characterized by insertion of hydrophobic sidechains into the bilayer interior. Computational studies of model peptides that bind membranes peripherally have indicated that physical defects in the membrane aid in amino acid insertion[227,265], and that conically shaped lipids can enhance the occurrence of these defects[223]**.** To investigate this possibility, we simulated membranes with the compositions of the PC and CL^{-2} systems, without peptide, and calculated lipid defects using the PackMem tool[264].

Figure A1.6A shows the probability of encountering a membrane defect with (at least) a given area (see methods for more details). A defect is calculated as a patch of membrane that (i) is not covered in the z dimension by head group atoms, and thus exposes acyl chains, and (ii) the defect extends below the level of the interfacial glycerol moiety. The TOCL2 composition system displayed a larger probability of defects over all defect sizes. **Figure A1.6B** shows the relative probability fraction between the two bilayers. The difference in defect probability between the two systems increases with increasing defect size. It has been estimated that a relevant defect size for amino acid side chain insertion is on the order of 0.2 nm^2. In this regime, a sizeable defect is ~1.5 times more likely to occur in the CL-containing bilayer than the PC-only bilayer, supporting the idea that accessibility to acyl chains may be the mechanism by which CL enhances tim23 binding.

The role of Glycine 6

Mutation studies of glycine 6 indicate that it is a key residue for tim23-membrane binding. We conducted 6 simulations of a glycine to proline mutant in the presence of bilayers with 20% TOCL (-2), and found that binding of tim23N was reduced (**figure A1.7 A**), in qualitative agreement with experiments. Interestingly, we observed several loose binding events followed by unbinding in these simulations, a trend that had only been observed with PC-only simulations in the wild-type protein.

In tight binding simulations, G6 exists in the interfacial region as the protein kinks out of the membrane (**figure A1.1 D**). It may be that the flexibility of G6 in this specific membrane region that is key for tim23 binding. We calculated the lateral pressure profiles of the membrane-only simulations to better understand the local membrane structure. The overall profiles between the POPC and TOCL2 systems were quite similar figure (figure A1.S1), with a slightly more prominent positive peak in the membrane core of the CL-containing simulation, due to additional unsaturated bonds. We then mapped the average z coordinates of the first 6 residues onto the pressure profile for loosely and tightly bound states (**Figure A1.7 B and C, respectively**). In the loosely bound state, the amino acids are on average positioned above the large positive headgroup peak, while in the tightly bound state the aromatic residues have inserted into the negative interfacial tension peak, while the position of the glycine lies close to the positive pressure peak. We speculate that the conformational flexibility and lack of a bulky sidechain in glycine 6 is key to bridging this tightly packed region of the bilayer.

Conclusions

We have successfully reproduced the differential binding behavior of tim23 to POPC and CL containing bilayers. With the high spatial resolution of MD simulations, we were able

to discriminate between a reversible loose binding mode and an irreversible tight binding mode, characterized by insertion of the hydrophobic hook of residues 3-5. We examined several possible mechanisms of differential binding, finding evidence of a defect-based mode of CL-binding enhancement. Finally, we show that glycine 6 is key for tight binding, and point to its location in the bilayer with respect to the lateral pressure profile as a possible reason for its importance.

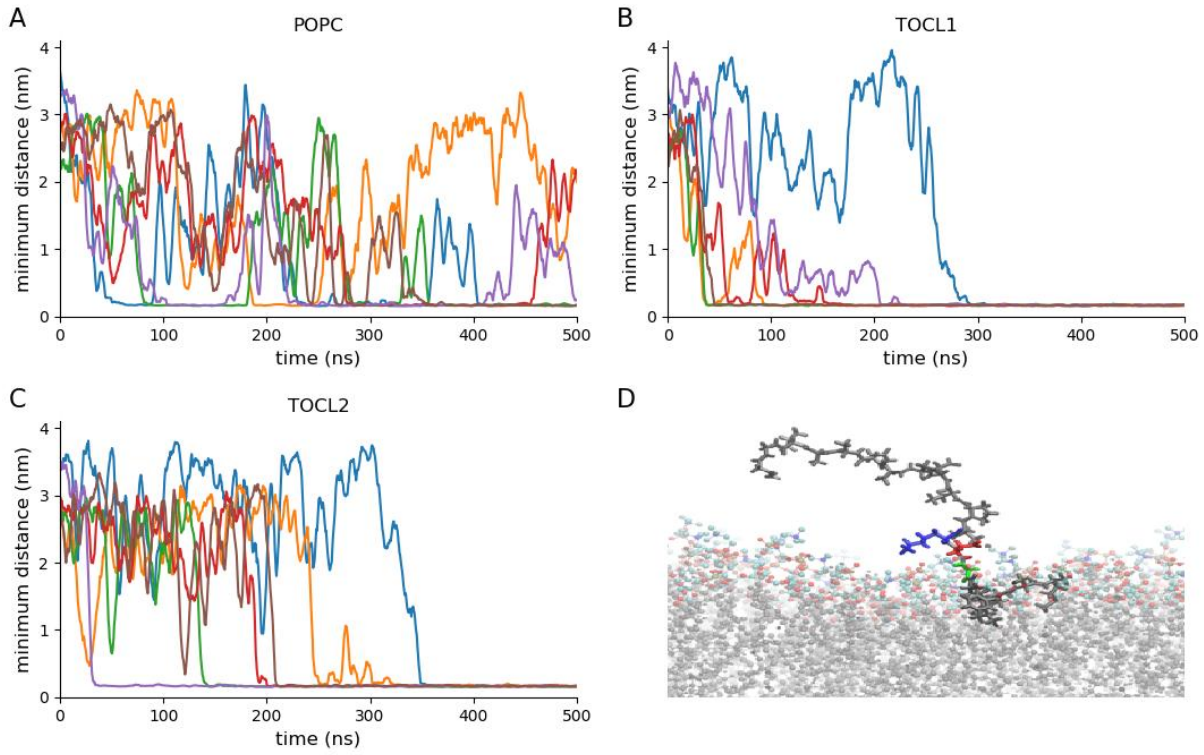

Figure A1.1. tim23-membrane binding distances. (A, B, C) – the minimum distance between the N-terminal 20 residues of tim23 and bilayers for the POPC, TOCL1, and TOCL2 systems, respectively. Each color represents one of 6 trials. D) Representative snapshot of a bound state, with G6 colored green, D7 colored red, and K8 colored blue.

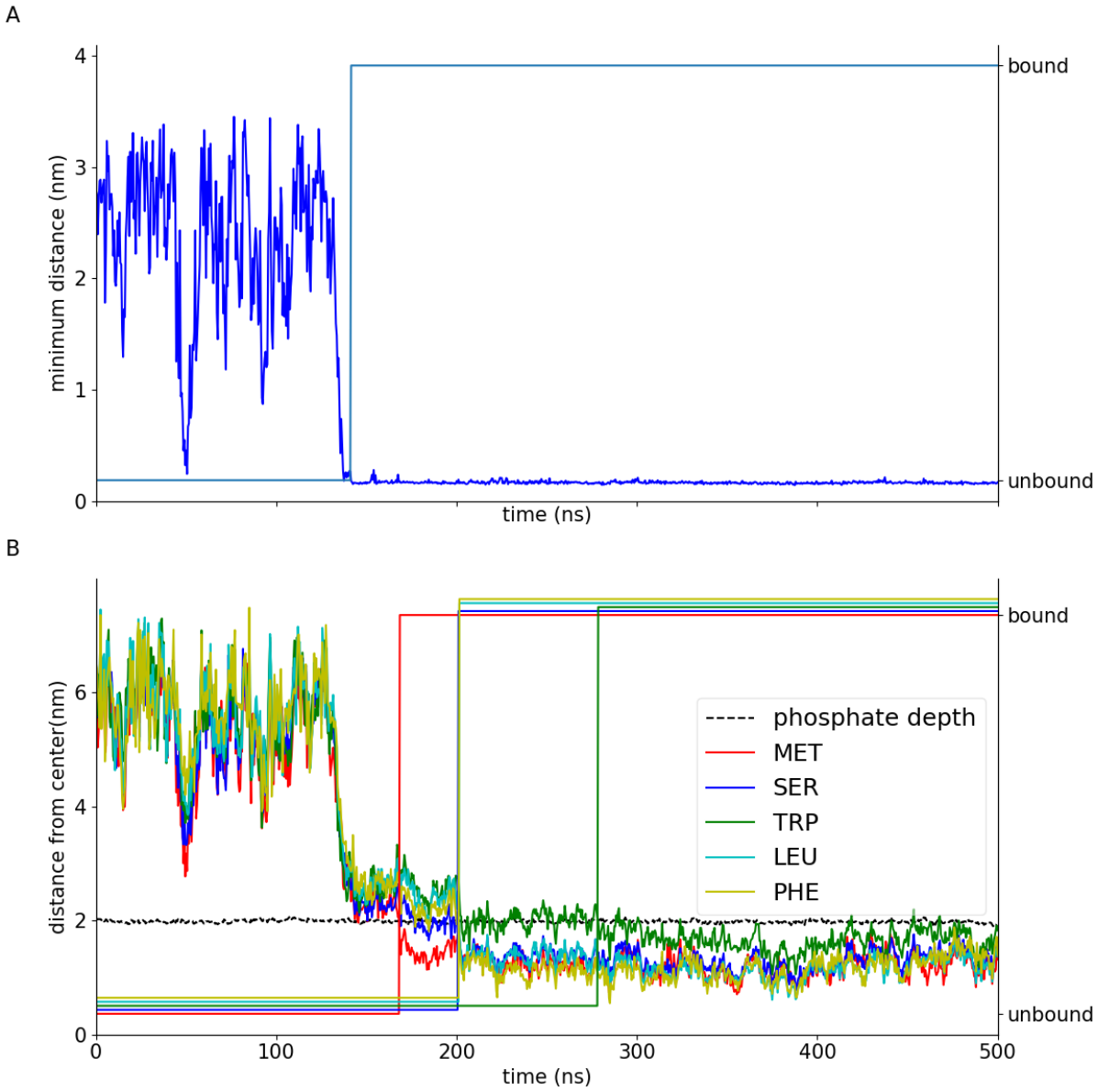

Figure A1.2. Quantifying tim23 binding time-series. A) The minimum distance between protein and membrane for one TOCL2 trial. The light blue line indicates the measurement of unbound vs loosely bound. B) Center of mass z-dimensional distance between amino acid side chains 1-5 and the center of the bilayer. The dotted black line indicates the level of the average phosphate coordinate. Right axis indicates whether side chains are deeply inserted

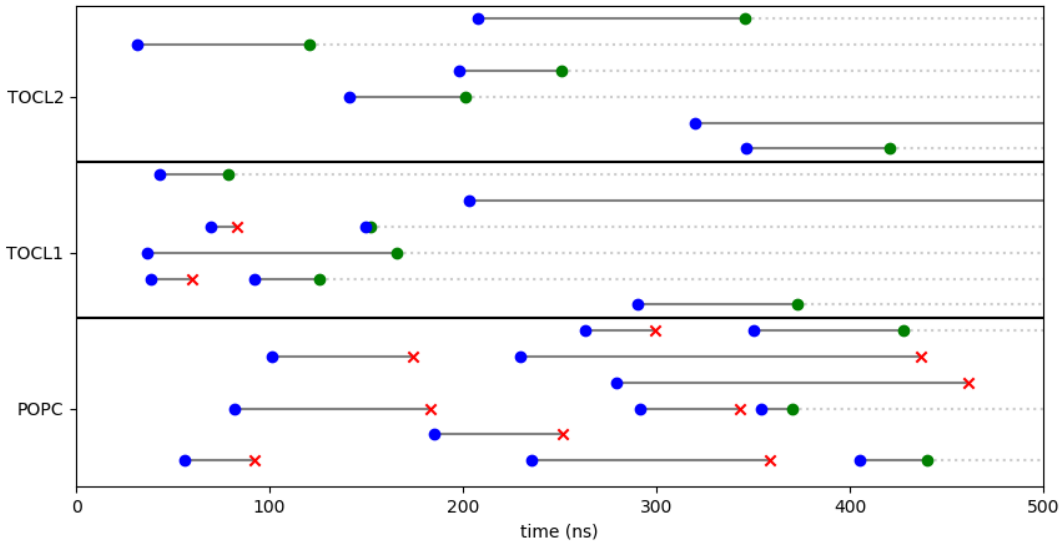

Figure A1.3. Summarized binding behavior of tim23 to membranes. Lack of a line indicates that tim23 is in solution. Blue dots represent loose binding events, and the subsequent solid line is the duration of loose binding. Loose binding can terminate in a tight binding event (green dot, followed by a dashed line) or an unbinding event (red x)

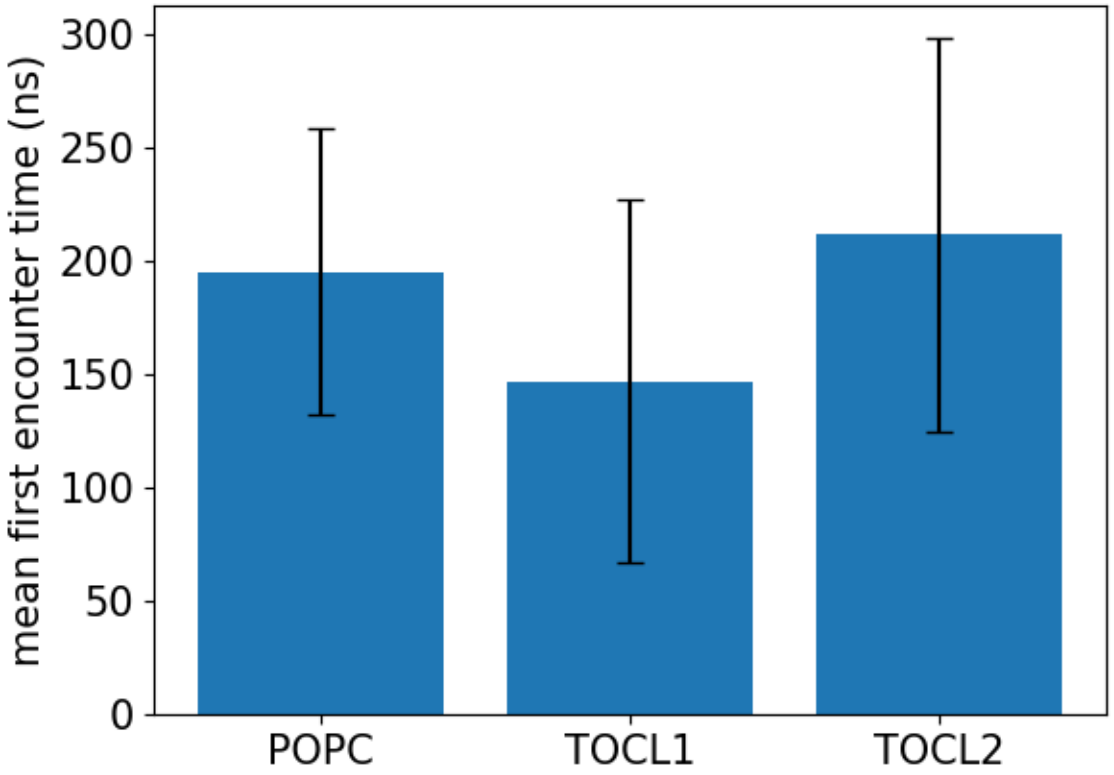

Figure A1.4. Mean first protein-membrane encounter time over replicates, measured as the time from the start of the simulation to when a loose binding event first occurs (figure 2). Error bars indicate 95% confidence intervals

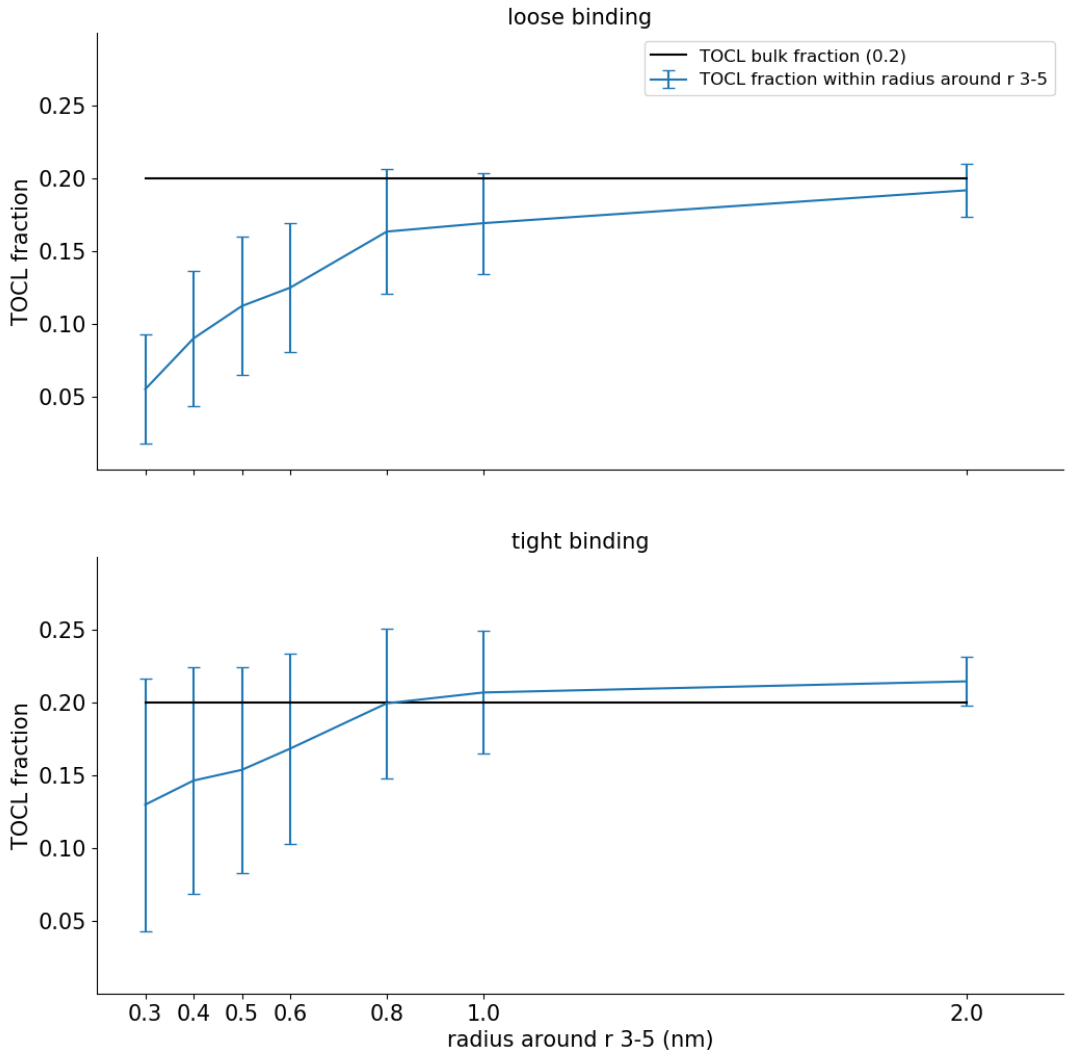

Figure A1.5. Local CL concentration around tim23 near binding events. Top) The fractional concentration of TOCL within 10 ns of loose binding events. Bottom) The fractional concentration of TOCL within 10 ns of tight binding events. Data is averaged over every loose and tight binding event in all TOCL2 replicates. Radii are with respect to the center of mass of residues 3 to 5. Error bars are 95% confidence intervals measured by standard error of the mean.

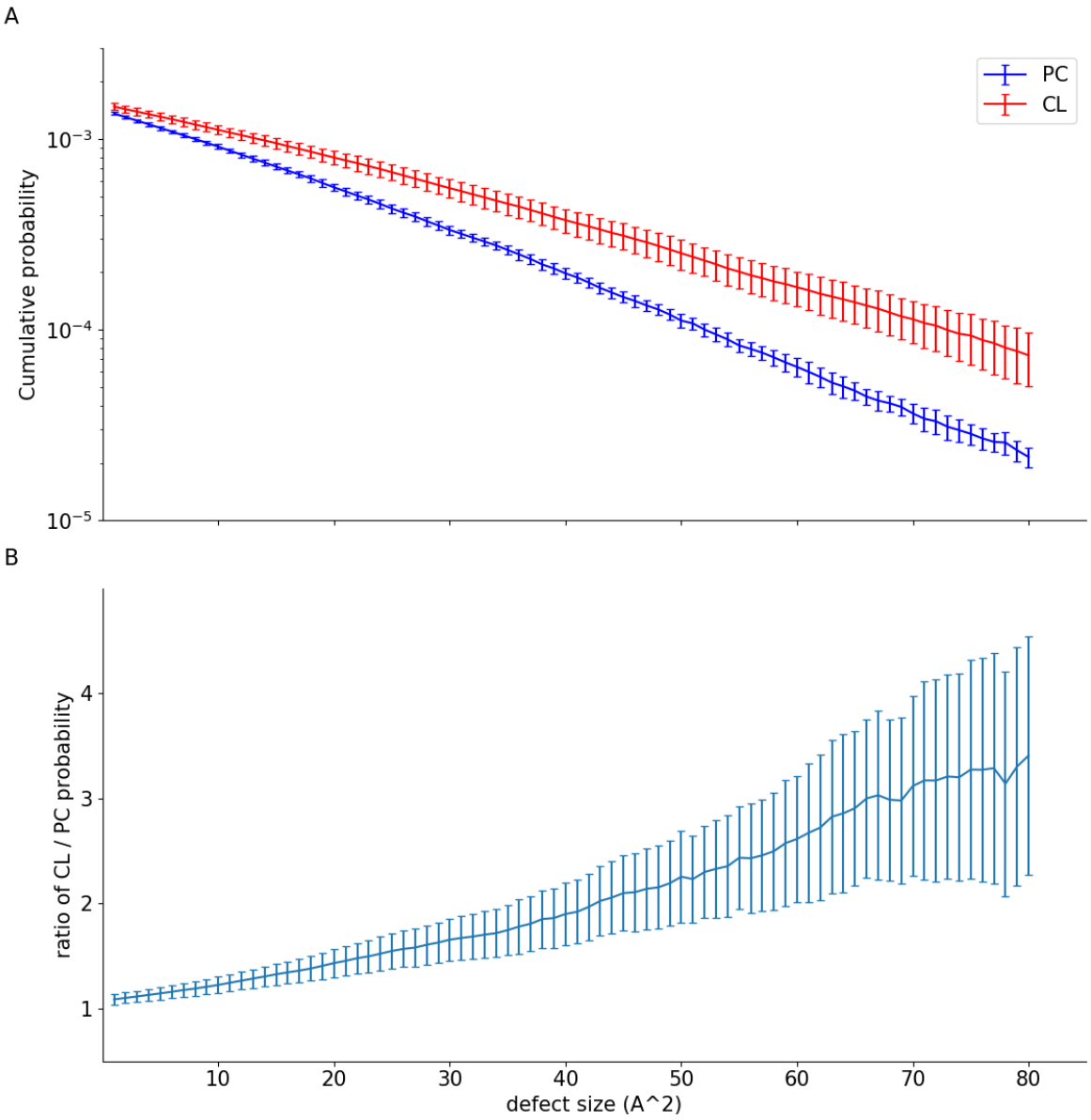

Figure A1.6. Defects in CL-containing bilayers. A) Cumulative probability of finding a surface defect of at least a given area, for the POPC and TOCL2 bilayers. B) Ratio of (TOCL/POPC) defect probability for each defect area. Error bars are 95% confidence intervals measured by standard error of the mean.

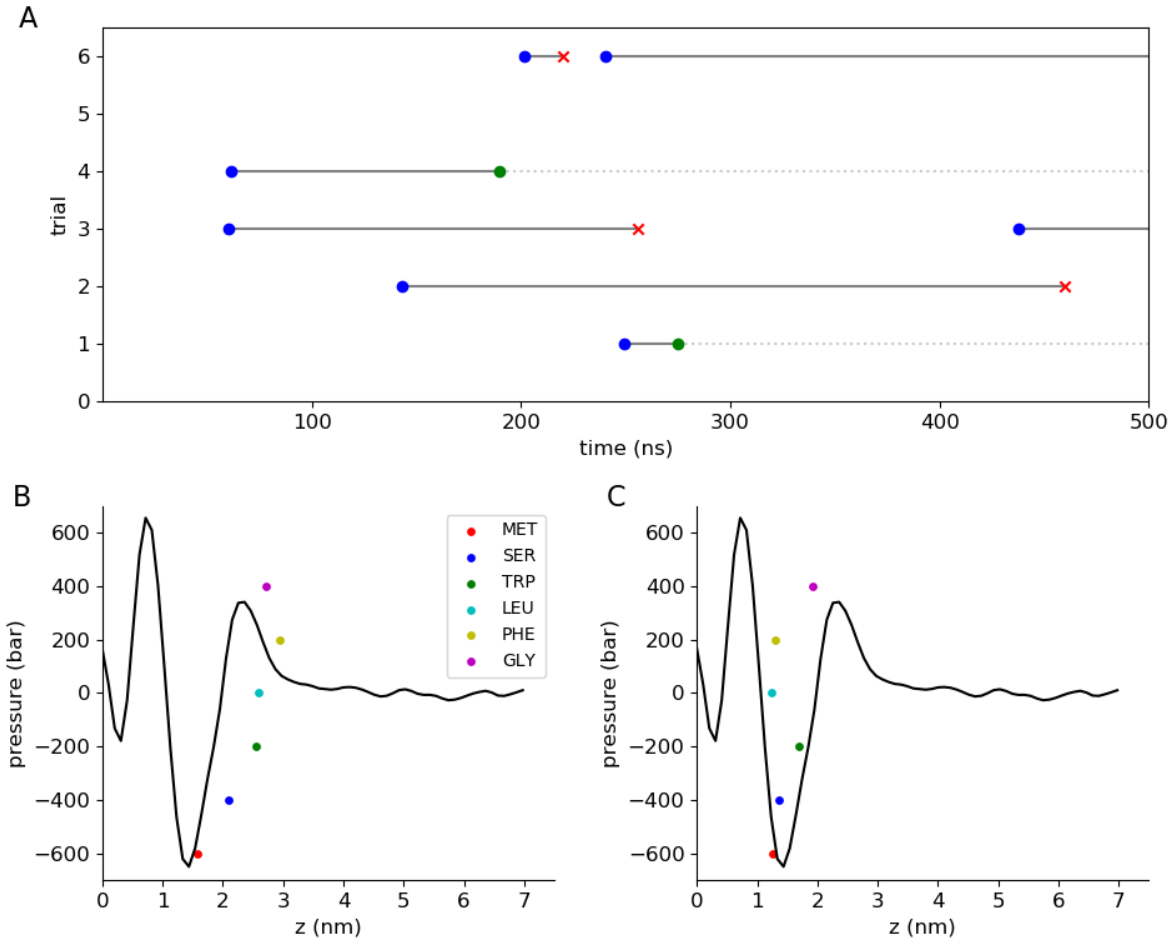

Figure A1.7 The importance of Glycine 6. A) Binding time course for a G6P mutant and a TOCL2 bilayer. B) Average side chain positions of residues 1-6 for a native tim23 protein bound to a TOCL2 bilayer, in the loosely bound configuration, mapped onto the lateral pressure profile of the TOCL2 pure membrane system. C) The same system in a tightly bound configuration. Errors are smaller than marker sizes.

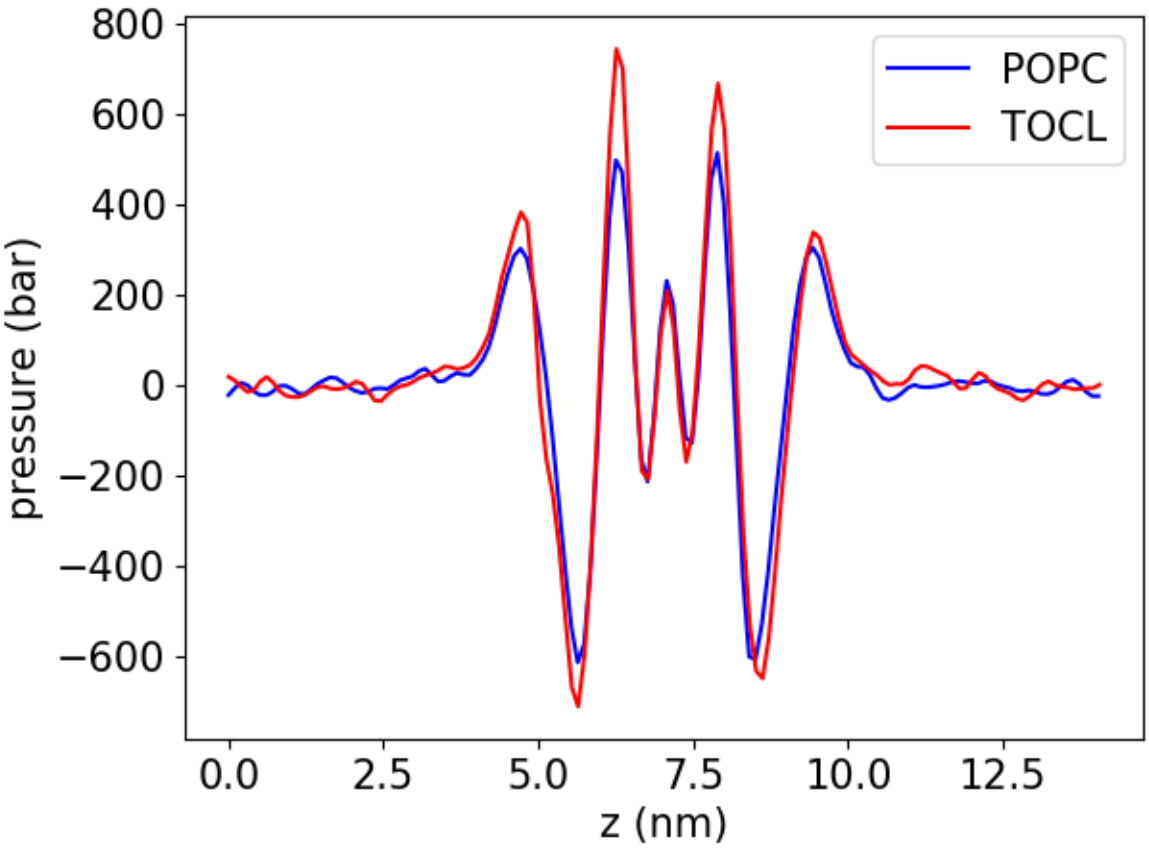

Figure A1.S1. Lateral pressure profiles of pure membrane systems, for POPC (blue) and TOCL (red)

References

1. Deserno, M. Fluid lipid membranes: From differential geometry to curvature stresses. *Chem. Phys. Lipids* **185**, 11–45 (2015).
2. Rawicz, W., Olbrich, K. C., McIntosh, T., Needham, D. & Evans, E. Effect of chain length and unsaturation on elasticity of lipid bilayers. *Biophys. J.* **79**, 328–339 (2000).
3. Evans, E., Heinrich, V., Ludwig, F. & Rawicz, W. Dynamic tension spectroscopy and strength of biomembranes. *Biophys. J.* **85**, 2342–2350 (2003).
4. Hu, M., Briguglio, J. J. & Deserno, M. Determining the Gaussian curvature modulus of lipid membranes in simulations. *Biophys. J.* **102**, 1403–1410 (2012).
5. Taupin, C., Dvolaitzky, M. & Sauterey, C. Osmotic pressure-induced pores in phospholipid vesicles. *Biochemistry* **14**, 4771–4775 (1975).
6. Litster, J. D. Stability of lipid bilayers and red blood cell membranes. *Phys. Lett. A* **53**, 193–194 (1975).
7. Baumgart, T., Hess, S. T. & Webb, W. W. Imaging coexisting fluid domains in biomembrane models coupling curvature and line tension. *Nature* **425**, 821–824 (2003).
8. Helfrich, W. Elastic properties of lipid bilayers: theory and possible experiments. *Z Naturforsch C* **28**, 693–703 (1973).
9. Marsh, D. Elastic curvature constants of lipid monolayers and bilayers. *Chem. Phys. Lipids* **144**, 146–159 (2006).
10. Safran, S. *Statistical thermodynamics of surfaces, interfaces, and membranes.* (Addison-Wesley, 1994).
11. Frolov, V. A., Shnyrova, A. V. & Zimmerberg, J. Lipid polymorphisms and membrane shape. *Cold Spring Harb. Perspect. Biol.* **3**, a004747 (2011).
12. Luckey, M. *Membrane Structural Biology: With Biochemical and Biophysical Foundations*. (Cambridge University Press, 2008).
13. Templer, R. H., Khoo, B. J. & Seddon, J. M. Gaussian Curvature Modulus of an Amphiphilic Monolayer. *Langmuir* **14**, 7427–7434 (1998).
14. Siegel, D. P. & Kozlov, M. M. The gaussian curvature elastic modulus of N-monomethylated dioleoylphosphatidylethanolamine: relevance to membrane fusion and lipid phase behavior. *Biophys. J.* **87**, 366–374 (2004).
15. Siegel, D. P. The Gaussian Curvature Elastic Energy of Intermediates in Membrane Fusion. *Biophys. J.* **95**, 5200–5215 (2008).
16. Siegel, D. P. Determining the Ratio of the Gaussian Curvature and Bending Elastic Moduli of Phospholipids from QII Phase Unit Cell Dimensions. *Biophys. J.* **91**, 608–618 (2006).
17. Baumgart, T., Das, S., Webb, W. W. & Jenkins, J. T. Membrane Elasticity in Giant Vesicles with Fluid Phase Coexistence. *Biophys. J.* **89**, 1067–1080 (2005).
18. Semrau, S., Idema, T., Holtzer, L., Schmidt, T. & Storm, C. Accurate determination of elastic parameters for multi-component membranes. *Phys. Rev. Lett.* **100**, (2008).
19. Vanegas, J. M., Torres-Sánchez, A. & Arroyo, M. Importance of Force Decomposition for Local Stress Calculations in Biomembrane Molecular Simulations. *J. Chem. Theory Comput.* **10**, 691–702 (2014).
20. Hu, M., de Jong, D. H., Marrink, S. J. & Deserno, M. Gaussian curvature elasticity determined from global shape transformations and local stress distributions: a comparative study using the MARTINI model. *Faraday Discuss.* **161**, 365–382 (2013).
21. Templer, R. H., Castle, S. J., Curran, A. R., Rumbles, G. & Klug, D. R. Sensing isothermal changes in the lateral pressure in model membranes using di-pyrenyl

phosphatidylcholine. *Faraday Discuss.* **111**, 41–53 (1999).
22. Bernardi, R. C., Melo, M. C. R. & Schulten, K. Enhanced sampling techniques in molecular dynamics simulations of biological systems. *Biochim. Biophys. Acta BBA - Gen. Subj.* **1850**, 872–877 (2015).
23. Ikebe, J., Umezawa, K. & Higo, J. Enhanced sampling simulations to construct free-energy landscape of protein–partner substrate interaction. *Biophys. Rev.* **8**, 45–62 (2016).
24. Bashford, D. & Case, D. A. Generalized born models of macromolecular solvation effects. *Annu. Rev. Phys. Chem.* **51**, 129–152 (2000).
25. Risselada, H. J., Mark, A. E. & Marrink, S. J. Application of Mean Field Boundary Potentials in Simulations of Lipid Vesicles. *J. Phys. Chem. B* **112**, 7438–7447 (2008).
26. Arnarez, C. *et al.* Dry Martini, a Coarse-Grained Force Field for Lipid Membrane Simulations with Implicit Solvent. *J. Chem. Theory Comput.* **11**, 260–275 (2015).
27. Marrink, S. J., Risselada, H. J., Yefimov, S., Tieleman, D. P. & de Vries, A. H. The MARTINI force field: coarse grained model for biomolecular simulations. *J. Phys. Chem. B* **111**, 7812–7824 (2007).
28. de Jong, D. H., Baoukina, S., Ingólfsson, H. I. & Marrink, S. J. Martini straight: Boosting performance using a shorter cutoff and GPUs. *Comput. Phys. Commun.* **199**, 1–7 (2016).
29. Michalowsky, J., Zeman, J., Holm, C. & Smiatek, J. A polarizable MARTINI model for monovalent ions in aqueous solution. *J. Chem. Phys.* **149**, 163319 (2018).
30. Yesylevskyy, S. O., Schäfer, L. V., Sengupta, D. & Marrink, S. J. Polarizable water model for the coarse-grained MARTINI force field. *PLoS Comput. Biol.* **6**, 1–17 (2010).
31. Michalowsky, J., Schäfer, L. V., Holm, C. & Smiatek, J. A refined polarizable water model for the coarse-grained MARTINI force field with long-range electrostatic interactions. *J. Chem. Phys.* **146**, 054501 (2017).
32. Srivastava, A. & Voth, G. A. Hybrid Approach for Highly Coarse-Grained Lipid Bilayer Models. *J. Chem. Theory Comput.* **9**, 750–765 (2013).
33. Simunovic, M., Srivastava, A. & Voth, G. A. Linear aggregation of proteins on the membrane as a prelude to membrane remodeling. *Proc. Natl. Acad. Sci. U. S. A.* **110**, 20396–401 (2013).
34. Cooke, I. R. & Deserno, M. Solvent-free model for self-assembling fluid bilayer membranes: Stabilization of the fluid phase based on broad attractive tail potentials. *J. Chem. Phys.* **123**, 224710 (2005).
35. Cooke, I. R. & Deserno, M. Coupling between Lipid Shape and Membrane Curvature. *Biophys. J.* **91**, 487–495 (2006).
36. Drouffe, J. M., Maggs, A. C. & Leibler, S. Computer simulations of self-assembled membranes. *Science* **254**, 1353–1356 (1991).
37. Dimova, R. Recent developments in the field of bending rigidity measurements on membranes. *Adv. Colloid Interface Sci.* **208**, 225–234 (2014).
38. Nagle, J. F., Jablin, M. S. & Tristram-Nagle, S. Sugar does not affect the bending and tilt moduli of simple lipid bilayers. *Chem. Phys. Lipids* **196**, 76–80 (2016).
39. Lindahl, E. & Edholm, O. Mesoscopic Undulations and Thickness Fluctuations in Lipid Bilayers from Molecular Dynamics Simulations. *Biophys. J.* **79**, 426–433 (2000).
40. Goetz, R., Gompper, G. & Lipowsky, R. Mobility and Elasticity of Self-Assembled Membranes. *Phys. Rev. Lett.* **82**, 221–224 (1999).
41. May, E. R., Narang, A. & Kopelevich, D. I. Role of molecular tilt in thermal fluctuations of lipid membranes. *Phys. Rev. E* **76**, 021913 (2007).

42. Watson, M. C., Brandt, E. G., Welch, P. M. & Brown, F. L. H. Determining Biomembrane Bending Rigidities from Simulations of Modest Size. *Phys. Rev. Lett.* **109**, 028102 (2012).
43. Allolio, C., Haluts, A. & Harries, D. A local instantaneous surface method for extracting membrane elastic moduli from simulation: Comparison with other strategies. *Chem. Phys.* (2018). doi:10.1016/j.chemphys.2018.03.004
44. Doktorova, M., Harries, D. & Khelashvili, G. Determination of bending rigidity and tilt modulus of lipid membranes from real-space fluctuation analysis of molecular dynamics simulations. *Phys. Chem. Chem. Phys.* **19**, 16806–16818 (2017).
45. Johner, N., Harries, D. & Khelashvili, G. Curvature and Lipid Packing Modulate the Elastic Properties of Lipid Assemblies: Comparing HII and Lamellar Phases. *J. Phys. Chem. Lett.* **5**, 4201–4206 (2014).
46. den Otter, W. K. & Briels, W. J. The bending rigidity of an amphiphilic bilayer from equilibrium and nonequilibrium molecular dynamics. *J. Chem. Phys.* **118**, 4712–4720 (2003).
47. Kawamoto, S., Nakamura, T., Nielsen, S. O. & Shinoda, W. A guiding potential method for evaluating the bending rigidity of tensionless lipid membranes from molecular simulation. *J. Chem. Phys.* **139**, 034108 (2013).
48. Harmandaris, V. A. & Deserno, M. A novel method for measuring the bending rigidity of model lipid membranes by simulating tethers. *J. Chem. Phys.* **125**, 204905 (2006).
49. Sodt, A. J. & Pastor, R. W. Bending Free Energy from Simulation: Correspondence of Planar and Inverse Hexagonal Lipid Phases. *Biophys. J.* **104**, 2202–2211 (2013).
50. Feller, S. E. & Pastor, R. W. Constant surface tension simulations of lipid bilayers: The sensitivity of surface areas and compressibilities. *J. Chem. Phys.* **111**, 1281–1287 (1999).
51. Doktorova, M., LeVine, M. V., Khelashvili, G. & Weinstein, H. A new computational method for membrane compressibility: Bilayer mechanical thickness revisited. *bioRxiv* 360792 (2018). doi:10.1101/360792
52. Pan, J. *et al.* Structural and mechanical properties of cardiolipin lipid bilayers determined using neutron spin echo, small angle neutron and X-ray scattering, and molecular dynamics simulations. *Soft Matter* **11**, 130–138 (2015).
53. Różycki, B. & Lipowsky, R. Spontaneous curvature of bilayer membranes from molecular simulations: Asymmetric lipid densities and asymmetric adsorption. *J. Chem. Phys.* **142**, 054101 (2015).
54. Helfrich, W. Liquids at Interfaces, Les Houches Session XXXV. *Amphiphilic Mesophases Made Defects* 716–755 (1981).
55. Orsi, M., Haubertin, D. Y., Sanderson, W. E. & Essex, J. W. A Quantitative Coarse-Grain Model for Lipid Bilayers. *J. Phys. Chem. B* **112**, 802–815 (2008).
56. Boyd, K. J., Alder, N. N. & May, E. R. Molecular Dynamics Analysis of Cardiolipin and Monolysocardiolipin on Bilayer Properties. *Biophys. J.* **114**, 2116–2127 (2018).
57. den Otter, W. K. Free energies of stable and metastable pores in lipid membranes under tension. *J. Chem. Phys.* **131**, 205101 (2009).
58. Zelisko, M., Ahmadpoor, F., Gao, H. & Sharma, P. Determining the Gaussian Modulus and Edge Properties of 2D Materials: From Graphene to Lipid Bilayers. *Phys. Rev. Lett.* **119**, 068002 (2017).
59. Terzi, M. M. & Deserno, M. Novel tilt-curvature coupling in lipid membranes. *J. Chem. Phys.* **147**, 084702 (2017).
60. Sodt, A. J. & Head-Gordon, T. An implicit solvent coarse-grained lipid model with

correct stress profile. *J. Chem. Phys.* **132**, 205103 (2010).
61. Vanegas, J. M., Longo, M. L. & Faller, R. Crystalline, Ordered and Disordered Lipid Membranes: Convergence of Stress Profiles due to Ergosterol. *J. Am. Chem. Soc.* **133**, 3720–3723 (2011).
62. Cantor, R. S. The lateral pressure profile in membranes: a physical mechanism of general anesthesia. *Biochemistry* **36**, 2339–2344 (1997).
63. Sonne, J., Hansen, F. Y. & Peters, G. H. Methodological problems in pressure profile calculations for lipid bilayers. *J. Chem. Phys.* **122**, (2005).
64. LINCS: A linear constraint solver for molecular simulations - Hess - 1997 - Journal of Computational Chemistry - Wiley Online Library. Available at: https://onlinelibrary.wiley.com/doi/abs/10.1002/(SICI)1096-987X(199709)18:12%3C1463::AID-JCC4%3E3.0.CO;2-H. (Accessed: 27th April 2019)
65. Koldsø, H., Shorthouse, D., Hélie, J. & Sansom, M. S. P. Lipid Clustering Correlates with Membrane Curvature as Revealed by Molecular Simulations of Complex Lipid Bilayers. *PLOS Comput. Biol.* **10**, e1003911 (2014).
66. Gallop, J. L. *et al.* Mechanism of endophilin N-BAR domain-mediated membrane curvature. *EMBO J.* **25**, 2898–2910 (2006).
67. Blood, P. D. & Voth, G. A. Direct observation of Bin/amphiphysin/Rvs (BAR) domain-induced membrane curvature by means of molecular dynamics simulations. *Proc. Natl. Acad. Sci.* **103**, 15068–15072 (2006).
68. Yu, H. & Schulten, K. Membrane Sculpting by F-BAR Domains Studied by Molecular Dynamics Simulations. *PLoS Comput. Biol.* **9**, (2013).
69. Corradi, V. *et al.* Lipid–Protein Interactions Are Unique Fingerprints for Membrane Proteins. *ACS Cent. Sci.* **4**, 709–717 (2018).
70. Davies, K. M., Anselmi, C., Wittig, I., Faraldo-Gómez, J. D. & Kühlbrandt, W. Structure of the yeast F1Fo-ATP synthase dimer and its role in shaping the mitochondrial cristae. *Proc. Natl. Acad. Sci.* (2012). doi:10.1073/pnas.1204593109
71. Anselmi, C., Davies, K. M. & Faraldo-Gomez, J. D. Mitochondrial ATP synthase dimers spontaneously self-associate driven by a long-ranged membrane-induced force. *bioRxiv* 272146 (2018). doi:10.1101/272146
72. Schindler, T., Kröner, D. & Steinhauser, M. O. On the dynamics of molecular self-assembly and the structural analysis of bilayer membranes using coarse-grained molecular dynamics simulations. *Biochim. Biophys. Acta BBA - Biomembr.* **1858**, 1955–1963 (2016).
73. Skjevik, Å. A. *et al.* Simulation of lipid bilayer self-assembly using all-atom lipid force fields. *Phys. Chem. Chem. Phys.* **18**, 10573–10584 (2016).
74. Dahlberg, M. Polymorphic phase behavior of cardiolipin derivatives studied by coarse-grained molecular dynamics. *J. Phys. Chem. B* **111**, 7194–200 (2007).
75. May, E. R., Kopelevich, D. I. & Narang, A. Coarse-Grained Molecular Dynamics Simulations of Phase Transitions in Mixed Lipid Systems Containing LPA, DOPA, and DOPE Lipids. *Biophys. J.* **94**, 878–890 (2008).
76. Lee, H. & Pastor, R. W. Coarse-Grained Model for PEGylated Lipids: Effect of PEGylation on the Size and Shape of Self-Assembled Structures. *J. Phys. Chem. B* **115**, 7830–7837 (2011).
77. Sun, S., Y. Wong, J. T. & Zhang, T.-Y. Effects of external electric fields on the self-assembly of phospholipids / water mixtures—coarse-grained molecular dynamics simulations. *Soft Matter* **7**, 9307–9310 (2011).

78. Fuhrmans, M., Knecht, V. & Marrink, S. J. A Single Bicontinuous Cubic Phase Induced by Fusion Peptides. *J. Am. Chem. Soc.* **131**, 9166–9167 (2009).
79. Boyd, K. J., Alder, N. N. & May, E. R. Buckling Under Pressure: Curvature-Based Lipid Segregation and Stability Modulation in Cardiolipin-Containing Bilayers. *Langmuir* **33**, 6937–6946 (2017).
80. Wu, Q.-Y. & Liang, Q. Interplay between Curvature and Lateral Organization of Lipids and Peptides/Proteins in Model Membranes. *Langmuir* **30**, 1116–1122 (2014).
81. Stecki, J. Correlations in simulated model bilayers. *J. Chem. Phys.* **120**, 3508–3516 (2004).
82. den Otter, W. K. Area compressibility and buckling of amphiphilic bilayers in molecular dynamics simulations. *J. Chem. Phys.* **123**, 214906 (2005).
83. Noguchi, H. Anisotropic surface tension of buckled fluid membranes. *Phys. Rev. E - Stat. Nonlinear Soft Matter Phys.* **83**, (2011).
84. Diggins, P., McDargh, Z. A. & Deserno, M. Curvature Softening and Negative Compressibility of Gel-Phase Lipid Membranes. *J. Am. Chem. Soc.* **137**, 12752–12755 (2015).
85. Hu, M., Diggins IV, P. & Deserno, M. Determining the bending modulus of a lipid membrane by simulating buckling. *J. Chem. Phys.* **138**, (2013).
86. Wang, X. & Deserno, M. Determining the Lipid Tilt Modulus by Simulating Membrane Buckles. *J. Phys. Chem. B* **120**, 6061–6073 (2016).
87. Wang, X. & Deserno, M. Determining the pivotal plane of fluid lipid membranes in simulations. *J. Chem. Phys.* **143**, 164109 (2015).
88. Elías-Wolff, F., Lindén, M., P. Lyubartsev, A. & G. Brandt, E. Curvature sensing by cardiolipin in simulated buckled membranes. *Soft Matter* **15**, 792–802 (2019).
89. Elias-Wolff, F., Lindén, M., Lyubartsev, A. P. & Brandt, E. G. Computing curvature sensitivity of biomolecules in membranes by simulated buckling. *J. Chem. Theory Comput.* (2018).
90. Masone, D., Uhart, M. & Bustos, D. M. Bending Lipid Bilayers: A Closed-Form Collective Variable for Effective Free-Energy Landscapes in Quantitative Biology. *J. Chem. Theory Comput.* (2018). doi:10.1021/acs.jctc.8b00012
91. Huang, C.-H. Phosphatidylcholine vesicles. Formation and physical characteristics. *Biochemistry* **8**, 344–352 (1969).
92. de Vries, A. H., Mark, A. E. & Marrink, S. J. Molecular Dynamics Simulation of the Spontaneous Formation of a Small DPPC Vesicle in Water in Atomistic Detail. *J. Am. Chem. Soc.* **126**, 4488–4489 (2004).
93. Marrink, S. J. & Mark, A. E. Molecular Dynamics Simulation of the Formation, Structure, and Dynamics of Small Phospholipid Vesicles. *J. Am. Chem. Soc.* **125**, 15233–15242 (2003).
94. Marrink, S. J. & Mark, A. E. The Mechanism of Vesicle Fusion as Revealed by Molecular Dynamics Simulations. *J. Am. Chem. Soc.* **125**, 11144–11145 (2003).
95. Smeijers, A. F., Markvoort, A. J., Pieterse, K. & Hilbers, P. A. J. A Detailed Look at Vesicle Fusion. *J. Phys. Chem. B* **110**, 13212–13219 (2006).
96. Lin, C.-M., Li, C.-S., Sheng, Y.-J., Wu, D. T. & Tsao, H.-K. Size-Dependent Properties of Small Unilamellar Vesicles Formed by Model Lipids. *Langmuir* **28**, 689–700 (2012).
97. Risselada, H. J. & Marrink, S. J. Curvature effects on lipid packing and dynamics in liposomes revealed by coarse grained molecular dynamics simulations. *Phys Chem Chem Phys* **11**, 2056–2067 (2009).

98. Markvoort, A. J., van Santen, R. A. & Hilbers, P. A. J. Vesicle Shapes from Molecular Dynamics Simulations. *J. Phys. Chem. B* **110**, 22780–22785 (2006).
99. Risselada, H. J., Marrink, S. J. & Müller, M. Curvature-Dependent Elastic Properties of Liquid-Ordered Domains Result in Inverted Domain Sorting on Uniaxially Compressed Vesicles. *Phys. Rev. Lett.* **106**, 148102 (2011).
100. Parton, D. L., Klingelhoefer, J. W. & Sansom, M. S. P. Aggregation of Model Membrane Proteins, Modulated by Hydrophobic Mismatch, Membrane Curvature, and Protein Class. *Biophys. J.* **101**, 691–699 (2011).
101. Barragán Vidal, I. A., Rosetti, C. M., Pastorino, C. & Müller, M. Measuring the composition-curvature coupling in binary lipid membranes by computer simulations. *J. Chem. Phys.* **141**, 194902 (2014).
102. Qi, Y. *et al.* CHARMM-GUI Martini Maker for Coarse-Grained Simulations with the Martini Force Field. *J. Chem. Theory Comput.* **11**, 4486–4494 (2015).
103. Litman, B. J. Determination of molecular asymmetry in the phosphatidylethanolamine surface distribution in mixed phospholipid vesicles. *Biochemistry* **13**, 2844–2848 (1974).
104. Yeagle, P. L., Hutton, W. C. & Martin, R. B. Transmembrane asymmetry of vesicle lipids. *J. Biol. Chem.* **251**, 2110–2112 (1976).
105. Baoukina, S., Marrink, S. J. & Tieleman, D. P. Molecular structure of membrane tethers. *Biophys. J.* **102**, 1866–1871 (2012).
106. Baoukina, S., Ingólfsson, H. I., Marrink, S. J. & Tieleman, D. P. Curvature-Induced Sorting of Lipids in Plasma Membrane Tethers. *Adv. Theory Simul.* **1**, 1800034 (2018).
107. Pinot, M. *et al.* Polyunsaturated phospholipids facilitate membrane deformation and fission by endocytic proteins. *Science* **345**, 693–697 (2014).
108. Kozlovsky, Y., Chernomordik, L. V. & Kozlov, M. M. Lipid intermediates in membrane fusion: formation, structure, and decay of hemifusion diaphragm. *Biophys. J.* **83**, 2634–2651 (2002).
109. Norizoe, Y., Ch. Daoulas, K. & Müller, M. Measuring excess free energies of self-assembled membrane structures. *Faraday Discuss.* **144**, 369–391 (2010).
110. Smirnova, Y. G., Marrink, S.-J., Lipowsky, R. & Knecht, V. Solvent-Exposed Tails as Prestalk Transition States for Membrane Fusion at Low Hydration. *J. Am. Chem. Soc.* **132**, 6710–6718 (2010).
111. Kawamoto, S. & Shinoda, W. Free energy analysis along the stalk mechanism of membrane fusion. *Soft Matter* **10**, 3048–54 (2014).
112. Kawamoto, S., Klein, M. L. & Shinoda, W. Coarse-grained molecular dynamics study of membrane fusion: Curvature effects on free energy barriers along the stalk mechanism. *J. Chem. Phys.* **143**, 243112 (2015).
113. Risselada, H. J., Bubnis, G. & Grubmüller, H. Expansion of the fusion stalk and its implication for biological membrane fusion. *Proc. Natl. Acad. Sci.* **111**, 11043–11048 (2014).
114. Gardner, J. M. & Abrams, C. F. Rate of hemifusion diaphragm dissipation and ability to form three-junction bound HD determined by lipid composition. *J. Chem. Phys.* **147**, 134903 (2017).
115. Nishizawa, M. & Nishizawa, K. Curvature-driven lipid sorting: coarse-grained dynamics simulations of a membrane mimicking a hemifusion intermediate. *J. Biophys. Chem.* **1**, 86–95 (2010).
116. Goksu, E. I. *et al.* Silica xerogel/aerogel-supported lipid bilayers: Consequences of surface corrugation. *Biochim. Biophys. Acta BBA - Biomembr.* **1798**, 719–729 (2010).

117. Liang, Q. & Ma, Y. Q. Curvature-induced lateral organization in mixed lipid bilayers supported on a corrugated substrate. *J. Phys. Chem. B* **113**, 8049–8055 (2009).
118. Rózycki, B., Weikl, T. R. & Lipowsky, R. Stable patterns of membrane domains at corrugated substrates. *Phys. Rev. Lett.* **100**, 098103 (2008).
119. de Jong, D. H. & Heuer, A. The influence of solid scaffolds on flat and curved lipid membranes. *AIP Adv.* **7**, 075007 (2017).
120. Yesylevskyy, S. O., Rivel, T. & Ramseyer, C. The influence of curvature on the properties of the plasma membrane. Insights from atomistic molecular dynamics simulations. *Sci. Rep.* **7**, 16078 (2017).
121. Yesylevskyy, S., Rivel, T. & Ramseyer, C. Curvature increases permeability of the plasma membrane for ions, water and the anti-cancer drugs cisplatin and gemcitabine. *bioRxiv* 602177 (2019). doi:10.1101/602177
122. Marrink, S.-J. & Tieleman, D. P. Molecular Dynamics Simulation of a Lipid Diamond Cubic Phase. *J. Am. Chem. Soc.* **123**, 12383–12391 (2001).
123. Marrink, S.-J. & Peter Tieleman, D. Molecular Dynamics Simulation of Spontaneous Membrane Fusion during a Cubic-Hexagonal Phase Transition. *Biophys. J.* **83**, 2386–2392 (2002).
124. Wennberg, C. L., Narangifard, A., Lundborg, M., Norlén, L. & Lindahl, E. Structural Transitions in Ceramide Cubic Phases during Formation of the Human Skin Barrier. *Biophys. J.* **114**, 1116–1127 (2018).
125. Bruce, C. D., Berkowitz, M. L., Perera, L. & Forbes, M. D. E. Molecular Dynamics Simulation of Sodium Dodecyl Sulfate Micelle in Water: Micellar Structural Characteristics and Counterion Distribution. *J. Phys. Chem. B* **106**, 3788–3793 (2002).
126. Marrink, S. J., Tieleman, D. P. & Mark, A. E. Molecular Dynamics Simulation of the Kinetics of Spontaneous Micelle Formation. *J. Phys. Chem. B* **104**, 12165–12173 (2000).
127. Tieleman, D. P., van der Spoel, D. & Berendsen, H. J. C. Molecular Dynamics Simulations of Dodecylphosphocholine Micelles at Three Different Aggregate Sizes: Micellar Structure and Chain Relaxation. *J. Phys. Chem. B* **104**, 6380–6388 (2000).
128. K. Cherniavskyi, Y., Ramseyer, C. & O. Yesylevskyy, S. Interaction of C 60 fullerenes with asymmetric and curved lipid membranes: a molecular dynamics study. *Phys. Chem. Chem. Phys.* **18**, 278–284 (2016).
129. Koshiyama, K., Taneo, M., Shigematsu, T. & Wada, S. Bicelle to Vesicle Transition of a Binary Phospholipid Mixture Guided by Controlled Local Lipid Compositions: A Molecular Dynamics Simulation Study. *J. Phys. Chem. B* (2019). doi:10.1021/acs.jpcb.8b10682
130. Walther, T. C. & Farese, R. V. Lipid droplets and cellular lipid metabolism. *Annu. Rev. Biochem.* **81**, 687–714 (2012).
131. Bacle, A., Gautier, R., Jackson, C. L., Fuchs, P. F. J. & Vanni, S. Interdigitation between Triglycerides and Lipids Modulates Surface Properties of Lipid Droplets. *Biophys. J.* **112**, 1417–1430 (2017).
132. Friedman, R. *et al.* Understanding Conformational Dynamics of Complex Lipid Mixtures Relevant to Biology. *J. Membr. Biol.* **251**, 609–631 (2018).
133. Jo, S., Kim, T., Iyer, V. G. & Im, W. CHARMM-GUI: A web-based graphical user interface for CHARMM. *J. Comput. Chem.* **29**, 1859–1865 (2008).
134. Huang, J. & MacKerell, A. D. CHARMM36 all-atom additive protein force field: validation based on comparison to NMR data. *J. Comput. Chem.* **34**, 2135–2145 (2013).
135. Han, W., Wan, C.-K., Jiang, F. & Wu, Y.-D. PACE Force Field for Protein Simulations.

1. Full Parameterization of Version 1 and Verification. *J. Chem. Theory Comput.* **6**, 3373–3389 (2010).
136. Wassenaar, T. A., Ingolfsson, H. I., Bockmann, R. A., Tieleman, D. P. & Marrink, S. J. Computational Lipidomics with insane: A Versatile Tool for Generating Custom Membranes for Molecular Simulations. *J. Chem. Theory Comput.* **11**, 2144–2155 (2015).
137. Ghahremanpour, M. M., Arab, S. S., Aghazadeh, S. B., Zhang, J. & van der Spoel, D. MemBuilder: a web-based graphical interface to build heterogeneously mixed membrane bilayers for the GROMACS biomolecular simulation program. *Bioinformatics* **30**, 439–441 (2014).
138. Knight, C. J. & Hub, J. S. MemGen: a general web server for the setup of lipid membrane simulation systems. *Bioinformatics* **31**, 2897–2899 (2015).
139. Bovigny, C., Tamò, G., Lemmin, T., Maïno, N. & Dal Peraro, M. LipidBuilder: A Framework To Build Realistic Models for Biological Membranes. *J. Chem. Inf. Model.* **55**, 2491–2499 (2015).
140. Martínez, L., Andrade, R., Birgin, E. G. & Martínez, J. M. PACKMOL: A package for building initial configurations for molecular dynamics simulations. *J. Comput. Chem.* **30**, 2157–2164 (2009).
141. Durrant, J. D. & Amaro, R. E. LipidWrapper: an algorithm for generating large-scale membrane models of arbitrary geometry. *PLoS Comput. Biol.* **10**, e1003720 (2014).
142. Boyd, K. J. & May, E. R. BUMPy: A Model-Independent Tool for Constructing Lipid Bilayers of Varying Curvature and Composition. *J. Chem. Theory Comput.* **14**, 6642–6652 (2018).
143. Cheng, X., Jo, S., Lee, H. S., Klauda, J. B. & Im, W. CHARMM-GUI Micelle Builder for Pure/Mixed Micelle and Protein/Micelle Complex Systems. *J. Chem. Inf. Model.* **53**, 2171–2180 (2013).
144. Krüger, D. M. & Kamerlin, S. C. L. Micelle Maker: An Online Tool for Generating Equilibrated Micelles as Direct Input for Molecular Dynamics Simulations. *ACS Omega* **2**, 4524–4530 (2017).
145. Jo, S. *et al.* CHARMM-GUI 10 years for biomolecular modeling and simulation. *J. Comput. Chem.* **38**, 1114–1124 (2017).
146. Vogel, F., Bornhövd, C., Neupert, W. & Reichert, A. S. Dynamic subcompartmentalization of the mitochondrial inner membrane. *J. Cell Biol.* **175**, 237–247 (2006).
147. Gilkerson, R. W., Selker, J. M. L. & Capaldi, R. A. The cristal membrane of mitochondria is the principal site of oxidative phosphorylation. *FEBS Lett.* **546**, 355–358 (2003).
148. Cogliati, S. *et al.* Mitochondrial Cristae Shape Determines Respiratory Chain Supercomplexes Assembly and Respiratory Efficiency. *Cell* **155**, 160–171 (2013).
149. Song, D. H. *et al.* Biophysical significance of the inner mitochondrial membrane structure on the electrochemical potential of mitochondria. *Phys. Rev. E Stat. Nonlin. Soft Matter Phys.* **88**, 062723 (2013).
150. Jendrach, M., Mai, S., Pohl, S., Vöth, M. & Bereiter-Hahn, J. Short- and long-term alterations of mitochondrial morphology, dynamics and mtDNA after transient oxidative stress. *Mitochondrion* **8**, 293–304 (2008).
151. Tondera, D. *et al.* SLP-2 is required for stress-induced mitochondrial hyperfusion. *EMBO J.* **28**, 1589–1600 (2009).
152. Molina, A. J. a *et al.* Mitochondrial Networking Protects Beta Cells from Nutrient

Induced Apoptosis. *Diabetes* **58**, 2303–2315 (2009).
153. Harner, M. *et al.* The mitochondrial contact site complex, a determinant of mitochondrial architecture. *EMBO J.* **30**, 4356–4370 (2011).
154. Horvath, S. E. *et al.* Role of membrane contact sites in protein import into mitochondria. *Protein Sci.* **24**, 277–297 (2015).
155. Rabl, R. *et al.* Formation of cristae and crista junctions in mitochondria depends on antagonism between Fcj1 and Su e/g. *J. Cell Biol.* **185**, 1047–63 (2009).
156. Strauss, M., Hofhaus, G., Schröder, R. R. & Kühlbrandt, W. Dimer ribbons of ATP synthase shape the inner mitochondrial membrane. *EMBO J.* **27**, 1154–1160 (2008).
157. Davies, K. M. *et al.* Macromolecular organization of ATP synthase and complex I in whole mitochondria. *Proc. Natl. Acad. Sci.* **108**, 14121–14126 (2011).
158. Dudkina, N. V., Heinemeyer, J., Keegstra, W., Boekema, E. J. & Braun, H. P. Structure of dimeric ATP synthase from mitochondria: An angular association of monomers induces the strong curvature of the inner membrane. *FEBS Lett.* **579**, 5769–5772 (2005).
159. Epand, R. F., Martinou, J.-C., Fornallaz-Mulhauser, M., Hughes, D. W. & Epand, R. M. The Apoptotic Protein tBid Promotes Leakage by Altering Membrane Curvature. *J. Biol. Chem.* **277**, 32632–32639 (2002).
160. John, G. B. *et al.* The mitochondrial inner membrane protein mitofilin controls cristae morphology. *Mol Biol Cell* **16**, 1543–1554 (2005).
161. Sathappa, M. & Alder, N. N. The ionization properties of cardiolipin and its variants in model bilayers. *Biochim. Biophys. Acta* **1858**, 1362–1372 (2016).
162. Olofsson, G. & Sparr, E. Ionization constants pKa of cardiolipin. *PloS One* **8**, e73040 (2013).
163. Malyshka, D., Pandiscia, L. A. & Schweitzer-Stenner, R. Cardiolipin containing liposomes are fully ionized at physiological pH. An FT-IR study of phosphate group ionization. *Vib. Spectrosc.* **75**, 86–92 (2014).
164. Kooijman, E. E. *et al.* Magic angle spinning 31P NMR spectroscopy reveals two essentially identical ionization states for the cardiolipin phosphates in phospholipid liposomes. *Biochim. Biophys. Acta BBA - Biomembr.* **1859**, 61–68 (2017).
165. Kates, M., Syz, J. Y., Gosser, D. & Haines, T. H. pH-dissociation characteristics of cardiolipin and its 2'-deoxy analogue. *Lipids* **28**, 877–882 (1993).
166. Nichols-Smith, S. & Kuhl, T. Electrostatic interactions between model mitochondrial membranes. *Colloids Surf. B Biointerfaces* **41**, 121–127 (2005).
167. Hielscher, R., Wenz, T., Hunte, C. & Hellwig, P. Monitoring the redox and protonation dependent contributions of cardiolipin in electrochemically induced FTIR difference spectra of the cytochrome bc(1) complex from yeast. *Biochim. Biophys. Acta* **1787**, 617–625 (2009).
168. Sidiq, S., Verma, I. & Pal, S. K. pH-Driven Ordering Transitions in Liquid Crystal Induced by Conformational Changes of Cardiolipin. *Langmuir ACS J. Surf. Colloids* **31**, 4741–4751 (2015).
169. Pfeiffer, K. *et al.* Cardiolipin Stabilizes Respiratory Chain Supercomplexes. *J. Biol. Chem.* **278**, 52873–52880 (2003).
170. Seddon, J. M., Kaye, R. D. & Marsh, D. Induction of the lamellar-inverted hexagonal phase transition in cardiolipin by protons and monovalent cations. *Biochim. Biophys. Acta BBA - Biomembr.* **734**, 347–352 (1983).
171. Arslan, P., Beltrame, M. & Muscatello, U. Ultrastructural characterization of cardiolipin liquid-crystalline structures in the absence and the presence of divalent cations. *Micron 1969* **11**,

115–125 (1980).
172. Cullis, P. R., Verkleij, A. J. & Ververgaert, P. H. J. Th. Polymorphic phase behaviour of cardiolipin as detected by 31P NMR and freeze-fracture techniques. Effects of calcium, dibucaine and chlorpromazine. *Biochim. Biophys. Acta BBA - Biomembr.* **513**, 11–20 (1978).
173. De Kruijff, B. *et al.* Further aspects of the Ca2+-dependent polymorphism of bovine heart cardiolipin. *Biochim. Biophys. Acta* **693**, 1–12 (1982).
174. Killian, J. A. *et al.* Effect of divalent cations on lipid organization of cardiolipin isolated from Escherichia coli strain AH930. *Biochim. Biophys. Acta* **1189**, 225–232 (1994).
175. Ortiz, A., Killian, J. A., Verkleij, A. J. & Wilschut, J. Membrane fusion and the lamellar-to-inverted-hexagonal phase transition in cardiolipin vesicle systems induced by divalent cations. *Biophys. J.* **77**, 2003–2014 (1999).
176. Rand, R. P. & Sengupta, S. Cardiolipin forms hexagonal structures with divalent cations. *Biochim. Biophys. Acta BBA - Biomembr.* **255**, 484–492 (1972).
177. Vail, W. J. & Stollery, J. G. Phase changes of cardiolipin vesicles mediated by divalent cations. *BBA - Biomembr.* **551**, 74–84 (1979).
178. Khalifat, N., Puff, N., Bonneau, S., Fournier, J.-B. & Angelova, M. I. Membrane Deformation under Local pH Gradient: Mimicking Mitochondrial Cristae Dynamics. *Biophys. J.* **95**, 4924–4933 (2008).
179. Khalifat, N., Fournier, J.-B., Angelova, M. I. & Puff, N. Lipid packing variations induced by pH in cardiolipin-containing bilayers: the driving force for the cristae-like shape instability. *Biochim. Biophys. Acta* **1808**, 2724–2733 (2011).
180. Planas-Iglesias, J. *et al.* Cardiolipin Interactions with Proteins. *Biophys. J.* **109**, 1282–1294 (2015).
181. Bajaj, R., Munari, F., Becker, S. & Zweckstetter, M. Interaction of the intermembrane space domain of Tim23 protein with mitochondrial membranes. *J. Biol. Chem.* **289**, 34620–34626 (2014).
182. Acehan, D. *et al.* Distinct effects of tafazzin deletion in differentiated and undifferentiated mitochondria. *Mitochondrion* **9**, 86–95 (2009).
183. Acehan, D. *et al.* Cardiolipin affects the supramolecular organization of ATP synthase in mitochondria. *Biophys. J.* **100**, 2184–2192 (2011).
184. Mileykovskaya, E. & Dowhan, W. Visualization of phospholipid domains in Escherichia coli by using the cardiolipin-specific fluorescent dye 10-N-nonyl acridine orange. *J. Bacteriol.* **182**, 1172–1175 (2000).
185. Kawai, F. *et al.* Cardiolipin Domains in Bacillus subtilis Marburg Membranes. *J. Bacteriol.* **186**, 1475–1483 (2004).
186. Romantsov, T. *et al.* Cardiolipin promotes polar localization of osmosensory transporter ProP in Escherichia coli. *Mol. Microbiol.* **64**, 1455–1465 (2007).
187. Parthasarathy, R., Yu, C. & Groves, J. T. Curvature-Modulated Phase Separation in Lipid Bilayer Membranes. *Langmuir* **22**, 5095–5099 (2006).
188. Sorre, B. *et al.* Curvature-driven lipid sorting needs proximity to a demixing point and is aided by proteins. *Proc. Natl. Acad. Sci. U. S. A.* **106**, 5622–6 (2009).
189. Callan-Jones, A., Sorre, B. & Bassereau, P. Curvature-Driven Lipid Sorting in Biomembranes. *Cold Spring Harb. Perspect. Biol.* **3**, a004648 (2011).
190. Reynwar, B. J. *et al.* Aggregation and vesiculation of membrane proteins by curvature-mediated interactions. *Nature* **447**, 461–464 (2007).
191. Dahlberg, M. & Maliniak, A. Molecular Dynamics Simulations of Cardiolipin Bilayers.

J. Phys. Chem. B **112**, 11655–11663 (2008).
192. Pöyry, S., Róg, T., Karttunen, M. & Vattulainen, I. Mitochondrial membranes with mono- and divalent salt: changes induced by salt ions on structure and dynamics. *J. Phys. Chem. B* **113**, 15513–21 (2009).
193. Róg, T. *et al.* Role of cardiolipins in the inner mitochondrial membrane: insight gained through atom-scale simulations. *J. Phys. Chem. B* **113**, 3413–22 (2009).
194. Dahlberg, M. & Maliniak, A. Mechanical Properties of Coarse-Grained Bilayers Formed by Cardiolipin and Zwitterionic Lipids. *J. Chem. Theory Comput.* **6**, 1638–49 (2010).
195. Aguayo, D., González-Nilo, F. D. & Chipot, C. Insight into the Properties of Cardiolipin Containing Bilayers from Molecular Dynamics Simulations, Using a Hybrid All-Atom/United-Atom Force Field. *J. Chem. Theory Comput.* **8**, 1765–1773 (2012).
196. Berendsen, H. J. C., van der Spoel, D. & van Drunen, R. GROMACS: A message-passing parallel molecular dynamics implementation. *Comput. Phys. Commun.* **91**, 43–56 (1995).
197. Parrinello, M. & Rahman, A. Polymorphic transitions in single crystals: A new molecular dynamics method. *J. Appl. Phys.* **52**, 7182–7190 (1981).
198. Nosé, S. & Klein, M. L. Constant pressure molecular dynamics for molecular systems. *Mol. Phys.* **50**, 1055–1076 (1983).
199. Nichols-Smith, S., Teh, S.-Y. & Kuhl, T. L. Thermodynamic and mechanical properties of model mitochondrial membranes. *Biochim. Biophys. Acta* **1663**, 82–8 (2004).
200. Lea, P. J., Temkin, R. J., Freeman, K. B., Mitchell, G. a & Robinson, B. H. Variations in mitochondrial ultrastructure and dynamics observed by high resolution scanning electron microscopy (HRSEM). *Microsc. Res. Tech.* **27**, 269–77 (1994).
201. Ju, W.-K. *et al.* Elevated hydrostatic pressure triggers mitochondrial fission and decreases cellular ATP in differentiated RGC-5 cells. *Invest. Ophthalmol. Vis. Sci.* **48**, 2145–2151 (2007).
202. Chen, Y.-F., Tsang, K.-Y., Chang, W.-F. & Fan, Z.-A. Differential dependencies on [Ca2+] and temperature of the monolayer spontaneous curvatures of DOPE, DOPA and cardiolipin: effects of modulating the strength of the inter-headgroup repulsion. *Soft Matter* **11**, 4041–4053 (2015).
203. Levine, Z. A. *et al.* Determination of Biomembrane Bending Moduli in Fully Atomistic Simulations. *J. Am. Chem. Soc.* **136**, 13582–13585 (2014).
204. Khelashvili, G., Kollmitzer, B., Heftberger, P., Pabst, G. & Harries, D. Calculating the Bending Modulus for Multicomponent Lipid Membranes in Different Thermodynamic Phases. *J. Chem. Theory Comput.* **9**, 3866–3871 (2013).
205. Krebs, J. J. R., Hauser, H. & Carafoli, E. Asymmetric distribution of phospholipids in the inner membrane of beef heart mitochondria. *J Biol Chem* **254**, 5308–5316 (1979).
206. Javanainen, M. *et al.* Anomalous and normal diffusion of proteins and lipids in crowded lipid membranes. *Faraday Discuss* **161**, 397–417 (2013).
207. Derganc, J. Curvature-driven lateral segregation of membrane constituents in Golgi cisternae. *Phys. Biol.* **4**, 317 (2007).
208. Huang, K. C., Mukhopadhyay, R. & Wingreen, N. S. A curvature-mediated mechanism for localization of lipids to bacterial poles. *PLoS Comput. Biol.* **2**, 1357–1364 (2006).
209. Horvath, S. E. & Daum, G. Lipids of mitochondria. *Prog. Lipid Res.* **52**, 590–614 (2013).
210. Lu, Y.-W. & Claypool, S. M. Disorders of phospholipid metabolism: an emerging class of mitochondrial disease due to defects in nuclear genes. *Front. Genet.* **6**, 3 (2015).
211. Beranek, A. *et al.* Identification of a cardiolipin-specific phospholipase encoded by the

gene CLD1 (YGR110W) in yeast. *J. Biol. Chem.* **284**, 11572–11578 (2009).
212. Hsu, Y.-H., Dumlao, D. S., Cao, J. & Dennis, E. A. Assessing Phospholipase A2 Activity toward Cardiolipin by Mass Spectrometry. *PLOS ONE* **8**, e59267 (2013).
213. Schlame, M. & Ren, M. Barth syndrome, a human disorder of cardiolipin metabolism. *FEBS Lett.* **580**, 5450–5455 (2006).
214. Esposti, M. D., Cristea, I. M., Gaskell, S. J., Nakao, Y. & Dive, C. Proapoptotic Bid binds to monolysocardiolipin, a new molecular connection between mitochondrial membranes and cell death. *Cell Death Differ.* **10**, 1300–1309 (2003).
215. Powell, G. L. & Marsh, D. Polymorphic phase behavior of cardiolipin derivatives studied by 31P NMR and X-ray diffraction. *Biochemistry* **24**, 2902–2908 (1985).
216. Abraham, M. J. *et al.* GROMACS: High performance molecular simulations through multi-level parallelism from laptops to supercomputers. *SoftwareX* **1–2**, 19–25 (2015).
217. Klauda, J. B. *et al.* Update of the CHARMM all-atom additive force field for lipids: Validation on six lipid types. *J. Phys. Chem. B* **114**, 7830–7843 (2010).
218. Lee, J. *et al.* CHARMM-GUI Input Generator for NAMD, GROMACS, AMBER, OpenMM, and CHARMM/OpenMM Simulations Using the CHARMM36 Additive Force Field. *J. Chem. Theory Comput.* **12**, 405–413 (2016).
219. Nosé, S. A unified formulation of the constant temperature molecular dynamics methods. *J. Chem. Phys.* **81**, 511–519 (1984).
220. Hoover, W. G. Canonical dynamics: Equilibrium phase-space distributions. *Phys. Rev. A* **31**, 1695–1697 (1985).
221. Humphrey, W., Dalke, A. & Schulten, K. VMD: Visual molecular dynamics. *J. Mol. Graph.* **14**, 33–38 (1996).
222. Das, C., Noro, M. G. & Olmsted, P. D. Simulation studies of stratum corneum lipid mixtures. *Biophys. J.* **97**, 1941–1951 (2009).
223. Vamparys, L. *et al.* Conical lipids in flat bilayers induce packing defects similar to that induced by positive curvature. *Biophys. J.* **104**, 585–593 (2013).
224. Kooijman, E. E. *et al.* Spontaneous Curvature of Phosphatidic Acid and Lysophosphatidic Acid. *Biochemistry* **44**, 2097–2102 (2005).
225. Camley, B. A., Lerner, M. G., Pastor, R. W. & Brown, F. L. H. Strong influence of periodic boundary conditions on lateral diffusion in lipid bilayer membranes. *J. Chem. Phys.* **143**, (2015).
226. Venable, R. M. *et al.* Lipid and Peptide Diffusion in Bilayers: The Saffman–Delbrück Model and Periodic Boundary Conditions. *J. Phys. Chem. B* **121**, 3443–3457 (2017).
227. Vanni, S. *et al.* Amphipathic Lipid Packing Sensor Motifs: Probing Bilayer Defects with Hydrophobic Residues. *Biophys. J.* **104**, 575–584 (2013).
228. Lizana, L., Bauer, B. & Orwar, O. Controlling the rates of biochemical reactions and signaling networks by shape and volume changes. *Proc. Natl. Acad. Sci.* **105**, 4099–4104 (2008).
229. Zick, M., Rabl, R. & Reichert, A. S. Cristae formation-linking ultrastructure and function of mitochondria. *Biochim. Biophys. Acta* **1793**, 5–19 (2009).
230. Kozjak-Pavlovic, V. The MICOS complex of human mitochondria. *Cell Tissue Res.* **367**, 83–93 (2017).
231. Davies, K. M., Daum, B., Kühlbrandt, W., Anselmi, C. & Faraldo-Gómez, J. Structure of the mitochondrial ATP synthase and its role in shaping mitochondria cristae. *Microsc. Microanal. Off. J. Microsc. Soc. Am. Microbeam Anal. Soc. Microsc. Soc. Can.* **18 Suppl 2**, 56–7 (2012).

232. Duncan, A. L., Robinson, A. J. & Walker, J. E. Cardiolipin binds selectively but transiently to conserved lysine residues in the rotor of metazoan ATP synthases. *Proc. Natl. Acad. Sci.* **113**, 8687–8692 (2016).
233. Guo, H., Bueler, S. A. & Rubinstein, J. L. Atomic model for the dimeric FO region of mitochondrial ATP synthase. *Science* **358**, 936–940 (2017).
234. Eswar, N. *et al.* Comparative protein structure modeling using Modeller. *Curr. Protoc. Bioinforma.* **Chapter 5**, Unit-5.6 (2006).
235. McGibbon, R. T. *et al.* MDTraj: A Modern Open Library for the Analysis of Molecular Dynamics Trajectories. *Biophys. J.* **109**, 1528–1532 (2015).
236. Chodera, J. D. A Simple Method for Automated Equilibration Detection in Molecular Simulations. *J. Chem. Theory Comput.* **12**, 1799–1805 (2016).
237. Scherer, M. K. *et al.* PyEMMA 2: A Software Package for Estimation, Validation, and Analysis of Markov Models. *J. Chem. Theory Comput.* **11**, 5525–5542 (2015).
238. Allen, R. D., Schroeder, C. C. & Fok, A. K. An investigation of mitochondrial inner membranes by rapid-freeze deep-etch techniques. *J. Cell Biol.* **108**, 2233–2240 (1989).
239. Dudkina, N. V., Oostergetel, G. T., Lewejohann, D., Braun, H.-P. & Boekema, E. J. Row-like organization of ATP synthase in intact mitochondria determined by cryo-electron tomography. *Biochim. Biophys. Acta BBA - Bioenerg.* **1797**, 272–277 (2010).
240. Javanainen, M., Martinez-Seara, H. & Vattulainen, I. Excessive aggregation of membrane proteins in the Martini model. *PLOS ONE* **12**, e0187936 (2017).
241. May, E., Narang, A. & Kopelevich, D. Molecular modeling of key elastic properties for inhomogeneous lipid bilayers. **33**, 787–797 (2007).
242. Wu, E. L. *et al.* CHARMM-GUI Membrane Builder Toward Realistic Biological Membrane Simulations. *J. Comput. Chem.* **35**, 1997–2004 (2014).
243. McConnell, H. M. & Kornberg, R. D. Inside-outside transitions of phospholipids in vesicle membranes. *Biochemistry* **10**, 1111–1120 (1971).
244. Rand, R. P., Fuller, N. L., Gruner, S. M. & Parsegian, V. A. Membrane curvature, lipid segregation, and structural transitions for phospholipids under dual-solvent stress. *Biochemistry* **29**, 76–87 (1990).
245. Zacharias, M., Straatsma, T. P. & McCammon, J. A. Separation-shifted scaling, a new scaling method for Lennard-Jones interactions in thermodynamic integration. *J. Chem. Phys.* **100**, 9025–9031 (1994).
246. Pitera, J. W. & Gunsteren, W. F. van. A Comparison of Non-Bonded Scaling Approaches for Free Energy Calculations. *Mol. Simul.* **28**, 45–65 (2002).
247. Saffman, P. G. & Delbrück, M. Brownian motion in biological membranes. *Proc. Natl. Acad. Sci.* **72**, 3111–3113 (1975).
248. Chen, Z. & Rand, R. P. Comparative Study of the Effects of Several n-Alkanes on Phospholipid Hexagonal Phases. *Biophys. J.* **74**, 944–952 (1998).
249. Shearer, J. & Khalid, S. Communication between the leaflets of asymmetric membranes revealed from coarse-grain molecular dynamics simulations. *Sci. Rep.* **8**, 1805 (2018).
250. Rafiee, R. & Moghadam, R. M. On the modeling of carbon nanotubes: A critical review. *Compos. Part B Eng.* **56**, 435–449 (2014).
251. Jefferys, E., Sands, Z. A., Shi, J., Sansom, M. S. P. & Fowler, P. W. Alchembed: A Computational Method for Incorporating Multiple Proteins into Complex Lipid Geometries. *J. Chem. Theory Comput.* **11**, 2743–2754 (2015).
252. Marrink, S. J. & Tieleman, D. P. Perspective on the Martini model. *Chem. Soc. Rev.* **42**,

6801–6822 (2013).
253. Chacinska, A., Koehler, C. M., Milenkovic, D., Lithgow, T. & Pfanner, N. Importing mitochondrial proteins: machineries and mechanisms. *Cell* **138**, 628–644 (2009).
254. Gadir, N., Haim-Vilmovsky, L., Kraut-Cohen, J. & Gerst, J. E. Localization of mRNAs coding for mitochondrial proteins in the yeast Saccharomyces cerevisiae. *RNA N. Y. N* **17**, 1551–1565 (2011).
255. Chacinska, A. *et al.* Mitochondrial presequence translocase: switching between TOM tethering and motor recruitment involves Tim21 and Tim17. *Cell* **120**, 817–829 (2005).
256. Martin, J., Mahlke, K. & Pfanner, N. Role of an energized inner membrane in mitochondrial protein import. Delta psi drives the movement of presequences. *J. Biol. Chem.* **266**, 18051–18057 (1991).
257. Truscott, K. N. *et al.* A presequence- and voltage-sensitive channel of the mitochondrial preprotein translocase formed by Tim23. *Nat. Struct. Biol.* **8**, 1074–1082 (2001).
258. Donzeau, M. *et al.* Tim23 links the inner and outer mitochondrial membranes. *Cell* **101**, 401–412 (2000).
259. Qian, X. *et al.* Structural basis for the function of Tim50 in the mitochondrial presequence translocase. *J. Mol. Biol.* **411**, 513–519 (2011).
260. Bajaj, R., Jaremko, Ł., Jaremko, M., Becker, S. & Zweckstetter, M. Molecular basis of the dynamic structure of the TIM23 complex in the mitochondrial intermembrane space. *Struct. Lond. Engl. 1993* **22**, 1501–1511 (2014).
261. Bauer, M. F., Sirrenberg, C., Neupert, W. & Brunner, M. Role of Tim23 as voltage sensor and presequence receptor in protein import into mitochondria. *Cell* **87**, 33–41 (1996).
262. *The PyMOL Molecular Graphics System*. (Schrödinger, LLC).
263. Best, R. B. *et al.* Optimization of the additive CHARMM all-atom protein force field targeting improved sampling of the backbone φ, ψ and side-chain χ(1) and χ(2) dihedral angles. *J. Chem. Theory Comput.* **8**, 3257–3273 (2012).
264. Gautier, R. *et al.* PackMem: A Versatile Tool to Compute and Visualize Interfacial Packing Defects in Lipid Bilayers. *Biophys. J.* **115**, 436–444 (2018).
265. Pinot, M. *et al.* Feedback between membrane tension, lipid shape and curvature in the formation of packing defects. *bioRxiv* 389627 (2018). doi:10.1101/389627